Electroweak Corrections to Dilepton-plus-Photon Production at the LHC

Dissertation
zur
Erlangung der naturwissenschaftlichen Doktorwürde
(Dr. sc. nat.)

vorgelegt der
Mathematisch-naturwissenschaftlichen Fakultät
der
Universität Zürich
von
Christoph Meier
aus Deutschland

Promotionskomitee

Prof. Dr. Daniel Wyler	(Vorsitz)
PD. Dr. Ansgar Denner	(Leitung der Dissertation)
Prof. Dr. Thomas Gehrmann	

Zürich 2005

Zusammenfassung

Ziel dieser Arbeit ist die Berechnung elektroschwacher Korrekturen zur hadronischen Produktion von γZ und γW Paaren am LHC, wobei W und Z leptonisch zerfallen. Die experimentelle Hauptmotivation für die Betrachtung dieser Prozesse ist die Möglichkeit, die fundamentalen Wechselwirkungen der Natur auf ihre Eichstruktur zu testen. Jede nicht als Eichtheorie formulierte Theorie sagt im Vergleich zum Standardmodell große, positive Abweichungen im Wirkungsquerschnitt bei hohen Energien voraus. Um der hohen Präzision der LHC-Experimente Rechnung zu tragen, ist die Berechnung von Strahlungskorrekturen zu diesen Verteilungen nötig. Frühere Rechnungen haben hier gezeigt, daß sowohl die QCD-Korrekturen als auch die elektroschwachen Korrekturen bei hohen Energien im allgemeinen sehr groß sind. Da dies auch die Phasenraumregion ist, in der die Effekte von anomalen Vektor-Boson Kopplungen den größten Beitrag liefern, haben Strahlungskorrekturen oft einen beachtlichen Einfluss auf die Ergebnisse der entsprechenden experimentellen Analysen.

Die Berechnung von Wirkungsquerschnitten für Vektor-Boson Paarproduktion wird durch das Auftreten von Resonanzen erschwert, die durch die endliche Zerfallsbreite der betrachteten Vektor-Bosonen beschrieben werden müssen. Dabei treten im allgemeinen jedoch Probleme mit der Eichinvarianz auf. Weiterhin erhalten die elektroschwachen Korrekturen eines solchen Prozesses Beiträge von mehreren hundert Feynman-Diagrammen, was die Berechnung der Amplitude sehr aufwendig macht. Eines der Hauptresultate dieser Arbeit ist deshalb das `Mathematica` Paket `Pole`, das als eine Erweiterung der bereits existierenden Programmpakete `FeynArts` and `FormCalc` funktioniert. Die Grundidee unseres Programms ist die Anwendung der so genannten Leading Pole Approximation auf die Berechnung elektroschwacher Korrekturen. Diese Näherung führt zu einer eichinvarianten Vorschrift zur Beschreibung der Breiteneffekte von Vektor-Boson-Zerfällen, sowie zu einer oft drastischen Reduktion der Anzahl beitragender Diagramme. Unser Paket `Pole` gibt dem Benutzer die Möglichkeit, automatisch die Amplituden eines Prozesses zu generieren, der nicht nur durch den Anfangs- und Endzustand, sondern auch durch einen Zwischenzustand definiert ist. Diese Information wird benutzt, um die Amplituden nach Kombinationen von resonanten Propagatoren aufzuteilen, und um alle nichtresonanten Beiträge zu vernachlässigen. Im Gegensatz zu `FeynArts` erlaubt `Pole` auch hadronische Anfangszustände. Die resultierenden Amplituden können dann als `Fortran`-Code ausgegeben werden, der automatisch an den generischen Phasenraumgenerator `Lusifer` gekoppelt wird. Um eine konsistente

Behandlung der Infrarotdivergenzen und der kollinearen Singularitäten in den virtuellen und reellen Korrekturen zu erreichen, wurde `Lusifer` durch die Implementierung des sogenannten Phase-Space Slicings und der Subtraktionsmethode erweitert. Unser Programmpaket kann auf jeden Prozess mit festem Zwischenzustand angewandt werden, und funktioniert weitgehend unabhängig vom betrachteten Modell. Neben einer Beschreibung der generellen Strategie unser Berechnungen enthält diese Arbeit eine detaillierte Beschreibung der Benutzung und Funktionsweise von `Pole`.

Im letzten Teil dieser Arbeit wenden wir `Pole` zur Berechnung elektroschwacher Korrekturen zu γZ und γW Paarproduktion am LHC an. Während frühere Berechnungen nur die Korrekturen zum Produktionsprozess in Betracht ziehen, und die reellen Korrekturen nur in den Infrarot- und kollinearen Limites oder gar nicht miteinschliessen, berechnen wir die vollständigen resonanten Beiträge zu den elektroschwachen Korrekturen, und behandeln die Bremsstrahlungsbeiträge exakt. Um die automatische Erzeugung der Amplituden und die numerischen Auswertung zu testen, berechnen wir unabhängig die meisten Amplituden ein zweites mal von Hand und führen eine Reihe von Konsistenztests durch. Unsere Resultate zeigen, daß die elektroschwachen Korrekturen zu den Winkelverteilungen der betrachteten Prozesse am LHC im allgemeinen vernachlässigbar sind. Im Gegensatz dazu erhalten wir große negative Korrekturen bei hohen Transversalimpulsen und Energien der Endzustandsteilchen, die genauso groß oder sogar größer als die entsprechenden QCD-Korrekturen sein können. Eine Berücksichtigung unserer Resultate bei der experimentellen Analyse ist deshalb unumgänglich um eine Fehlinterpretation möglicher Abweichungen der experimentellen Verteilungen von den in führender Ordnung berechneten Standardmodellvorhersagen zu vermeiden.

Abstract

Goal of this thesis is the calculation of electroweak corrections to hadronic γZ and γW pair production at the LHC, with the Z boson and W boson decaying into two leptons. Experimentally, the main motivation for considering these processes is the possibility to probe the gauge structure of the fundamental interactions of nature. Compared to the Standard Model, any theory not based on the gauge principle predicts large positive deviations in the considered cross-sections in the high-energy domain. To match the high precision of the LHC experiments and to obtain reliable results from the experimental analysis, the calculation of radiative corrections to these distributions is mandatory. Previous calculations have shown that both the QCD corrections and the electroweak corrections can be rather large in the high-energy domain of phase-space. Since this is also the phase-space region where the effect of non-standard vector-boson couplings is the most pronounced, the radiative corrections have a considerable impact on the outcome of the corresponding experimental analysis.

In calculating cross-sections for vector-boson pair-production one encounters resonances, which have to be described by including the effects of the finite widths of the decaying particles. This leads in general to problems with gauge invariance. Furthermore, the electroweak corrections receive contributions from several hundreds of Feynman diagrams, which may render the calculation quite cumbersome. One of the main results of this thesis is the `Mathematica` package `Pole` which works as a extension of the already existing computer algebra packages `FeynArts` and `FormCalc`. The basic idea is here to employ the Leading Pole Approximation to the calculation of the electroweak corrections. This approximation leads to a gauge-invariant prescription to incorporate finite-width effects in a perturbative calculation and considerably reduces the number of contributing diagrams. Our package `Pole` provides the opportunity to automatically generate amplitudes to processes, which are specified not only by the initial and final state, but also by an intermediate state. This input is then used to divide the amplitudes according to combinations of resonant propagators, and to exclude all diagrams not contributing in Leading Pole Approximation. In contrast to `FeynArts`, `Pole` allows furthermore for hadronic initial states. The so-generated amplitudes can be translated into `Fortran` code, which is automatically linked to the generic Monte-Carlo generator `Lusifer` to perform the phase-space integration. For a consistent treatment of the soft and collinear singularities appearing in the virtual and real corrections, we extended `Lusifer` to incorporate the phase-space slicing technique and the subtraction method. Note that `Pole` is designed to work for any process with a definite intermediate state and for calculations in an arbitrary model. Besides a description of the general strategy of our calculation, this thesis contains a detailed manual of `Pole`.

In the last part of this work, we apply `Pole` to the calculation of the electroweak corrections to γW and γZ production at the LHC. Whereas earlier results take into account only the corrections to the production process and restrict the treatment of the real correc-

tions to the soft and collinear limits or do not consider real corrections at all, we calculate the full leading-pole contributions to the electroweak corrections, and treat the real corrections exactly. To test the amplitude generation as well as the numerical evaluation in the framework of `Pole`, we compare to independent by-hand calculations wherever this was possible, and perform a series of consistency checks. As a result we find, that the electroweak corrections to angular distributions can generally be neglected for the experimental analysis at the LHC. On the other hand, our results for the electroweak corrections to the distributions in the transverse momenta and energies of the final-state particles show large negative contributions of the same size or even larger than the QCD corrections, which well exceed the systematical and statistical errors to be expected at the LHC. Accordingly, our results have to be included in the experimental analysis when probing for the effects of non-standard gauge interactions in order to avoid a misinterpretation of possible deviations of the experimental distributions from the Standard Model leading-order predictions.

Contents

Chapter 1

Introduction

The shutdown of the electron-positron storage ring LEP2 at CERN in autumn 2000 marked the end of one of the most successful experiments in the history of physics. Main goal of this experiment was the measurement of precision observables used to probe the properties and interactions of the elementary particles of nature. In this respect, the most successful model was found to be the Standard Model of Particle Physics, which up to today correctly predicts the experimental results with unprecedented accuracy. From a mathematical point of view, the Standard Model is a gauge theory with spontaneous symmetry breaking. This class of theories permits to associate the fundamental forces acting between the elementary particles with the exchange of gauge bosons. A unified description of the electromagnetic and weak interaction in this framework was first formulated by Glashow, Weinberg and Salam [1, 2, 3] and was followed by the description of the strong interaction known as Quantum Chromodynamics [4, 5, 6]. A consistent description of the gravitational force has up to today not been achieved.

In spite of the big successes of the Standard Model, most people therefore assume the existence of an underlying theory describing all four fundamental interactions of nature. To explain the current experimental results, this theory has to reproduce the predictions of the Standard Model in the LEP energy region below 209 GeV. To investigate deviations of the underlying theory from the Standard Model, it is thus necessary to perform experiments on higher energy scales. However, the use of an electron-positron ring accelerator like LEP is limited by the large energy loss due to synchrotron radiation. Accordingly, two different accelerator concepts have been chosen for future experiments. The idea of the Next Linear Collider (NLC) is to avoid synchrotron radiation by accelerating the colliding electrons and positrons along a straight line in opposite directions. As an alternative, the 1.8 TeV proton-anti-proton ring accelerator Tevatron at Fermilab is based on the idea to suppress synchrotron radiation by using more massive collision partners. The same concept is currently about to being realized in the construction of the Large Hadron Collider (LHC) at CERN, where proton-proton collisions at a centre-of-mass collision energy of 14 TeV are to be investigated. Whereas the run II of Tevatron was launched recently, the LHC and the NLC will not start data taking before 2007 and 2020, respectively.

The primary goal of future collider experiments is the detection of the so-called Higgs particle, the last particle predicted by the Standard Model which has so far not been experimentally observed. Furthermore, the experiments will look for effects of theories beyond the Standard Model, as for example Supersymmetry or theories involving Large Extra Dimensions. One of the most important questions is if such a theory can be described in the framework of a gauge theory like the Standard Model. This question can be addressed by measuring the couplings of the gauge bosons, which are the most direct consequence of the formulation of a given model as a gauge theory. The Standard Model predictions for the couplings of the gauge bosons to the fermions have been confirmed by the LEP2 experiment to an accuracy of 0.1-1% [7]. However, the triple and quartic couplings of the gauge bosons among each other have been determined to much lower accuracy [8, 9]. Since the form and coupling strength of these interactions allow for the direct conclusion if the theory underlying the fundamental interactions of nature involves the same gauge structure as the Standard Model, it will be one of the primary goals of future experiments to determinate the vector-boson self-couplings experimentally. The corresponding results can then be used to probe for deviations from the Standard Model predictions as a signal for theories which incorporate modified or entirely new vector-boson interactions.

In practice, the gauge sector of the Standard Model is usually analyzed in the framework of the phenomenology of *anomalous vector-boson couplings*. The idea is here to keep the particle content of the Standard Model, but to extend the electroweak interactions to all gauge-boson couplings respecting Lorentz invariance. This leads to a deviation of the Standard Model gauge couplings on one hand, and to the appearance of entirely new gauge couplings like e.g. $ZZ\gamma$ or $Z\gamma\gamma$ on the other hand. To reduce the number of possible terms, one often imposes additional requirements such as a maximal dimensionality for the newly introduced operators, C and P invariance and electromagnetic gauge invariance. To analyze the implications of these anomalous vector-boson couplings phenomenologically, the latter are parameterized by a set of new coupling constants [10] and are added to the Standard Model Lagrangian, where the parameterization is chosen such that one retains the Standard Model if setting anomalous coupling constants to zero. Note that the anomalous couplings generally violate unitarity in the high-energy limit, and have thus to be suppressed kinematically by multiplying them with form factors. Moreover, the additional terms in the gauge sector are not renormalizable, such that the corresponding Lagrangian has to be treated as an effective model resulting from the low-energy limit of a more generally valid renormalizable theory. Keeping this in mind, the modified Lagrangian can be used to calculate cross-sections for processes involving couplings of vector bosons among each other, which can then be fitted to the measured reaction rates to obtain numerical values for both, the standard and the anomalous gauge couplings. Any deviation of the anomalous coupling constants from zero would here provide a clean signal that the fundamental interactions of nature are to be described by a theory different from the Standard Model.

For the experimental analysis, the effects of anomalous couplings are best observed in phase-space regions where these effects are especially sizable or where the Standard Model background is especially small. In this respect the measurement of the cross-sections and kinematical distributions for vector-boson pair-production processes turns out to be especially suited. Nonzero values for the anomalous couplings lead here to a violation of gauge cancellations, which should be visible in the LHC experiments as a considerable excess of events in the high-energy domain of the considered phase-space. In case of non-observation of this effect, the experimental results can be used to put bounds on the anomalous couplings.

Another interesting physical observable is the so-called radiation zero of the partonic amplitudes for $W\gamma$ and WZ production. For a certain kinematical configuration, these amplitudes vanish for all helicity combinations, which manifests itself in a dip in the angular distributions of the total cross-section (see e.g. Ref.[11] and references therein). On the other hand, the radiation zero arises from gauge cancellations, which have been shown to be a unique property of the Standard Model [12]. Any deviation from the gauge structure of the Standard Model therefore tends to fill the dip at the radiation zero, thus providing a clean possibility to probe for physics beyond the Standard Model.

Finally, vector-boson pair-production processes provide important background contributions in the search for new particles not appearing in the Standard Model. For example, γZ production with the Z boson decaying into a pair of neutrinos will be measured in the detector as a gamma along with missing energy. The same signature is expected for processes where the photon is produced in association with one or more heavy particles which escape the detector without being seen, either because they are weakly interacting or because they dissociate into invisible decay products. Many extensions of the Standard Model predict the existence of such processes. For example, some string models [13, 14, 15] incorporate gravity propagating in Large Extra Dimensions and predict the possibility to observe the production of a photon along with the invisible graviton. Moreover, models incorporating Supersymmetry with a Gauge-Mediated Supersymmetry Breaking mechanism [16, 17, 18, 19] typically predict that the gravitino is the lightest supersymmetric particle. The latter is only weakly interacting and stable if R-parity is conserved. The same models predict that the next-to-lightest supersymmetric particle may be the neutralino, which then decays into a gravitino plus a photon. Accordingly, a process where the neutralino is pair-produced with a gravitino will lead to a final state containing two gravitinos and a photon. Since the gravitino is only weakly interacting, it will escape undetected from the detector, resulting in a detection signature of one photon and missing energy, as in the case of $Z\gamma$ production with the Z decaying into neutrinos. The photon energy has to balance the mass of the undetected particles, such that the missing energy distribution will in this case show an excess of events in the high-energy region as compared to the Standard Model. Note that this effect appears independently of the considered model for all processes with a final state containing a photon along with a non-standard, undetectable heavy particle.

Experimental results for the reaction rates of vector-boson pair production at LEP2 and the Tevatron can be found in Ref.[20, 21] and Ref.[22, 23, 24, 25, 26], respectively. In addition, the radiation zero of the $W\gamma$ amplitude has been studied in Ref.[27, 28]. Finally, a detailed study of processes leading to the production of a photon plus missing energy can be found in Ref.[29] for LEP2 and in Ref.[30] for the Tevatron. All these experimental results are perfectly matched by the Standard Model predictions, and thus do neither provide a hint for the existence of anomalous gauge-boson couplings nor do they point towards the production of any non-standard heavy particles. On the other hand, the production rates for vector-boson pairs at LEP2 and the Tevatron are relatively low due to the comparably modest luminosity, such that the experimental constraints still leave much space for Physics beyond the Standard Model. At the LHC, on the other hand, the experiments will collect thousands of events for vector-boson pair production [31], which will lead to much more restrictive bounds on the anomalous coupling constants and the production rates for new particles. To match the precision of these experiments, the cross-sections for vector-boson pair-production processes have to be calculated beyond leading order. Monte-Carlo programs incorporating the complete amplitudes for all pair-production processes including QCD-corrections and anomalous couplings have been presented in Ref.[32] and Ref.[33, 34]. As a general feature, the QCD-corrections may modify the leading-order cross-sections for vector-boson pair production at the LHC by a positive amount of several tens of per cent and have thus a considerable impact on the experimental analysis of the anomalous gauge-boson couplings.

At this point, the question arises if the electroweak corrections to vector-boson pair-production processes at the LHC lead to similarly sizable effects. For hadron collider experiments, the corresponding contributions are usually only taken into account as universal radiative corrections to e.g. the running of α or the ρ-parameter. This approach is based on the common belief that the electroweak corrections only contribute significantly in the high-energy domain, where the statistics at the LHC will be too low to extract any physics from the experimental data. The leading logarithmic electroweak corrections for WW, WZ and ZZ production have been calculated in Ref.[35, 36], whereas corresponding results for γW production and the full corrections to γZ production have been presented in Ref.[36] and Ref.[37], respectively. All these publications point to a negative contribution of the electroweak corrections of up to -20%, which well exceeds the statistical errors. The reason for their considerable size is that the electroweak corrections contain so-called Sudakov Logarithms, i.e. double logarithms of the process energy over the vector-boson mass, which enhance the size of the corrections in the high-energy regions of phase-space. As was said above, this is also the phase-space region were the effects of the anomalous couplings and the effects of the production of so far unknown heavy particles are the most pronounced. The electroweak corrections have thus to be taken into account to make sure that an experimentally observed deviation from the QCD-corrected Standard Model predictions due to electroweak effects is not misinterpreted as a signal for physics beyond the Standard Model.

Whereas the latest results for the electroweak corrections to WW, WZ and ZZ production have been calculated including the corrections to the decay process as well as real corrections, the corrections to γW have been calculated in leading logarithmic order and for the production subprocess only. The corrections to γZ production have so far only been determined for an on-shell Z, i.e. without taking into account decay effects. Furthermore, the real corrections for both processes have been included only in the soft and collinear limits or not at all. The goal of this thesis is therefore the calculation of the electroweak corrections to the cross-section and the kinematical distributions for the full processes

$$P + P \to V + \gamma \to f_3 + \bar{f}_4 + \gamma + (\gamma), \qquad V = W, Z, \tag{1.1}$$

including real corrections. Here P denotes the proton, and we restrict ourselves to processes with the leptonic final-state fermions $f_3, f_4 = e, \mu, \nu_e, \nu_\mu, \nu_\tau$. Final states containing quarks make the inclusion of jet definitions necessary, which goes beyond the scope of our work presented here.

To outline this thesis, we discuss the strategy of our calculation in Chapter 2. We calculate the electroweak corrections in the so-called Leading Pole Approximation [38, 39, 40, 41, 42], whereas for the real corrections we use the full matrix elements. For a consistent treatment of soft and collinear singularities, we discuss two independent methods known as the phase-space slicing technique and the subtraction method. Since our approach can be applied largely independent of the considered process, we chose to automatize our strategy in a `Mathematica` package called `Pole`, which works as an extension of the computer-algebra programs `FeynArts` and `FormCalc`. In short, our package provides the user with the possibility to automatically generate the necessary amplitudes for the calculation of 1-loop corrected cross-sections in Leading Pole Approximation. For numerical evaluation, the amplitudes can be translated into `Fortran` code, which comes with a set of generic driver files. The latter incorporate the generic Monte-Carlo generator `Lusifer` [43] to integrate the squared amplitudes over phase-space. Whereas our package has so far been tested for the processes (1.1) relevant to our work only, it is designed to be applicable to calculations of the hadronic or partonic cross-sections for any process involving a definite intermediate state. In Chapter 3 and Chapter 4, we provide a detailed manual of the amplitude generation and the numerical evaluation in the framework of `Pole`. Finally, Chapter 5 contains a discussion of the input and tests used to demonstrate the validity of our approach. In the same chapter, we present and discuss numerical results for the electroweak corrections to total cross-section and experimentally interesting distributions for the processes (1.1).

In Appendix A, we summarize the main features of the Weyl-van der Waerden formalism as presented in Ref.[44]. In the framework of `Pole`, this formalism is used to reduce fermionic chains to Weyl-spinor products, where we largely follow the approach discussed in Ref.[45]. Appendix B contains our analytical results for the amplitudes of the Born process, the non-factorizable virtual corrections as well as the real corrections to the partonic processes corresponding to (1.1), which we calculated by hand to cross-check the amplitude generation as implemented in `Pole`. Our approach to the treatment of the

non-factorizable corrections for a general process in the computer-algebraical amplitude generation is presented in Appendix C, whereas Appendix D contains the necessary formulas for the two methods used to deal with the soft and collinear singularities. Finally, the main features of the Monte-Carlo phase-space integration as implemented in `Lusifer` is reviewed in Appendix E.

Chapter 2

Strategy of the Calculation

In this chapter we give an overview over a general strategy for the calculation of loop corrections to the hadronic cross sections for processes involving three or more particles in the final state. One here encounters three major problems. The first problem arises from the fact that for hadronic initial states, the colliding particles are not the hadrons, but rather given by the partonic substructure of the latter. The cross-section of such a process generally depends on effects of the hadron binding which are not accessible by perturbation theory. As discussed in Section 2.1, by carefully separating low-energy and high-energy contributions, the hadronic cross-section can generally be written as a convolution of the so-called Parton Distribution Functions to be measured experimentally with a perturbatively accessible cross-sections for the partonic subprocesses.

The second problem arises if one is to calculate virtual corrections to the partonic cross-section. For three or more particles in the final state, the number of diagrams contributing to the corresponding amplitudes can be quite large. Apart from this rather technical complication, one also encounters the conceptional problem that processes involving multi-particle final-states generally involve the production and decay of unstable particles. As discussed in Section 2.2, this requires to take into account the experimental fact that such particles have a finite decay width. In our work, this is accomplished by means of the *Pole-Expansion Method*, which has also the advantage to reduce the number of diagrams contributing to a given process.

The third problem is given by the appearance of soft and collinear divergences in the virtual corrections, which complicate the numerical evaluation of the partonic cross-section. As pointed out in Section 2.3, these singular terms cancel if taking into account the real corrections to the considered process. However, this cancellation requires a careful book-keeping of the divergent terms, and we present two methods suitable to keep the soft and collinear singularities under control.

Finally, in Section 2.4 we summarize our strategy in a Master Formula for the hadronic cross-section.

2.1 The Hadronic Cross Section

The main difficulty in calculating observables for hadron collider experiments arises from the hadron being a bound state of partons rather than an elementary particle. The confinement of the partons to the hadronic bound state has its origin in the fact that the coupling constant of the strong interaction rises with falling energy and thus with growing distance. As a consequence, the parton binding within a hadron is generally not accessible by perturbation theory, which requires a small value of the coupling constant. On the other hand, when considering hadron collisions, the initial state of the actual reaction is not given by the colliding hadrons, but by the partons of which the considered hadrons are composed. Since the coupling constant of the strong interactions decreases with increasing energy and thus with decreasing distance, the cross-section of the corresponding partonic process can be calculated in perturbation theory. Generally, one therefore writes the cross-section of a hadronic process as a convolution of the perturbatively calculated partonic cross-section times the so-called Parton Distribution Functions (PDFs)

$$\sigma_{\mathrm{P_1P_2}}(S) = \sum_{q_1,q_2=u,\bar{u},..} \int_0^1 \mathrm{d}x_1 \int_0^1 \mathrm{d}x_2 \Phi_{q_1|P_1}(x_1)\Phi_{q_2|P_2}(x_2)\sigma_{q_1q_2}(x_1x_2S), \tag{2.1}$$

where the latter are supposed to parametrize the low-energetic parton binding within the hadron. They can be interpreted as probability distributions for finding the parton q_i in the hadron P_i with a fraction x_i of the total hadron momentum. As part of the hadronic binding structure, the PDFs are not accessible by perturbation theory, and are thus to be determined experimentally. This is usually done in Deep Inelastic Scattering experiments, as will be discussed below.

As a complication, perturbation theory does not lead automatically to a separation of high-energy and low-energy contributions, and the perturbatively calculated partonic cross-section in the integrand of (2.1) generally contains a mixture of both. To be explicit, the partonic cross section to a given process in first-order perturbation theory generally receives three types of contributions

$$\sigma_{q_1q_2}(\hat{s}) = \sigma^{(0)}_{q_1q_2}(\hat{s}) + \sigma^{\mathrm{virt}}_{q_1q_2}(\hat{s}) + \sigma^{\mathrm{real}}_{q_1q_2}(\hat{s}), \tag{2.2}$$

where the term $\sigma^{(0)}_{q_1q_2}$ denotes the *Born cross-section*, $\sigma^{\mathrm{virt}}_{q_1q_2}$ are the *virtual corrections*, $\sigma^{\mathrm{real}}_{q_1q_2}$ are the so-called *real corrections* or *Bremsstrahlung contributions* and we wrote $\hat{s} = x_1x_2S$ for the partonic centre-of-mass energy.

Experimentally speaking, the real corrections have to be included to account for the fact that a detector in a realistic experiment is not sensitive to particles which are produced with too low energies or with too small angles relative to the particle emitting them. However, the emission angle as well as the energy of a final-state particles are restricted from below by the mass of the emitted particle and the mass of the emitting particle. Only light particles can therefore have a small enough energy to escape the detector without

being seen, and only light particles emitted by light particles can have small enough angles with respect to their emitter to escape measurement. As a consequence, the one-loop cross-section for a given process receives contributions from processes with an undetected extra massless particle in the final state. Due to the coupling of this extra particle, the real corrections are of the same order in the coupling constant as the virtual corrections and thus contribute to the same order of the perturbation series.

From a technical point of view, the real corrections have to be added to the virtual corrections to insure the finiteness of the physical cross section. In general, the virtual corrections to a given process contain infrared as well as collinear singularities. Infrared singularities always appear if a massless virtual particle is emitted with vanishing energy, whereas collinear singularities result from contributions, where a virtual, massless particle is emitted by an also massless particle in the limit of vanishing emission angle. The regularization of the collinear singularities can be achieved by introducing a small mass parameter for the emitting particle, whereas the infrared divergences can be regularized by additionally addressing a finite but small mass to the emitted particle. The infrared and collinear singularities then show up as terms of the form $\log[\lambda^2]$ and $\log[m^2]$, respectively, where λ^2 and m^2 are the regularization parameters for the masses of the emitted and the emitting particle. After regularization, the partonic cross-section thus depends logarithmically on the unphysical mass parameter λ as well as on the light fermion masses m_f, giving rise to large logarithmic contributions. The infrared singularities [46] and, for inclusive enough observables, also the collinear singularities originating from the final state [47, 48] cancel when adding the Bremsstrahlung contributions to the virtual corrections. However, this cancellation requires careful bookkeeping of the logarithms arising from the infrared and collinear singularities, as we will see in Section 2.3. Furthermore, the partonic cross-section still depends on initial-state collinear singularities, i.e. on logarithms in the masses of the initial-state partons. Technically speaking, this constitutes a problem, since the initial state quarks are not free particles but bound states, such that it is not clear what is meant by a mass of such a state. This in turn leads to a large uncertainties in the evaluation of the above logarithms in the quark masses and thus of the virtual corrections.

For hadronic reactions, this problem can be cured by considering the experimental determination of the PDFs in some more detail. As was mentioned above, the PDFs are not accessible by perturbation theory and are generally determined in Deep Inelastic Scattering (DIS) experiments, as e.g. neutrino-nucleon scattering. To outline the method, the hadronic cross-section of the considered DIS experiment is first written as a convolution of the partonic cross-section with the Parton Distribution Function of the initial-state parton

$$\sigma_{\mathrm{P}}^{\mathrm{DIS}}(S) = \sum_{q=u,\bar{u},..} \int_0^1 \mathrm{d}x \Phi_{q|P}(x) \sigma_q^{\mathrm{DIS}}(xS), \tag{2.3}$$

leading to an expression similar to (2.1). The partonic DIS cross-section σ_q^{DIS} can then again be calculated by perturbation methods, whereas the hadronic cross-section $\sigma_{\mathrm{P}}^{\mathrm{DIS}}$ is

determined experimentally. The only unknown quantities in the above equation are given by the PDFs, which can therefore be obtained by a fit of the phenomenologically calculated right-hand side to the experimental results for the left-hand side. However, as was said above, perturbation theory does not lead automatically to a separation of the low-energy hadron binding from the high-energy perturbative domain. The partonic cross-section in (2.3) contains initial-state collinear singularities as in the case of the hadronic cross-section (2.1). What is more, the actual form of these singular terms is *universal*, i.e. they appear in exactly the same form in (2.3), (2.1) and any other process involving the same hadrons in the initial state. Technically speaking, the initial-state collinear singularities arise from the phase-space region of low momentum transfer, such that in the division of the hadronic cross-section in high-energy and low-energy terms discussed above, they rather contribute to low-energy terms parameterized by the PDFs rather than to the high-energy terms parameterized by the partonic cross-section. Experimentally speaking, the singularities arise from collinear initial state radiation, in which case the emitted particle cannot be distinguished by measurement from the colliding hadron, and thus contributes to the hadronic binding rather than to the partonic collision. In short, the low-energy terms should be taken as a contribution to the universal binding property of the hadron, and thus to the PDFs, rather than as a contribution to the partonic cross-section.

The above considerations can be taken into account by noticing, that the only constraint on the exact form of the hadronic DIS cross-section (2.3) is the universality of the quantity convoluted with the partonic cross-section. In fact, one is always free to subtract universal terms from the partonic cross-section, such that in the subsequent fit these terms are measured as a contribution of the PDFs. In this way, one does not determine the parton distributions in (2.3), but rather redefined PDFs

$$\overline{\Phi}_{q_i|P_i}(x_i,\mu_{\rm F}) = \Phi_{q_i|P_i}(x_i) + \frac{\alpha}{2\pi}\delta\Phi_{q_i|P_i}(x_i,\mu_{\rm F}), \qquad i=1,2 \tag{2.4}$$

which contain all the low energy terms of the partonic DIS cross-section. The quantity $\mu_{\rm F}$ is the so-called factorization scale, which is given by an in principle arbitrary energy scale and is introduced to define the borderline between low-energy and high-energy regime. In DIS, it is usually set to the momentum transfer between the colliding particles. The dependence of the total cross-section on the factorization scale remains manifest for a fixed-order perturbative calculation, but decreases with increasing order and vanishes in the limit of infinite order in perturbation theory. It is in this sense, that the dependence of the hadronic cross-section on the factorization scale can be used as a check on the quality of the perturbative expansion up to the considered order.

Since both, the original PDFs $\Phi_{q_i|P_i}$ and the universal low-energy terms $\delta\Phi_{q_i|P_i}$ are universal, the so-determined parton-distribution functions can now be used for any process involving the same hadrons in the initial state. However, to do so one has first to remove two ambiguities arising from the above experimental definition of the PDFs. The first problem is given by the fact, that a general process usually involves an energy scale differ-

ent from the DIS momentum transfer. Since the low-energy terms and with them also the PDFs depend on this scale, one has to find a way to perform an evolution of the PDFs from DIS scale to the typical energy scale of the considered process. This evolution is governed by the GLAP-equations [49, 50], a set of differential equations in the factorization scale, which can be solved using the experimentally determined PDFs as an initial condition. The second ambiguity arises from the fact that whereas the exact form of the collinear singularities to be reabsorbed in the PDFs is fixed, one is free to include any additional universal non-singular term appearing in the partonic cross-section. To remove this ambiguity, one has therefore to fix a *factorization scheme*, which specifies which terms were included in the PDFs before determining them experimentally. The two most common factorization schemes are the so-called DIS-scheme and the $\overline{\text{MS}}$-scheme. Whereas PDFs determined using the DIS-scheme also contain universal non-singular terms, we will use the $\overline{\text{MS}}$-scheme in this work, where only singular terms are reabsorbed in the PDFs.

Having in this way uniquely defined the PDFs at arbitrary energy scales, the latter can now be used to re-express (2.1) in terms of the measured PDFs by inserting (2.4)

$$\begin{aligned}
\sigma_{\mathrm{P_1P_2}}(S) &= \sum_{q_1,q_2=u,\bar{u},..} \int_0^1 \mathrm{d}x_1 \int_0^1 \mathrm{d}x_2 \Phi_{q_1|P_1}(x_1)\Phi_{q_2|P_2}(x_2)\sigma_{q_1q_2}(x_1x_2S) \\
&= \sum_{q_1,q_2=u,\bar{u},..} \int_0^1 \mathrm{d}x_1 \int_0^1 \mathrm{d}x_2 \overline{\Phi}_{q_1|P_1}(x_1,Q^2)\overline{\Phi}_{q_2|P_2}(x_2,Q^2)\sigma_{q_1q_2}(x_1x_2S) \\
&\quad - \frac{\alpha}{2\pi} \sum_{q_1,q_2=u,\bar{u},..} \int_0^1 \mathrm{d}x_1 \int_0^1 \mathrm{d}x_2 \; \sigma_{q_1q_2}(x_1x_2S) \\
&\qquad \times \left(\delta\Phi_{q_1|P_1}(x_1,\mu_\mathrm{F})\overline{\Phi}_{q_2|P_2}(x_2,Q^2) + \delta\Phi_{q_2|P_2}(x_2,\mu_\mathrm{F})\overline{\Phi}_{q_1|P_1}(x_1,Q^2)\right) \\
&\quad + \mathcal{O}(\alpha^2),
\end{aligned} \tag{2.5}$$

where Q is the typical energy scale of the considered process up to which the PDFs have been evolved. As we show in Appendix D.1, the corrections term in the last two lines can by simple substitution be written as

$$\begin{aligned}
&-\frac{\alpha}{2\pi} \sum_{q_1,q_2=u,\bar{u},..} \int_0^1 \mathrm{d}x_1 \int_0^1 \mathrm{d}x_2 \left(\delta\Phi_{q_1|P_1}(x_1,\mu_\mathrm{F})\overline{\Phi}_{q_2|P_2}(x_2,Q^2)\right. \\
&\qquad\qquad \left. + \delta\Phi_{q_2|P_2}(x_2,\mu_\mathrm{F})\overline{\Phi}_{q_1|P_1}(x_1,Q^2)\right) \sigma_{q_1q_2}(x_1x_2S) \\
&= -\frac{\alpha}{2\pi} \sum_{q_1,q_2=u,\bar{u},..} \int_0^1 \mathrm{d}x_1 \int_0^1 \mathrm{d}x_2 \overline{\Phi}_{q_1|P_1}(x_1,Q^2)\overline{\Phi}_{q_2|P_2}(x_2,Q^2)\sigma^{\mathrm{PDF}}_{q_1q_2\mathrm{sing.}}(\hat{s},Q^2),
\end{aligned} \tag{2.6}$$

where the mass-singular correction term $\sigma^{\mathrm{PDF}}_{q_1q_2,\mathrm{sing.}}$ is generally given by a convolution of the partonic cross-section times the so-called *splitting kernels*. Inserting (2.6) in (2.5), the

hadronic cross-section

$$\sigma_{\mathrm{P_1P_2}}(S,Q^2) = \sum_{q_1,q_2=u,\bar{u},..} \int_0^1 \mathrm{d}x_1 \int_0^1 \mathrm{d}x_2 \overline{\Phi}_{q_1|P_1}(x_1,Q^2)\overline{\Phi}_{q_2|P_2}(x_2,Q^2)\sigma^{\mathrm{IR-safe}}_{q_1q_2}(x_1x_2S,Q^2), \tag{2.7}$$

is now given by a convolution of the experimentally measured PDFs with a redefined partonic cross-section

$$\sigma^{\mathrm{IR-safe}}_{q_1q_2}(\hat{s},Q^2) = \sigma_{q_1q_2}(\hat{s}) - \sigma^{\mathrm{PDF}}_{q_1q_2,\mathrm{sing}}(\hat{s},Q^2). \tag{2.8}$$

An analytic expression for the correction term $\sigma^{\mathrm{PDF}}_{q_1q_2,\mathrm{sing.}}(\hat{s},Q^2)$ is given in Appendix D.1, where we discuss the treatment of the initial-state collinear singularities in more detail. It is this term which corrects for the fact that if one simply inserts the experimentally determined PDFs into the hadronic cross-section (2.1), the latter contains the universal low-energy terms twice, once as part of the PDFs and once as part of the partonic cross-section. The low energy terms, and with them the initial-state collinear singularities, thus cancel in the sum (2.8), and the partonic cross-section is now *infrared safe*, which means that it does not contain any infrared or collinear divergences anymore.

2.2 The Pole Expansion Method

In the two following sections, we discuss our approach for the calculation of the first two contributions to the partonic cross-section (2.2), which are given by the Born cross-section as well as the virtual corrections. Apart from the large number of diagrams contributing to the virtual corrections, one here encounters the problem that both, the amplitude for the Born cross-section and for the virtual correction receive contributions from diagrams involving the production and decay of unstable particles. Restricting ourselves for simplicity to the case of one resonance, the amplitude corresponding to such diagrams is proportional to the resonant propagator

$$\mathcal{A}_{q_1q_2,V}(k^2) \propto \frac{1}{k^2 - m^2_{0,V}}, \tag{2.9}$$

where k is the momentum and $m_{0,V}$ the bare mass of the unstable particle. The amplitude therefore exhibits a singularity at the pole $k^2 = m^2_{0,V}$. This divergence is of course unphysical, since the resonance of a decaying particle always has a finite width which shifts the propagator pole to the complex plane

$$m^2_{0,V} \to M^2_V - \mathrm{i}\mathrm{M_V}\Gamma_\mathrm{V}, \tag{2.10}$$

where M_V and Γ_V denote the physical mass and width of the unstable particle, respectively. In perturbation theory, the finite width of an unstable particle arises naturally from higher-order corrections. This is because the propagator of the unstable particle receives corrections in form of self-energy insertions, which have to be summed up to infinite order. Here and in the following we assume the use of some renormalization scheme, which defines

the renormalized mass m_V and the renormalized self-energy Σ in terms of the bare mass $m_{0,V}$ and the unrenormalized self-energy Σ_0 by

$$m_{0,V}^2 - \Sigma_0(k^2) = m_V^2 - \Sigma(k^2), \tag{2.11}$$

such that the resummation yields

$$\mathcal{A}_{q_1 q_2, V}(k^2) = \frac{W(k^2)}{k^2 - m_{0,V}^2} \sum_{n=0}^{\infty} \left(\frac{-\Sigma_0(k^2)}{k^2 - m_{0,V}^2} \right)^n = \frac{W(k^2)}{k^2 - m_V^2 + \Sigma(k^2)}. \tag{2.12}$$

The problematic propagator becomes in this way regularized by the renormalized self-energy as the decaying particle approaches its mass shell. In (2.12), the quantity $W(k^2)$ contains the Born contribution and virtual corrections to the production and decay subprocesses and is thus regular at $k^2 = m_V^2$. In a next step, one has to divide the renormalized self-energy in the denominator of (2.12) in contributions to the physical mass and in contributions to the physical width to yield a consistent definition of these quantities. A gauge-invariant way to obtain such definitions is the so-called *Pole Definition*. The basic idea is to define the physical mass, as in the case of stable particles, as the zero of the inverse propagator. However, after the resummation (2.12) this zero is in general complex, such that one has to introduce a complex physical mass μ_V by

$$\mu_V^2 = m_V^2 - \Sigma(\mu_V^2). \tag{2.13}$$

The physical mass M_V and the corresponding width Γ_V can then be defined by

$$\mu_V^2 = M_V^2 - \mathrm{i} M_V \Gamma_V, \tag{2.14}$$

such that for $k^2 \approx M_V^2$ the inverse Propagator reads

$$\begin{aligned} k^2 - m_V^2 + \Sigma(k^2) &= k^2 - m_V^2 + \Sigma(\mu_V^2) + (k^2 - m_V^2)\Sigma'(\mu_V^2) + \mathcal{O}((k^2 - \mu_V^2)^2) \\ &\approx \left(k^2 - M_V^2 + \mathrm{i} M_V \Gamma_V\right) \left(1 + \Sigma'(\mu_V^2)\right). \end{aligned} \tag{2.15}$$

A perturbative definition of the pole mass M_V and the pole width Γ_V can be obtained by setting

$$\mu_V^2 = M_V^2 - \mathrm{i} M_V \Gamma_V = m_V^2 - \Sigma(M_V^2 - \mathrm{i} M_V \Gamma_V). \tag{2.16}$$

Expanding on the right-hand side the self-energy in Γ_V and equating real and imaginary parts of both sides, one is left with two interdependent equations in M_V and Γ_V, which can be solved to yield

$$\begin{aligned} M_V^2 &= m_V^2 - \mathrm{Re}\Sigma(m_V^2) - \mathrm{Im}\Sigma(m_V^2)\mathrm{Im}\Sigma'(m_V^2) + \mathcal{O}\left(\alpha^3\right) \\ M_V \Gamma_V &= \mathrm{Im}\Sigma(m_V^2) \left[1 - \mathrm{Re}\Sigma'(m_V^2) + \left(\mathrm{Re}\Sigma'(m_V^2)\right)^2 - \frac{1}{2}\mathrm{Im}\Sigma(m_V^2)\mathrm{Im}\Sigma''(m_V^2) + \mathcal{O}\left(\alpha^3\right)\right]. \end{aligned} \tag{2.17}$$

Note that up to first order in perturbation theory, the definition of the pole mass corresponds exactly to the definition of the on-shell mass of the unstable particle. On the other hand, the on-shell mass definition breaks gauge invariance in calculations beyond one loop [51], but the Pole Definition is gauge-independent to all orders. Inserting (2.15) in (2.12), one is left with

$$\mathcal{A}_{q_1 q_2, V}(k^2) = \frac{W(k^2, \ldots)}{(k^2 - M_V^2 + \mathrm{i} M_V \Gamma_V)\,(1 + \Sigma'(\mu_V^2))}, \tag{2.18}$$

and the amplitude is finite as the unstable particle approaches its mass shell.

However, whereas the Pole Definition of the physical mass and the corresponding width is gauge-invariant, the introduction of a finite width into a perturbatively calculated amplitude of fixed order leads in general to a gauge dependence of the calculated observables. This is because in a perturbative calculation, the symmetries of the full amplitude are only respected order by order in the coupling constant, but the resummation procedure described above mixes different orders of perturbation theory.

Several methods to include finite-width effects in a perturbative calculation without violating gauge invariance have been discussed in literature [38, 39, 40, 41, 52, 53, 54, 55, 56, 57, 58, 59, 60]. A first commonly used method is the *Narrow-Width Approximation* (NWA). The idea of this approximation is to write the cross section for a process including the production and decay of an unstable particle as the product of the cross section for the production subprocess and the cross section for the decay subprocess

$$\sigma_V^{\mathrm{NWA}} = \sum_{\lambda_V} \sigma^{\lambda_V, \mathrm{prod}}(k_V^2 = M_V^2) \times \mathrm{Br}(\lambda_V, k_V^2 = M_V^2), \tag{2.19}$$

where $\sigma^{\lambda_V, \mathrm{prod}}(k_V^2 = M_V^2)$ is the cross-section for the on-shell production of the decaying particle V, $\mathrm{Br}(\lambda_V, k_V^2 = M_V^2)$ denotes the branching ratio for the subsequent decay and the sum in (2.19) runs over the physical polarizations of V. In NWA, gauge invariance is guaranteed by factorizing the cross section into two separately gauge-invariant parts for production and decay of the unstable particle. On the other hand, all propagator effects and all corrections of the order of width over mass of the resonance are neglected. In the case of the Standard Model, these corrections are of the order $\Gamma_V/M_V \approx 1/40$ for $V = W, Z$, i.e. they contribute with 2.5% of the Born cross section to the full result. This is also of the order of the corrections in first-order perturbation theory in many perturbative calculations, such that keeping finite-width effects in such a calculation is inevitable to obtain consistent results. On the other hand, the NWA has the advantage that only loop corrections to the production and decay suprocesses contribute, which may reduce the number of diagrams and thus the amount of work considerably.

Another possibility for a gauge-invariant implementation of a finite width in a perturbatively calculated amplitude is given by the *Complex Mass Scheme* [54]. Here one intends to preserve gauge invariance by introducing the finite width already on the level of the

Lagrangian. This can be done by replacing the mass term for the unstable particle by

$$\Delta\mathcal{L}_V = m_V^2 V_\mu V^\mu \longrightarrow (M_V^2 - \mathrm{i}M_V\Gamma_V)V_\mu V^\mu + \mathrm{i}\Gamma_V M_V V_\mu V^\mu. \tag{2.20}$$

The first term results then in a complex mass for the particle V, as well as a complex mixing angle $\cos\theta_W = M_W/M_Z$ in the case of the Standard Model, whereas the second term can be treated perturbatively as a two-particle interaction. However, the Complex Mass Scheme introduces a finite width for *all* propagators appearing in a diagram, even for those that cannot become resonant for kinematical reasons. For example, in deep-inelastic scattering the W boson exchanged in the t channel obtains a width in the Complex Mass Scheme, even though the imaginary part of the self-energy vanishes for space-like momenta. The treatment of an unstable particle propagator therefore depends on the kinematics of the process in the sense, that only those propagators which kinematically can become resonant should be resummed to get a finite width. All other propagators should be treated perturbatively. On the other hand, the error introduced by addressing a finite width to all propagators is of higher-order in perturbation theory, and can thus be neglected. Furthermore, the Complex Mass Scheme is valid in the whole phase-space region of the considered process, and can thus also be applied around the production threshold. Compared to the Narrow-Width Approximation, the Complex Mass Scheme has the main disadvantage that it does not reduce the number of diagrams to be calculated, and that quite complicated loop integrals with complex mass arguments may occur.

In this thesis, we use the so-called *Pole-Expansion Method* discussed in Ref. [38, 39, 40, 41, 42]. As to be discussed below, this method combines the above-discussed advantages of the Complex Mass Scheme and the Narrow Width Approximation in the sense that it provides a gauge-invariant prescription to include finite width effects *and* reduces the number of contributing diagrams. The basic idea of the Pole-Expansion Method is to perform a double expansion of the full amplitude, a perturbative one in the coupling constant and the second one in the distance of the squared momentum of the unstable particle from the pole. In this way, one is able to make sure that finite-width effects of the same order of magnitude as corrections of higher order in perturbation theory are not neglected. As a starting point, the amplitude (2.12), summed up to infinite order in perturbation theory, is split into a *resonant* part showing a singular behavior as the decaying particle approaches its mass shell, and a *non-resonant* part which is finite in this limit

$$\mathcal{A}_{q_1q_2,V}(k^2) = \mathcal{A}^{\mathrm{res}}_{q_1q_2,V}(k^2) + \mathcal{A}^{\mathrm{nres}}_{q_1q_2,V}(k^2). \tag{2.21}$$

To do so, one has first to sort out the diagrams which can actually lead to resonant contributions. Clearly, this holds for all contributions originating from diagrams of the type shown on the left hand side in Figure 2.1, i.e. for all diagrams, where the resonant propagator appears only outside the loops. In the following, we refer to this group as the *factorizable diagrams*. These are exactly the diagrams appearing in the Narrow-Width Approximation. The corresponding amplitude is proportional to the propagator of the unstable particle, such that the resummation (2.12) can be done directly.

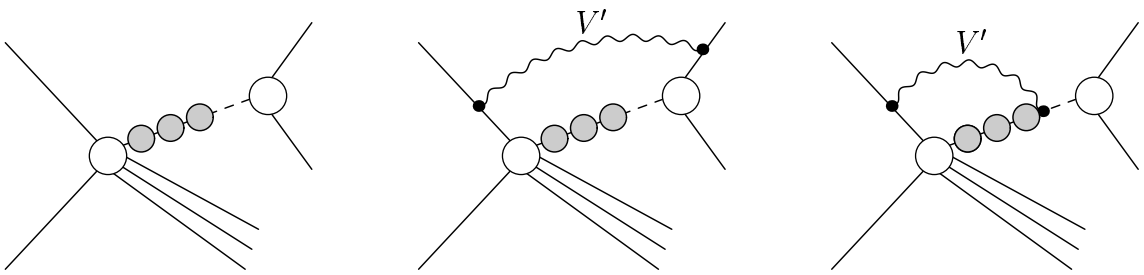

Figure 2.1: Examples for a factorizable diagram (left), a non-factorizable diagram (middle) and a diagram, which contains both, factorizable as well as non-factorizable contributions. In order to lead to a resonance, the virtual particle V' in the diagrams in the middle and on the right-hand side has to be massless.

The second type of diagrams that can lead to resonant contributions are the *non-factorizable diagrams*, a typical representative of which is shown in the middle of Figure 2.1. Here a virtual particle connects the production and decay subprocesses, or two decay subprocesses with each other. The amplitude corresponding to this type of diagram is a priory not proportional to the resonant propagator, since the latter is contained in a loop integral. As can be seen by simple power counting, on the mass shell of the resonance the latter shows here up as a linear divergence in the infrared limit of vanishing loop momentum if, and only if, the virtual particle is massless. A possibility to isolate the singular structure of such a diagram is thus to set the loop momentum to zero wherever this does not lead to a resonance. Evaluated in this so-called *Extended Soft-Photon Approximation* (ESPA), the amplitude corresponding to a non-factorizable diagram is proportional to the resonant propagator after integrating out the loop momentum and the resummation of the self-energy insertions can then again be done as in (2.12). The contribution of the non-factorizable diagrams to the non-resonant part of the amplitude (2.21) is accordingly given by the full contribution of these diagrams minus the contribution evaluated in ESPA.

Finally, the remaining diagrams form a third group, which we refer to as the *non-resonant* diagrams in what follows. They are finite in the on-shell limit for the momentum of the resonant particle and therefore contribute only to the non-resonant part in (2.21).

Evaluating the non-factorizable diagrams in ESPA, the resonant part of the amplitude is proportional to the resonant propagator. As was pointed out before, only the self-energy contributions to this propagator should be resummed, whereas all other propagators should be treated perturbatively. After the resummation, the splitting (2.21) can be written in the general form

$$\mathcal{A}_{q_1 q_2, V}(k^2) = \frac{W(k^2)}{k^2 - m_V^2 + \Sigma(k^2)} + \mathcal{B}^{\text{nres}}_{q_1 q_2, V}(k^2), \tag{2.22}$$

where $\mathcal{B}^{\text{nres}}_{q_1q_2,V}(k^2)$ denotes the non-resonant contributions. However, the numerator $W(k^2)$ in the resonant part may still contain terms which vanish in the on-shell limit, and thus lead to a finite contribution to the amplitude at the pole. Since we defined the resonant contributions as the sum of only those terms which are divergent on the resonance, one has to isolate these finite terms by subtracting and adding again the leading contribution to the amplitude at the pole

$$\mathcal{A}_{q_1q_2,V}(k^2) = \left[\frac{W(k^2)}{k^2 - m_V^2 + \Sigma(k^2)} - \frac{W(\mu_V^2)}{k^2-\mu_V^2}\frac{1}{1+\Sigma'(\mu_V^2)}\right] + \mathcal{B}^{\text{nres}}_{q_1q_2,V}(k^2) + \frac{W(\mu_V^2)}{k^2-\mu_V^2}\frac{1}{1+\Sigma'(\mu_V^2)}, \quad (2.23)$$

where we used (2.15) for the inverse propagator at the pole as well as the definition (2.16) for the pole mass μ_V of the unstable particle. The first two terms in (2.23) are regular in the limit $k^2 \to \mu_V^2$ and can thus be identified with the non-resonant contributions

$$\mathcal{A}^{\text{nres}}_{q_1q_2,V}(k^2) = \mathcal{B}^{\text{nres}}_{q_1q_2,V}(k^2) + \frac{W(k^2)}{k^2 - m_V^2 + \Sigma(k^2)} - \frac{W(\mu_V^2)}{(k^2-\mu_V^2)}\frac{1}{1+\Sigma'(\mu_V^2)}, \quad (2.24)$$

whereas the last term in (2.23) contains the resonant contributions

$$\mathcal{A}^{\text{res}}_{q_1q_2,V}(k^2) = \frac{W(\mu_V^2)}{k^2-\mu_V^2}\frac{1}{1+\Sigma'(\mu_V^2)}. \quad (2.25)$$

However, so far we did not pay attention to the fact that the numerator $W(k^2)$ generally depends on the angles of the resonant momentum as well. Taking k^2 off the real axis can also result in complex value for these angles, such that for practical purposes it is not clear how to evaluate the numerators in (2.24) and (2.25) at $k^2 = \mu_V^2$. To relate the above expressions to perturbatively calculable quantities, the amplitude (2.22) is expanded in a Laurent Series about $k^2 = m_V^2$

$$\mathcal{A}_{q_1q_2,V}(k^2) = \frac{W(k^2)}{k^2-m_V^2}\sum_{n=0}^{\infty}\left(\frac{\Sigma(k^2)}{k^2-m_V^2}\right)^n + \mathcal{B}_{q_1q_2,V}(k^2) = N(k^2) + \frac{W_{-1}}{k^2-m_V^2} + \sum_{n=2}^{\infty}\frac{W_{-n}}{(k^2-m_V^2)^n}. \quad (2.26)$$

By expanding the left hand side of (2.26) in orders of $\Sigma \propto \alpha$, the coefficients on the right-hand side can be shown to read

$$W_{-1} = \sum_{n=0}^{\infty}\frac{1}{n!}\frac{\mathrm{d}^2}{(\mathrm{d}k^2)^n}\left[W(k^2)\Sigma^n(k^2)\right]_{k^2=m_V^2},$$
$$N(k^2) = \mathcal{B}_{q_1q_2,V}(k^2) + \sum_{l=1}^{\infty}\left(k^2-m_V^2\right)^{l-1}\sum_{n=0}^{\infty}\frac{1}{(n+l)!}\frac{\mathrm{d}^{n+l}}{(\mathrm{d}k^2)^{n+l}}\left[W(k^2)\Sigma^n(k^2)\right]_{k^2=m_V^2}. \quad (2.27)$$

The residuum W_{-1} and the term $N(k^2)$ only involve the numerator $W(k^2)$ at k^2 equal to the real mass m_V^2, such that they can be evaluated without introducing complex angles for the resonant momentum. To obtain the desired connection to the quantities appearing in (2.24) and (2.25), the expressions (2.27) are expanded around $k^2 = \mu_V^2$, yielding

$$\begin{aligned} W_{-1} &= \frac{W(\mu_V^2)}{1+\Sigma'(\mu_V^2)}, \\ N(k^2) &= \mathcal{B}^{\text{nres}}_{q_1 q_2, V}(k^2) + \frac{W(k^2)}{k^2 - m_V^2 + \Sigma(k^2)} - \frac{W(\mu_V^2)}{(k^2-\mu_V^2)}\frac{1}{1+\Sigma'(\mu_V^2)}. \end{aligned} \tag{2.28}$$

A prove that this statement is true to all orders in perturbation theory can be found in the appendix of Ref. [39]. As a final result, the amplitude (2.23) divided into resonant and non-resonant contributions can thus be written as

$$\mathcal{A}_{q_1 q_2, V}(k^2) = \mathcal{A}^{\text{res}}_{q_1 q_2, V}(k^2) + \mathcal{A}^{\text{nres}}_{q_1 q_2, V}(k^2) = \frac{W_{-1}}{k^2 - \mu_V^2} + N(k^2). \tag{2.29}$$

Note that the residuum of the resonant contributions at the pole is a gauge-invariant quantity, since a change of gauge cannot change a resonant contribution into a non-resonant one. Due to the gauge invariance of the full amplitude as well as the gauge invariance of the Pole Definition of the complex mass for the resonance, the non-resonant contributions are separately gauge-invariant as well.

Besides providing a gauge-invariant prescription to incorporate finite-width effects in a perturbatively calculated amplitude, the Pole-Expansion Method has therefore the advantage of leading to a gauge-invariant splitting of the amplitude in resonant and non-resonant parts. With respect to the non-resonant contribution of order n in perturbation theory, the resonant contribution of the same order has a peak of height M_V/Γ_V and width Γ_V, such that the non-resonant contribution σ_V^{nres} to the full cross section are suppressed by a factor

$$\frac{\sigma_V^{\text{nres}}(k^2)}{\sigma_V^{\text{res}}(k^2)} \approx \frac{\Gamma_V}{M_V} \propto \alpha. \tag{2.30}$$

Regarding the above-mentioned double expansion of the amplitude in the coupling constant and the distance of the resonant momentum from the pole, the non-resonant contributions are thus of higher order. By virtue of the Pole-Expansion Method, these higher-order terms are gauge-invariant, such that they can be dropped without violating the gauge invariance of the resulting amplitude. Considering a perturbative calculation of fixed order n, the non-resonant parts have then only to be calculated up to order $n-1$ and one is left with the calculation of the factorizable diagrams and the non-factorizable diagrams of order n only. This so-called *Leading Pole Approximation* greatly simplifies the calculation of the virtual corrections in the sense that the number of diagrams contributing to the latter is substantially reduced.

However, the on-shell evaluation of the residuum at the pole causes problems in evaluating the contributions of the non-factorizable diagrams. As was said above, the amplitude corresponding to these diagrams is only proportional to the resonant propagator after integrating out the loop momentum. After this integration the infrared divergences show up as additional logarithmic singularities of the type $\log[k^2 - m_V^2]$, which renders the expansion of the amplitude in the squared resonant momentum around the pole undefined. As discussed in Ref. [39], the Pole-Expansion Method is in this case still applicable if one writes the amplitude as a sum of fundamental loop integrals times coefficient functions. The fundamental loop integrals are a set of linearly independent integrals in terms of which all tensor integrals can be expressed. Due to this independence, their coefficients must be gauge-invariant. Moreover, the coefficients of fundamental loop integrals depending on gauge-dependent masses must vanish. One is therefore free to introduce a finite width in the propagators of the fundamental loop integrals without violating gauge invariance. An obvious advantage of this is the fact that the resummation (2.12) of the self-energy insertions for the resonant propagator can now be done *before* the loop momenta are integrated out. The infrared divergences mentioned above then appear as logarithms $\log[k^2 - \mu_V^2]$, i.e. they are regularized by the off-shellness $k^2 - \mu_V^2$.

The idea to regularize the infrared divergences by the off-shellness can in principle be applied to the the full amplitude of the virtual corrections. However, we here follow the approach of Ref.[42] to treat the resonant factorizable and the resonant non-factorizable virtual corrections separately. As to be discussed below, this has the advantage that the complete amplitude for the non-factorizable corrections can be evaluated in ESPA, which simplifies the calculation considerably. On the other hand, the separate treatment of the factorizable and non-factorizable contributions to the virtual corrections requires a gauge-invariance separation of these parts. However, the diagrammatic definition of the factorizable and non-factorizable contributions adopted so far is a priori not gauge-invariant. The reason for this is that the factorizable corrections receive contributions from diagrams of the type shown on the right-hand side of Figure 2.1, where a virtual massless particle connects the resonance with particles in the production or decay subprocesses. According to our above definition, these diagrams belong to the group of factorizable diagrams, and are as such evaluated on-shell, with potential infrared divergences regularized by a mass regulator for the virtual massless particle. On the other hand, these diagrams lead in the on-shell limit to an infrared divergence, which is according to our definition rather a characteristic of a non-factorizable diagram. At the diagrammatic level, the vertex on the resonant propagator could be counted as a part of the production process, resulting in a factorizable diagram, or as a part of the decay process, which results in a non-factorizable diagram. This indicates that diagrams with a virtual massless particle coupling to the resonance contain both, factorizable and non-factorizable contributions.

To obtain a gauge-invariant separation of the amplitude into factorizable and non-factorizable parts, we adopt the approach presented in [61]. The basic idea is here to *define* the factorizable contribution of each diagram with a coupling of a virtual massless particle to

the resonance by

$$\mathcal{A}^{\text{res}}_{q_1 q_2, V, \text{fac}}(k^2) = \frac{1}{k^2 - \mu_V^2} \sum_{\lambda_V = \pm} W_{-1}^{\lambda_V, \text{prod}}(m_V^2) W_{-1}^{\lambda_V, \text{dec}}(m_V^2), \tag{2.31}$$

where, $W_{-1}^{\lambda_V,\text{prod}}$ and $W_{-1}^{\lambda_V,\text{dec}}$ denote the matrix elements of the on-shell production and decay subprocesses, respectively, and the sum runs over the physical polarizations of the decaying particle. The infrared divergences are regularized by a finite mass parameter for the massless virtual particle. To avoid double counting, the non-factorizable contribution of the considered diagram must then be defined as the difference of the diagram evaluated off-shell as described above minus the factorizable part (2.31), which is evaluated on-shell using a mass regulator. It is due to the difference in the regularization procedure of the infrared divergences, that this subtraction does not lead to an exact cancellation. The advantage of this procedure is twofold. Due to the gauge invariance of the complete amplitude and the gauge invariance of the factorizable corrections defined by (2.31), the non-factorizable corrections obtained by the above subtraction are gauge-invariant as well. Both, the factorizable and non-factorizable contributions can then be calculated separately without violating gauge invariance. As a second advantage, the difference of a given diagram evaluated as a non-factorizable diagram minus the same diagram evaluated as a factorizable diagram can in Leading Pole Approximation be shown to be exactly equal to this difference in ESPA. Therefore, not only the contributions of the non-factorizable diagrams but the *complete* non-factorizable contributions to the virtual corrections can be evaluated in ESPA, which simplifies the evaluation of the corresponding loop integrals. A more detailed description on the separation of the factorizable and non-factorizable parts of the amplitude is given in Appendix B.2, where we demonstrate our definition of the non-factorizable contributions using a specific example, as well as in Appendix C, where we apply the above method to a general process.

To illustrate the use of the Leading Pole Approximation, we explicitly apply the latter to the case of a perturbative one-loop calculation in the remainder of this chapter. To start with, evaluated up to first-order perturbation theory the equations (2.29) and (2.27) yield

$$\mathcal{A}^{(0+1),\text{LPA}}_{q_1 q_2, V}(k^2) = \mathcal{A}^{(0+1),\text{res}}_{q_1 q_2, V}(k^2) + \mathcal{A}^{(0),\text{nres}}_{q_1 q_2, V}(k^2), \tag{2.32}$$

where

$$\begin{aligned}
\mathcal{A}^{(0+1),\text{res}}_{q_1 q_2, V}(k^2) &= \frac{W_{-1}^{(0)}(m_V^2) + W_{-1}^{(1)}(m_V^2) + \frac{\mathrm{d}}{\mathrm{d}k^2}[W_{-1}^{(0)}(k^2)\Sigma^{(1)}(k^2)]_{k^2=m_V^2}}{k^2 - \mu_V^2} \\
\mathcal{A}^{(0),\text{nres}}_{q_1 q_2, V}(k^2) &= \frac{W_{-1}^{(0)}(k^2) - W_{-1}^{(0)}(m_V^2)}{k^2 - m_V^2} + \mathcal{B}^{(0)}_{q_1 q_2, V}(k^2).
\end{aligned} \tag{2.33}$$

The pole position μ_V in (2.33) is here defined by

$$\mu_V^2 = m_V^2 - \Sigma^{(1+2)}(\mu_V^2) =: M_V^2 + \mathrm{i}\Gamma_V M_V, \tag{2.34}$$

with $\Sigma^{(n)}$ denoting the n-loop self-energy of the decaying particle. Besides the Born amplitude and the one-loop corrections, the two additional derivative terms

$$\frac{W^{(0)}(m_V^2)\frac{\mathrm{d}}{\mathrm{d}k^2}[\Sigma^{(1)}(k^2)]_{k^2=m_V^2}}{k^2-\mu_V^2}+\frac{\frac{\mathrm{d}}{\mathrm{d}k^2}[W^{(0)}(k^2)]_{k^2=m_V^2}\Sigma^{(1)}(m_V^2)}{k^2-\mu_V^2} \tag{2.35}$$

contribute to the resonant amplitude. They contain the leading order k^2 dependence of the self-energy of the decaying particle as well as the leading order k^2 dependence of the Born amplitude, respectively. However, the second of these contributions involves the derivative of the numerator $W^{(0)}$ at the pole. Such a derivative is hard to implement in a numerically stable way, such that in praxis one often replaces the tree-level contributions by the full Born amplitude, with the resonant propagator being replaced by one including a finite width

$$\begin{aligned}
&\mathcal{A}^{(0),\mathrm{res}}_{q_1q_2,V}(k^2)+\mathcal{A}^{(0),\mathrm{nres}}_{q_1q_2,V}(k^2)\\
&\quad=\frac{W^{(0)}_{-1}(m_V^2)+\frac{\mathrm{d}}{\mathrm{d}k^2}[W^{(0)}_{-1}(k^2)\Sigma^{(1)}(k^2)]_{k^2=m_V^2}}{k^2-\mu_V^2}+\frac{W^{(0)}_{-1}(k^2)-W^{(0)}_{-1}(m_V^2)}{k^2-m_V^2}+\mathcal{B}^{(0)}_{q_1q_2,V}(k^2)\\
&\quad\approx\frac{W^{(0)}_{-1}(k^2)}{k^2-\mu_V^2}+\mathcal{B}^{(0)}_{q_1q_2,V}(k^2).
\end{aligned} \tag{2.36}$$

In this way, gauge invariance is of course broken again, but the resulting effect has been shown to be numerically small (see e.g. Ref.[54, 55, 62, 63]) by comparing the results obtained from (2.36) to those obtained from using other, gauge-invariant finite width schemes, as e.g. the Complex Mass Scheme. The virtual corrections in Leading Pole Approximation are then given by

$$\mathcal{A}^{(1),\mathrm{LPA}}_{q_1q_2,V}(k^2)=\mathcal{A}^{(1),\mathrm{res}}_{q_1q_2,V}(k^2)=\frac{W^{(1)}_{-1}(m_V^2)}{k^2-\mu_V^2}. \tag{2.37}$$

Following our discussion above, the amplitude can be divided into factorizable and non-factorizable contributions

$$\mathcal{A}^{(1),\mathrm{LPA}}_{q_1q_2,V,\mathrm{fac}}(k^2)=\frac{W^{(1)}_{-1,\mathrm{fac}}(m_V^2)}{k^2-\mu_V^2},\qquad \mathcal{A}^{(1),\mathrm{LPA}}_{q_1q_2,V,\mathrm{nfac}}(k^2)=\frac{W^{(1),\mathrm{ESPA}}_{-1,\mathrm{nfac}}(m_V^2,k^2-\mu_V^2)}{k^2-\mu_V^2}, \tag{2.38}$$

where the factorizable part of the residuum is evaluated on-shell with the infrared singularities regularized by a mass regulator. In the non-factorizable part, the second argument of the numerator indicates that besides the resonant propagator, the momentum of the decaying particle is kept off-shell wherever the on-shell limit leads to a infrared divergence. After the subtraction of the terms already contained in the virtual corrections, the residuum can then be evaluated in ESPA. As we show in Appendix C, the non-factorizable 1-loop corrections then take the process-independent form

$$\mathcal{A}^{(1),\mathrm{LPA}}_{q_1q_2,V,\mathrm{nfac}}(k^2)=\frac{1}{2}\mathcal{A}^{(0),\mathrm{LPA}}_{q_1q_2,V}(k^2)\delta^{(1),\mathrm{virt}}_{\mathrm{nfac}}, \tag{2.39}$$

where

$$\mathcal{A}^{(0),\mathrm{LPA}}_{q_1 q_2, V}(k^2) = \frac{W^{(0)}_{-1}(m_V^2)}{k^2 - \mu_V^2} \tag{2.40}$$

denotes the factorizable tree-level amplitude in Leading Pole Approximation. As opposed to the Born amplitude (2.36), the virtual corrections in Leading Pole Approximation as presented here are manifestly gauge-invariant. In practice, the two amplitudes in (2.38) have to be evaluated using two different phase-spaces. The off-shell phase-space, which is used to evaluate the resonant propagators as well as the off-shellness appearing in the numerator of the non-factorizable part of the amplitude, as well as the on-shell phase-space, which is given by a projection of the off-shell momenta on the mass-shell of the resonant particle and is used wherever an on-shell limit does not lead to a singularity.

Note that the Leading Pole Approximation is not restricted to the case of a single resonance only. In case of an amplitude involving several resonances, the Pole-Expansion Method can be applied by performing again a double expansion of the amplitude in the coupling constant and the squared resonant momenta around the poles. The Leading Pole Approximation then corresponds to keeping only the contributions where all resonances are on-shell simultaneously. A limit of the Pole-Expansion Method is given by processes where the amplitude exhibits several overlapping resonance structures leading to the same final state, in which case it is not clear around which resonance the amplitude should be expanded. As a second drawback, the Pole-Expansion Method does not give an answer to the question how to evaluate the amplitude in the phase-space region around the threshold of the considered process. As was pointed out before, the introduction of a finite width depends on the kinematics of the considered process in the sense that only those propagators that can kinematically become resonant should obtain a finite width. If the invariant mass of the initial state is below the production threshold of the considered process, it is not possible that all resonant propagators become simultaneously on-shell, such that the Leading Pole Approximation cannot be applied and one obtains the original singularity when approaching the threshold from below. Both problems do not appear if one applies appropriate cuts on the invariant masses of the initial state and reconstruction cuts on the invariant masses of the resonances. On the other hand, the phenomenological analysis is in this way restricted to observables evaluated far from the threshold. A discussion of the behaviour of the most common finite-width schemes around the production threshold can be found in Ref. [40, 54, 55, 63].

2.3 The Treatment of Soft and Collinear Singularities

We mentioned in section (2.1), that the cross-section of the virtual corrections to a given process generally contains soft and collinear singularities and that these singularities cancel partially when adding the real corrections to the 1-loop cross-section. However, the terms canceling in this sum are generally given by logarithms in the mass of the emitting light particle over a typical energy scale of the process. The corresponding contributions to

the virtual corrections are thus very large, such that the cancellation of soft and collinear singularities is numerically quite delicate. In this section, we present our approach to deal with these divergences. The general strategy is to divide the virtual corrections and the Bremsstrahlung corrections into singular and finite parts, and to cancel the divergences analytically by adding the two singular contributions. We here present two independent approaches to the question how this can be accomplished in practice, referred to as *phase-space slicing* [64, 65] and the *dipole subtraction* [66, 67] in what follows. Both concepts were also discussed in Ref. [42] and are well-suited for an implementation in combination with a Monte-Carlo phase-space integration.

To start with, we denote the cross section for the Bremsstrahlung process by

$$\sigma^{\text{real}}_{q_1 q_2}(\hat{s}) = \frac{1}{2\hat{s}} \int \mathrm{d}\Phi_{\text{real}} \left| \mathcal{A}^{\text{real}}_{q_1 q_2}(\Phi_{\text{real}}) \right|^2 , \tag{2.41}$$

where $\hat{s}$ is the partonic centre-of-mass energy, $\mathrm{d}\Phi_{\text{real}}$ denotes the phase-space element for the Bremsstrahlung process, and $\mathcal{A}^{\text{real}}_{q_1 q_2}$ is the corresponding amplitude. Note that a finite width has here to be introduced as well to regularize potential resonance peaks. In our work, we apply the fixed-width scheme to the real corrections. As in the case of the Born amplitude discussed above, this breaks gauge invariance, but the effect can be expected to be numerically small.

The basic idea of the phase-space slicing is to impose a cut δ_s on the Bremsstrahlung energy as well as a cut δ_c on the angles between the momenta of the emitters and the momentum of the Bremsstrahlung particle. The phase-space for the Bremsstrahlung process is in this way split in a subspace where the squared amplitude is singular and a subspace where the squared amplitude is finite, such that

$$\sigma^{\text{real}}_{q_1 q_2}(\hat{s}) = \sigma^{\text{real,slic.}}_{q_1 q_2,\text{sing.}}(\hat{s}) + \sigma^{\text{real,slic.}}_{q_1 q_2,\text{finite}}(\hat{s}), \tag{2.42}$$

Denoting collectively the angles between the momenta of the emitting particles and the momentum of the Bremsstrahlung particle by θ and the energy of the Bremsstrahlung particle by E, the finite piece is given by

$$\sigma^{\text{real,slic.}}_{q_1 q_2,\text{finite}}(\hat{s}) = \frac{1}{2\hat{s}} \int_{\substack{E \,>\, \delta_s \sqrt{\hat{s}}/2 \\ \cos(\theta) \,<\, 1-\delta_c}} \mathrm{d}\Phi_{\text{real}} \left| \mathcal{A}^{\text{real}}_{q_1 q_2} \Phi_{\text{real}}) \right|^2 , \tag{2.43}$$

whereas the singular part can be divided further in a part containing all soft singularities and a part containing only collinear singularities

$$\sigma^{\text{real,slic.}}_{q_1 q_2,\text{sing.}}(\hat{s}) = \sigma^{\text{real}}_{q_1 q_2,\text{soft}}(\hat{s}) + \sigma^{\text{real}}_{q_1 q_2,\text{coll.}}(\hat{s}). \tag{2.44}$$

The soft part contains all contributions with $E < \delta_s \sqrt{s}/2$, whereas the collinear part is defined by the phase space region where $E > \delta_s \sqrt{s}/2$ and $1 - \delta_c < \cos(\theta) < 1$. Both, the singular and the finite piece then depend on the actual numerical values of the cut

parameters δ_s and δ_c, but this dependence cancels when summing all contributions in the final result. All terms of order one in the cut parameters are neglected, i.e. the cut has to be sufficiently small to justify this approximation, but it has on the other hand to be large enough to yield numerically stable results. The finite piece does not contain any infrared or collinear divergences, such that the corresponding phase-space integration is numerically stable without the introduction of regularization parameters. The soft and collinear singular pieces, on the other hand, are generally universal, and the integration over the momentum of the Bremsstrahlung particle can be done analytically. To this end, appropriate regularization parameters have to be introduced, like e.g. mass parameters for the emitted Bremsstrahlung particle and the emitting fermion. Explicit expressions for the two singular components $\sigma^{\text{real}}_{q_1 q_2,\text{soft}}$ and $\sigma^{\text{real}}_{q_1 q_2,\text{coll.}}$ of the cross section are given in Appendix D.2, where we discuss the method of phase-space slicing in some more detail.

The dipole subtraction method, on the other hand, is based on a somewhat different approach. Here the basic idea is to construct a simple auxiliary function, which coincides with the amplitude of the Bremsstrahlung processes in the infrared and collinear limits, and to subtract this function from the real corrections on the level of squared amplitudes. As in the case of the phase-space slicing, the cross section for the Bremsstrahlung process can then be split like in (2.42), with the finite piece given by

$$\sigma^{\text{real,subtr.}}_{q_1 q_2,\text{finite}}(\hat{s}) = \frac{1}{2\hat{s}} \int \mathrm{d}\Phi_{\text{real}} \left(\left| \mathcal{A}^{\text{real}}_{q_1 q_2}(\Phi_{\text{real}}) \right|^2 - \left| \mathcal{A}^{\text{subtr}}_{q_1 q_2}(\Phi_{\text{real}}) \right|^2 \right), \tag{2.45}$$

where we denoted the subtraction function by $\mathcal{A}^{\text{subtr}}_{q_1 q_2}$. The phase-space integration in (2.45) is numerically stable, since the integrand is now zero in the soft and collinear limits, and finite elsewhere. To compensate for this subtraction, the auxiliary function integrated over the full phase-space has to be added again. To evaluate the resulting singular contribution

$$\sigma^{\text{real,subtr.}}_{q_1 q_2,\text{sing.}}(\hat{s}) = \frac{1}{2\hat{s}} \int \mathrm{d}\Phi_{\text{real}} \left| \mathcal{A}^{\text{subtr}}_{q_1 q_2}(\Phi_{\text{real}}) \right|^2, \tag{2.46}$$

the idea is again to introduce mass regulators for the divergences and to perform the integration over the Bremsstrahlung momentum analytically. The subtraction function must thus be chosen such that it contains all infrared and collinear singularities, but has on the other hand to be simple enough to make an analytical integration over the momentum of the Bremsstrahlung particle feasible. The question how to construct the subtraction function $\mathcal{A}^{\text{subtr}}_{q_1 q_2}$ is addressed in Appendix D.3, where we also give an analytical expression for the singular part (2.46).

Both methods sketched here result in a splitting of the Bremsstrahlung cross-section into a finite piece, which can be integrated over phase-space numerically, and a singular piece containing the soft and collinear divergences, which arises from analytically integrating out the momentum of the Bremsstrahlung particle. After this integration, the singular piece depends only on the momenta of the original process, and can thus be added to the

virtual corrections regularized in the same way before integrating the latter over phase-space. As was said before, the soft and the final-state collinear singularities cancel in this sum, and the final result becomes independent of the corresponding regularization parameters. However, this is only the case if evaluating the full virtual corrections and the full Bremsstrahlung contributions. As discussed in the preceding section, we intend to evaluate the virtual corrections in Leading Pole Approximation, which produces a mismatch between the singularities appearing in the virtual corrections on one hand and in the Bremsstrahlung contributions on the other hand.

To solve this problem, we follow the approach presented in Ref.[42]. Here the infrared and collinear singularities are extracted from the virtual corrections *before* applying the Leading Pole Approximation

$$\begin{aligned}\sigma^{\text{virt+real}}_{q_1 q_2}(\hat{s}) &= \sigma^{\text{virt}}_{q_1 q_2}(\hat{s}) + \sigma^{\text{real}}_{q_1 q_2}(\hat{s}) \\ &= \sigma^{\text{virt}}_{q_1 q_2}(\hat{s}) - \sigma^{\text{virt}}_{q_1 q_2,\text{sing}}(\hat{s}) + \sigma^{\text{virt}}_{q_1 q_2,\text{sing}}(\hat{s}) + \sigma^{\text{real}}_{q_1 q_2,\text{sing.}}(\hat{s}) + \sigma^{\text{real}}_{q_1 q_2,\text{finite}}(\hat{s}), \quad (2.47)\end{aligned}$$

where $\sigma^{\text{virt}}_{q_1 q_2,\text{sing}}$ is constructed such that it contains all collinear and infrared divergences appearing in the virtual corrections. An analytical expression for this term is given in Appendix D.4. Using (2.47), the sum of the virtual corrections and Bremsstrahlung cross-section can be written as a sum of three finite pieces. The first piece is given by the finite virtual corrections, i.e. the difference of the first two terms in (2.47). It is this contribution, to which we apply the Leading Pole Approximation

$$\sigma^{\text{virt,LPA}}_{q_1 q_2,\text{finite}}(\hat{s}) = \sigma^{\text{virt,LPA}}_{q_1 q_2}(\hat{s}) - \sigma^{\text{virt,LPA}}_{q_1 q_2,\text{sing}}(\hat{s}). \quad (2.48)$$

The second piece is given by the finite real corrections contained in the last term of (2.47), which in case of using the phase-space slicing is given by the squared Bremsstrahlung amplitude integrated over the phase-space limited by the technical cuts δ_s and δ_c, whereas in case of using the subtraction method it is given by (2.45). Finally, the third piece comprises the sum of the singular contributions of the Bremsstrahlung cross-section as well as the singular contribution to the virtual corrections. After integrating out the momentum of the Bremsstrahlung particle, the singular Bremsstrahlung contributions only depend on the phase-space of the original process, such that the sum

$$\sigma^{\text{virt+real}}_{q_1 q_2,\text{sing}}(\hat{s}) = \sigma^{\text{virt}}_{q_1 q_2,\text{sing}}(\hat{s}) + \sigma^{\text{real}}_{q_1 q_2,\text{sing.}}(\hat{s}) \quad (2.49)$$

can be performed on the level of the squared amplitudes before integrating over phase-space. As we explicitly show in Appendix D.5, the soft and the final-state collinear divergences then cancel, since we treated both contributions exactly, i.e. without using the Leading Pole Approximation. In the same section we show that the remaining initial state collinear singularities vanish when subtracting the correction term arising form the redefinition of the PDFs according to (2.8). In this way, one is left with an infrared-safe partonic cross-section which can be integrated over phase-space without encountering any numerical instabilities.

2.4 The Master Formula

To conclude this chapter, we give a summary our strategy for the calculation of the hadronic cross section

$$\sigma_{\mathrm{P_1P_2}}(S,Q^2) = \sum_{q_1,q_2=u,\bar{u},..} \int_0^1 \mathrm{d}x_1 \int_0^1 \mathrm{d}x_2 \overline{\Phi}_{q_1|P_1}(x_1,Q^2)\overline{\Phi}_{\bar{q}_2|P_2}(x_2,Q^2)\sigma^{\mathrm{IR-safe}}_{q_1\bar{q}_2}(\hat{s},Q^2). \quad (2.50)$$

in first-order perturbation theory. Here $\overline{\Phi}_{q|P}$ denote the Parton Distribution Function of the parton q in the proton P, the quantities S and $\hat{s} = x_1x_2S$ are the squared center of mass energies of the hadronic process and the partonic subprocesses, respectively, and Q denotes the typical energy scale of the considered process. Following our discussion in the preceding sections, the infrared-safe partonic cross-section can be summarized in the Master Formula

$$\sigma^{\mathrm{IR-safe}}_{q_1\bar{q}_2}(\hat{s},Q^2) = \sigma^{(0)}_{q_1q_2}(\hat{s}) + \sigma^{\mathrm{virt,LPA}}_{q_1q_2,\mathrm{finite}}(\hat{s}) + \sigma^{\mathrm{virt+real}}_{q_1q_2,\mathrm{finite}}(\hat{s},Q^2) + \sigma^{\mathrm{real}}_{q_1q_2,\mathrm{finite}}(\hat{s}). \quad (2.51)$$

The first term is here given by the Born cross-section, whereas the last three terms contain contributions of the virtual and real corrections as well as the contributions arising from the redefinition of the Parton Distribution Functions presented in Section 2.1.

Following the discussion in Section 2.3, the definition of the last three terms in (2.51) is motivated by a consistent treatment of the collinear and infrared divergences. Considering first the *virtual corrections*, these divergences arise from the soft and collinear limits of the loop integration. In our work, the singularities are here regularized by introducing small but finite mass parameters the massless virtual particles as well as for the light external particles. The virtual corrections are then finite, but the singularities appear as large logarithmic contributions in the above regularization parameters. In order to avoid numerical instabilities in the evaluation of these logarithms, an auxiliary function containing all collinear and infrared singular terms is subtracted from the virtual corrections, such that one ends up with in a finite contribution given by

$$\sigma^{\mathrm{virt}}_{q_1q_2,\mathrm{finite}}(\hat{s}) = \sigma^{\mathrm{virt}}_{q_1q_2} - \sigma^{\mathrm{virt}}_{q_1q_2,\mathrm{sing}}(\hat{s}). \quad (2.52)$$

As discussed below, we evaluate this part in Leading Pole Approximation, which yields

$$\sigma^{(1),\mathrm{LPA}}_{q_1q_2,\mathrm{finite}}(\hat{s}) = \sigma^{(1),\mathrm{LPA}}_{q_1q_2}(\hat{s}) - \sigma^{\mathrm{virt,LPA}}_{q_1q_2,\mathrm{sing}}(\hat{s}). \quad (2.53)$$

In the same way, the *real corrections* are divergent in the limit of soft or collinear emission of the Bremsstrahlung particle. In Section 2.3, we presented two methods to deal with the resulting numerical instabilities in the phase-space integration. Both methods lead to a separation of the real corrections into a piece that is finite in the soft and collinear limits, and a piece that contains all the singularities. In case of using the phase-space slicing technique, the finite real corrections, i.e. the last term in (2.51), is defined as the

full squared matrix element integrated over a phase-space limited by technical cuts on the energy and the production angle of the Bremsstrahlung particle

$$\sigma^{\text{real,slic.}}_{q_1 q_2,\text{finite}}(\hat{s}) = \frac{1}{2\hat{s}} \int_{\substack{E > \delta_s \sqrt{\hat{s}}/2 \\ \cos(\theta) < 1-\delta_c}} \mathrm{d}\Phi_{\text{real}} \left| \mathcal{A}^{\text{real}}_{q_1 q_2} \Phi_{\text{real}}) \right|^2 . \tag{2.54}$$

In case of using the subtraction method, the finite real corrections are defined by constructing an auxiliary function containing the soft and collinear divergences, and by subtracting this function from the squared amplitude before integrating over the full phase-space of the Bremsstrahlung process

$$\sigma^{\text{real,subtr.}}_{q_1 q_2,\text{finite}}(\hat{s}) = \frac{1}{2\hat{s}} \int \mathrm{d}\Phi_{\text{real}} \left(\left| \mathcal{A}^{\text{real}}_{q_1 q_2}(\Phi_{\text{real}}) \right|^2 - \left| \mathcal{A}^{\text{subtr}}_{q_1 q_2}(\Phi_{\text{real}}) \right|^2 \right) . \tag{2.55}$$

Finally, the third term in (2.51) is given by

$$\sigma^{\text{virt+real}}_{q_1 q_2,\text{finite}}(\hat{s}, Q^2) = \sigma^{\text{virt}}_{q_1 q_2,\text{sing}}(\hat{s}) + \sigma^{\text{PDF}}_{q_1 q_2,\text{sing.}}(\hat{s}, Q^2) + \sigma^{\text{real}}_{q_1 q_2,\text{sing.}}(\hat{s}). \tag{2.56}$$

Here, the first term compensates for the subtraction (2.52), the second term comprises the contributions arising from the redefinition of the Parton Distribution Functions and the third term is given by the singular parts of the real corrections. In case of the subtraction method, the latter compensates for the subtraction of the infrared and collinear singularities described above, and is thus given by the auxiliary function integrated over the full Bremsstrahlung phase-space. In case of the phase-space slicing technique the singular real corrections are given by the full squared matrix element for the Bremsstrahlung process integrated over the piece of the phase-space which was cut off in the definition of the finite real corrections. In both cases, the Bremsstrahlung momentum can be integrated out analytically, with the singularities regularized by small but finite mass parameters for the emitting and the emitted particle. After integrating out the momentum of the Bremsstrahlung particle, this leads again to large logarithms in the regulators. However, the singular real corrections then depend on the same phase-space as the first and second term in (2.56), such that the cancellation of the soft and collinear singularities can be done analytically on the level of squared amplitudes. The subsequent phase-space integration then leads to numerically stable results. We explicitly calculate an analytical, process-independent expression for the sum of singular parts (2.56) in Appendix D.

As discussed in the first section of this chapter, the Born cross section and the virtual corrections are treated in our approach by means of the *Pole-Expansion Method*. The latter has the advantage to yield a gauge-invariant prescription for the introduction of a finite width in the resonant propagators, as well as a gauge-invariant division of the Born amplitude and the virtual corrections in resonant and non-resonant parts. In *Leading Pole Approximation*, the non-resonant contributions to the virtual corrections is in first order perturbation theory of higher order in the Pole Expansion, such that the amplitude reads

$$\mathcal{A}^{(0+1)}_{q_1 q_2, V}(k^2) = \mathcal{A}^{(0+1)\text{res}}_{q_1 q_2, V}(k^2) + \mathcal{A}^{(0)\text{nres}}_{q_1 q_2, V}(k^2), \tag{2.57}$$

As is shown in (2.36), we approximate the Born contributions plus the leading k^2 dependence of Born cross-section and the self-energy of the resonant particles by the full Born cross-section, with a finite width introduced in the resonant propagator

$$\mathcal{A}^{(0),\text{res}}_{q_1q_2,V,\text{fac}}(k^2) \approx \frac{W^{(0)}_{-1}(k^2)}{k^2-\mu_V^2}, \qquad \mathcal{A}^{(0)\text{nres}}_{q_1q_2,V}(k^2) = \mathcal{B}^{(0)}_{V}(k^2), \tag{2.58}$$

where W_{-1} denotes the residuum of the Born amplitude at the pole, and $\mathcal{B}^{(0)}_{q_1q_2,V}$ comprises all Born contributions not containing the resonant propagator. The virtual corrections in Leading Pole Approximation are then given by

$$\mathcal{A}^{(1),\text{LPA}}_{q_1q_2,V}(k^2) = \frac{W^{(1)}_{-1}(m_V^2)}{k^2-\mu_V^2}, \tag{2.59}$$

where the on-shell evaluation of the numerator requires a projection of the external momenta on the mass-shell of the resonance. As discussed in section (2.2), the amplitude can be split into a resonant factorizable and a resonant non-factorizable part

$$\mathcal{A}^{(1),\text{LPA}}_{q_1q_2,V}(k^2) = \mathcal{A}^{(1),\text{LPA}}_{q_1q_2,V,\text{fac}}(k^2) + \mathcal{A}^{(1),\text{LPA}}_{q_1q_2,V,\text{nfac}}(k^2) = \frac{W^{(1)}_{-1,\text{fac}}(m_V^2)}{k^2-\mu_V^2} + \frac{W^{(1)}_{-1,\text{nfac}}(m_V^2,k^2-\mu_V^2)}{k^2-\mu_V^2}. \tag{2.60}$$

The factorizable part receives contributions from all diagrams with the resonant propagator outside the loops, and the infrared singularities are regularized by a mass parameter. The non-factorizable part receives contributions from all diagrams, where a virtual massless particle connects the production and decay subprocess, one of the latter with a resonance, as well as two resonances or decay subprocesses with each other. The infrared singularities are regularized by keeping the resonant momentum off-shell wherever the on-shell limit leads to a singularity. Furthermore, the loop integrals involving a coupling of the virtual massless particle to a resonance are evaluated as the difference between their non-factorizable and their factorizable contributions. To extract the resonant contributions, the Extended Soft Photon Approximation is applied to the resulting expression. The resonant non-factorizable corrections are then proportional to the Born matrix element in Leading Pole Approximation

$$\mathcal{A}^{(1),\text{LPA}}_{q_1q_2,V,\text{nfac}}(k^2) = \frac{W^{(1),\text{ESPA}}_{-1,\text{nfac}}(m_V^2,k^2-\mu_V^2)}{k^2-\mu_V^2} = \frac{1}{2}\mathcal{A}^{(0),\text{LPA}}_{q_1q_2,V}\delta^{(1),\text{virt}}_{\text{nfac}}, \tag{2.61}$$

where

$$\mathcal{A}^{(0),\text{LPA}}_{q_1q_2,V}(k^2) = \frac{W^{(0)}_{-1}(m_V^2)}{k^2-\mu_V^2}. \tag{2.62}$$

Altogether, the cross-sections for the Born Amplitude and the virtual corrections then read

$$\sigma^{(0)}_{q_1q_2}(\hat{s}) = \frac{1}{2\hat{s}}\int \text{d}\Phi \ \left|\mathcal{A}^{(0)\text{res}}_{q_1q_2,V,\text{fac}}(k^2) + \mathcal{A}^{(0)\text{nres}}_{q_1q_2,V}(k^2)\right|^2, \tag{2.63}$$

$$\sigma^{\text{virt,LPA}}_{q_1q_2}(\hat{s}) = \frac{1}{2\hat{s}}\int \text{d}\Phi \ 2\text{Re}\left[\left(\mathcal{A}^{(0),\text{LPA}}_{q_1q_2,V}(k^2)\right)^\star\left(\mathcal{A}^{(1),\text{LPA}}_{q_1q_2,V,\text{fac}}(k^2) + \mathcal{A}^{(1),\text{LPA}}_{q_1q_2,V,\text{nfac}}(k^2)\right)\right]. \tag{2.64}$$

Whereas our discussion was so-far restricted to the case of a single resonance only, our approach can easily be generalized to an arbitrary number of resonances. The above procedure can then be divided in the following steps

- Generate the diagrams for the Born process, and divide the latter into diagrams containing the resonant propagators and diagrams that do not contain the propagators,
- Generate all 1-loop diagrams where the resonant propagator appears outside the loops, and all diagrams where a virtual massless particle connects the production subprocess, the decay subprocesses and the resonances among each other,
- Generate all diagrams for the real corrections,
- Calculate the amplitudes corresponding to the diagrams generated in step one to three. The non-resonant Born contribution $B_V^{(0)}(k^2)$ in (2.58) is given by the amplitude resulting from the Born diagrams not containing the resonant propagator. Extract for each resonance the residues $W_{-1}^{(0)}$, $W_{-1,\text{fac}}^{(1)}$ and $W_{-1,\text{nfac}}^{(1)}$ from the amplitudes corresponding to the resonant diagrams. Introduce a fixed width for the resonant propagators in the amplitude for the real corrections,
- Replace the loop integrals arising from diagrams where a virtual massless particle couples to the resonance by the difference of non-factorizable evaluation minus factorizable evaluation. Apply the ESPA to the resulting expression for the non-factorizable corrections to obtain the residuum $W_{-1,\text{nfac}}^{(1),\text{ESPA}}$,
- Square all amplitudes and subtract the collinear and infrared divergences from the virtual corrections according to (2.52), as well as from the real corrections if using the subtraction method,
- Implement the generic expression for the sum of the singular parts (2.56) calculated in Appendix D,
- Multiply all contributions by the Parton Distribution Functions, and integrate the resulting expressions over the partonic energy fractions x_1 and x_2 as well as the respective phase-spaces. Project the generated momenta on-shell for the evaluation of the residues $W_{-1}^{(0)}$, $W_{-1}^{(1,\text{fac})}$ and $W_{-1}^{(1,\text{nfac})}$, but evaluate the resonant momentum off-shell in the resonant propagator and the non-factorizable parts of the loop-integrals. If using phase-space slicing, impose the corresponding technical cuts on the phase-space integration for the real corrections.

As will be discussed in the next two chapters, we implemented this procedure for a general process in a `Mathematica` package called `Pole`. The latter can be divided into two parts. The first part to be presented in Chapter 3 is dedicated to the generation of the amplitudes, i.e. to the implementation of the above steps one to five. The second part is discussed in Chapter 4 and contains our implementation of the steps six to eight, i.e. the numerical evaluation as well as the phase-space integration of the squared amplitudes.

Chapter 3

The Computer-Algebraical Generation of the Amplitudes

In this chapter, we discuss how the amplitudes needed in the framework of our approach can be calculated in practice. For most processes the number of diagrams contributing to the Born cross-section, the non-factorizable virtual corrections, as well as the Bremsstrahlung cross-section is generally small enough to calculate the corresponding amplitudes by hand. The factorizable virtual corrections for a processes with multi-particle final states, on the other hand, generally involve some hundreds or even thousands of Feynman diagrams to evaluate, which rather suggests a computer-algebraical approach to the calculation of the corresponding amplitude.

In the past years, the `Mathematica` package `FeynArts` [68] has become a standard tool for the computer-algebraical generation of amplitudes in the framework of perturbative calculations. In short, the strategy of amplitude generation using `FeynArts` can be divided in three steps. First, all topologies for a given number of initial and final-state particles are created. Secondly, a field content is addressed to the various lines of the topologies. In the last step, the Feynman rules are applied to the resulting list of inserted topologies, leaving the user with an analytical expression for the amplitude of the considered process. Due to this generic structure, `FeynArts` is largely working independent of the considered model or process, such that it can be applied to a vast variety of phenomenological problems.

However, as discussed in Chapter 2, the amplitude for a given process generally involves the production and decay of instable particles. Due to the corresponding resonant propagators, this leads to poles in the amplitude, which are regularized by the finite widths of the decaying particles. `FeynArts` does not distinguish between stable and decaying particles. Furthermore, the model files used by `FeynArts` do not allow for initial states containing hadrons, such that the partonic cross-sections of a hadronic reaction have to be calculated separately from each other. Regarding the fact that a one-loop Feynman amplitude for processes with three or more particles in the final state can be quite sizable, it would be desirable to extend the basic functions of `FeynArts` to a consistent treatment of a finite

width, as for example the Pole Expansion Method as presented in Section 2.2. This and the treatment of hadronic initial states was our main motivation to create the `Mathematica` package `Pole`.

The basic philosophy for the design of `Pole` can be outlined as follows. Instead of altering directly the source code of `FeynArts`, it is designed to work as an extension of the main functions of the latter, thereby keeping the three-step concept of `FeynArts`. Correspondingly, our package replaces each main function of `FeynArts` by extended versions which partly have the same names, but are able to handle an input involving hadronic initial states as well as definite intermediate states. This input is then used to split the amplitude according to resonance structures and partonic subprocesses. In short, `Pole` provides the following file structure

`Pole.m`	the main program
`Pole/`	
`CreateTopologies.m`	contains the `Mathematica` functions for the extension of the generation of topologies,
`InsertFields.m`	contains the `Mathematica` functions for the extension of the generation of inserted topologies,
`CreateFeynAmp.m`	contains the `Mathematica` functions for the extension of the generation the amplitudes,
`ModelDependence.m`	contains the `Mathematica` functions depending on the `FeynArts` Model files, like e.g. the functions related to the treatment of small masses, the hadron definitions and the interface to the nomenclature of `Lusifer`,
`CalcFeynAmp.m`	contains the `Mathematica` functions for simplifying the amplitudes,
`WvdW.m`	contains the `Mathematica` functions for the Weyl-van der Waerden formalism,
`PoleToFortran.m`	contains the `Mathematica` functions for the output of `Fortran` code for the numerical evaluation,
`drivers/`	contains the generic `Fortran` drivers for the numerical evaluation.

Apart from the main function, the file content of `Pole` can be divided into two subsets. In this chapter, we describe the use of the first three files in the directory `Pole`, which are related to the generation of analytical expressions for the amplitudes. The remaining files are needed to evaluate the so-generated amplitudes numerically and are described in the next chapter in some detail. To use the amplitude generation, one has to load first `FeynArts`

(version 3.1 or higher) and then `Pole` in the current `Mathematica` session, whereas if one is to use both, the amplitude generation and the part related to the numerical evaluation, on has to load first `FeynArts`, then `FormCalc` and finally `Pole`.

3.1 Creating Topologies

The first step in generating an amplitude using `FeynArts` is to construct the topologies for the considered process. This is done by using the function `CreateTopologies`, which takes as an input the loop order up to which the amplitude is to be determined, as well as the number of particles in initial and final states. Using the information of how many lines can be joined by a vertex of the considered model, the external particles are then connected by propagators in all possible ways.

As was said in the last chapter, we intend to generate amplitudes in first-order perturbation theory using the Leading Pole Approximation. The latter has the advantage of providing a gauge-invariant prescription for the introduction of a finite width, and to reduce the number of diagrams which have to be calculated. An amplitude calculated in this approximation receives in first-order perturbation theory contributions from the resonant Born diagrams, the non-resonant Born diagrams, the resonant factorizable one-loop diagrams, the resonant non-factorizable one-loop diagrams as well as the diagrams for the real corrections. However, the division of diagrams in resonant and non-resonant contributions requires some knowledge about the resonance structure of the considered process. The basic idea of topology generation using `Pole` is therefore to provide the user with the opportunity to specify not only the numbers n_{in} and n_{out} of initial and final state particles, but also the number n_{int} of particles in the *intermediate* state. To reduce the amount of work at an as early stage as possible, this information is then used already on the topological level to exclude all topologies not leading to the five types of diagrams listed above.

To start with, we said in Section 2.4 that we approximate the sum of the Born amplitude in Leading Pole Approximation plus the leading dependence of the latter on the resonant momentum by the full Born amplitude. The Born cross-section thus receives contributions from all tree-level diagrams, and no information on the resonances is required to generate the corresponding topologies. The latter can accordingly be constructed by simply applying the `FeynArts` function `CreateTopologies` to the full process $n_{\text{in}} \to n_{\text{out}}$.

Turning next to the virtual corrections, the amplitude receives in Leading Pole Approximation contributions from the diagrams corresponding to the resonant factorizable virtual corrections and from the diagrams corresponding to the resonant non-factorizable corrections. Furthermore, it is shown in Appendix D.4 that the resonant factorizable part of the Born cross-section is needed to subtract the soft and collinear singularities from the virtual corrections. Starting with the generation of the resonant factorizable diagrams, the graphs are here characterized by the fact that they involve the resonant propagators, and that the

latter appear outside the loops. To put it in another way, the corresponding topologies can be disconnected into the production subprocess and the decay subprocesses by cutting the lines corresponding to the resonances. Therefore, `Pole` generates the topologies for the factorizable diagrams by separately creating the topologies for the production and decay subprocesses, and by combining the latter in all possible ways. The topologies for the production subprocess are generated by invoking the `FeynArts` function `CreateTopologies` for a process with $n_{\rm in}$ particles in the initial state and $n_{\rm int}$ particles in the final state. To generate the topologies for the decay subprocesses, one has to determine which decays are actually possible for given numbers of intermediate state and final state particles. To do so, one requires the additional information how many particles in the intermediate state are actually decaying, and how many particles are stable in the sense that they appear in both, the intermediate and the final state. Given the corresponding numbers $n_{\rm int}^{\rm dec}$ and $n_{\rm int}^{\rm stab}$, one can then determine all possible decay scenarios. The corresponding topologies are then again created by means of the `FeynArts` function `CreateTopologies`, and the so-obtained list of decay topologies is combined with the topologies of the production process in all possible ways. Combining topologies for the production and decay subprocesses of lowest order, this leads to the generation of the topologies for the resonant factorizable Born diagrams, whereas the topologies for the resonant factorizable 1-loop diagrams can be generated by combination of first-order topologies for the production (decay) subprocesses with lowest-order topologies for the decay (production) subprocesses. The topologies of the corresponding counter-term diagrams can be generated in exactly the same way by using the `FeynArts` function `CreateCTTopologies` instead of `CreateTopologies`.

Turning next to the non-factorizable 1-loop diagrams, the latter are basically given by the resonant Born diagrams with an additional virtual massless particle connecting the resonances, the production subprocess and the decay subprocesses among each other. The generation of the corresponding topologies can accordingly be done by first generating all factorizable Born topologies, and by adding an extra propagator with the above properties in all possible ways. Note that the topologies where the extra propagator couples to one of the resonances are already contained in the topologies for the factorizable diagrams. However, the corresponding amplitudes contain both, factorizable and non-factorizable parts, such that on a topological level one cannot decide to which group the diagrams have to be addressed to. We thus generate these topologies twice, and avoid double counting by a separate evaluation of the corresponding amplitudes, as will be discussed in Section 3.3.

Finally, the topologies for the Bremsstrahlung diagrams need to be generated. According to the summary of our approach in Section 2.4, the corresponding amplitudes are treated exactly, i.e. without applying the Leading Pole Approximation. The corresponding topologies can thus be generated by applying the `FeynArts` function `CreateTopologies` to the full process $n_{\rm in} \to n_{\rm out} + 1$, where $n_{\rm in}$ and $n_{\rm out}$ denote the number of initial-state and final-state particles of the Born process.

In order to be able to treat the various contributing topologies in one go, the above-described features have been implemented in the `Mathematica` functions

`CreateFactorizableTopologies[`l, n_{in}`->`$\{n_{\text{int}}^{\text{dec}}, n_{\text{int}}^{\text{stab}}\}$`->`$n_{\text{out}}$ `, Options]`

Creates factorizable topologies of loop order l for a process with n_{in} incoming legs, n_{out} outgoing legs and an intermediate state containing $n_{\text{int}}^{\text{dec}}$ decaying particles and $n_{\text{int}}^{\text{stab}}$ stable particles.

`CreateFactorizableCTTopologies[`l, n_{in}`->`$\{n_{\text{int}}^{\text{dec}}, n_{\text{int}}^{\text{stab}}\}$`->`$n_{\text{out}}$ `, Options]`

Creates factorizable counter-term topologies of loop order l for a process with n_{in} incoming legs, n_{out} outgoing legs and an intermediate state containing $n_{\text{int}}^{\text{dec}}$ decaying particles and $n_{\text{int}}^{\text{stab}}$ stable particles.

`CreateNonFactorizableTopologies[`l, n_{in}`->`$\{n_{\text{int}}^{\text{dec}}, n_{\text{int}}^{\text{stab}}\}$`->`$n_{\text{out}}$ `, Options]`

Creates non-factorizable topologies of loop order l for a process with n_{in} incoming legs, n_{out} outgoing legs and an intermediate state containing $n_{\text{int}}^{\text{dec}}$ decaying particles and $n_{\text{int}}^{\text{stab}}$ stable particles.

The output of these functions is a list of the general form

```
PoleTopList[
    PoleTop[{{i1, i2, ...},{i3, i4, ...},...}][
        TopologyList[
                ⋮
            Topology[sym][
                        ⋮
                        Propagator[Resonant[i1, i2, ...]][...],
                        Propagator[Resonant[i3, i4, ...]][...],
                        Propagator[NonFac][...],...,
                        ⋮
                        further propagators],
                ⋮
            further topologies]],
        ⋮
    further topology lists of type PoleTop ].
```

A list of type `ResTop[{{i1,i2,...},{i3,i4,...},...}]` contains all topologies involving the decay of a resonance to the final state particles number $i_1, i_2, \ldots$, the decay of a second resonance to the final state particles number $i_3, i_4, \ldots$ and so on. If invoked with loop order zero, `CreateFactorizableTopologies` generates additionally a sublist of type `ResTop` with empty argument, which contains the full set of Born topologies. If the intermediate state is specified to be empty, `FactorizableTopologies` and `FactorizableCTTopologies` only generate the topologies and counter-term topologies of the full process, which e.g. can be used to generate the topologies for the real corrections.

The above functions accept essentially the same options as the `FeynArts` function `CreateTopologies`, e.g. `ExcludeTopologies->AllBoxes` excludes all box topologies. However, in calculating virtual corrections to a cross-section, one is sometimes interested in the virtual corrections to the production or decay subprocess only. We therefore built in two new options

option	*default value*	
`ProductionOnly`	`False`	Create only topologies with a loop in the production subprocess,
`DecayOnly`	`False`	Create only topologies with a loop in the decay subprocess.

As indicated above, `Pole` introduces compared to the `FeynArts` function `CreateTopologies` two new types of propagators

`Propagator[Resonant[i1,i2,...]][Vertex[i][j],Vertex[k][l]]`

A resonant propagator, which connects the vertices `Vertex[i][j]` and `Vertex[k][l]` and decays into the final-state particles number `i1,i2,...`.

`Propagator[NonFac][Vertex[i][j],Vertex[k][l]]`

The propagator of a non-factorizable topology, which connects the production subprocess, the decay subprocess, and the resonances among each other.

These new propagators are to be used later to select the resonant insertions for a given topology, as will be discussed in the next section.

3.2 Inserting Fields

In a second step of amplitude generation, `Pole` addresses a field content to the various lines of a given topology by means of the `FeynArts` function `InsertFields`. Considering the topologies created as described above, we here encounter the problem that a factorizable topology can lead to a resonant as well as a non-resonant diagram. For example, if one is interested in diagrams with a Z boson decaying into two charged fermions, one has always a second insertion with the Z boson replaced by a photon, which leads to a non-resonant diagram with respect to the considered resonance. As a second problem, we mentioned above that in case of a hadronic reaction we want to treat the partonic subprocesses in one go, a feature not contained in `FeynArts`.

To solve these problems, `Pole` extends the `FeynArts` function `InsertFields` to accept a new input

`InsertFields[`*tops*`,{`$i_1^{\text{in}}, i_2^{\text{in}}$`}->{`$j_1^{\text{dec}}$`,...,`$j_1^{\text{stab}}$`,...}->{`$i_1^{\text{out}}, i_2^{\text{out}}, \ldots$`},Options]`

Addresses a field content corresponding to the process $\{i_1^{\text{in}}, i_2^{\text{in}}\} \to \{i_1^{\text{out}}, i_2^{\text{out}}, \ldots\}$ to the topology list *tops* of type `ResTopList`, and selects the diagrams which are resonant with respect to the intermediate state $\{j_1^{\text{dec}}, \ldots, j_1^{\text{stab}}, \ldots\}$.

Note that `InsertFields` uses the structure of the list *tops* to decide if the original `FeynArts` function or the extended version provided by `Pole` is to be applied. Of course, an input involving an intermediate state can only be specified if the topologies were generated using a corresponding input for the functions presented in the last section. Note that the specification of a fixed particle content for the intermediate state restricts the applicability of `Pole` to processes involving decays into stable particles only, such that it is not possible to treat decay chains of unstable particles decaying into unstable particles. The specification of the particle content of the initial and the final state can essentially be done in the same way as in `FeynArts`, e.g. `F[1,{1}]` denotes an electron neutrino, `V[1]` denotes a photon and so on. However, the input of `Pole` may contain two additional types of particles

particle	
`H[i]`	An initial-state hadron.
`-H[i]`	An initial-state anti-hadron.
`X[dec]`	An intermediate-state decaying particle.

The stable particles in the input for the intermediate state are specified as in `FeynArts`, whereas decaying particles must be specified by an additional label, such that e.g. `V[3][dec]` denotes a decaying W^--boson, `-V[3][dec]` denotes a decaying W^+-boson, and so on. `Pole` uses this information to apply a filter to the inserted topologies, which determines the mass pattern of the intermediate state specified in the input, and compares it to the masses of the fields addressed to the propagators of type `Propagator[Resonant]`. If the two sets of masses are not equal, the considered inserted topology is discarded. Furthermore, since only non-factorizable diagrams containing a massless particle in the loop lead to resonant contributions, the filter selects only those non-factorizable topologies where the propagator of type `Propagator[NonFac]` carries a massless particle.

Besides decaying intermediate-state particles, the `Pole` version of `InsertFields` accepts hadronic particles in the initial state. If not specified otherwise, `Pole` knows the hadrons $\pm$ `H[1]` which denote the proton and the anti-proton. Per default, the partonic content of the (anti) proton is given by all Standard Model quarks and anti-quarks except for the top, as well as the gluon and the photon. In order to specify a modified particle content or to define other hadrons, the `Pole` version of `InsertFields` accepts the option

option

`PartonicContent->H[i][`*Parton1*`,` *Parton1*`, ...]`

Specifies the partonic substructure of the hadron `H[i]` to contain the partons *Parton1*, *Parton1*,....

The other options accepted by `InsertFields` are those provided by `FeynArts`. Given the particle content, `Pole` simply determines all partonic initial states compatible with the charge of the final state, and applies `InsertFields` using as an input all so-obtained partonic subprocesses.

If invoked as above, the output of `InsertFields` is then of the general form

`PoleInsList[`*Hadronic Process*`][`
⋮
`PoleIns[{{`$\mathtt{i}_1, \mathtt{i}_2, \ldots$`},`$\mathtt{M}_1$`},{{`$\mathtt{i}_3, \mathtt{i}_4, \ldots$`},`$\mathtt{M}_2$`},...}][`
`TopologyList[`*Inserted topologies for partonic process 1*`],`
`TopologyList[`*Inserted topologies for partonic process 2*`]],`
⋮
further partonic processes`],`
⋮
further insertion lists of type `PoleIns`],

where an argument $\{\{\mathtt{i}_1, \mathtt{i}_2, \ldots\}, \mathtt{M}_1\}$ of `PoleIns` specifies that the corresponding sublist contains inserted topologies involving the decay of a resonance with mass $\mathtt{M}_1$ into the final state particles number $\mathtt{i}_1, \mathtt{i}_2, \ldots$ and so on. For example, in case of considering the production of two Z bosons decaying into two electron-positron pairs, there are two different resonance sets. The first set is given by the first (second) of the Z bosons decaying in electron number 3 (5) and the anti-electron number 4 (6), and the second set is given by the first (second) of the Z bosons decaying in electron number 3 (5) and the anti-electron number 6 (4). Accordingly, the output of `InsertFields` will contain two sublists `PoleIns[`$\{\{3,4\},M_Z\},\{\{5,6\},M_Z\}$`]` and `PoleIns[`$\{\{3,6\},M_Z\},\{\{4,5\},M_Z\}$`]` which contain the contributions to the amplitude which are resonant with respect to the two resonance sets. If applying `InsertFields` to a list of Born Topologies as created by `FactorizableTopologies` for this example, the output will additionally contain a list of type `PoleIns[{{}}]` which contains the full set of inserted Born topologies for the considered process.

Finally, to be able to paint the inserted topologies `Pole` extends the `Paint` function of `FeynArts` to also accept lists of type `PoleInsList`

`Paint[`*Ins*`,Options]`

Paints the diagrams for the list *Ins* of inserted topologies.

If the list *Ins* of inserted topologies has been created by applying `InsertFields` to the output of `CreateTopologies`, our extension will automatically apply the original `FeynArts` version of `Paint`. The syntax and the options are the same as in `FeynArts`, but the output is slightly different. For example, if applying the function `Paint` to the list of inserted Born topologies for the above example of the production of a ZZ pair decaying into two electron-positron pairs, the option `DisplayFunction->(Display["born.ps",#]&)` paints the inserted topologies for the full Born process to the file `"born_full.ps"`, whereas the inserted topologies contained in the sublists of type `PoleIns` with an non-empty arguments are painted to the files "`born_res1.ps`" and "`born_res2.ps`". If the user does not specify a diagram title by the `FeynArts` option `SheetHeader`, `PaintDiagrams` adds a title specifying the partonic subprocess and the resonance structure of the painted diagrams.

3.3 Creating Amplitudes

In a last step of amplitude generation using `Pole`, the inserted topologies generated by the methods discussed in the last two sections are translated into Feynman amplitudes by means of the `FeynArts` function `CreateFeynAmp`. However, to further pursue our approach

to treat the factorizable and non-factorizable contributions to the amplitude separately, one has to implement a gauge-invariant splitting of these two contributions. As said before, this splitting cannot be done at a diagrammatic level, since the non-factorizable diagrams with the virtual massless particle coupling to the resonance contain both, factorizable and non-factorizable corrections. In the procedure of amplitude generation presented so far, these diagrams where generated twice, once as a part of the factorizable corrections, and once as a part of the non-factorizable corrections.

As discussed in Section 2.4, a gauge invariant splitting of the amplitude in factorizable and non-factorizable parts can be achieved by subtracting the factorizable contribution of each such diagram from the corresponding non-factorizable contribution. This subtraction does not lead to a complete cancellation, since the loop integrals in the non-factorizable case are evaluated off-shell, whereas in the factorizable case the loop integrals are evaluated on-shell using a mass regulator. After the subtraction, the resonant part of the non-factorizable corrections are extracted by applying the Extended Soft Photon Approximation to the latter, which corresponds to setting the loop momentum equal to zero wherever this does not lead to a resonance.

In `Pole`, the Feynman rules are therefore separately applied to the factorizable and non-factorizable part of a given amplitude

`CreateFeynAmp[`*Ins*`,Options]`

Applies the Feynman rules to the list *Ins* of inserted topologies as generated by `InsertFields`.

`CreateESPAFeynAmp[`*Ins*`,Options]`

Applies the Feynman rules to the inserted non-factorizable topologies contained in the list *Ins*, and evaluates the resulting amplitude in Extended Soft Photon Approximation.

The first of these functions has the same syntax and options as in `FeynArts`, but was in `Pole` extended to accept also inserted topology lists of type `PoleInsList`. Here the structure of the list *Ins* is used to decide if the original or the extended version of `CreateFeynAmp` is to be used to insert the Feynman rules. The second function incorporates the above-described treatment to the non-factorizable corrections. To this end, `CreateESPAFeynAmp` takes as an input a list of inserted topologies generated by applying `InsertFields` to the output of `CreateNonFactorizableTopologies`, and translates this list in a Feynman amplitude as done in `FeynArts`. In a second step, `CreateESPAFeynAmp` replaces each loop integral by the difference of its non-factorizable contribution minus its factorizable contribution, with

this difference evaluated in ESPA. The exact form of the replacement rules used here are listed in Appendix C, where we discuss the treatment of the non-factorizable corrections in the framework of `Pole` in some more detail.

As is shown there, the amplitude for the non-factorizable corrections then only depends on a generic set of seven types of scalar loop integrals containing maximally five propagators. These loop integrals generally depend on complex masses, and can therefore not be evaluated numerically with standard libraries like `LoopTools`. We therefore provided the `Fortran` part of `Pole` to be discussed in the next chapter with an additional library for the numerical evaluation of the loop integrals in the non-factorizable corrections, where we use the analytic expressions listed in Appendix C. Note, however, that these expressions have been derived assuming massless external particles. As a consequence, the amplitude generation for the non-factorizable corrections as presented here can be applied to any process, whereas the numerical evaluation can only be used for the case of massless external particles.

To be able to treat the above-discussed integrals separately from the loop integrals appearing in the factorizable corrections, `CreateESPAFeynAmp` introduces new symbols

`B0c[`*Args*`], C0c[`*Args*`], D0c[`*Args*`], E0c[`*Args*`]`

The two-point functions, three-point functions, four-point functions, and five-point functions introduced by applying the ESPA to the non-factorizable corrections. The arguments *Args* are to be evaluated with the resonant momentum off-shell and a complex mass for the resonance.

,

The exact form of the arguments these loop integrals depend on is displayed in Appendix C. To pass the information which momenta are to be evaluated off-shell to the numerical evaluation, `Pole` introduces expressions of the type

`OffShell[`$\mathtt{p}^2_{\mathtt{res}}$`]-`$\mathtt{M}^2_{\mathtt{res}} - \mathtt{i}\mathtt{M}_{\mathtt{res}}\mathtt{G}_{\mathtt{res}}$

The off-shellness for a resonance with momentum $\mathtt{p}^2_{\mathtt{res}}$, mass $\mathtt{M}_{\mathtt{res}}$ and width $\mathtt{G}_{\mathtt{res}}$.

for the off-shellness appearing in the resonant propagators as well as the non-factorizable loop integrals discussed above.

Finally, the output of `CreateFeynAmp` and `CreateESPAFeynAmp` is a list of the general form

`PoleAmplitude[{`*Hadronic Process*`}][`
⋮
`PoleAmpList[Resonances ->` $\{\{i_1, i_2, \ldots\}, M_1\}, \{\{i_3, i_4, \ldots\}, M_2\}, \ldots\}$`][`
`FeynAmpList[`*Partonic Process 1*`][`*Diagram 1, Diagram 2,...*`],`
`FeynAmpList[`*Partonic Process 2*`][`*Diagram 1, Diagram 2,...*`],`
⋮
further partonic processes`],`
`PoleAmpList[Resonances ->` $\{\{j_1, j_2, \ldots\}, M_3\}, \{\{j_3, j_4, \ldots\}, M_4\}, \ldots\}$`][...],`
⋮
further amplitudes of type `PoleAmpList],`

where a resonance of mass M_1 decaying into the final-state particles number $i_1, i_2, \ldots$ is again denoted by a list $\{\{i_1, i_2, \ldots\}, M_1\}$.

3.4 Example

In this last section of this chapter we demonstrate the use of `Pole` for hadronic $W\gamma$ production, with the W decaying into an electron along with an anti-electron neutrino. If setting the CKM matrix to unity, the two possible partonic initial states are given by a reaction of an down quark and an anti-up quark, as well as a strange quark reacting with an anti-charm. Since these two partonic reactions are kinematically equivalent, we specify the colliding protons to contain partons of type up and down only. Furthermore, we set the masses of the light fermions to zero in the sense that we exclude the Higgs couplings of the light fermions. A program which calculates the partonic Born amplitude, the partonic factorizable and non-factorizable 1-loop amplitudes as well as the real QED-corrections and paints the corresponding diagrams might then look like

```
<<FeynArts.m
<<Pole.m


(*Set CKM Matrix to unity *)

CKM[A_,B_]:=IndexDelta[A,B];
dCKM1[A_,B_]:=0;
```

```
(*Options*)

SetOptions[CreateFactorizableTopologies,
                        ExcludeTopologies->{Tadpoles, WFCorrections}];
SetOptions[CreateFactorizableCTTopologies,
                        ExcludeTopologies->{TadpoleCTs, WFCorrectionCTs}];
SetOptions[CreateNonFactorizableTopologies,
                        ExcludeTopologies->{Tadpoles, WFCorrections}];
SetOptions[InsertFields, Model ->"SMc",InsertionLevel->{Classes},
          Restrictions->{NoQuarkMixing,NoLightFHCoupling},
          PartonicContent->{H[1][F[3,{1}],-F[3,{1}],F[4,{1}],-F[4,{1}]]}];
SetOptions[Paint,PaintLevel->{Classes},ColumnsXRows->4];


Reaction={H[1],H[1]}->{V[3][star],V[1]}->{F[2,1],-F[1,1],V[1]};


(*The Born Amplitudes*)
borntops=CreateFactorizableTopologies[0,2->{1,1}->3];
ampsborn=InsertFields[borntops,Reaction];
Paint[ampsborn,DisplayFunction->(Display["diagrams/born.ps",#]&)];
ampsborn=CreateFeynAmp[ampsborn];

(*The Factorizable Virtual Corrections*)
factops=CreateFactorizableTopologies[1,2->{1,1}->3];
ampsfac=InsertFields[factops,Reaction];
Paint[ampsfac,DisplayFunction->(Display["diagrams/fac.ps",#]&)];
ampsfac=CreateFeynAmp[ampsfac];

(*The Counter-Terms for the Factorizable Virtual Corrections*)
factopsct=FactorizableCTTopologies[1,2->{1,1}->3];
ampsfacct=InsertFields[factopsct,Reaction];
Paint[ampsfacct,DisplayFunction->(Display["diagrams/fac.ps",#]&)];
ampsfacct=CreateFeynAmp[ampsfacct];
```

```
(*The Non-Factorizable Virtual Corrections*)
nfactops=CreateNonFactorizableTopologies[1,2->{1,1}->3];
ampsnfac=InsertFields[nfactops,Reaction];
Paint[ampsnfac,DisplayFunction->(Display["diagrams/nfac.ps",#]&)];
ampsnfac=CreateESPAFeynAmp[ampsnfac];

(*The QED Bremsstrahlung corrections*)
Reaction={H[1],H[1]}->{}->{F[2,1],-F[1,1],V[1],V[1]};

bremstops=CreateFactorizableTopologies[1,2->{}->4]
ampsbrems=InsertFields[bremstops,Reaction];
Paint[ampsbrems,DisplayFunction->(Display["diagrams/brems.ps",#]&)];
ampsbrems=CreateFeynAmp[ampsbrems];
```

On a PC with an AMD Athlon (1.4 GHz) processor, the above program takes about 40 seconds of CPU time. The amplitudes stored in the variables `ampsborn`, `ampsfac`, `ampsfacct`, `ampsnfac` and `ampsbrems` can then by passed to the numerical evaluation part of `Pole` to be discussed in the next chapter, where the example presented here is continued at the end of Section 4.2.

Chapter 4

Numerical Evaluation

In the last chapter, we discussed how the amplitudes necessary for the calculation of a one-loop cross-section in Leading Pole Approximation can be generated analytically by computer-algebraical methods. However, the so-generated amplitudes are not yet suited for numerical evaluation. This is because the amplitudes generally contain fermionic spinor chains, which have to be reduced to products in the momenta of the external particles to be able to evaluate them numerically. Furthermore, a numerical evaluation for the loop integrals and a phase-space integration over the momenta of the final-state particles has to be implemented in order to be able to calculate physical observables.

A widely used tool for the numerical evaluation of amplitudes as generated by `FeynArts` is the `Mathematica` package `FormCalc` [69]. The basic idea is here to interface the analytical expression for a given amplitude to `Form` [70], to square the amplitude and to apply trace techniques to the resulting products of Dirac spinor chains in order to reduce the latter to scalar products in the external momenta. Furthermore, the length of the amplitudes is reduced by introducing abbreviations. The final `FormCalc` output consists of `Fortran` subroutines calculating numerical values for the so-determined amplitudes, which are combined with a set of generic drivers files to perform the phase-space integration.

When applying `FormCalc` to the amplitudes generated by `Pole`, one encounters two major problems. Firstly, when squaring an amplitude containing N Dirac spinor chains by means of trace techniques, one has to evaluate $\mathcal{O}(N^2)$ traces over gamma matrices. A 1-loop amplitude involving three or more particles in the final state generally contains a quite large number of such chains, such that the calculation of these traces can be quite costly in CPU time. Secondly, the numerical phase-space integration in the framework of `FormCalc` has been implemented for processes with up to three final-state particles only.

Taking this as a motivation, we extended the content of `Pole` by two more functions. In the file structure displayed in the beginning of the last chapter, these functions use the content of the last four files in the directory `Pole`. The basic idea is here to reduce the fermion chains contributing to a given amplitude in the framework of the Weyl-van der

Waerden formalism as presented in Appendix A of this work. As main advantage, the amplitude can in this formalism be reduced to a very compact form before taking the square, which speeds up the treatment of fermion chains quite considerably. Note that this feature has been built into the latest version of `FormCalc` [71], which was however to be released after we finished our work on the Weyl-van der Waerden part of `Pole`.

To cure the problem of a numerical phase-space integration, we interfaced the amplitudes to the generic Monte-Carlo generator `Lusifer` [43], which works for processes with any number of final-state particles. Note that `Lusifer` is a pure tree-level generator, such that we had to extend it by a proper treatment of the Bremsstrahlung phase-space. The reduction of fermion chains by means of the Weyl-van der Waerden formalism and the interface to `Lusifer` made it necessary to entirely rewrite the `Fortran` part of `FormCalc`. On the other hand, we further pursued our philosophy for the design of `Pole` as presented in the last chapter, and kept the syntax of the two new `Mathematica` functions as close as possible to the syntax of their `FormCalc` counterparts. To be able to use the above extension of `Pole`, one has to load first `FeynArts` (version 3.1 or higher), then `FormCalc` (version 3.1 or 3.2) and finally `Pole` in a `Mathematica` session. In the following, we present the main features of the numerical evaluation in the framework of `Pole`.

4.1 Simplifying the Amplitudes

The first step towards the numerical evaluation of physical observables using `FormCalc` is to apply the `Mathematica` function `CalcFeynAmp` to the output of `CreateFeynAmp`. As was said above, we intend to extend this function to incorporate the Weyl-van der Waerden Formalism for the reduction of spinor chains. Furthermore, in order to be able to apply `CalcFeynAmp` to the output of the `Pole`-version of `CreateFeynAmp`, the latter has to accept lists of type `PoleAmplitude` which contain the partonic amplitudes of a given process divided according to resonant propagators. To avoid this problem, `Pole` provides an extension of the `FormCalc` function `CalcFeynAmp`

`CalcFeynAmp[`*Amps*`,Options]`

Reduces all kinematical objects contained in the list of amplitudes *Amps* by means of the Weyl-van der Waerden Formalism, splits the resulting expression into helicity amplitudes and introduces abbreviations.

If the list of amplitudes *Amps* is of type `FeynAmpList`, i.e. if it has been generated by the `FeynArts` version of `CreateFeynAmp`, the above function will automatically use `FormCalc` to reduce the fermion chains and to introduce abbreviations. If *Amps* is of type

`PoleAmplitude`, on the other hand, the `Pole` version is used. The latter basically applies the `FormCalc` version of `CalcFeynAmp` to the subamplitudes of definite resonance structure and partonic subprocesses in the output of `CreateFeynAmp`. However, instead of evaluating the square of the amplitudes by means of trace techniques, the extended version of `CalcFeynAmp` applies the Weyl-van der Waerden formalism as presented in Appendix A to the list of introduced abbreviations for fermion chains, scalar products and ϵ-tensors, and returns all kinematical objects in this list as products of Weyl-spinor products and Kronecker deltas in the helicities of the external particles. In a next step, the fermion chains are reinserted in the amplitudes $\mathcal{A}$ corresponding to a given partonic subprocess and a given resonance structure, which can then be decomposed into pieces corresponding to different colour and helicity structures

$$\mathcal{A} = \sum_{\mathrm{col}=1}^{\mathrm{ncol}} C_{\mathrm{col}}^{c_1,\ldots,c_n} \sum_{\mathrm{hel}=1}^{\mathrm{nhel}} \Delta_{\sigma(\mathrm{hel})}^{\sigma_1,\ldots,\sigma_n} \mathcal{A}_{\mathrm{col,hel}}, \tag{4.1}$$

where the factors C_{col} are generally given by a product of SU(3) generators depending on the colours $c_1, \ldots, c_n$ of the n external particles. The quantities Δ_{hel}, on the other hand, are given by products of Kronecker deltas in the external helicities $\sigma_1, \ldots, \sigma_n$, where it is understood that the second sum in (4.1) only receives a nonzero contribution for the helicity combination $\sigma(\mathrm{hel}) = \{\sigma_1, \ldots, \sigma_n\}$. The output of `CalcFeynAmp` is then given by a list

`PoleAmplitude[{`*Hadronic Process*`}][`
⋮
`PoleAmpList[Resonances ->` $\{\{\mathtt{i}_1, \mathtt{i}_2, \ldots\}, \mathtt{M}_1\}, \{\{\mathtt{i}_3, \mathtt{i}_4, \ldots\}, \mathtt{M}_2\}, \ldots\}$`][`
⋮
`PartonicAmplitude[Process->`*Partonic Process 1*`][`
⋮
`ColAmp[Colours->`$C_{\mathrm{col}}^{c_1,\ldots,c_n}$`][`
⋮
`HelAmp[Helicity->`$\Delta_{\sigma(\mathrm{hel})}^{\sigma_1,\ldots,\sigma_n}$`][`*helicity amplitude 1*`],`
`HelAmp[Helicity->`$\Delta_{\sigma(\mathrm{hel})}^{\sigma_1,\ldots,\sigma_n}$`][`*helicity amplitude 2*`],`
⋮
further helicity amplitudes`],`
⋮
further colour structures`],`
⋮
further partonic processes`],`
⋮
further amplitudes of type `PoleAmpList],`

where each lists of type `HelAmp[]` contains one of the helicity amplitudes $\mathcal{A}_{\text{col,hel}}$ in (4.1). If applying `CalcFeynAmp` to the output of `CreateFeynAmp` for the Born process and the real corrections, the above output list will contain a sublist with an empty resonance specification, which contains the amplitudes for the full processes. The sublists with non-empty resonance specification in the output lists for the Born amplitudes and for the virtual corrections, on the other hand, contain the resonant parts of the considered amplitudes.

To optimize the numerical evaluation of the helicity amplitudes, `CalcFeynAmp` introduces abbreviations, which are given back in two separate lists

`AbbrNConst[]`	Returns the list of phase-space dependent abbreviations,
`AbbrConst[]`	Returns the list of phase-space independent abbreviations,
`ClearAbbrNConst[]`	Deletes the phase-space dependent abbreviations,
`ClearAbbrConst[]`	Deletes the phase-space independent abbreviations.

The commands `ClearAbbrNConst[]` and `ClearAbbrConst[]` delete the contents of the lists `AbbrNConst[]` and `AbbrConst[]`, respectively, which can be used if one does not want the abbreviations for the amplitudes calculated so far to be put in the same list as the abbreviations for the amplitudes to be calculated next. The abbreviations on these lists are denoted by

abbreviation	*contained in the list*	*denotes*
`Cpl1,Cpl2,...`	`AbbrConst[]`	couplings,
`Prp1,Prp2,...`	`AbbrNConst[]`	propagators,
`WProd1,WProd2,...`	`AbbrNConst[]`	products of Weyl-van der Waerden products,
`OffSh1,OffSh2,...`	`AbbrNConst[]`	the resonant momenta to be evaluated off-shell,
`LInt1,LInt2,...`	`AbbrNConst[]/AbbrConst[]`	loop integrals,
`dZe1,dMWsq1,...`	`AbbrConst[]`	renormalization constants.

The list `AbbrConst[]` of phase-space independent abbreviations generally contains the definition of the couplings, the constant loop integrals and the renormalization constants, where the latter are denoted as in `FormCalc`. In addition, `CalcFeynAmp` calculates the constant

$$\texttt{dZR1} = \left.\frac{\partial\Sigma^\gamma(k^2)}{\partial k^2}\right|_{k^2=0} - \frac{\cos^2\theta_W}{\sin^2\theta_W}\left(\frac{\Sigma^Z(M_Z^2)}{M_Z^2} - \frac{\Sigma^W(M_W^2)}{M_W^2}\right) + \frac{\Sigma^W(0) - \Sigma^W(M_W^2)}{M_W^2} + 2\frac{\cos\theta_W}{\sin\theta_W}\frac{\Sigma^{\gamma Z}(0)}{M_Z^2} + \frac{\alpha}{4\pi\sin^2\theta_W}\left(6 + \frac{7-4\sin^2\theta_W}{2\sin^2\theta_W}\log\cos^2\theta_W\right)$$

The quantity $\Delta r^{(1)}$ needed to evaluated an amplitude in the α_{G_F}-scheme,

and we will come back to the use of this quantity in Section 4.3.

The phase-space dependent abbreviations in the list `AbbrNConst[]`, on the other hand, contains the definitions of the abbreviations for products of Weyl-spinor products, phase-space dependent loop integrals and propagators. Compared to `FormCalc`, they involve the additional kinematical structures

`Prod[i,j,l,m]` $= \langle k_{i,j} k_{l,m}\rangle$

The Weyl-spinor product between the eigenvector number j of $\sigma_\mu k_i^\mu$ with the corresponding momentum spinor $k_{l,m}$,

`ProdC[i,j,l,m]` $= \langle k_{i,j} k_{l,m}\rangle^\star$

The corresponding complex conjugate Weyl-spinor product,

`Prp[p^2,M,Γ]` $= (p^2 - M^2 + \mathrm{i}M\Gamma)^{-1}$

A propagator of momentum p^2, Mass M and decay width Γ.

The numerical evaluation of these quantities is discussed in Section 4.5. Note, that each amplitude corresponding to a given resonance structure has later to be evaluated numerically using a different on-shell projected phase-space. Accordingly, the abbreviations for each such amplitude are separately introduced, which results in a division of the list `AbbrNConst[]` according to resonance structures.

The `Pole` version of `CalcFeynAmp` accepts all options implemented in `FormCalc`, plus the two additional options

option	*default value*	
`ParticleWidths`	`{V[2],-V[3],V[3],S[1]}`	Specifies which particles receive a finite width,
`SmallFermionMasses`	{}	Specifies which fermion masses are to be set to zero.

Generally, `CalcFeynAmp` uses the fixed-width scheme in the full Born amplitude and the real corrections, i.e. here a finite width is introduced in all propagators which depend on the masses of the particles specified by the option `ParticleWidths` to receive a finite width. In the resonant factorizable parts of the Born amplitudes and the resonant factorizable and non-factorizable virtual corrections, on the other hand, a finite width is only introduced in the resonant propagators. The option `SmallFermionMasses->`$\{m_{\text{light},1}, m_{\text{light},2}, \ldots\}$ sets the specified fermion masses in all propagators, spinor chains and couplings to zero, except if a given coupling multiplies a loop integral of type `DB0,DB1,DB00` or `DB11` depending on light masses m_{light} only. In that case, these loop integrals scale like $1/m^2_{\text{light}}$, such that a factor m_{light} contained in a coupling multiplying such a loop integral cannot be set to zero. To avoid singularities, the light masses are kept if they appear in the argument of a loop integral.

Note that the calculation of an amplitude including finite masses for external fermions generally may lead to a quite drastic increase in the needed CPU time. Furthermore, `CalcFeynAmp` sets internally the option `Mandelstam` of `CalcFeynAmp` to `False`, such that it is not possible to use this option anymore.

4.2 Generating Fortran Codes

As a last feature of `Pole`, we show in this section how the amplitudes generated by the methods presented so far can be evaluated numerically. We here follow the basic idea of `FormCalc` to translate the `Mathematica` output of `CalcFeynAmp` into `Fortran` code, which is then combined with a set of generic drivers files providing the phase-space integration for a general hadronic cross-section. However, the abbreviations introduced by the `Pole` version of `CalcFeynAmp` are completely different from the output of the `FormCalc` version. Furthermore, the `Fortran` part of `FormCalc` does not incorporate the evaluation of the amplitudes in Leading Pole Approximation and no treatment of soft and collinear singularities in the real and virtual corrections has been implemented. As a consequence, we had to entirely rewrite the `Fortran` part of `FormCalc`.

To be able to treat the output of the `Pole` version of `CalcFeynAmp` numerically, we extended our package by the `Mathematica` function

`PoleToFortran`[$\{A_1, A_2, \ldots, abbr_{\mathrm{A}}\}$,$\{B_1, B_2, \ldots, abbr_{\mathrm{B}}\}$,...,$abbr_{\mathrm{Const}}$,$Dir$]

Writes `Fortran` codes for the amplitudes A_1, A_2,... B_1, B_2,... etc. to be evaluated using the phase-space dependent abbreviations $abbr_{\mathrm{A}}^{\mathrm{NConst}}$, $abbr_{\mathrm{B}}^{\mathrm{NConst}}$ etc. along with the phase-space independent abbreviations to the directory Dir, and creates all drivers files necessary for the numerical evaluation in the same directory.

Here the list $abbr_{\mathrm{A}}$ has to contain the phase-space-dependent abbreviations for the amplitudes $A_1, A_2, \ldots$ and $abbr_{\mathrm{Const}}$ contains the constant abbreviations for all generated amplitudes. Invoked as specified above, `PoleToFortran` creates the following file structure

Dir/
- `makefile`
- `main.F`
- `input_sm.F`
- `input_pdfs.F`
- `input_cuts.F`
- `input_onshell.F`
- `utils.F`
- `params.h`
- `process.h`
- `allcommon.h`
- `Cteq61Pdf.F`
- `cteq6m.tbl`

Dir/int/
- `integration.F`
- `cuts.F`
- `model_lusifer.F`
- `lusifer.F`
- `hadroncs.F`
- `resonances.F`

Dir/amps/
- `squaredME.F`
- `ampcom.h`
- `ampvars.h`
- `kinematics.F`
- `looptools_nfac.F`
- `A1.F`
- `A2.F`
- ⋮
- $\mathtt{abbr}_{\mathtt{A}}$`.F`
- $\mathtt{abbr}_{\mathtt{B}}$`.F`
- ⋮
- $\mathtt{abbr}_{\mathtt{Const}}$`.F`

Dir/histo
- `histograms.F`

As indicated here, the `Fortran` files generated by `Pole` come in four different categories. The uppermost level of the directory *Dir* contains the input files, header files and the auxiliary functions which are used globally. The remaining three directories *int*, *amps* and *histo* contain the files related to the phase-space integration, to the numerical evaluation of the amplitudes and to the generation of histograms, respectively.

Before explaining the content of the above file structure in the three sections to follow, we illustrate the syntax of `CalcFeynAmp` and `PoleToFortran` by applying these functions to the example in Section 3.4. Note that one here has to load first `FeynArts`, then `FormCalc`, and finally `Pole` in the current `Mathematica` session before starting the generation of amplitudes. A program to simplify the amplitudes for the case of massless external particles and to provide a `Fortran` output for the numerical evaluation in the directory `fortran` then looks like

```
<<FeynArts.m
<<FormCalc.m
<<Pole.m
⋮
```
Code of the example in Section 3.4
```
⋮
(*Options*)
SetOptions[CalcFeynAmp, SmallFermionMasses->{MU,MD,MC,MS,MB,ME,MM,ML}]

(*The Born Amplitudes*)
ampsBorn=CalcFeynAmp[ampsBorn];
abbrBorn=AbbrNConst[];ClearAbbrNConst[];

(*The Virtual Corrections*)
ampsfac=CalcFeynAmp[ampsfac];
ampsnfac=CalcFeynAmp[ampsnfac];
ampsct=CalcFeynAmp[ampsfacct];
abbrvirt=AbbrNConst[];ClearAbbrNConst[];

(*The QED Bremsstrahlung corrections*)
ampsbrems=CalcFeynAmp[ampsbrems];
abbrbrems=AbbrNConst[];ClearAbbrNConst[];

abbrconst=AbbrConst[];ClearAbbrConst[];

PoleToFortran[{ampsBorn,abbrBorn},{ampsfac,ampsnfac,ampsfacct,abbrvirt},
                              {ampsbrems,abbrsbrems},abbrconst,"fortran"];
```

On a PC with an AMD Athlon (1.4 GHz) processor, the whole program takes about three minutes of CPU time.

4.3 Structure and Input of the Fortran Code

In the following, we sketch the general structure of the `Fortran` output of `Pole` and describe the necessary input to run the latter. The main function of the phase-space integration is given by the `subroutine integrate` contained in the file `int/integration.F`, which calls the generic Monte-Carlo generator `Lusifer` [43] for phase-space generation. The necessary functions are here provided by the files `int/lusifer.F` and `int/model_lusifer.F`. To flatten possible resonance peaks, `Lusifer` is designed to employ the multi-channel importance sampling technique, which is discussed in Appendix E of our work in more detail. If processes with different final-states contribute to the total cross-section, the phase-space generation is done for each final state separately. For example, consider the case that one is to calculate a cross-section for a given process including real QED corrections with an extra final-state photon and two QCD Bremsstrahlung processes with an extra final state gluon and an extra final-state quark, respectively. The generator number one will then generate the phase-space for the Born process, which is used to calculate the Born cross-section, the virtual corrections as well as the singular parts in virtual and real corrections, whereas the generators number two, three and four will generate the phase-space used to calculate the finite contributions of the Bremsstrahlung processes for the QED and the two QCD Bremsstrahlung processes. The program then uses the routines in `int/cuts.F` to check a given event is compatible with the cuts conditions to be discussed below. If an event is accepted, the routines in `int/hadron_cs.F` calculate the weights for the various contributions to the hadronic cross-section and averages the result over the number of generated phase-space points to yield the Monte-Carlo estimate as well as the corresponding standard deviation for the total hadronic cross-section.

For the calculation of the weights for the hadronic cross-section, the numerical evaluation of the squared partonic amplitudes is done by the routines in the file `amps/squaredME.F`. The latter makes use of the subroutines in the files `A1.F`, `A2.F`,..., which contain the `Fortran` code for the amplitudes generated by `PoleToFortran`. The couplings, the constant loop integrals and the renormalization constants are calculated by the subroutine in $\texttt{abbr}_{\text{Const}}\texttt{.F}$, which is called before starting the phase-space integration. The files $\texttt{abbr}_{\text{A}}\texttt{.F}, \texttt{abbr}_{\text{B}}\texttt{.F}, \ldots$ contain the code for the calculation of the phase-space dependent abbreviations. Here, the Weyl-spinor products and propagators are determined by the subroutines in the file `amps/kinematics.F`. The loop integrals for the factorizable amplitudes do not contain complex masses and can therefore be evaluated using the `FF` based library `LoopTools` [72, 73]. The form of the loop integrals appearing in the non-factorizable part of the virtual corrections, on the other hand, is largely process-independent, and the corresponding numerical evaluation is done in the file `amps/looptools_nfac.F`.

A more detailed description of the various files and subroutines related to the phase-space integration and to the numerical evaluation of the squared partonic amplitudes is given in Section 4.4 and 4.5, respectively.

Main Program

The main program combining the above file structure is provided by the file `main.F`. Besides the program output, the necessary parameters for the phase-space integration like the hadronic centre-of-mass energy $\sqrt{S}$ or the number of generated phase-space points can be specified here. For the output of intermediate results, a value for the parameter `nsteps` can be chosen, which specifies that the intermediate results are written out every `nsteps` events. The adaptive optimization for the multi-channel phase-space integration as discussed in Appendix E can be switched on by choosing a nonzero values for the variables `nadapt` and `adaptsteps`. The latter two parameters specify how many times the adpative optimization is to be applied, where the number of events to be generated between two optimization steps is given by `adaptsteps` times the number of channels for the considered process.

Furthermore, if considering real corrections, `main.F` provides the possibility to choose between the phase-space slicing and the subtraction method for the treatment of the soft and collinear divergences. In case of using the method of phase-space slicing, the slicing cuts δ_c on the production angles as well as the cut δ_s on the energy of the Bremsstrahlung particle have to be fixed. In case of using the subtraction method, on the other hand, the emission angle and the energy of the Bremsstrahlung particle can become arbitrarily small. Analytically this is not a problem, since in these limits the subtraction terms coincide exactly with the Bremsstrahlung matrix element and the overall contribution of the finite real corrections to the total cross-section vanishes. Numerically, however, a too small emission angle or energy of the Bremsstrahlung particle may cause instabilities in the evaluation of the amplitude, which spoils the matching of the latter with the subtraction terms. This in turn may lead to large contributions to the finite real corrections in the above limits, such that the integrand has to be set to zero by hand if emission energy and/or the emission angles become too small. Both limits can be treated in one go by imposing the technical cut `tcut` on the invariant masses

$$(p_i + k_{\mathrm{brems}})^2 > \texttt{tcut} \tag{4.2}$$

for all emitters i, where k_{brems} is the momentum of the Bremsstrahlung particle. A further parameter in `main.F` related to the Bremsstrahlung processes is given by the variable `inclusive`, which if set to zero imposes a exclusive treatment of the Bremsstrahlung processes, whereas a value equal to one will lead to a fully inclusive treatment. The exclusive treatment is implemented by simply discarding all events, for which the corresponding momenta are not affected by the recombination procedure to be discussed below. Moreover, `main.F` provides the possibility to specify a precision goal for the numerical integration. If choosing the latter different from zero, the phase-space integration for the finite virtual corrections and for the sum of the singular virtual and real corrections is stopped if the corresponding integration errors in per cent of the Born cross-section drop below the specified value for the precision goal.

For the evaluation of the amplitudes, the input scheme for the electromagnetic coupling constant can be chosen in `main.F`, and numerical values for the UV and infrared regulators can be fixed. Generally, the amplitudes are calculated using $\alpha = \alpha_0$. However, if the parameter `qalp` in `main.F` is set to one, the α_{G_F}-scheme is used to parameterize the electromagnetic coupling constant. To this end, all amplitudes, numerically evaluated with $\alpha = \alpha_0$, are internally multiplied by a factor

$$w_{G_F} = \sqrt{\frac{\alpha_{G_F}}{\alpha_0}} \tag{4.3}$$

for each coupling in the Born amplitude that is to be parameterized with α_{G_F}. The number of such couplings can be specified in `main.F` by choosing the parameter `ndZR1` different from zero. However, the virtual corrections have then to be corrected for the evolution of the electromagnetic coupling constant to the mass of the W boson. This can be done by subtracting the Born cross-section times the quantity

$$\begin{aligned}\Delta r^{(1)} = {} & \left.\frac{\partial \Sigma^\gamma(k^2)}{\partial k^2}\right|_{k^2=0} - \frac{\cos^2\theta_W}{\sin^2\theta_W}\left(\frac{\Sigma^Z(M_Z^2)}{M_Z^2} - \frac{\Sigma^W(M_W^2)}{M_W^2}\right) + \frac{\Sigma^W(0) - \Sigma^W(M_W^2)}{M_W^2} \\ & + 2\frac{\cos\theta_W}{\sin\theta_W}\frac{\Sigma^{\gamma Z}(0)}{M_Z^2} + \frac{\alpha}{4\pi\sin^2\theta_W}\left(6 + \frac{7 - 4\sin^2\theta_W}{2\sin^2\theta_W}\log(\cos^2\theta_W)\right). \end{aligned} \tag{4.4}$$

from the virtual corrections once for each of the `ndZR1` couplings in the Born matrix elements which are to be parameterized with $\sqrt{\alpha_{G_F}}$. The parameter $\Delta r^{(1)}$ corresponds to the parameter `dZR1` calculated by the `Mathematica` function `CalcFeynAmp`, which was mentioned in Section 4.1. The necessity of this subtraction arises from the fact that the parameterization of α in terms of the Fermi constant effectively resums higher-order contributions to the vertex corrections. The resummed 1-loop terms are then contained twice in the first-order perturbative cross-section, once as part of α_{G_F}, and once as contribution to the vertex corrections. They have thus to be subtracted to avoid double counting. As a consequence, the number of couplings in the Born matrix element that have to be parameterized by α_{G_F} is given by the number of couplings involving a large momentum transfer, whereas couplings evaluated at small momentum transfer should be parameterized by α_0. Note that the multiplication of the cross-section with (4.3) and the subtraction of (4.4) from the virtual corrections are in the framework of our program done automatically as soon as the parameter `ndZR1` is chosen different from zero.

Finally, if one is to scan the dependence of the total cross-section on process or model parameters, the range and the steps of the scan can be specified in `main.F` by a loop over the considered parameter.

Input for the Model Parameters

The input connected to the parameters of the considered model is provided by the files `input_sm.F`. This file contains the numerical values for the Standard Model parameters, which are then used to fill these values in the mass arrays for leptons and quarks. Note that the model input for the `Fortran` output of `Pole` is provided for the Standard Model only. If a different model was used during amplitude generation, one has to replace all routines contained in `input_sm.F` by corresponding input routines for the considered model.

Input for the Parton Distribution Functions

When calculating hadronic observables, one has to specify how the Parton Distribution Functions are to be convoluted with the partonic cross-section. The corresponding input is provided by the file `input_pdf.F`. Here the `subroutine getfscale(Q,klab)` specifies how the typical energy scale `Q` needed for the evaluation of the Parton Distribution Functions is to be calculated from the momentum matrix `klab` in the laboratory frame. The `subroutine dldtaudx(dldtdx,x1,x2,Q)` then calculates the product

$$\texttt{dldtdx(procnr)(x1, x2, Q)} = \overline{\Phi}_{P_1|q_1}(\texttt{x1}, \texttt{Q})\overline{\Phi}_{P_2|q_2}(\texttt{x2}, \texttt{Q}), \tag{4.5}$$

where q_1 and q_2 are the initial-state partons of the partonic subprocess number `procnr`, and `x1` and `x2` are the corresponding energy fractions. Note that in considering massless partons, the partonic cross-sections are often invariant under an exchange of the initial-state quarks within the same quark family. In that case, the corresponding partonic cross-section needs to be calculated for one flavour combination in the initial state only, and the above product of parton distributions can be replaced by the corresponding products summed over the initial-state flavours. Per default, `Pole` uses the Parton Distribution Functions of the CTEQ6M set [74] to calculate the product (4.5). To use a different set, one has to replace the file `Cteq61Pdf.F` as well as the table file `cteq6m.tbl` by corresponding files for the Parton Distribution Functions to be used. Furthermore, one has to edit the `makefile` to link the file replacing `Cteq61Pdf.F` to the main program. Finally, in the file `input_pdf.F` one has to insert the initialization and the function call for the considered set of Parton Distributions.

Input for the Cut Parameters

To obtain realistic results for cross-sections and kinematical distributions, one has to specify how the considered processes can be defined experimentally. In doing so, one has to account for the finite detector resolution of the considered experiment. For example, one has to consider the fact that two particles hitting the detector too close to each other cannot be separated by measurement. The corresponding event can then not be distinguished from an event where only one of the particles is produced. Similarly a particle which hits the detector too close to the beam-pipe or with too low energy cannot be detected at all,

such that the corresponding event cannot be distinguished from an event where the particle is not produced. In practice, the problem of taking into account the finite detector resolutions is usually dealt with by imposing *phase-space cuts* on the momenta of the final-state particles. When analyzing experimental data, this is equivalent to considering only the events where all final-state particles are well separated. For a theoretical calculation, imposing phase-space cuts means that one must not integrate over the whole phase-space, but only over a sub-volume defined by all sets of momenta which fulfill the corresponding separation requirements.

In the framework of the `Fortran` output of `Pole`, the process definition can be specified in the file `input_cuts.F`. To ensure that only events are counted, where all particles have a large enough energy and a large enough emission angle to be detected, a lower cut `ptcut` on the transverse momentum

$$p_{\mathrm{T}} = \sqrt{p_x^2 + p_y^2} \tag{4.6}$$

and a upper cut `etacut` on the absolute values of the pseudo rapidity

$$\eta = -\log\left(\tan\frac{\theta}{2}\right), \tag{4.7}$$

can be required, where θ is the angle of the considered particle with respect to the beam. Alternatively, lower cuts `ecut` and `ccut` can be imposed on the energies of the final-state particles and the cosines of the corresponding emission angles with respect to the beam. Furthermore, one has to make sure that only events are considered where the final-state particles are separated by a minimal angle from each other. This requirement can be met by imposing a lower cut `Rcut` on the rapidity-azimuthal angle separation between all detected particles

$$\Delta R_{ij} = \sqrt{(\eta_i - \eta_j)^2 + (\varphi_i - \varphi_j)^2}, \tag{4.8}$$

where φ_i denotes the azimuthal angle of the momentum of particle i with respect to the beam. For a final state containing one or more neutrinos, neither the rapidity nor the transverse momentum of these particles can be measured. The only experimentally accessible quantity is in this case the missing transverse momentum

$$p_{\mathrm{T}}^{\mathrm{miss}} = \sqrt{\left(\sum_{i,\mathrm{vis.}} p_{i,x}\right)^2 + \left(\sum_{i,\mathrm{vis.}} p_{i,y}\right)^2}, \tag{4.9}$$

where the sums are taken over all particles visible in the detector. In `input_cuts.F`, a lower cut `ptmcut` can be imposed on the missing transverse momentum. To be able to introduce different cuts for different final-state particles, the above cut variables usually have the extension `l,q,p,g` and `b` denoting charged leptons, quarks, photons, gluons and the beam, respectively. For example, `ccutpb` denotes an angular cut of all final-state photons and gluons with the beam, `ptcutl` denotes the cut on the transverse momentum of all final-state charged leptons and so on.

As was said in Section 2.4, the calculation of virtual corrections in Leading Pole Approximation generally makes use of the assumption that the main contribution to the total cross-section originates from the phase-space regions where the squared momenta of the decaying particles are close to the mass shell. While this introduces an error of width over mass of the decaying particles in the total cross-section, the difference between the exact results to the results in Leading Pole Approximation might be larger when considering distributions. To obtain consistent predictions, it is therefore often necessary to only take into account events where the resonant momenta are close to the corresponding masses. In case that all decay products of a given resonance are visible in the detector, this requirement can be met by restricting the invariant mass of the decay products to an interval around the mass of the decaying particle. In case of a resonance decaying into a visible particle l and an invisible particle, an upper bound on the transverse mass

$$M_{\mathrm{T}} = \sqrt{(|p_{\mathrm{T}}^{\mathrm{miss}}| + |p_{\mathrm{T},l}|)^2 - (p_x^{\mathrm{miss}} + p_{x,l})^2 - (p_y^{\mathrm{miss}} + p_{y,l})^2}. \tag{4.10}$$

is appropriate for this purpose. In the file `input_cuts.F` these so-called *reconstruction cuts* are denoted by `dminvcut` and `dmtcut`, respectively. A value of these parameters different from zero will restrict the invariant mass m_{inv} or the transverse mass M_T of the decaying particles to intervals around the mass M of the resonance

$$M - \texttt{dminvcut} < m_{\mathrm{inv}} < M + \texttt{dminvcut}, \qquad M_{\mathrm{T}} < M + \texttt{dmtcut}. \tag{4.11}$$

To this end, the cut initialization routines check how many of the decay products of a given resonance are neutrinos. If this number is equal to zero, a cut on the invariant mass is applied. In case that this number is smaller than the total number of decay products but larger than zero, the cut on the transverse mass is used, whereas if the resonance decays exclusively into neutrinos, no cut is applied. Considering for example a Z resonance, a cut on the invariant mass is imposed if the Z boson decays into charged leptons, but not if the resonance decays into neutrinos. For a W resonance decaying into a charged lepton and a neutrino, on the other hand, the cut on the transverse mass of the resonance is applied. Finally, if one is interested in high-energy observables only, and if all final-state particles are visible in the detector, a lower cut on the invariant mass of the parton process

$$\sqrt{\hat{s}} = \sqrt{(p_3 + \ldots + p_n)^2} \tag{4.12}$$

can be imposed by choosing the parameter `minvcutfinal` in `input_cuts.F` different from zero, where n denotes in (4.12) the number of external particles of the considered process.

However, if considering a one-loop corrected cross-section including Bremsstrahlung corrections, the Bremsstrahlung particle is not bound to be visible, such that in the fully inclusive case the corresponding momentum has to be integrated out without any cut restrictions. In a Monte-Carlo phase-space integration, this can be taken into account by imposing the cut conditions only on the momenta of the particles appearing in the Born process as well.

On the other hand, in the case where the Bremsstrahlung particle has not enough energy to be detected or a too small angle with respect to the beam-pipe, it will only be visible in the detector as missing momentum. From a theoretical point of view, the Bremsstrahlung momentum has then to be added to the missing momentum, but the event has otherwise to be treated as if the Bremsstrahlung particle has not been produced. Similarly, if the Bremsstrahlung particle is emitted with a momentum k too close to the momentum p of another detected particle, the detector measures only one effective particle with a total momentum $p + k$. From a theoretical point of view, the Bremsstrahlung momentum has in this case to be added to the momentum of the final-state particle close to it, and the separation cut conditions have to be applied to the recombined momentum $p + k$ of the detected effective particle rather than to the momentum p. For a consistent definition of a process including real corrections, one therefore has to specify a second set of cuts, the so-called *recombination cuts*, which define the phase-space region around the final-state particles or the beam pipe within which the Bremsstrahlung particle cannot be separately detected. In `input_cuts.F` the recombination cuts `ptcutrec`, `etacutrec`, `ecutrec` and `ccutrec` on the transverse momentum, the rapidity, the energy and the production angle of the Bremsstrahlung particle can be specified. The Bremsstrahlung momentum is here counted as missing momentum if one of the conditions

$$p_{\mathrm{T}}^{\mathrm{brems}} < \texttt{ptcutrec}, \quad |\eta^{\mathrm{brems}}| > \texttt{etacutrec}, \quad E^{\mathrm{brems}} < \texttt{ecutrec}, \quad |\cos\theta^{\mathrm{brems}}| < \texttt{ccutrec} \tag{4.13}$$

is fulfilled. Furthermore, the Bremsstrahlung momentum is recombined with the momentum of another final-state particle if the rapidity-azimuthal angle separation (4.8) is smaller than the value specified for `rcutrec` in `input_cuts.F`. As was said above, in case that the parameter `inclusive` in the file `main.F` is set equal to zero, our program will impose an exclusive treatment of the Bremsstrahlung by discarding all events which do not fulfill the above recombination cut conditions.

If one is to implement other cuts than those listed in `input_cuts.F`, the file `README_NEWCUTS` contains the necessary instructions.

On-Shell Projection

The evaluation of a cross-section in Leading Pole Approximation requires a projection of the external momenta on the mass shells of the resonances. Since this projection depends on the considered process, one has to specify how the projected momenta are to be calculated from the original momenta before starting the phase-space integration. In the framework of our program, this can be done in the `subroutine onshell(resnr,K,Knew,osh)` contained in the file `input_onshell.F`. This subroutine takes as an input a matrix $\texttt{K} = \texttt{K}(\texttt{n}_\texttt{p}, 0:3)$ containing the four-momenta of the $\texttt{n}_\texttt{p}$ external particles at a given phase-space point. The output momentum matrix `Knew` contains the momenta of the external particles after projection on the masses of the resonance set number `resnr`. Since the specification of an onshell-projection requires knowledge about the internal numbering of the reso-

nances as well as of the momenta appearing in the corresponding resonant propagators, `WriteToFortran` automatically generates the file `int/resonances.F`, where this information is stored in the variables `resmass(0:nres,npole)` and `resmoms`$(0:\texttt{nres},\texttt{n}_\texttt{p})$. Here, the array `resmass(i,j)` contains the mass of the pole number `j` of the resonance structure number `i`, whereas `resmoms`$(\texttt{i},\texttt{k}) = \texttt{j}$ if the momentum of the external particle number `k` contributes to the pole number `j` of the resonance structure number `i`. The resonance number zero always corresponds to the off-shell case. To give an example, suppose that one is considering a process involving two Z bosons decaying into electron-positron pairs with momenta k_3, k_4, k_5, k_6. In that case, there are two possible decay scenarios, one where the two Z bosons decay into the lepton pairs with momenta k_3, k_4 and k_5, k_6, respectively, and one where the bosons decay into the pairs k_3, k_6 and k_4, k_5. The file `int/resonances.F` then contains the arrays

$$\begin{aligned}
&\texttt{resmass}(0,1) = 0, \quad \texttt{resmass}(0,2) = 0, \\
&\texttt{resmoms}(0,3) = 0, \quad \texttt{resmoms}(0,4) = 0, \quad \texttt{resmoms}(0,5) = 0, \quad \texttt{resmoms}(2,6) = 0, \\
&\\
&\texttt{resmass}(1,1) = M_Z, \quad \texttt{resmass}(1,2) = M_Z, \\
&\texttt{resmoms}(1,3) = 1, \quad \texttt{resmoms}(1,4) = 1, \quad \texttt{resmoms}(1,5) = 2, \quad \texttt{resmoms}(1,6) = 2, \\
&\\
&\texttt{resmass}(2,1) = M_Z, \quad \texttt{resmass}(2,2) = M_Z, \\
&\texttt{resmoms}(2,3) = 1, \quad \texttt{resmoms}(2,4) = 2, \quad \texttt{resmoms}(2,5) = 2, \quad \texttt{resmoms}(3,6) = 1.
\end{aligned} \tag{4.14}$$

The on-shell projection has then for `resnr=1` to return the momentum `knew` resulting from the projection of k on the mass-shells $(k_3 + k_4)^2 = M_Z^2$, $(k_5 + k_6)^2 = M_Z^2$, whereas for `resnr=2`, the returned momentum matrix has to contain the momenta `k` projected on the mass-shells $(k_3 + k_6)^2 = M_Z^2$ and $(k_4 + k_5)^2 = M_Z^2$. Finally, if the on-shell projection fails, the switch `osh` has to be given back equal to zero, which tells the phase-space integration to discard the considered event, whereas in case `osh=1` the event is accepted.

Creating Histograms

To be able to calculate also distributions of the total cross-sections in the kinematical variables, the file `histo/histograms.F` contains the necessary subroutines and instructions. It contains a `subroutine settings`, which is called by the `subroutine integrate`. Assuming that one is to create the histogram number i for the kinematical quantity $x = x(\texttt{klab})$ calculated from the momentum matrix `klab` in the laboratory frame, the command

`call histogram(x(klab),`$\texttt{x}_{\min}$`,`$\texttt{x}_{\max}$`,'histo/x',nbins,i)`

will create a file `histo/x` containing the necessary information to plot a histogram for the variable x in the range $[\texttt{x}_{\min},\texttt{x}_{\max}]$ with `nbins` bins. Note that the program generates every `nsteps` events a new file `histo/x` containing the intermediate results for the considered

histogram, where `nsteps` is to be specified in `main.F`. Each line in this file then corresponds to one bin, where the first column contains the value for x in the middle of the considered bin. The remaining columns contain the contributions of the considered bin to the Monte Carlo averages of the various parts of the total hadronic cross-section, the corresponding contributions to the standard deviations as well as the number of events which was generated in the considered bin.

Auxiliary Functions

Among the remaining files in the directory *Dir*, the file `utils.F` contains auxiliary functions like scalar products or the Kronecker delta. Of the three header files in the directory *Dir*, `params.h` specifies process parameters as the maximal number of external particles, the number of partonic subprocesses, the maximal number of colour and helicity structures as well as the number of resonance structures contributing to the considered processes. It also contains the maximal dimensions for the variable arrays needed by the Monte-Carlo generator. The header file `allcommon.h` contains the definitions for all global variables and the common blocks, whereas `process.h` lists the information on the considered processes, like the names and charges of the external particles, average factors, spinor ranges, colour and helicity factors as well as the flavours of the initial-state partons.

Running the Program

Given the input specified as above, the commands

```
gmake
pole
```

will start the phase-space integration to calculate the total hadronic cross-section. To be able to check the specified input, the chosen model parameters, the values for the cuts, the chosen method for the treatment of the real corrections, the regulators and the technical cuts, as well as the output for the generator initialization are displayed before starting the phase-space integration. If including Bremsstrahlung contributions, the latter is generally performed by several phase-space generators, each corresponding to one of the considered final states. For each generator, the program will provide an output of the intermediate results for the various subcontributions if the number of generated events is a multiple of the parameter `nsteps` to be specified in `main.F`. Note that if considering hadronic reactions, there are two kinematically possible configurations for each phase-space point, one with the quark number one (two) taken from the hadron number one (two), and one with the quark number one (two) taken from the hadron number two (one). The intermediate results for the two configurations are separately displayed. After the phase-space integration has been finished for all generators, the output for the final results comprises the Monte Carlo average, the corresponding integration error as well as the maximal weight for each subcontribution to the total hadronic cross-section. Furthermore, the results for

the partonic subprocesses as well as the percentage of events rejected by each of the specified cuts is written out. Finally, the Monte Carlo average and the corresponding standard deviation summed over the bins for each generated histograms is given back. This sum can be compared to the final results for the total cross-section to estimate the size of the contribution lying outside the specified boundaries of a given histogram. All of the above results are given in units of femtobarn (fb).

4.4 The Monte Carlo Phase-Space Integration

In this chapter we discuss the details of the phase-space integration as implemented in the `Fortran` part of `Pole`. As we said before, the program is designed to handle processes involving the decay of unstable intermediate particles, which lead to resonance peaks in the squared amplitude of the considered process. As a consequence, the integration of the latter over phase-space is difficult to keep numerically stable, since the kinematical region of such a peak, and thus the kinematical region where the amplitude contributes most, is generally quite small. In the framework of a Monte-Carlo integration, one therefore needs a quite high number of events until enough phase-space points have been generated in the peak regions to obtain sufficiently precise results.

To solve this problem, we interfaced the amplitudes as generated by `Pole` to the generic Monte-Carlo generator `Lusifer`, which uses the *multi-channel importance sampling* approach as a solution to the above-described problem. As discussed in Appendix E in more detail, the basic idea of the phase-space generation is here to decompose each diagram contributing to the amplitude of the considered process into $2 \to 2$ scattering subdiagrams and $1 \to 2$ decays. In that way, the complete phase-space factorizes into a product of phase-spaces for these subdiagrams. Each of the factors in this product can then be parameterized by the invariant appearing in the respective t-channel and s-channel propagators and the corresponding reaction angles, such that the phase-space integration is replaced by an integration over invariants and angles.

To generate random numbers for the latter in the framework of a Monte-Carlo phase-space integration, these invariants have furthermore to be mapped on random numbers $r \in [0, 1]$. However, the actual form of this mapping is completely arbitrary. The idea of the *importance sampling* technique is now to substitute the invariants by random numbers in such a way that the corresponding Jacobian essentially reproduces the peaking structure of the integrand. The resulting integration can in that way be done with an essentially flat integrand and is as such very stable. To put it in another way, the mapping is by this substitution chosen such that the bulk of events is generated in the phase-space region where the squared amplitude is large, hence the name importance sampling.

However, the amplitude for a given process generally involves many different combinations of s-type and t-type subprocesses, which lead each to a different phase-space parameteriza-

tion. The idea of the *multichannel* approach is therefore to write the phase-space integral as a sum over all possible parameterizations or *channels*. In that way, the integrand is flattened over the whole phase-space, which considerably speeds up the convergence of the phase-space integration.

In the framework of `Pole` the main function governing the phase-space integration is given by the `subroutine integrate(out,average,sigma)`, which is contained in the file `int/integration.F`. This subroutine is invoked by the main program in `main.F`, with the input given by the variable `out` which denotes the stream to which the output is written. The output arrays `average` and `sigma` contain the final results for the Monte-Carlo estimate and the corresponding standard deviation. A schematic overview over the steps performed by this subroutine is shown in Figure 4.1, which provides the guideline for the discussion in the remainder of this section.

Initialization

As can be seen from Figure 4.1, before starting the actual phase-space integration, the `subroutine integrate` initializes the input specified as discussed in Section 4.3. In a second step, the phase-space integration is initialized, the constant abbreviations are calculated and the initialization output is written to the stream `out` in the argument of the `subroutine integrate`.

To determine the various scattering and decay subprocesses used to parameterize the phase-space, the `subroutine integrate` calls the initialization routine `initphasespace` contained in the file `int/lusifer.F`. The latter takes as an input the process as well as the properties and couplings of the particles appearing in the considered model. The phase-space initialization is then done by connecting the final state and the initial state of the considered process in all possible ways. The invariants, masses and widths of the propagators needed for this connection are stored and passed later to the phase-space generators, where this information is used to construct momenta for the final-state particles.

Note that the original version of `Lusifer` contains the necessary information on the particles and couplings for the Standard Model only. To make the phase-space generator applicable to calculations in other models as well, we modified the generator in the sense that all model information was deleted from the original source code. In the new version, the model information is now contained in the file `int/model_lusifer.F`, which is automatically generated by the `Fortran` output routine `PoleToFortran`. The latter basically extracts the particle properties and their couplings from the corresponding `FeynArts` model file, and translates this information into `Fortran` code compatible with the phase-space initialization as done by `Lusifer`. Apart from the particle content of a given model, a set of auxiliary particles is introduced, which is used for evaluating all four-vertices as a product of two three-vertices. Furthermore, it may some of the propagators within a given channel involve interdependent invariants which cannot be mapped simultaneously

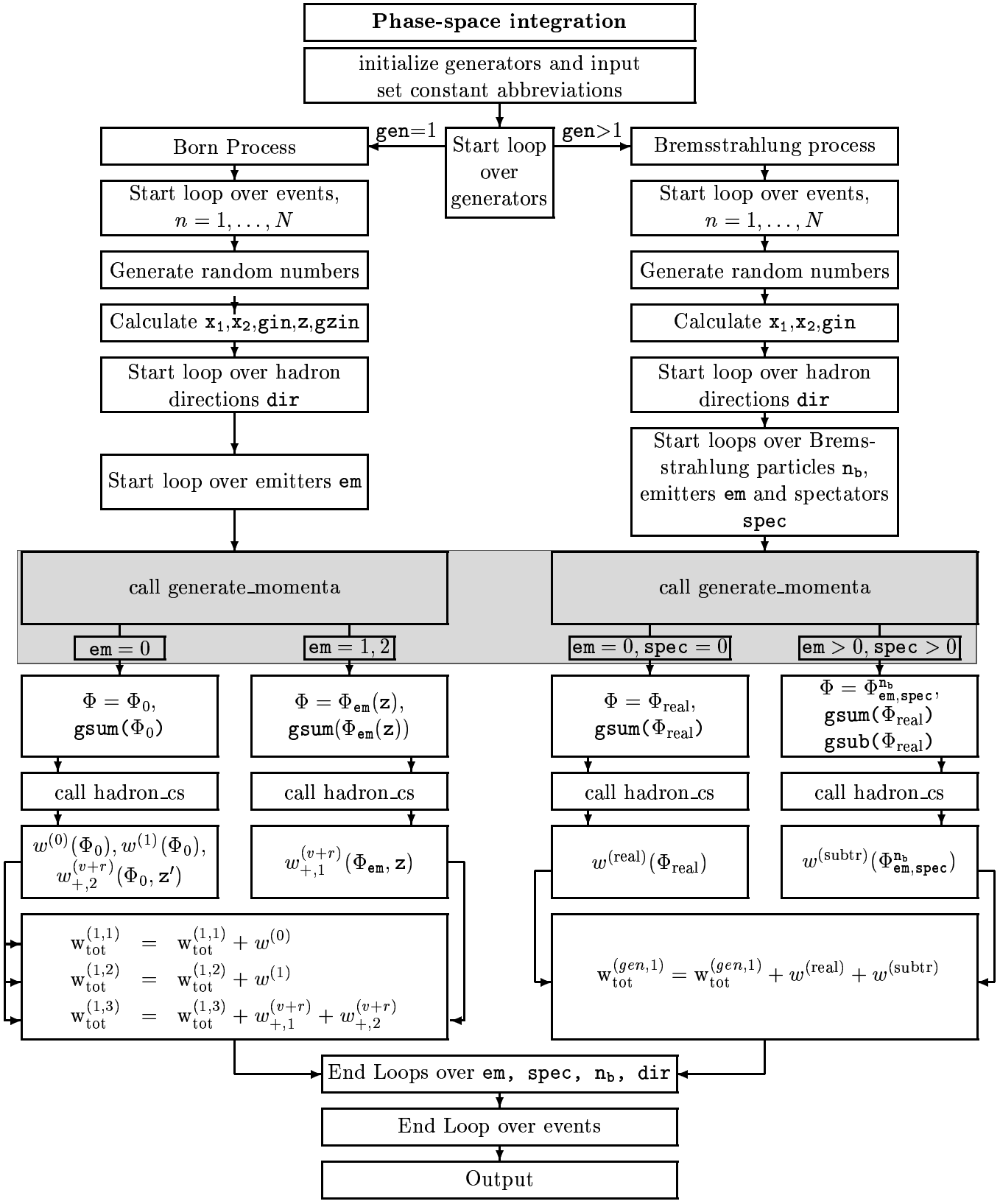

Figure 4.1: Schematic overview of the Monte-Carlo phase-space integration.

to flatten the corresponding propagator peaks. To avoid the resulting numerical instabilities, `PoleToFortran` introduces for every particle with a finite mass a massless auxiliary particle with the same couplings and a flat mapping. In this way, the problematic channel is replaced by a set of channels involving all possible mapping combinations, from a flat mapping for none of the propagators to a flat mapping for all propagators.

Note that if masses were set to zero by the `SmallMasses` option of `CalcFeynAmp` during the amplitude generation, the corresponding masses are set to zero in `int/model_lusifer.F` as well. In the same way, the generator uses a finite width only for those particles, for which a finite width has been introduced by the `IntroduceWidth` option of `CalcFeynAmp`. By the extension described above, we were able to transfer the model-independence of `FeynArts` to the phase-space integration using `Lusifer`, such that the latter can now be used for calculations in e.g. the MSSM as well.

Classification of Phase-Spaces

As shown in Figure 4.1, the `subroutine integrate` invokes after the initialization procedure a series of parameter loops. The reason for this is that in considering real corrections, several phase-spaces involving different numbers of final-state particles contribute to the cross-section. Accordingly, the phase-space integration has to be done for each such final state separately. Furthermore, for a hadronic process one cannot tell from which of the colliding hadrons the initial-state partons have been taken. For a given event, the hadronic cross-section has therefore to be evaluated as a sum over two configurations, one with parton number one (two) taken from hadron number one (two), and one with parton number one (two) taken from hadron number two (one). Finally, to be able to consistently take into account real corrections, one has to employ a method to deal with the resulting soft and collinear singularities. Whereas `Lusifer` is designed as a pure tree-level Monte-Carlo generator, we extended the latter by two such methods, the phase-space slicing technique and the subtraction method, which are both discussed in Appendix D. As can be seen from (D.57) and (D.59), the resulting expressions for the sum of the singular virtual and singular real corrections generally involve not only the phase-spaces Φ_0 and Φ_{real} of the Born and Bremsstrahlung processes, but also the phase-spaces $\Phi_i(z)$ where Bremsstrahlung emission has reduced the momentum of emitter number i by a factor of z. Moreover, if using the subtraction method, the phase-spaces $\tilde{\Phi}_{ij}^{\mathtt{n_b}}$ in the subtraction functions (D.23) depend on the emitter index i, the spectator index j as well as on the number n_b of the Bremsstrahlung particle. The latter index is important when considering Bremsstrahlung processes where the Bremsstrahlung particle appears more than once in the final state, as for example for the Bremsstrahlung process $PP \to l\bar{l}\gamma\gamma$. In this case one has to introduce a separate subtraction terms for each Bremsstrahlung particle, which involve each a different embedding of the Bremsstrahlung phase-space into the phase-space of the Born process.

In short, the phase-spaces contributing to the hadronic cross-section can be uniquely classified by five indices, one index for the considered generator, one index specifying from

which of the colliding hadrons the initial-state partons were taken, and three indices `em`, `spec` and $\mathtt{n_b}$ to specify the emitter, the spectator and the number of the Bremsstrahlung particle. As shown in Figure 4.1, the `subroutine integrate` therefore invokes in a first step a loop over an index labeling the phase-space generators. To give an example, if one is to calculate the cross-section of a given process including a QED-Bremsstrahlung process with an extra photon in the final state as well as a QCD-Bremsstrahlung process with an extra gluon, the Born process is labeled by `gen=1`, whereas the phase-spaces for the Bremsstrahlung processes are generated for $\mathtt{gen} = 2$ and $\mathtt{gen} = 3$. Information on the numbering of the generators can be found in the file `process.h`. For each generator, the numerical integration is then started by a loop over the events, which is finished if the total number of events specified in `main.F` has been generated, or if the precision goal, to be specified in the same file, for a given subcontribution is reached.

In a next step, the routine creates for each event a set of quasi random-numbers by means of the so-called Rcarry-algorithm. Three of these random numbers are passed to the subroutines `map_initial_state` and `mapz` contained in the file `int/lusifer.F`, which calculate the values for the partonic energy fractions $\mathtt{x_1}, \mathtt{x_2}$, the energy fraction `z` as well as the corresponding Jacobians `gin` and `gzin`. The actual form of the mappings used here are discussed in the beginning of Appendix E. Note that two values `z` and $\mathtt{z}'$ are generated for z, which are to be used later to parameterize the two parts of the (+)-distributions in (D.57) and (D.59). As we said before, the phase-space integral is in the multi-channel approach written as a sum over channels. As shown in Appendix E, this sum can be replaced by the integral (E.37) such that each channel is attributed to a subinterval of $[0, 1]$. The size of each subinterval then represents the probability that the corresponding channel is used to parameterize the phase-space. The integration can in this way by optimized by adapting the size of a given subinterval according to how much the corresponding channel contributes to the total cross-section. In practice, the `subroutine integrate` therefore generates a further random number, checks in which of the subintervals this random number is contained and uses the corresponding channel to parameterize the phase-space. To be able to calculate the invariants parameterizing the chosen channel, the `subroutine integrate` finally generates $3n_f - 4$ more random numbers, where n_f denotes the number of final-state particles of the considered subprocess.

As shown in Figure 4.1, the `subroutine integrate` invokes in case of a hadronic reaction a further loop over the index $\mathtt{dir} = 1, 2$, which specifies from which of the colliding hadrons the initial-state partons have been taken. Using the values for energy fractions x_1 and x_2 generated before, the partonic initial-state momenta for $\mathtt{dir} = 1$ are then fixed to read

$$\mathtt{dir} = 1: \qquad p_1^{\text{in}} = x_1(\sqrt{S}/2, 0, 0, \sqrt{S}/2), \qquad p_2^{\text{in}} = x_2(\sqrt{S}/2, 0, 0, -\sqrt{S}/2), \quad (4.15)$$

where S is the square of the hadronic centre-of-mass energy specified in `main.F`. The case $\mathtt{dir} = 2$ essentially differs from the above case only by an interchange of the colliding

hadrons, such that

$$\texttt{dir} = 2: \qquad p_1^{\rm in} = x_2(\sqrt{S}/2, 0, 0, -\sqrt{S}/2), \qquad p_2^{\rm in} = x_1(\sqrt{S}/2, 0, 0, \sqrt{S}/2), \quad (4.16)$$

Note that the energy fractions x_1 and x_2 have for $\texttt{dir} = 2$ also to be switched in the product (4.5) of Parton Distribution Functions. Finally, the `subroutine integrate` starts three loops over the emitters, spectators and the possible Bremsstrahlung particles. The set of the five indices discussed above, the random numbers for the invariants, the values for x_1, x_2 and z, the number of the considered channel, as well as the above initial-state momenta are then used to generate the corresponding phase-space.

Phase-space generation

For the sake of overview, we display the various steps related to the phase-space generation separately in Figure 4.2. In the framework of `Pole` the phase-space generation is governed by the

```
subroutine generate_momenta(klab,kcms,g,gsum,nocut,nrejected,techrej,
                            random,kbeam,z,channel,gen,nb,em,spec)
```

contained in the file `int/integration.F`. The input is here provided by the variables in the second line. To start with, `random` is the above array of $3n_f - 4$ random numbers to be used to construct the phase-space for the chosen channel number `channel`. The initial-state momenta (4.15) or (4.16) are contained in the matrix $\texttt{kbeam} = \{p_1^{\rm in}, p_2^{\rm in}\}$, `z` denotes the energy fraction of the Bremsstrahlung particle and `gen`, `nbrems`, `em` and `spec` are again the indices classifying the phase-space. The output variables in the first line are given by momentum matrices `klab` of the considered phase-space in the laboratory frame, the corresponding momenta `kcms` obtained by a boost to the centre-of-mass frame as well as the Jacobian `g` and the phase-space density `gsum` to be discussed below. Furthermore, the switch `nocut` is used to store the information if a given event has been accepted or rejected by the cut routines. Finally, the variable `techrej` as well as the array `nrejected` contains the information which of the various cuts has rejected the event.

As is shown in Figure 4.2, the `subroutine generate_momenta` invokes in a first step the `subroutine phasespace` contained in the file `int/lusifer.F`. The latter takes as input the random number array, the initial-state momenta as well as the considered channel, calculates the corresponding invariants, and uses these invariants to construct the final-state momenta for the considered process. If considering real corrections, altogether three types of phase-spaces are generated. For the Born process labeled by $\texttt{gen} = 1$, the `subroutine phasespace` is for $\texttt{em} = 0$ invoked with the input $p_1 = p_1^{\rm in},\ p_2 = p_2^{\rm in}$ for the initial-state momenta, whereas for $\texttt{em} = 1$ and $\texttt{em} = 2$, the initial-state momenta are set to $p_1 = \texttt{z}p_1^{\rm in},\ p_2 = p_2^{\rm in}$ and $p_1 = p_1^{\rm in},\ p_2 = \texttt{z}p_2^{\rm in}$, respectively. In the first case, one obtains in this way the phase-space of the Born process Φ_0, whereas in the latter two cases the constructed final-state momenta correspond to the phase-spaces $\Phi_{\texttt{em}}(\texttt{z}), \texttt{em} = 1, 2$ in (D.57)

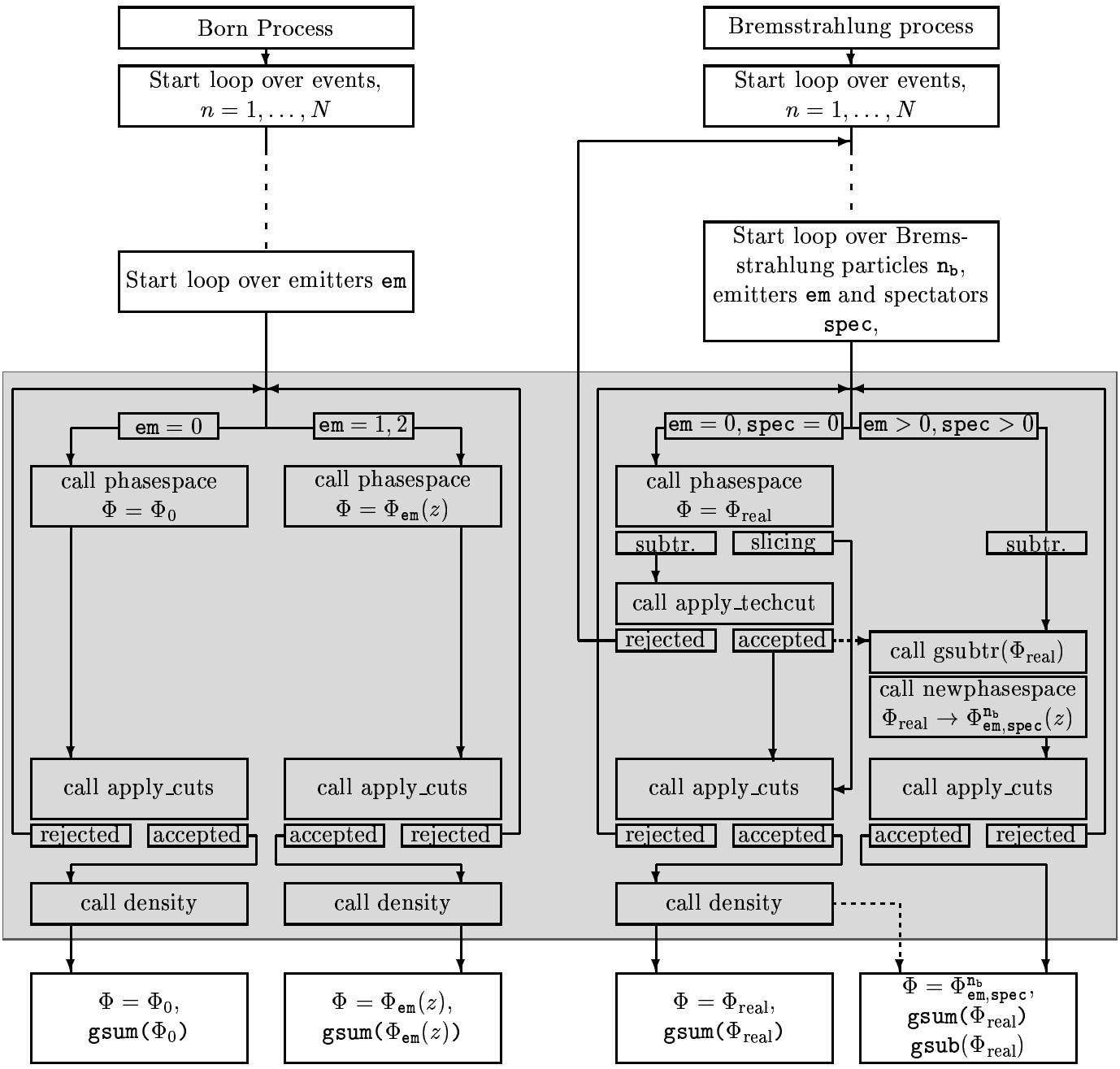

Figure 4.2: Schematic overview of the phase-space generation

and (D.59). For the Bremsstrahlung processes labeled by `gen` > 1, on the other hand, the `subroutine phasespace` calls the phase-space generator number `gen` with initial-state momenta $p_1 = p_1^{\rm in},\ p_2 = p_2^{\rm in}$, which gives then back the phase-space $\Phi_{\rm real}$ for the Bremsstrahlung process number `gen`.

Applying Cuts

In a next step, the `subroutine generate_momenta` checks if the so-obtained final-state momenta are compatible with the various cut conditions. For the Born process `gen=1`, these conditions arise only from the phase-space cuts specified in `int/input_cuts.F` and are applied to the phase-spaces Φ_0 and $\Phi_{\tt em}, {\tt em} = 1, 2$ by invoking the `subroutine apply_cuts` contained in the file `int/cuts.F`. If an event for a given emitter index is rejected, the corresponding Monte-Carlo weight is set to zero, and the phase-space for the next emitter is calculated.

For the Bremsstrahlung processes labeled by `gen` > 1, the cuts applied to a given event depend on the chosen method for the treatment of soft and collinear singularities. If choosing the phase-space slicing technique, the event is directly passed to the `subroutine apply_cuts` as in the Born case. However, the latter routine now performs altogether three operations. Firstly, it is checked if the event is compatible with the slicing cuts δ_s and δ_c specified in `main.F`. Note that the slicing cuts have to be applied to the momenta in the centre-of-mass frame, as opposed to the phase-space cuts which are imposed on the momenta in the laboratory frame. The reason for this is that the analytical integration over the Bremsstrahlung momentum leading to the expressions (D.57) and (D.59) is done under the assumption of a centre-of-mass kinematics. If the slicing cut conditions are not fulfilled, the Monte-Carlo weight for the considered event is set to zero and new random numbers for the next event are generated. If the event is accepted, the momenta are passed in a second step to the `subroutine recombine` contained in `int/cuts.F`, which applies the recombination procedure for the Bremsstrahlung momentum as described in Section 4.3. If the parameter `inclusive` in the file `main.F` is set to zero, all events for which the corresponding momenta pass the recombination procedure unaltered are discarded. Finally, the routine checks if the resulting momenta fulfill the conditions arising from the phase-space cuts. However, in the fully inclusive case, i.e. if the parameter `inclusive` in the file `main.F` is set to one, the phase-space cuts are not to be applied to the Bremsstrahlung particle. This leads to a complication if the final state contains the latter more than once, since in this case it is not clear which of the momenta are subject to the cut conditions and which of the momenta have to be integrated out. As a consequence, the `subroutine apply_cuts` stores internally the information which of the final-state momenta are rejected, and does not discard a given event until at least two final-state momenta corresponding to a potential Bremsstrahlung particle do not fulfill the phase-space cut conditions.

For the subtraction method, the procedure is somewhat more complicated. Here the event is first checked for compatibility with the technical cut `tcut` specified in `main.F`.

If the condition (4.2) is not fulfilled, the entire event is rejected in the sense that both, the weight for the Bremsstrahlung cross-section and the weights for the subtraction term are set to zero, and the routine jumps back to the generation of new random numbers. If the event is accepted, the momenta in Φ_{real} are stored, and read out again if the subroutine `generate_momenta` is called for the same event with input $\texttt{em} > 0$ and $\texttt{spec} > 0$. As shown in Figure 4.2 the stored momenta are for this input passed to the `subroutine gsubtr` in the file `int/hadroncs.F`. The latter calculates the function `gsub` in (D.34) for the considered emitter and spectator index, which is to be used later for the subtraction of the soft and collinear singularities. Furthermore, the stored momenta Φ_{real} are passed to the `subroutine newphasespace` contained in the file `int/lusifer.F`, which uses the prescriptions (D.28), (D.30) and (D.31) to project the Bremsstrahlung phase-space onto the phase-space $\Phi^{\texttt{nb}}_{\texttt{em,spec}}$. If using the subtraction method, one therefore ends up with the phase-space Φ_{real} of the Bremsstrahlung process, and the phase-spaces $\Phi^{\texttt{n}_\texttt{b}}_{\texttt{em,spec}}$ for the subtraction terms. The corresponding momenta are then passed to the `subroutine apply_cuts`, which here applies the recombination procedure to Φ_{real} and imposes the phase-space cuts on Φ_{real} and $\Phi^{\texttt{nb}}_{\texttt{em,spec}}$ as discussed above. Note that if the phase-space cuts reject a given event, the loop over emitters and spectators is continued, such that one can encounter the situation where the weight for the subtraction term is nonzero, but the weight for the Bremsstrahlung cross-section vanishes, and vice versa.

Calculation of the Phase-Space Densities

As is shown in Figure 4.2, if one of the phase-spaces Φ_0, $\Phi_{\texttt{em}}, \texttt{em} = 1, 2$ and Φ_{real} pass the cut routines, the corresponding momenta are used as an input for the `subroutine density` contained in `int/lusifer.F`. The latter calculates the value of the inverse Jacobian `g` for the considered channel, which originates from the mapping of the corresponding invariants on random numbers. The phase-space density `gsum` is then given by the sum of these Jacobians over all channels. In the context of the multi-channel importance sampling technique described in Section E, the value for `g` is used for the adaptive optimization if the number `nadapt` of optimization steps in `main.F` is chosen different from zero. The density `gsum` mimics the peaking structure of the squared amplitude and is thus used to stabilize the numerical integration over the resonance peaks. Note that no phase-space density is calculated for the momenta in $\Phi^{\texttt{nb}}_{\texttt{em,spec}}$. This is because dividing the squared amplitude for the Bremsstrahlung process by $\texttt{gsum}(\Phi_{\text{real}})$ and the squared amplitudes for the subtraction terms by $\texttt{gsum}(\Phi^{\texttt{nb}}_{\texttt{em,spec}})$ might lead to a mismatch of the so-calculated weights in the soft and collinear limits due to numerical instabilities in the evaluation of `gsum`.

Calculation of the Monte-Carlo Weights

Turning now back to Figure 4.1, the momenta, phase-space densities and subtraction terms given back by the `subroutine generate_momenta` are now used to calculate the Monte-Carlo weights for the various contributions to the hadronic cross-section. This is done in the subroutines contained in the file `int/hadroncs.F`.

The main function is here given by the

```
subroutine hadron_cs(weight,klab,kcms,x1,x2,z,gsum,gin,gzin,
                                              gen,nb,em,spec),
```

which is called by the `subroutine integrate` after the generation of the phase-spaces. The input consists of the momentum matrices `klab` and `kcms` in the laboratory frame and the centre-of-mass frame, the partonic energy fractions `x1` and `x2`, the energy fraction `z` of the Bremsstrahlung particle and the densities `gsum`, `gin` and `gzin`. The phase-space density `gsum` is again given by the inverse Jacobian arising from the mapping of the process invariants on random numbers, whereas the densities `gin` and `gzin` are given by the corresponding quantities originating from the mapping of the energy fractions $\mathtt{x}_1$, $\mathtt{x}_2$ and `z`. The last four arguments of `subroutine hadron_cs` are again the phase-space labels. As a general outline, the `subroutine hadron_cs` invokes in a first step the input specified in `input_pdfs` to calculate the typical energy scale Q for the considered process from the momentum `klab` in the laboratory frame. The scale Q as well as the partonic energy fractions $\mathtt{x}_1$ and $\mathtt{x}_2$ are then used to determine the products (4.5) of the Parton Distribution Functions. In a next step, the squared amplitudes for the various subcontributions to the hadronic cross-section are calculated and divided by the respective phase-space densities `gsum`, `gin` and `gzin`. The resulting expressions are multiplied by the products (4.5) as well as by the symmetry and phase-space factors and are finally returned in the array `weight` to be discussed below. Which part of the hadronic Monte-Carlo weight is actually contained in this array depends on the input phase-space labeled by the input variables `gen`,$\mathtt{n_b}$,`em` and `spec`, as to be discussed in the following.

To start with, for generator index `gen` $= 1$ and emitter index `em` $= 0$, the input momenta correspond to the phase-space Φ_0 of the Born process. As indicated in Figure 4.1, the `subroutine hadron_cs` calculates in this case altogether three different types of weights, the weight for the Born-cross-section, the weight for the finite virtual corrections and the Φ_0-dependent parts of the weight for the sum of singular virtual and singular real corrections. To be explicit, these weights read

$$w^{(0)}(\Phi_0) = \rho(\Phi_0)\frac{\left|\mathcal{A}^{(0)}_{q_1 q_2}(\Phi_0)\right|^2}{g_{\rm tot}(\Phi_0)} w_{\rm in}(x_1, x_2), \tag{4.17}$$

for the Born cross-section,

$$w^{(1)}(\Phi_0) = \rho(\Phi_0)\frac{\left|\mathcal{A}^{(1)}_{q_1 q_2}(\Phi_0)\right|^2}{g_{\rm tot}(\Phi_0)} w_{\rm in}(x_1, x_2). \tag{4.18}$$

for the virtual corrections, as well as

$$w^{(v+r)}_{+,2}(\Phi_0, z') = \rho(\Phi_0)\frac{\left|\mathcal{A}^{({\rm v+r}),+,2}_{q_1 q_2}(\Phi_0, z')\right|^2}{g_{\rm tot}(\Phi_0)} w_{\rm in}(x_1, x_2). \tag{4.19}$$

for the Φ_0-dependent parts of the sum of singular virtual and singular real corrections. The calculation of the squared amplitudes is discussed below, and the quantity ρ is given by the phase-space factor

$$\rho(\Phi) = \frac{1}{2\hat{s}}(2\pi)^{(-3n_f-4)}\frac{1}{n_{\rm av}}\frac{1}{n_{\rm sym}}, \tag{4.20}$$

where n_f is the number of final-state particles of the considered process and $\hat{s}$ denotes the partonic centre-of-mass energy. The denominators $n_{\rm av}$ and $n_{\rm sym}$ are given by the average factors for the colour and helicity summations as well as by the factor accounting for the symmetry of the squared matrix elements under the exchange of identical final-state particles. Note that if the parameter `wgt` in `main.F` has a value different from one, (4.20) is multiplied with this factor, which can be used to calculate the cross-section summed over kinematically equivalent final-state flavour combinations. If considering a hadronic reaction, the function $w_{\rm in}$ is given by the product (4.5) divided by the input Jacobian `gin` for the mapping of the partonic energy fractions

$$w_{\rm in} = \frac{1}{g_{\rm in}}\overline{\Phi}_{P_1|q_1}(\texttt{x1},\texttt{Q})\overline{\Phi}_{P_2|q_2}(\texttt{x2},\texttt{Q}). \tag{4.21}$$

If one is to convolute the partonic cross-section with a expression different from (4.5), the corresponding input can be set in the file `input_pdfs.F` and is automatically passed to the `subroutine hadron_cs` to calculate $w_{\rm in}$. For a hadronic process the weights (4.17), (4.18) and (4.19) are generally given by an array containing the weights for each partonic subprocess.

To calculate the squared matrix elements in the expressions for the above weights, the `subroutine hadron_cs` invokes in a first step the `subroutine Msquared` to be discussed in Section 4.5 to calculate the square of the full Born amplitude amplitude $\mathcal{A}^{(0)}$. In a second step, the same subroutine is invoked to calculate the square of the amplitude $\mathcal{A}^{(0),\rm LPA}_{q_1q_2}$ for the Born process in Leading Pole Approximation, as well as the square of the corresponding amplitude $\mathcal{A}^{\rm virt,LPA}_{q_1q_2}$ for the virtual corrections. Both are then passed to the `subroutine Msquvirtfinite`, which uses this input to determine the squared matrix element for the finite virtual corrections by subtracting

$$\left|\mathcal{A}^{(1)}_{q_1q_2}(\Phi_0)\right|^2 = \left|\mathcal{A}^{\rm virt,LPA}_{q_1q_2}(\Phi_0)\right|^2 - \left|\mathcal{A}^{\rm virt,LPA}_{q_1q_2,\rm sing}(\Phi_0)\right|^2 - n_{\Delta r}\left|\mathcal{A}^{(0),\rm LPA}_{q_1q_2}(\Phi_0)\right|^2\Delta r^{(1)}. \tag{4.22}$$

The second term is here given by the singular virtual corrections (D.52) and is subtracted to cancel the soft and collinear singularities. The subtraction of the third term corrects for the evolution of the electromagnetic coupling to the W mass as discussed in Section 4.3. Here, the quantity $\Delta r^{(1)}$ is given by (4.4), whereas $n_{\Delta r}$ corresponds to the input parameter `ndZR1` to be specified in `main.F`. Note that this parameter is automatically set to zero if the α_0 scheme is chosen to parameterize the electromagnetic coupling constant.

Finally, the squared matrix element in (4.19) for the sum of singular real and singular virtual corrections can be divided in three parts. The first two parts arising from initial-state Bremsstrahlung emission are calculated by the `subroutine Msquvrinitial` in the file `int/hadroncs.F`, whereas the final-state contributions are determined by means of the `subroutine Msquvrfinal` in the same file. By adding these contributions, the `subroutine hadron_cs` obtains for the case of using the phase-space slicing technique the squared matrix element

$$\left|\mathcal{A}^{(\mathrm{v+r}),+2}_{q_1q_2}(\Phi_0,z')\right|^2 = \left|\mathcal{A}^{(\mathrm{v+r}),\mathrm{init.}}_{q_1q_2,\mathrm{finite}}(\Phi_0)\right|^2 + \frac{\left|\mathcal{A}^{(\mathrm{v+r}),\mathrm{init},+,2}_{q_1q_2,\mathrm{finite}}(\Phi_0,z')\right|^2}{g_{z'}(z')} + \left|\mathcal{A}^{(\mathrm{v+r}),\mathrm{final}}_{q_1q_2,\mathrm{finite}}(\Phi_0)\right|^2, \quad (4.23)$$

where the first and the third term are given by initial-state contribution (D.54) and the final-state contribution (D.55), respectively. The amplitude $\mathcal{A}^{(\mathrm{v+r}),\mathrm{init.},+,2}_{q_1q_2,\mathrm{finite}}$ arises from the second part of the (+)-distribution in (D.58), which also depends on the phase-space $\Phi_0 = \Phi_i(1)$. If using the subtraction method, the squared amplitude in (4.19) contains the terms arising from the second part of the (+)-distribution in (D.60) and (D.61), such that

$$\left|\mathcal{A}^{(\mathrm{v+r}),+2}_{q_1q_2}(\Phi_0,z')\right|^2 = \frac{\left|\mathcal{A}^{(\mathrm{v+r}),\mathrm{init},+,2}_{q_1q_2,\mathrm{finite}}(\Phi_0,z')\right|^2}{g_{z'}(z')} + \frac{\left|\mathcal{A}^{(\mathrm{v+r}),\mathrm{final},+,2}_{q_1q_2,\mathrm{finite}}(\Phi_0,z')\right|^2}{g_{z'}(z')}. \quad (4.24)$$

Note that the amplitude exhibits for both cases a peak of the form $1/(1-z)$ in the limit $z \to 1$, and is thus evaluated using the mapping $z'(r)$ in equation (E.14) of Appendix E. As is shown in Figure 4.1, if called with `gen` $= 1$ and `em` $= i = 1,2$ the `subroutine hadron_cs` calculates next the weights for the contributions depending on the phase-space $\Phi_i(z)$. The latter take again the general form

$$w^{(v+r)}_{+,1}(\Phi_i(z)) = \rho(\Phi_i(z))\frac{\left|\mathcal{A}^{(\mathrm{v+r}),+,1}_{q_1q_2}(\Phi_i(z))\right|^2}{g_{\mathrm{tot}}(\Phi_i(z))} w_{\mathrm{in}}(x_1,x_2), \quad (4.25)$$

where we adopted the same notation for ρ, g_{tot} and w as above. In case of using the phase-space slicing technique, the squared amplitude is here given by the first part of the (+)-distribution in (D.54)

$$\left|\mathcal{A}^{(\mathrm{v+r}),+1}_{q_1q_2}(\Phi_i(z))\right|^2 = \frac{\left|\mathcal{A}^{(\mathrm{v+r}),\mathrm{init},+,1}_{q_1q_2,\mathrm{finite}}(\Phi_i(z))\right|^2}{g_z(z)}, \quad (4.26)$$

whereas in case of using the subtraction method, the squared amplitude receives contributions from the corresponding quantities in (D.60) and (D.61)

$$\left|\mathcal{A}^{(\mathrm{v+r}),+1}_{q_1q_2}(\Phi_i(z))\right|^2 = \frac{\left|\mathcal{A}^{(\mathrm{v+r}),\mathrm{init},+,1}_{q_1q_2,\mathrm{finite}}(\Phi_i(z))\right|^2}{g_z(z)} + \frac{\left|\mathcal{A}^{(\mathrm{v+r}),\mathrm{final},+,1}_{q_1q_2,\mathrm{finite}}(\Phi_i(z))\right|^2}{g_z(z)}. \quad (4.27)$$

The squared amplitudes are here again calculated by the `subroutine Msquvrinitial`. They contain a singularity of the form $1/z/(1-z)$ in the limits $z \to 0$ and $z \to 1$, and are thus parameterized by the mapping z in equation (E.12) of Appendix E.

Finally, consider the case on the right-hand side of Figure 4.1, where the `subroutine hadron_cs` is called with an generator index `gen` > 1. For emitter index `em` $= 0$ and spectator index `spec` $= 0$ the `subroutine Msquared` is here invoked to return the square of matrix element $\mathcal{A}^{\text{real}}_{q_1 q_2}$ for the Bremsstrahlung process number `gen`. The corresponding weight is given by

$$w^{(\text{real})}(\Phi_{\text{real}}) = \rho(\Phi_{\text{real}}) \frac{\left|\mathcal{A}^{\text{real}}_{q_1 q_2}(\Phi_{\text{real}})\right|^2}{g_{\text{tot}}(\Phi_{\text{real}})} w_{\text{in}}(x_1, x_2). \tag{4.28}$$

For `em` > 0 and `spec` > 0, on the other hand, the `subroutine Msqusubtr` is invoked, which takes as an input the spectator index $i =$ `em`, the emitter index $j =$ `spec`, the number `nb` of the Bremsstrahlung particle as well as the corresponding phase-space $\Phi^{n_b}_{ij}$. The weight calculated by the `subroutine hadron_cs` then reads

$$w^{\text{subtr}}(\Phi^{n_b}_{ij}) = -\rho(\Phi_{\text{real}}) \frac{\left|\mathcal{A}^{\text{subtr}}_{q_1 q_2}(\Phi^{n_b}_{ij})\right|^2}{g_{\text{tot}}(\Phi_{\text{real}})} w_{\text{in}}(x_1, x_2). \tag{4.29}$$

with

$$\left|\mathcal{A}^{\text{subtr}}_{q_1 q_2}(\Phi^{n_b}_{ij})\right|^2 = g^{\text{sub}}_{ij}(p_i, p_j, k_{b_b}) \left|\mathcal{A}^{(\text{sub},ij)}_{q_1 q_2}(\tilde{\Phi}^{n_b}_{ij})\right|^2. \tag{4.30}$$

The functions g^{sub}_{ij} are given by the auxiliary functions in (D.34) which were already calculated during phase-space generation discussed in Section 4.4. The explicit form of the amplitude $\mathcal{A}^{(\text{sub},ij)}_{q_1 q_2}$, on the other hand, is proportional to the Born matrix element and given by equation (D.24).

Monte-Carlo Average and Output

As shown in Figure 4.1, the weights calculated for the various indices labeling the generators, hadron directions, emitters, spectators and Bremsstrahlung particles are finally added up to yield the total weight w_{tot}. The latter is given by an array, where $w_{\text{tot}}(1,1)$ and $w_{\text{tot}}(1,2)$ contain the hadronic weights for the Born cross-section and the finite virtual corrections summed over the two hadron directions and the partonic subprocesses. The entry $w_{\text{tot}}(1,3)$ collects the hadronic weights for the Φ_0- and Φ_i-dependent contributions to the singular parts of the virtual and real corrections. Note that the two parts of the (+)-prescriptions discussed above were calculated separately but with the same array of random numbers. In this way, one is able to make sure that the corresponding contributions still cancel in the limit $z \to 1$. Finally, $w_{\text{tot}}(\texttt{gen}, 1)$ contains the weight for the Bremsstrahlung process number `gen` plus, if using the subtraction method, the weights for the subtraction terms (4.29) summed over emitters and spectators.

Given the above weights $w_{\rm tot}$ for the events $i = 1, \ldots, N$, the `subroutine integrate` separately determines for each contribution the Monte-Carlo estimate

$$\overline{I}_N = \frac{1}{N} \sum_{i=1}^{n} w_i, \tag{4.31}$$

as well as the corresponding standard deviation

$$\delta \overline{I}_N = \sqrt{\frac{\frac{1}{N} \sum_{i=1}^{n} w_i^2 - \overline{I}_N^2}{N_{\rm nonz}}}. \tag{4.32}$$

Note that we divide the variance in the numerator of (4.32) not by the number N of generated events, but by the number $N_{\rm nonz}$ of events with non-zero weight, which is given by N minus the number of events rejected by the cut routines. In doing so, we compensate for the fact that in considering hadronic reactions at high energies, the cut routines often reject the bulk of the events, such that the estimate for the Monte-Carlo error calculated with $N_{\rm nonz} = N$ tends to underestimate the actual integration error.

The `subroutine integrate` finally stores the so-determined Monte-Carlo averages summed over partonic subprocesses, hadron directions, emitters, spectators and Bremsstrahlung particles in an array `average` where `average(1,1)`, `average(1,2)` and `average(1,3)` contain the results for the Born cross-section, the virtual corrections as well as for the sum of the singular parts in virtual and real corrections, whereas `average(gen,1)` contains the result for the real corrections of Bremsstrahlung process number `gen`. The array `average` and a corresponding array `sigma` for the standard deviations are then given back to the main program in `main.F`, where the results can be written to output files.

4.5 Numerical Evaluation of the Partonic Amplitudes

The last part of the `Fortran` output of `Pole` that remains to be discussed is the numerical evaluation of the squared partonic amplitudes. As was said above, the latter are used by the `subroutine hadron_cs` to calculate the hadronic weights for the total cross-section. To illustrate the idea, consider a general amplitude evaluated in Leading Pole Approximation (LPA). Following our discussion in Section 2.2, the LPA corresponds to neglecting the non-resonant contributions, such that the amplitude can generally be written as a sum over resonant contributions

$$\mathcal{A}(\Phi) = \sum_{\rm res=1}^{\rm nres} \mathcal{A}^{\rm res}(\Phi, \Phi_{\rm osh}^{\rm res}). \tag{4.33}$$

Besides the original phase-space Φ of the considered process, the resonant contributions depend additionally on the phase-space $\Phi_{\rm osh}^{\rm res}$. The latter results from a projection of the external momenta on the mass-shells of the decaying particles contributing to the resonance

set number `res`. The dependence of the resonant contributions on two different phase-spaces indicates that the resonant momenta have to be kept off-shell in the propagators of the decaying particles and in the loop integrals for the non-factorizable virtual corrections, whereas all other objects have to be evaluated using the on-shell projected momenta.

Following our discussion in Section 4.1, the amplitude as generated by the `Mathematica` part of `Pole` is prepared for numerical evaluation by means of the function `CalcAmplitudes`. The latter employs the Weyl-van der Waerden Formalism as presented in Appendix A to reduce the spinor structures of the considered amplitudes. As a result, the full amplitudes of the Born process and the real corrections, collectively denoted by $\mathcal{A}$ in what follows, as well as the resonant contributions in (4.33) depend on phase-space via Weyl-spinor products only and can be decomposed according to colour and helicity structures

$$\mathcal{A}(\Phi) = \sum_{\mathrm{col}=1}^{\mathrm{ncol}} C_{\mathrm{col}}^{c_1,\ldots,c_n} \sum_{\mathrm{hel}=1}^{\mathrm{nhel}} \Delta_{\sigma(\mathrm{hel})}^{\sigma_1,\ldots,\sigma_n} \mathcal{A}_{\mathrm{col,hel}}(\Phi), \tag{4.34}$$

$$\mathcal{A}^{\mathrm{res}}(\Phi, \Phi_{\mathrm{osh}}^{\mathrm{res}}) = \sum_{\mathrm{col}=1}^{\mathrm{ncol}} C_{\mathrm{col}}^{c_1,\ldots,c_n} \sum_{\mathrm{hel}=1}^{\mathrm{nhel}} \Delta_{\sigma(\mathrm{hel})}^{\sigma_1,\ldots,\sigma_n} \mathcal{A}_{\mathrm{col,hel}}^{\mathrm{res}}(\Phi, \Phi_{\mathrm{osh}}^{\mathrm{res}}). \tag{4.35}$$

As was said in Section 4.1, the factors C_{col} are generally given by a product of SU(3) generators depending on the colours $c_1, \ldots, c_n$ of the n external particles. The quantities $\Delta_{\sigma(\mathrm{hel})}$, on the other hand, are given by products of Kronecker deltas in the external helicities $\sigma_1, \ldots, \sigma_n$, where it is understood that the second sum in (4.34) and (4.35) only receives a nonzero contribution for the helicity combination $\sigma(\mathrm{hel}) = \{\sigma_1, \ldots, \sigma_{\mathrm{n}}\}$. The function `CalcFeynAmp` returns an array of lists containing the helicity amplitudes $\mathcal{A}_{\mathrm{col,hel}}^{\mathrm{nres}}$ as well as the helicity amplitudes $\mathcal{A}_{\mathrm{col,hel}}^{\mathrm{res}}$ for each resonance set `res` and each partonic subprocess. The abbreviations introduced to simplify the helicity amplitudes are returned in two separate lists containing the phase-space dependent abbreviations and the phase-space independent abbreviations, respectively.

As was said in Section 4.2, the output of `CalcAmplitudes` can be translated into `Fortran` code by means of the `Mathematica` function `PoleToFortran`. The input of the latter is given by lists containing one or more amplitudes along with the corresponding list of phase-space dependent abbreviations. `PoleToFortran` then creates separate files for each input element in the directory `Dir/amps`. The file for the abbreviations contains a subroutine, which takes as an input the number `res` of the considered resonance set. In case of the Born cross-section and the real corrections, the abbreviations for the full amplitudes are calculated for `res=0`, whereas for `res>0` a given abbreviation file determines numerical values for the abbreviations in the resonant contribution number `res` to the corresponding amplitude. The variable declarations for the abbreviations are by `PoleToFortran` collectively written to the header file `ampvars.h`, whereas the numerical values for the abbreviations are passed to the subroutines calculating the amplitudes via the common blocks contained in the file `ampcom.h`.

Similarly, the files for the amplitudes contain a subroutine which takes as an input the resonance number `res`, and returns for `res` > 0 an array `A(proc,col,hel)` of helicity amplitudes, where each element corresponds to the above resonant helicity amplitude $\mathcal{A}^{\text{res}}_{\text{col,hel}}$ for the partonic subprocess number `proc`, the colour structure number `col` and the helicity combination number `hel`. For `res` $= 0$ the subroutines for the Born process and the real corrections give back corresponding arrays for the full amplitudes. Information on the numbering of the resonances, partonic subprocesses as well as the colour and helicity structures can be found as a comment in the header of each amplitude file.

Among the generic files copied to the directory `Dir/amps`, the library `looptools_nfac.F` contains the implementation of the loop integrals for the non-factorizable corrections as discussed in Appendix C. The loop integrals for the factorizable corrections, on the other hand, are evaluated by linking the abbreviation subroutines to the FF-based library `LoopTools` [72, 73]. Finally, numerical values for the propagators and Weyl-spinor products are determined by the subroutines in `int/kinematics.F`, and the file `squaredME.F` contains the subroutines relevant for squaring the amplitudes.

We give an general overview of the numerical evaluation of the squared amplitudes in Figure 4.3. Note that the amplitude evaluation is connected to the phase-space integration via three subroutine calls only. By providing the global files in the main directory `Dir` as well as the three subroutines `init_amps`, `abbr_const` and `Msquared` to be discussed below, it is therefore possible to use the files in the directory `Dir/int` to integrate other amplitudes than those generated by `Pole`. In the same way, if one is to use a different phase-space integration than the one provided by `Pole`, only the above three subroutine calls have to be build into the new phase-space generator.

Amplitude Initialization

To start with, the first two of the above-mentioned three subroutines are called in the `subroutine init_int` contained in `int/integration.F`. They are responsible for the initialization of the numerical evaluation of the amplitudes, and are thus called before starting the phase-space integration. The `subroutine init_amps(out)` is part of the file `amps/squaredME.F` and sets the numerical values for the infrared and UV regulators as specified in `main.F`. Moreover, it initializes `LoopTools`, calls the subroutines used to set the parameter input specified in `input_sm.F` and writes the initialization output to the stream `out`. The second part of the amplitude initialization involves the calculation of the phase-space independent abbreviations by the `subroutine abbr_const()`. The latter is automatically generated by the `Mathematica` function `PoleToFortran`, and calculates the abbreviations for couplings, renormalization constants and phase-space independent loop integrals. Note that the evaluation of loop integrals using `LoopTools` can be costly in CPU time, such that calculating the phase-space independent loop integrals before starting the phase-space integration can considerably speed up the numerical evaluation of the total cross-section.

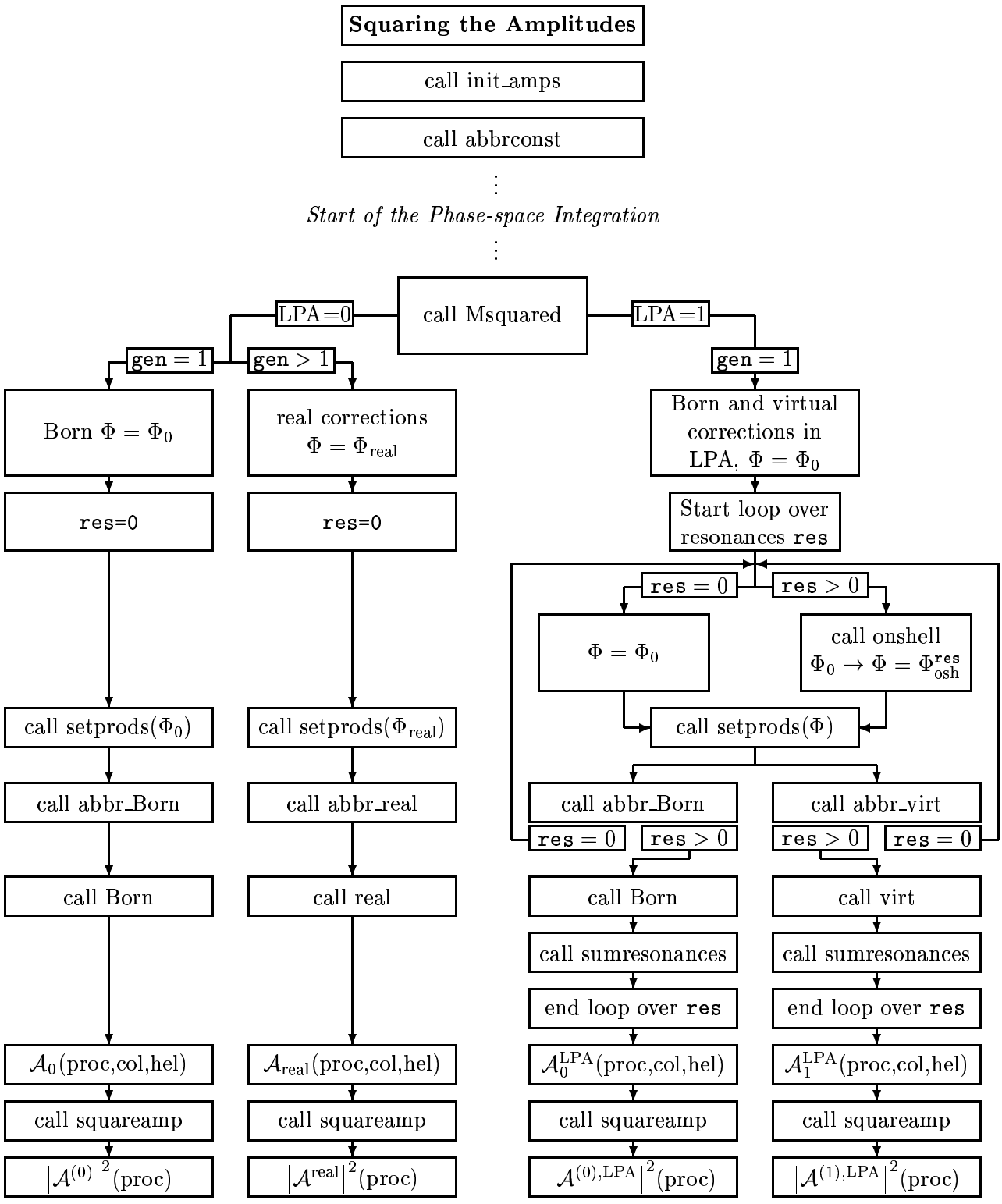

Figure 4.3: Schematic overview of the numerical evaluation of the squared amplitudes

Classification of the Amplitudes

As shown in Figure 4.3, after starting the Monte-Carlo integration, the generated phase-spaces are passed to the

```
subroutine Msquared(msqu0,msqu1,k,gen,LPA)
```

contained in `amps/squaredME.F`. Following our discussion in the last section, this routine is invoked by the function `hadron_cs`, which uses the squared amplitudes to calculate the hadronic weights. The input is provided by the momentum matrix `k` as well as the switches `gen` and `LPA` used to decide which amplitude is actually calculated. As discussed in the last section, altogether four amplitudes are contributing to the hadronic weights for the total cross-section. The Born amplitude and the amplitude for the Bremsstrahlung cross-sections are calculated for an input `LPA` $= 0$, whereas for `LPA` $= 1$ the amplitudes for the virtual corrections and Born amplitude evaluated in Leading Pole Approximation are returned. The output arrays `msqu0` and `msqu1` then contain the squares of these amplitudes for each partonic subprocess. If one is to use amplitudes other than those generated by `Pole`, one has to provide a `subroutine Msquared` with the same properties.

Calculating the Helicity Amplitudes

As can be seen for Figure 4.3, the `subroutine Msquared` is invoked with altogether three different input combinations. To start with, the first combination is given by `LPA` $= 0$, `gen` $= 1$, and the input momenta `k` corresponding to the phase-space Φ_0 for the Born process. As opposed to the case `LPA` > 0 to be discussed below, the phase-space is here left off-shell. The phase-space Φ_0 is passed to the `subroutine setprods`, which calculates the Weyl spinor products

$$\texttt{Prod}[\texttt{i},\texttt{j},\texttt{n},\texttt{m}] = \langle k_i^j k_n^m \rangle = k_{i,1}^j k_{n,2}^m - k_{i,2}^j k_{n,1}^m, \qquad \texttt{ProdC}[\texttt{i},\texttt{j},\texttt{n},\texttt{m}] = \langle k_i^j k_n^m \rangle^\star, \quad j,m = 1,2, \tag{4.36}$$

for each combination of the external momenta. For a given 4-momentum p_i, the two spinors k_i^1 and k_i^2 read

$$k_{i,A}^1 = \sqrt{\lambda_1} \begin{pmatrix} \mathrm{e}^{-\mathrm{i}\Phi_i} \cos\frac{\theta_i}{2} \\ \sin\frac{\theta_i}{2} \end{pmatrix}, \qquad k_{i,A}^2 = \sqrt{\lambda_2} \begin{pmatrix} \sin\frac{\theta_i}{2} \\ -\mathrm{e}^{\mathrm{i}\Phi_i} \cos\frac{\theta_i}{2} \end{pmatrix}, \tag{4.37}$$

$$\lambda_{1,2} = p_i^0 \pm |\mathbf{p_i}|, \qquad A = 1,2, \tag{4.38}$$

where the quantities θ_i and ϕ_i denote the polar and azimuthal angle of the external momenta p_i, $i = 1, \ldots n$. The so-determined spinor products are then transfered via a common block to the files responsible for the numerical evaluation of the abbreviations. In the next step, the `subroutine Msquared` invokes for resonance number `res` $= 0$ the subroutine calculating the abbreviations for the full Born amplitude, and subsequently the subroutine

containing the Born amplitude itself. The latter gives then back an array $\mathcal{A}_0(\text{proc}, \text{hel}, \text{col})$, where each element contains the contribution of the helicity combination number `hel` and the colour structure number `col` to the full Born amplitude of the partonic subprocess number `proc`. Note that the matrix elements are here determined from the off-shell phase-space Φ_0 only.

As can be seen from Figure 4.3, the second input combination for the `subroutine Msquared` is given by `LPA` $= 0$, `gen` > 1 and the input momenta `k` given by phase-space Φ_{real} of the Bremsstrahlung process number `gen`. The calculation of the helicity amplitudes is here done in exactly the same way as in the Born case. The amplitude subroutine for the real corrections is only called for `res` $= 0$, which results in the array $\mathcal{A}_{\text{real}}(\text{proc}, \text{hel}, \text{col})$ containing the helicity contributions to the full Bremsstrahlung amplitude.

Finally, the third input combination for the `subroutine Msquared` is given by the case `LPA` $= 1$ and `gen` $= 1$ illustrated on the right-hand side of Figure 4.3. The input matrix `k` contains here again the phase-space Φ_0 for the Born process. After starting the loop over the resonance structures, the phase-space Φ_0 is for `res` $= 0$ directly passed to the `subroutine setprods` to calculate the Weyl-spinor products, which are then used by the abbreviation subroutines for the Born amplitude and the corresponding routine for the virtual corrections to calculate off-shell values for the resonant momenta. These values are then stored, and the loop jumps directly to the case `res` > 1 without calculating any amplitudes. As shown in Figure 4.3, the phase-space is then passed to the `subroutine onshell`, which has to be specified in the file `input_onshell.F` before starting the phase-space integration. The latter projects the momenta in Φ_0 on the mass shells of the decaying particles of the resonance set number `res`, such that the subsequently calculated Weyl-spinor products and abbreviations are now determined from the on-shell projected phase-space $\Phi^{\text{res}}_{\text{osh}}$. The only exceptions are here the momenta in the resonant propagators and the resonant momenta in the non-factorizable loop integrals, which are set equal to the off-shell values stored before in the case `res` $= 0$. The `subroutine Msquared` then calls for each value `res` > 1 the amplitude subroutines, which return the helicity amplitudes $\mathcal{A}^{\text{res}}_{0,\text{hel,col}}$ of the Born process and the corresponding helicity amplitudes $\mathcal{A}^{\text{res}}_{1,\text{hel,col}}$ for the virtual corrections. Finally, the `subroutine sumresonances` sums again the amplitudes over resonance structures `res` > 1, and the resulting arrays

$$\mathcal{A}^{(0),\text{LPA}}(\text{proc}, \text{hel}, \text{col}) = \sum_{\text{res}=1}^{\text{nres}} \mathcal{A}^{(0),\text{res}}_{\text{hel,col}}(\Phi_0, \Phi^{\text{res}}_{\text{osh}}), \tag{4.39}$$

and

$$\mathcal{A}^{(1),\text{LPA}}(\text{proc}, \text{hel}, \text{col}) = \sum_{\text{res}=1}^{\text{nres}} \mathcal{A}^{(1),\text{res}}_{\text{hel,col}}(\Phi_0, \Phi^{\text{res}}_{\text{osh}}), \tag{4.40}$$

contain the helicity amplitudes for the Leading Pole contributions to the Born amplitude and to the virtual corrections for each partonic process. Note that instead of summing the amplitudes over resonances, the sum could also be done on the level of squared amplitudes.

The only difference of these two summation arises from the interference terms, which are however of higher order in Leading Pole Approximation.

Squaring the Amplitudes

After having calculated numerical values for the helicity amplitudes, the latter have to be squared and to be summed over the colours and helicities of the external particles. As indicated in Figure 4.3, this is done by the `subroutine squareamp`. To see how this works in detail, we re-express the full amplitude (4.33) by

$$\mathcal{A} = \sum_{\mathrm{col}=1}^{\mathrm{ncol}} C_{\mathrm{col}}^{c_1,\ldots,c_n} \sum_{\mathrm{hel}=1}^{\mathrm{nhel}} \Delta_{\mathrm{hel}}^{\sigma_1,\ldots,\sigma_n} \mathcal{A}_{\mathrm{col,hel}}, \tag{4.41}$$

where the quantities $\mathcal{A}_{\mathrm{col,hel}}$ are now the helicity amplitudes resulting from the above procedure, i.e. they are summed over all resonance structures if evaluated in Leading Pole Approximation. As was said in Section 4.1, by the virtue of the Weyl-van der Waerden formalism the helicity amplitudes can be numerically evaluated *before* squaring the full amplitude. However, it can be seen from (4.41) that the amplitude still contains the colour structures C_{col}, which are given by products of the generators of the $\mathrm{SU}(3)_{\mathrm{C}}$ gauge group. The amplitude is thus generally matrix-valued, and has to be reduced to a scalar expression for numerical evaluation. To see how this can be achieved, consider the square of (4.41) summed over all colour indices c_i and all helicities σ_i of the external particles

$$|\mathcal{A}|^2 = \sum_{\{c_i\}} \sum_{\mathrm{col}=1}^{\mathrm{ncol}} \sum_{\mathrm{col}'=1}^{\mathrm{ncol}} C_{\mathrm{col}}^{c_1,\ldots,c_n} C_{\mathrm{col}'}^{\dagger c_1,\ldots,c_n} \sum_{\{\sigma_i\}} \sum_{\mathrm{hel}=1}^{\mathrm{nhel}} \sum_{\mathrm{hel}'=1}^{\mathrm{nhel}} \Delta_{\mathrm{hel}}^{\sigma_1,\ldots,\sigma_n} \Delta_{\mathrm{hel}'}^{\sigma_1,\ldots,\sigma_n} \mathcal{A}_{\mathrm{col,hel}} \mathcal{A}^{\star}_{\mathrm{col}',\mathrm{hel}'}. \tag{4.42}$$

According to our definition of the helicity structures Δ_{hel}, the triple sum over the helicities of the external particles and the helicity combinations only yields a non-zero contributions for $\sigma(\mathtt{hel}) = \sigma(\mathtt{hel}') = \{\sigma_1, \ldots \sigma_n\}$, such that

$$|\mathcal{A}|^2 = \sum_{\{c_i\}} \sum_{\mathrm{col}=1}^{\mathrm{ncol}} \sum_{\mathrm{col}'=1}^{\mathrm{ncol}} C_{\mathrm{col}}^{c_1,\ldots,c_n} C_{\mathrm{col}'}^{\dagger c_1,\ldots,c_n} \sum_{\mathrm{hel}=1}^{\mathrm{nhel}} \mathcal{A}_{\mathrm{col,hel}} \mathcal{A}^{\star}_{\mathrm{col}',\mathrm{hel}}. \tag{4.43}$$

Considering next the colour structure, the product of SU(3) matrices

$$\mathcal{C}_{\mathrm{colcol}'} = \sum_{\{c_i\}} C_{\mathrm{col}}^{c_1,\ldots,c_n} C_{\mathrm{col}'}^{\dagger c_1,\ldots,c_n} \tag{4.44}$$

can be reduced to a scalar expression by repeatedly applying the Fierz identity

$$\sum_{c} \lambda_{ij}^{c} \lambda_{kl}^{c} = -\frac{2}{3} \delta_{ij} \delta_{kl} + 2 \delta_{il} \delta_{kj}. \tag{4.45}$$

The resulting matrix $\mathcal{C}$ is hermitian and can thus be diagonalized

$$\mathcal{C} = \mathcal{O}^\dagger \mathrm{diag}(\delta_1, \ldots, \delta_{\mathrm{ncol}})\mathcal{O} \tag{4.46}$$

with real eigenvalues $\delta_i, i = 1, \ldots, \mathrm{ncol}$. By inserting (4.46) in (4.43) one finally obtains the squared amplitude as a sum over all colour and helicity structures the full amplitude depends on

$$|\mathcal{A}|^2 = \sum_{\mathrm{hel}=1}^{\mathrm{nhel}} \sum_{\mathrm{col}=1}^{\mathrm{ncol}} \tilde{\mathcal{A}}^\dagger_{\mathrm{col,hel}} \tilde{\mathcal{A}}_{\mathrm{col,hel}}. \tag{4.47}$$

The advantage of the above procedure is, that each term in this sum is now given by the square of a *scalar*

$$\tilde{\mathcal{A}}_{\mathrm{col,hel}} = \sqrt{\delta_{\mathrm{col}}} \sum_{col'} \mathcal{O}_{\mathrm{col,col'}} \mathcal{A}_{\mathrm{col'},\mathrm{hel}}. \tag{4.48}$$

Besides the helicity amplitudes $\mathcal{A}_{\mathrm{col,hel}}$ determined by the procedure for the numerical evaluation as presented so far, the `subroutine squareamp` thus takes as an input the matrix $\mathcal{O}$ and the eigenvalues δ_{col}. The latter two are actually already determined in the `Mathematica` part of `Pole`. Here, the relevant routines simply read all colour structures from the output of `CalcFeynAmp`, which are then combined in all possible ways to products like (4.44). The matrix $\mathcal{O}$ and the eigenvalues δ_{col} are then as above determined by applying the Fierz identity and by diagonalizing the resulting matrix. The output routine `PoleToFortran` then writes the elements of $\mathcal{O}$ as well as the squared route of the eigenvalues δ_{col} to the header file `process.h`, which is linked to the `subroutine squareamp`. Provided with this input, the `subroutine squareamp` calculates numerical values for the entries of the matrix $\tilde{\mathcal{A}}$, which then have just to be squared and summed over the various helicity combinations and colour structures the full amplitude depends on.

As can be seen from Figure 4.3, the `subroutine Msquared` returns finally the square of the various amplitudes summed over the helicities and colours of the external particles. Note that no average factors for the initial state are included. To be specific, in case that `LPA` $= 0$ the ouput array `msqu0` contains for `gen` $= 1$ the square of the exact Born matrix elements for all partonic subprocesses, whereas for `gen` > 1 a corresponding array for the Bremsstrahlung process number `gen` is returned. The second output variable `msqu1` is here set to zero for both cases. If invoked with input switches `LPA` $= 1$ and `gen` $= 1$, on the other hand, the two output arrays contain the squared Leading Pole contributions to the Born matrix element as well as to the virtual corrections.

Chapter 5

Numerical Results

In this last chapter, we apply the methods presented in the course of our work so far to $W\gamma$ and $Z\gamma$ pair-production processes. The goal is the calculation of the electroweak corrections to the cross-sections and relevant distributions for the reactions (1.1). To be specific, we here consider the final states

$$\begin{aligned} P+P &\to Z+\gamma \to \nu_l + \bar{\nu}_l + \gamma\ (+\gamma), && l = e, \mu, \tau \\ P+P &\to Z+\gamma \to l\ + \bar{l}\ + \gamma\ (+\gamma), && l = e, \mu \\ P+P &\to W+\gamma \to l\ + \bar{\nu}_l + \gamma\ (+\gamma), && l = e, \mu. \end{aligned} \tag{5.1}$$

Note that the real corrections are treated inclusive, i.e. the cut routines also accept events with two photons in the final state.

We employ the `Mathematica` package `Pole` presented in the last two chapters for both the amplitude generation and the numerical evaluation. The necessary input comprises the parameters for the phase-space integration, numerical values for the model parameters, cut conditions, an on-shell projection as well as the parton distribution functions. We list our choice for this input in Section 5.1. As discussed in Section 5.2, our package can be tested by a series of consistency checks, as well as by comparing our results to literature or to the results calculated by other programs. In Section 5.3 we display and discuss the obtained numerical values for the electroweak corrections to the cross-sections of the processes (5.1), as well as the corresponding results for experimentally relevant distributions. Finally, in Section 5.4 we summarize our conclusions and give an outlook on further calculations and improvements to be done in the future.

5.1 Input Parameters and Process Definition

As was said in Section 4.3, the input necessary to run the `Fortran` code as produced by `Pole` is provided by five different files. To start with, in `main.F` the parameters needed to initialize the phase-space integration and the numerical evaluation of the amplitudes can be set. In our work, the hadronic centre-of-mass energy is fixed to its LHC value

$\sqrt{S} = 14$ TeV. Furthermore, the input scheme for the electromagnetic coupling constant is in our work chosen to be the α_{G_F}-scheme, i.e. we define the fine structure constant in terms of the Fermi constant

$$\alpha = \alpha_{G_F} = \frac{\sqrt{2}}{\pi} G_F M_W^2 \sin^2 \theta_W, \tag{5.2}$$

where we use the value $G_F = 1.16637 \times 10^{-5}$ GeV^{-2}. In (5.2), the quantity θ_W denotes the weak mixing angle defined by

$$\sin \theta_W = \sqrt{1 - \left(\frac{M_W}{M_Z}\right)^2}. \tag{5.3}$$

However, for the coupling of the real final-state photon in (5.1), we use the value $\alpha = \alpha_0 = 1/137.035999$ instead.

To motivate this choice, note that in the electroweak sector of the Standard Model, the vector bosons couple to fermions with a coupling strength $\alpha(p^2)$ given by the fine structure constant evaluated at the momentum squared of the considered boson. In case of the real final-state photon, the squared momentum vanishes, and the coupling strength is accordingly given by $\alpha(p^2 = 0) = \alpha_0$. On the other hand, when evaluating the cross-section in Leading Pole Approximation, the couplings of the decaying Z or W bosons in the intermediate states of (5.1) are evaluated at $p^2 = M_V^2, V = W, Z$. One has therefore to perform an evolution of the coupling constant from zero to the squared mass of the decaying boson by means of the renormalization group equations. However, on the one-loop level such an evolution generally introduces a logarithmic dependence of the virtual corrections on the masses of the Standard Model quarks and leptons. This dependence arises from closed fermion loops contributing to the self-energy of the photon, which enters the counter terms to the coupling of the considered boson as a derivative with respect to the photonic momentum squared. Due to the smallness of the masses of the light fermions with respect to the typical energy scales of the processes at hand, the logarithmic dependence of the virtual corrections on these parameters can be considerable, which in turn leads to a theoretical uncertainty arising from the choice of input parameters for the masses of the light quarks. One way to avoid this problem is to resum the large logarithms depending on the masses of the light Standard Model fermions, and to absorb the resulting factors in the coupling constants. Such a resummation can be achieved by defining the fine structure constant by (5.2) to all orders in perturbation theory. This has the further advantage to effectively include leading logarithmic higher-order contributions in the virtual corrections.

On the other hand, the definition (5.2) also resums one-loop terms already contained in the virtual corrections. Accordingly, these terms have to be subtracted from the finite virtual corrections (D.49) once for each vertex parameterized by α_{G_F}. In our case, we have two such couplings, such that the finite virtual corrections are evaluated according to

$$\sigma^{\text{virt,LPA}}_{q_1 q_2,\text{finite},\alpha_{G_F}}(\hat{s}) = \sigma^{\text{virt,LPA}}_{q_1 q_2,\text{finite}}(\hat{s}) - 2\sigma^{(0),\text{LPA}}_{q_1 q_2}(\hat{s}) \Delta r^{(1)}, \tag{5.4}$$

where the parameter $\Delta r^{(1)}$ is given by (4.4).

To implement the above settings in the framework of the `Fortran` output of `Pole`, we choose the parameter `qalp` in the file `main.F` equal to one, which corresponds to selecting the α_{G_F}-scheme. As discussed in Section 4.3, the number of couplings to be parameterized by α_{G_F} can be specified in the same file by choosing a nonzero value for the parameter `ndZR1`. Following the above discussion we choose `ndZR1` = 2, such that all cross-sections, evaluated in terms of α_0, are internally multiplied by a factor of α_{G_F}/α_0. For the above subtraction of the resummed higher-order terms, our program then automatically evaluates for these settings the finite virtual corrections according to (5.4) without requiring any additional input.

The sum over final-state flavours can be taken into account by choosing the parameter `wgt` in `main.F` equal to three in case of the first process in (5.1), and equal to two for the second and third process. Finally, the inclusive treatment of the Bremsstrahlung corrections can be implemented by setting the parameter `inclusive` in `main.F` equal to one.

Input For the Model Parameters

The second of the five input files is given by `input_sm.F` which contains the numerical values for the Standard Model parameters. We here largely adopt the values presented in Ref.[75]. To start with, after the subtraction (5.4), the cross-section contains no logarithms in the light fermion masses, and can therefore be written as a polynomial of these masses divided by the process energy. As an approximation, we can thus neglect the masses of all fermions and quarks except for the top quark, which is too heavy to justify this approximation. We keep the fermion masses in arguments of loop integrals as a regularization parameter for possible collinear divergences, where we use the values

$$\begin{aligned} &m_u = 0.066\ \text{GeV}, && m_c = 1.6\ \text{GeV}, && m_t = 178\ \text{GeV}, \\ &m_d = 0.066\ \text{GeV}, && m_s = 0.15\ \text{GeV}, && m_b = 4.9\ \text{GeV}, \\ &m_e = 5.109989 \times 10^{-4}\ \text{GeV}, && m_\mu = 0.105658369\ \text{GeV}, && m_\tau = 1.77699\ \text{GeV}. \end{aligned} \tag{5.5}$$

To implement this setting, we set the option `SmallMasses` of the function `CalcAmplitude` to `SmallMasses->{ME,MM,ML,MU,MD,MC,MS,MB}` during amplitude generation, and neglect all diagrams with a coupling of the Higgs boson to the light fermions. The remaining Standard Model mass parameters are set to

$$M_W = 80.425\ \text{GeV}, \qquad \Gamma_W = 2.124\ \text{GeV} \tag{5.6}$$

for the mass and the width of the W boson, whereas we take

$$M_Z = 91.1876\ \text{GeV}, \qquad \Gamma_Z = 2.4952\ \text{GeV} \tag{5.7}$$

for the corresponding Z-boson parameters. As to be discussed below, we neglect all loop corrections to quark mixing in case of the $W\gamma$-production process, and simply multiply

the cross-sections of the partonic subprocesses with the CKM matrix elements

$$\begin{aligned} V_{ud} &= 0.974, & V_{us} &= \sqrt{1 - V_{ud}^2}, & V_{ub} &= 0, \\ V_{cd} &= -\sqrt{1 - V_{ud}^2}, & V_{cs} &= 0.974, & V_{cb} &= 0, \\ V_{td} &= 0, & V_{tc} &= 0, & V_{tb} &= 1. \end{aligned} \tag{5.8}$$

The only remaining Standard Model parameter to be fixed is the Higgs boson mass. However, this parameter is not defined experimentally, as the Higgs particle has not yet been observed, and we fix the Higgs mass to

$$M_H = 115 \text{ GeV}, \tag{5.9}$$

which corresponds to the present lower experimental bound.

Input for the Parton Distribution Functions

The third input file is given by `input_pdfs.F`. Here the parameters related to the convolution of the partonic cross-section with the Parton Distribution Functions can be specified. For our work we use the CTEQ6M set [74] of Parton Distribution Functions, which is the default set for the numerical evaluation in the framework of `Pole`. Note that in the experimental determination of these distributions, only the low-energy terms arising from the QCD-corrections have been subtracted from the partonic DIS cross-section. However, in the framework of an electroweak calculation, one has to use Parton Distribution Functions corrected for both, the low-energy terms arising from QCD *and* the low-energy terms arising from QED in order to achieve a reduction of the dependence of the hadronic cross-section on the factorization scale. Such distributions became available recently [76], but for a consistent treatment of these parton densities one needs to take into account initial states involving photons, which is beyond the scope of this thesis. As a matter of fact, it was shown [77] that the impact of the QED corrections on the actual numerical values of the Parton Distribution Functions is negligible for all practical purposes. The reason for this is that the QED corrections are quite small compared to both, the QCD and the purely weak corrections, and thus provide an only small contribution to the DIS cross-section as well as to the evolution of the parton densities to the energy scale of the considered process. For this reason, one is able to obtain numerically consistent results for the electroweak corrections to a given hadronic cross-section in spite of using QCD corrected parton densities only.

In our calculation of the hadronic cross-section, we neglect all contributions of the initial states containing top and bottom quarks, an approximation which is justified due to the small values of the corresponding Parton Distribution Functions. Accordingly, the first and second process in (5.1) receive contributions from the initial states $u\bar{u}$, $c\bar{c}$, $d\bar{d}$ and $s\bar{s}$ only. However, since we neglect the masses of these particles, the first two as well as the third and fourth of these initial states are kinematically equivalent in the sense that

they lead to the same partonic cross-section. During amplitude generation, we therefore restrict the partonic content of the hadron to the up and down quark and the corresponding anti-quarks by means of the option `PartonicContent` of `InsertFieldContent`. The contributions of the two other initial states can then be included by simply convoluting the partonic cross-section for the $u\bar{u}$ initial state with the parton luminosity

$$\frac{\mathrm{d}\mathcal{L}}{\mathrm{d}x_1\mathrm{d}x_2}(x_1,x_2,Q) = \overline{\Phi}_{P|u}(x_1,Q)\overline{\Phi}_{P|\bar{u}}(x_2,Q) + \overline{\Phi}_{P|c}(x_1,Q)\overline{\Phi}_{P|\bar{c}}(x_2,Q), \tag{5.10}$$

whereas the partonic cross-section for $d\bar{d}$ is convoluted with

$$\frac{\mathrm{d}\mathcal{L}}{\mathrm{d}x_1\mathrm{d}x_2}(x_1,x_2,Q) = \overline{\Phi}_{P|d}(x_1,Q)\overline{\Phi}_{P|\bar{d}}(x_2,Q) + \overline{\Phi}_{P|s}(x_1,Q)\overline{\Phi}_{P|\bar{s}}(x_2,Q). \tag{5.11}$$

The third process in (5.1) receives contributions from the four initial states $d\bar{u}$, $s\bar{u}$, $d\bar{c}$ and $s\bar{c}$. Neglecting radiative corrections to quark mixing, the corresponding partonic cross-sections here only differ by the CKM matrix element in the coupling of the W to the initial state. However, for leptonic final states the CKM matrix element contributes as a factor to the partonic cross-section. During amplitude generation, we therefore set the CKM matrix to the unit matrix, as is done in the beginning of the example in Section 3.4, and calculate the cross-section for the initial state containing up and down-type quarks only. The effects of the CKM matrix as well as the contributions of the other initial states can then be taken into account by convoluting the so-determined partonic cross-section with

$$\begin{aligned}\frac{\mathrm{d}\mathcal{L}}{\mathrm{d}x_1\mathrm{d}x_2}(x_1,x_2,Q) = {} & |V_{ud}|^2\,\overline{\Phi}_{P|d}(x_1,Q)\overline{\Phi}_{P|\bar{u}}(x_2,Q) + |V_{cs}|^2\,\overline{\Phi}_{P|s}(x_1,Q)\overline{\Phi}_{P|\bar{c}}(x_2,Q) \\ & + |V_{cd}|^2\,\overline{\Phi}_{P|d}(x_1,Q)\overline{\Phi}_{P|\bar{c}}(x_2,Q) + |V_{us}|^2\,\overline{\Phi}_{P|s}(x_1,Q)\overline{\Phi}_{P|\bar{u}}(x_2,Q).\end{aligned} \tag{5.12}$$

Finally, one has to specify the typical energy scale Q of the considered process to numerically evaluate the parton luminosities specified above. As discussed before, the dependence of the hadronic cross-section on this parameter arises from the evolution of the Parton Distribution Functions from the DIS energy scale to the energy scale of the considered process. A reasonable choice for the evaluation of the Born cross-sections and the virtual corrections is for the processes (5.1) given by

$$Q^2 = \frac{1}{2}\left(M_V^2 + p_{\mathrm{T},V}^2 + p_{\mathrm{T},\gamma}^2\right), \qquad V = Z, W, \tag{5.13}$$

where $p_{\mathrm{T},V}$ denotes the transverse momentum of the resonance

$$p_{\mathrm{T},V} = \begin{cases} p_{\mathrm{T}}^{\mathrm{miss}} & \text{for } P+P \to Z+\gamma \to \nu_l + \bar{\nu}_l + \gamma, \\ \sqrt{(p_{\mathrm{T},x}^{l} + p_{\mathrm{T},x}^{\bar{l}})^2 + (p_{\mathrm{T},y}^{l} + p_{\mathrm{T},y}^{\bar{l}})^2} & \text{for } P+P \to Z+\gamma \to l + \bar{l} + \gamma, \\ \sqrt{(p_{\mathrm{T},x}^{l} + p_{\mathrm{T},x}^{\mathrm{miss}})^2 + (p_{\mathrm{T},y}^{l} + p_{\mathrm{T},y}^{\mathrm{miss}})^2} & \text{for } P+P \to W+\gamma \to l + \bar{\nu}_l + \gamma. \end{cases} \tag{5.14}$$

Again, $p_{\mathrm{T}}^{\mathrm{miss}}$ is here defined as the sum of the transverse momenta of all particles visible in the detector, whereas $p_{\mathrm{T},x}^{\mathrm{miss}}$ and $p_{\mathrm{T},y}^{\mathrm{miss}}$ denote missing momentum in x and y direction, respectively. In case of the Bremsstrahlung processes, the definition of Q depends on the detected signature. In case where the transverse momentum of the Bremsstrahlung particle can be reconstructed, an expression for the typical energy scale corresponding to (5.13) is given by

$$Q^2 = \frac{1}{2}\left(M_V^2 + p_{\mathrm{T},V}^2 + p_{\mathrm{T},\gamma_1}^2 + p_{\mathrm{T},\gamma_2}^2\right), \qquad V = Z, W. \tag{5.15}$$

However, this expression can only be used if the Bremsstrahlung particle is visible in the detector, such that its transverse momentum can be directly determined from the measured energy and the measured emission angle. An exception is here the case where the Bremsstrahlung particle in the second process in (5.1) cannot be seen. The transverse Bremsstrahlung momentum can then be reconstructed as the sum of the transverse momenta of the detected lepton pair and the detected final-state photon, such that (5.15) is an experimentally well-defined quantity. However, in case of the first and third processes in (5.1), it might happen that the detected final state contains one photon and only one or even no leptons, such that the transverse momentum of the Bremsstrahlung particle is not a measurable quantity. Following our discussion in Section 4.3, the Bremsstrahlung momentum contributes in these cases only to the missing momentum, or has to be recombined with the momentum of the next detected final-state particle. In all other respects, the event is treated as if the Bremsstrahlung particle is not produced. Accordingly, for final states containing one or more neutrinos and an invisible Bremsstrahlung photon, we use the recombined momentum and (5.13) to calculate the typical energy scale Q, rather than the original Bremsstrahlung phase-space and (5.15).

Input for the Cut Parameters

The details for the recombination procedure as well as the phase-space cut conditions can be specified in the fourth input file `input_cuts.F`. For the recombination, we treat a photon as detected, if the corresponding momentum fulfills

$$E^\gamma > E^{\mathrm{rec.}} = 2\ \mathrm{GeV}, \qquad |\eta| < \eta^{\mathrm{rec}} = 2.5, \tag{5.16}$$

where E^γ denotes the energy of the photon. Furthermore, if one of the photons is emitted within a cone defined by

$$\Delta R_{\gamma j} < R^{\mathrm{rec}} = 0.1, \qquad j = l, \gamma \tag{5.17}$$

around a charged lepton or another photon, we recombine the Bremsstrahlung momentum with the momentum of the particle close to it. The quantity $\Delta R_{\gamma j}$ is given by (4.8). If the requirement (5.17) is met for more than one lepton l, we recombine the momenta of the photon-lepton pair with the lowest value for $\Delta R_{\gamma,j}, j = l, \gamma$.

In addition, the phase-space cuts can be specified in `input_cuts.F`. For the processes (5.1) we consider an event to contribute to the cross-section, if the momenta for the leptons and the momentum of at least one of the final-state photons fulfill the following requirements

- $p_{\mathrm{T}}^{\gamma} > p_{\mathrm{T}}^{\gamma,c} = 50$ GeV (100 GeV) for at least one photon in case of $W\gamma$ ($Z\gamma$) production,
- $p_{\mathrm{T}}^{l} > p_{\mathrm{T}}^{l,c} = 20$ GeV for all final-state charged leptons,
- $p_{\mathrm{T}}^{\mathrm{miss}} > p_{\mathrm{T}}^{\mathrm{miss},c} = 50$ GeV (100 GeV) for the cut on the missing transverse momentum in case of $W\gamma$ ($Z\gamma$) production for final states containing at least one neutrino,
- $\Delta R_{ij} > \Delta R^{c} = 0.7,\ i,j = l,\gamma$ for the cut on the rapidity-azimuthal angle separation (4.8) between charged leptons and charged leptons, between charged leptons and photons,
- $|\eta| < \eta^{c} = 2.5$ for at least one of the final-state photons and all final-state charged leptons.

Furthermore, we discussed in Section 4.3 that in case of evaluating the virtual corrections in Leading Pole Approximation (LPA), it is often necessary to restrict the phase-space to the region around the resonances. This is because the error introduced by the LPA is in the total cross-section of order width over mass of the decaying particle, but this must not be true if considering distributions. To be sure that our results for the distributions are reliable, we impose the so-called reconstruction cut conditions

$$M_Z - 20\ \mathrm{GeV} < \sqrt{s_{34}} < M_Z + 20\ \mathrm{GeV} \tag{5.18}$$

on the phase-space for the second process in (5.1), where $s_{34} = (p_3 + p_4)^2$. For the case of γW-production, the neutrino momentum is not an observable, such that one has again to rely on the missing transverse momentum to restrict the squared energy of the lepton pair to the phase-space region around the resonance. To this end, a cut on the transverse mass

$$M_{\mathrm{T}}^{l\nu} < M_W + 20\ \mathrm{GeV} \tag{5.19}$$

is appropriate here, where the transverse mass for a lepton-neutrino pair $l\nu_l$ is defined as

$$M_{\mathrm{T}}^{l\nu} = \sqrt{(|p_{\mathrm{T}}^{\mathrm{miss}}| + |p_{\mathrm{T},l}^{2}|)^2 - (p_x^{\mathrm{miss}} + p_{x,l})^2 - (p_y^{\mathrm{miss}} + p_{y,l})^2}. \tag{5.20}$$

Finally, for the case of the Z boson decaying into two neutrinos none of the decay products is visible, and thus neither of the above reconstruction cuts can be imposed.

On-Shell Projection

Finally, we said in Section 4.3 that in order to be able to evaluate the virtual corrections in Leading Pole Approximation, an on-shell projection has to be specified to project the residuum of the amplitude at the Pole on the mass-shell of the decaying particles. For

the processes (5.1), a projection has to be found which maps a general set of momenta Φ on a set of momenta $\Phi_{\rm osh}$ such that $(p_3^{\rm osh} + p_4^{\rm osh})^2 = M_V^2$, where M_V is the mass of the decaying vector boson $V = W, Z$. Such a projection is given by

$$\tilde{p}_3 = x p_3, \qquad \tilde{p}_5 = z p_5, \qquad \tilde{p}_4 = p_1 + p_2 - \tilde{p}_3 - \tilde{p}_5, \tag{5.21}$$

where scaling variables x and z can be obtained from the mass-shell conditions for the resonance and for the momentum $\tilde{p}_4$

$$z = \frac{s - M_V^2}{2(p_1 + p_2)p_5}, \qquad x = \frac{M_V^2}{2(p_1 + p_2 - z p_5)p_3}. \tag{5.22}$$

Note that the on-shell projection as specified above only involves Lorentz-invariant quantities.

5.2 Tests

Before presenting our numerical results for the cross-sections and distributions of the processes (5.1), we summarize in this section the procedure used to test the amplitude generation as well as the numerical evaluation as provided by the `Fortran` output of `Pole`. To start with, a first obvious test is to check if `Pole` generates the correct diagrams for the considered first-order cross-section in Leading Pole Approximation. This can be done by once generating the diagrams for the full process using `FeynArts` and by dividing them in resonant and non-resonant, factorizable and non-factorizable diagrams. The so-obtained subsets of graphs can then be compared to the diagram output of `Pole`. In Table 5.1 we show the number of diagrams contributing to the full amplitude and to the amplitude in Leading Pole Approximation for the virtual corrections to the partonic processes of (5.1), as well as the number of the corresponding counter-term diagrams. Note that we do not include graphs with a coupling of the Higgs particle to the light external fermions. As can be seen, by applying the Leading Pole Approximation to the virtual corrections, the number of diagrams to be calculated is reduced by roughly a factor of two for the first and the third process in (5.1), whereas for the second process, the number of diagrams is reduced by a factor of five.

To test the amplitudes generated by `Pole` numerically, we furthermore performed an explicit paper-and-pencil calculation of those parts of the cross-section, which are compact enough to allow for such a treatment. This is possible for the Born amplitude, the non-factorizable virtual corrections and the real corrections, and we list the corresponding expressions in Appendix B. For the numerical comparison, we replaced the code for the amplitudes as generated by `Pole` by a corresponding code for the amplitude obtained from our by-hand calculations, and compared the numerical values for squared amplitudes at several phase-space points. Finally, we integrated the squared amplitudes over phase-space, and compared the resulting numerical values to the values for the total cross-sections obtained

	$u\bar{u} \to \nu_e \bar{\nu}_e \gamma$	$u\bar{u} \to e^- e^+ \gamma$	$d\bar{u} \to e^- \bar{\nu}_e \gamma$
virtual corrections	197	536	280
counter terms	16	48	23
virtual corrections ,LPA	105	107	130
counter terms, LPA	8	8	13

Table 5.1: The number of diagram contributing to the full amplitude of the virtual corrections and the corresponding counter terms, as well as the number of diagrams contributing in Leading Pole Approximation. Diagrams with a coupling of the Higgs particle to the external fermions were neglected.

by `Pole`. The factorizable virtual corrections, on the other hand, involve some hundreds of Feynman diagrams to evaluate, which makes a by-hand calculation quite cumbersome. To be able to check these contributions anyway, we generated the diagrams for the processes (5.1) by means of `FeynArts`, switched off the non-resonant and non-factorizable diagrams by hand and translated the corresponding amplitudes into `Fortran` code using `FormCalc4`. To incorporate finite-width effects, we then edited the so-generated amplitude files and replaced all resonant propagators by the corresponding propagators including a finite width. Finally, we wrote an interface of the amplitude evaluation in `FormCalc4` to the phase-space integration in `Pole` to be able to compare the amplitudes numerically. Again, the comparison was done at some isolated phase-space points and for the integrated cross-section. The above procedure was applied to all three final states (5.1), yielding in each case complete agreement.

Knowing now that both, the amplitude generation and the amplitude evaluation are correctly working, the next feature to be tested is the evaluation of the partonic cross-section. As stated in Section 2.4, the latter receives contributions from the Born cross-section, the finite virtual corrections, the sum of singular virtual and singular real corrections as well as the finite real corrections. To start with, we said in Section 2.4 that we evaluate the Born cross-section exactly, such that the corresponding contribution to the total hadronic cross-section can be obtained by simply integrating the squared amplitude tested as discussed above over phase-space. The finite virtual corrections, on the other hand, can be tested on UV-finiteness by numerically varying the regulator for the dimensional regularization. To do so, we changed the corresponding input value from $\mu = 1$ to $\mu = 10^{100}$, which results in a variation of our results in the nineth significant digit. Furthermore, after the subtraction of the singular parts according to (D.50), the finite virtual corrections must also be independent of the regulators for the infrared and collinear divergences, i.e. of the photon mass and the masses of the light external fermions. We show the dependence of our results on these parameters in Figure 5.1. The y-axis represents the contributions of the finite virtual corrections to the total hadronic cross-section. In the plots on the right-hand side, we set all external fermion masses equal to the parameter m on the x-axis. The cross-section was calculated using the standard cuts listed in Section 5.1. As can be seen, we find complete

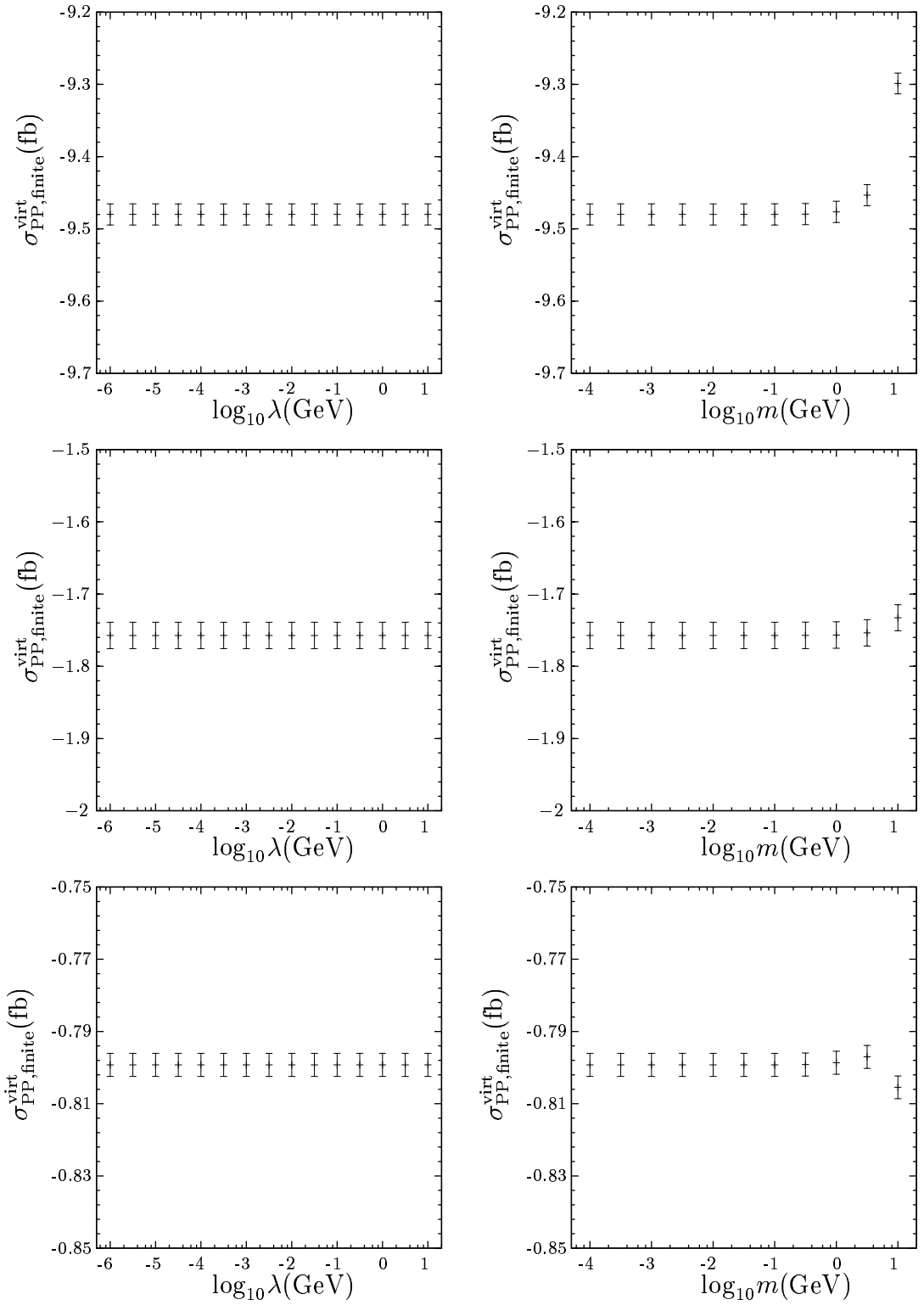

Figure 5.1: Independence of the finite virtual corrections for $P+P \to \nu\bar{\nu}\gamma$ (top), $P+P \to e^-e^+\gamma$ (middle), and $P+P \to e^-\bar{\nu}\gamma$ (bottom) of the mass regulators for the photon and the external fermions. The parameter m denotes collectively the masses of all external fermions.

independence of the finite virtual corrections of the photon mass regulator over the whole considered range, whereas for the masses of the external fermions we find an independence up to $m = 1$ GeV. For the results to be presented in the next section, we accordingly fixed the UV and infrared regulators to $\mu = 1$ and $\lambda = 10^{-8}$ GeV, respectively, whereas for the masses of the external fermions we took the values listed in (5.5).

The remaining contributions to the partonic cross-section which have to be tested are given by the sum of the singular real and singular virtual corrections, as well as the finite real corrections. As was said in Section 2.4, we implemented two entirely independent methods to calculate these contributions, the phase-space-slicing technique and the subtraction method. Both methods have of course to yield the same numerical result if adding the sum of the singular virtual and singular real corrections to the finite real corrections. In case of the phase-space slicing technique, this result must furthermore be independent of the slicing cut parameters δ_s and δ_c. As a problem, we mentioned in Section 2.3 that a too small choice for these parameters leads to numerical instabilities, whereas a too large value spoils the approximation that these parameters can be neglected wherever they do not appear in logarithms. In Figure 5.2 we show the dependence of our results on the slicing cut parameters. The quantity on the y-axis is given by the sum of the contributions of the singular real corrections, the singular virtual corrections and the finite real corrections to the total hadronic cross-section. The horizontal lines represent the error bars of our results obtained by employing the subtraction method. The cross-section shows a plateau over the full considered range for δ_c, whereas the variation of δ_s leads to a plateau in the region $10^{-5} < \delta_s < 10^{-3}$ for the $\nu\nu\gamma$ and $ll\gamma$ final states, and in the region $10^{-4} < \delta_s < 10^{-3}$ for the $l\nu\gamma$ final state. In addition, the numerical values obtained in these ranges agree with those obtained by using the subtraction method within the error bars. For the results to be presented in the next section, we accordingly fixed the slicing cuts to $\delta_s = 10^{-3}$ and $\delta_c = 10^{-4}$.

Finally, our implementation of the phase-space integration and of the on-shell evaluation of the virtual corrections can be tested by direct numerical comparison to the already published results of Ref.[36]. The authors present there numerical results for the exact Born cross-section and for the finite virtual corrections for hadronic $W\gamma$ production, i.e. for the third process in (5.1). However, the virtual corrections are determined for the production subprocess only, and the calculation was simplified by using the so-called High-Energy Approximation [78, 79, 80]. Furthermore, only the leading logarithmic contributions to the loop integrals of the form $\log^2 \hat{s}/M_W^2$, $\log \hat{s}/M_W^2 \log \hat{s}/\hat{x}$ and $\log \hat{s}/M_W^2$ were taken into account, where $x = \hat{t}, \hat{u}$ denotes one of the Mandelstam variables for the production subprocess. The use of the High-Energy Approximation is justified by imposing a large cut on the transverse momentum of the final-state photon, which results in large values for the partonic centre-of-mass energy $\hat{s}$ compared to the W mass, and thus to large values for the above leading logarithms. Moreover, the authors of Ref.[36] summed the helicities of the decaying W-boson over transverse polarizations only, whereas in our approach we also take into account the longitudinal helicity combinations, which are however kinematically suppressed in the high-energy limit.

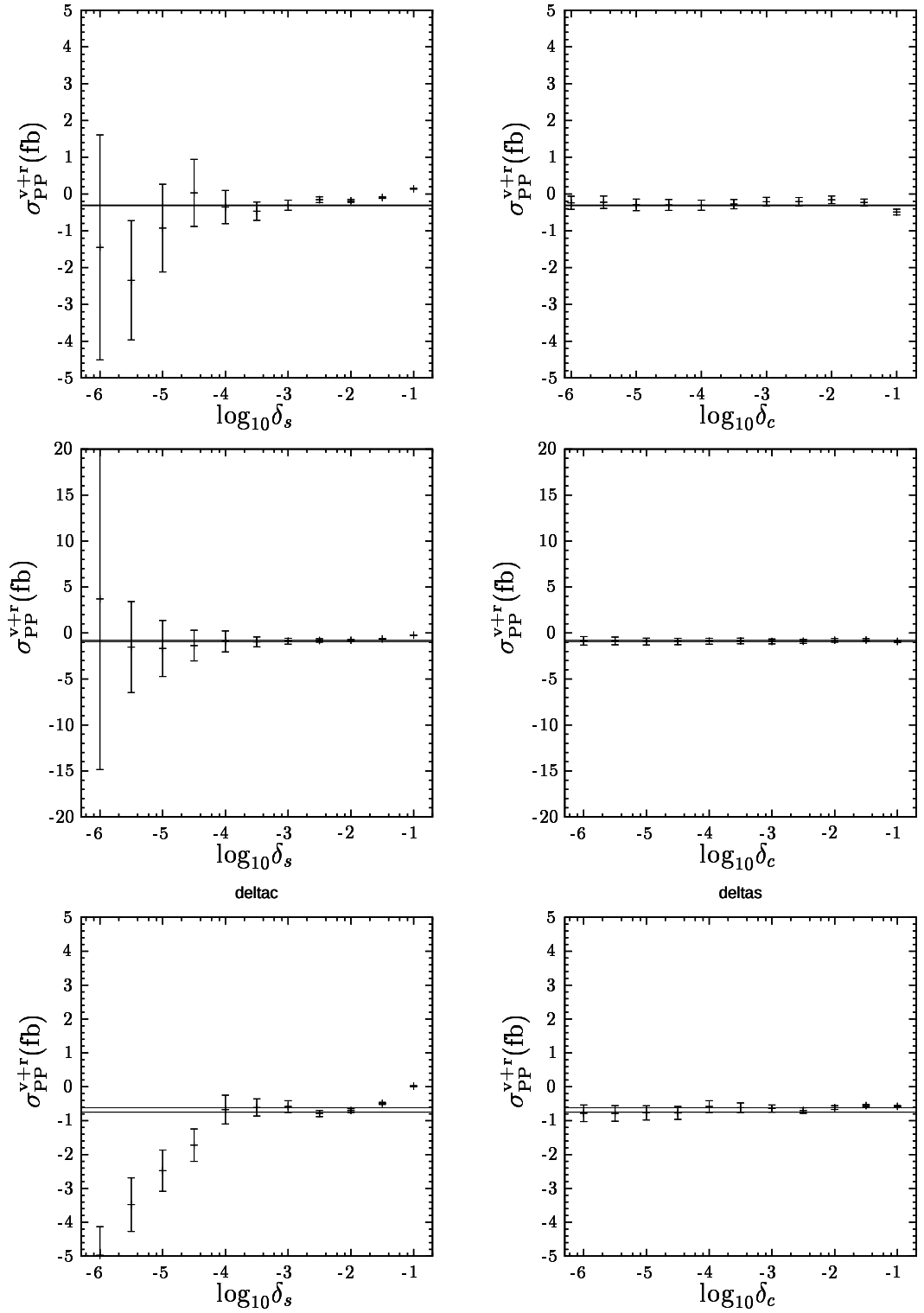

Figure 5.2: Independence of our results of the phase-space slicing cut parameters. On the y axis, we show the sum of singular virtual corrections, the singular real corrections and the finite real corrections for $P + P \to \nu_l \bar{\nu}_l \gamma + (\gamma)$ (top), $P + P \to l^- l^+ \gamma + (\gamma)$ (middle), and $P + P \to l^- \bar{\nu}_l \gamma + (\gamma)$ (bottom). The horizontal lines indicate the error bars of our results obtained by using the subtraction method.

Numerical Comparison for $P + P \to W\gamma \to l + \bar{\nu}_l + \gamma$						
	Ref.[36]			Our Results		
$p_{\mathrm{T}}^{\gamma,\mathrm{c}}$(GeV)	$\sigma_{\mathrm{PP}}^{(0)}$(fb)	$\sigma_{\mathrm{PP,finite}}^{\mathrm{virt}}$(fb)		$\sigma_{\mathrm{PP}}^{(0)}$(fb)	$\sigma_{\mathrm{PP,finite}}^{\mathrm{virt}}$(fb)	
250	6.01	-0.292	-4.86%	6.02(3)	$-0.637(3)$	-10.6%
450	0.712	-9.78×10^{-2}	-13.74%	0.711(4)	$-0.1343(7)$	-18.9%
700	9.30×10^{-2}	-2.06×10^{-2}	-22.12%	$9.31(6) \times 10^{-2}$	$-2.49(2) \times 10^{-2}$	-26.8%
1000	1.25×10^{-2}	-3.72×10^{-3}	-29.6%	$1.253(9) \times 10^{-2}$	$-4.26(3) \times 10^{-3}$	-34.0%

Table 5.2: Comparison of our results for the Born cross-section and for the finite virtual corrections to those of Ref.[36]. The virtual corrections are calculated for the production subprocess only.

To be able to check the hadronic cross-section obtained in Ref.[36] against our results, we generated the amplitudes for the virtual corrections to the $W\gamma$ production subprocess by using the option `ProductionOnly` $\to$ `True` of `CreateFactorizableTopologies` and evaluated the so-obtained amplitudes numerically by adapting the input to the parameter and cut values displayed in Ref.[36]. In order to estimate the effect of the High-Energy Approximation we furthermore varied the cut on the transverse momentum of the final-state photon. The resulting numerical values for the Born cross-section and the finite virtual corrections are shown in Table 5.2. Note that in comparing to our results the authors of Ref.[36] found an error in their implementation of the azimuthal-pseudorapidity separation (4.8), such that the values shown in Table 5.2 do not exactly correspond to the results presented in a similar table in their publication.

To start with, the results for the Born cross-section agree within the errorbars at the per-mille level. Note that the authors of Ref.[36] were also able to check our results for the Born cross-sections of the first and second process in (5.1) by including the corresponding independently calculated amplitudes in their phase-space generator. Furthermore, we numerically cross-checked the Born curves in the distributions to be presented in the next section for all three processes with the corresponding results obtained by an independent simulation of the authors of Ref.[36]. All these tests yielded complete agreement, which confirms our implementation of the phase-space integration, the cut routines and the histogram generation.

Comparing our results for the finite virtual corrections, one would expect that the use of the High-Energy Approximation in Ref.[36] results in a large difference for low values of $p_{\mathrm{T}}^{\gamma,\mathrm{c}}$, which decreases for higher values of this cut to the level of 1-2 per cent. However, the numbers in Table 5.2 point rather towards a constant difference of approximately 4-5%. In order to understand this effect, we used the fact that `LoopTools` numerically reduces all tensorial loop integrals onto a set of scalar basis integrals. To be able to investigate if the High-Energy Approximation is the source of the above discrepancy, we replaced each

Subcontributions to $\boldsymbol{\sigma^{(1)}}$						
$p_{\mathrm{T}}^{\gamma,\mathrm{c}}$(GeV)	$\sigma^{(1)}_{\mathrm{LLog}}$(fb)		$\Delta\sigma^{(1)}_{\mathrm{QED}}$(fb)		$\sigma^{(1)}_{\mathrm{NLLog}}$(fb)	
250	$-0.364(1)$	-6.05%	$8.6(1)\times10^{-2}$	1.43%	$-0.360(2)$	-5.99%
450	$-0.1026(4)$	-14.4%	$1.13(2)\times10^{-2}$	1.59%	$-4.29(2)\times10^{-2}$	-6.04%
700	$-2.11(1)\times10^{-2}$	-22.6%	$1.40(3)\times10^{-3}$	1.50%	$-5.31(3)\times10^{-3}$	-5.71%
1000	$-3.77(3)\times10^{-3}$	-30.1%	$1.74(5)\times10^{-4}$	1.39%	$-6.63(5)\times10^{-4}$	-5.29%

Table 5.3: The cross-section for the finite virtual corrections split up into leading logarithmic contributions $\sigma^{(1)}_{\mathrm{LLog}}$, the QED remnants $\Delta\sigma^{(1)}_{\mathrm{QED}}$ after subtraction of the QED contributions, as well as the non-leading logarithms and constants $\sigma^{(1)}_{\mathrm{NLLog}}$.

loop integral in this basis set by the corresponding expression in the High-Energy Approximation, which however was found to change the total cross-section by an only negligible amount. As a next potential source of error, we therefore checked if the discrepancy arises from neglecting the non-leading contributions. In order to do so, we split the high-energy expressions for the basic loop integrals in leading logarithms, QED-like logarithms as well as the remaining non-leading logarithms and constants. A fourth contribution arises from constant terms in the reduction of the tensor integrals to the basic scalar integrals. The numerical size of this fourth contribution can be determined by setting the basic integrals to zero. As shown in Table 5.3, the cross-section for the virtual corrections can in this way be split into three different terms.

The leading logarithmic contributions in the second and third column are here obtained by only keeping logarithms of type $\log^2 \hat{s}/M_W^2$, $\log \hat{s}/M_W^2 \log \hat{s}/\hat{x}$, $x = \hat{t}, \hat{u}$ and $\log \hat{s}/M_W^2$ for the evaluation of the basic loop integrals, and by subtracting the constant terms arising from the tensor reduction, i.e. the fourth contribution mentioned above, from the so-obtained cross-section. This is also the approximation used by the authors of Ref.[36]. As can be seen by comparing the numbers in the second and third column of Table 5.3 to their results presented in Table 5.2, the leading logarithmic contributions differ by about 1.2% for $p_{\mathrm{T}}^{\gamma,c} = 250$ GeV, but this difference decreases to the per-mille level for higher cut values. By only keeping the leading logarithms, we are thus able to reproduce the results of Ref.[36] to a satisfying accuracy. Turning next to the QED-contributions in the fourth and fifth column, the corresponding loop integrals are evaluated by only keeping logarithms in the regulators for the masses of the photon and the external light fermions. We here observe an energy-independent contribution of the order of about 1.5%. The reason for this is that in the approach as presented above, we used the High-Energy Approximation to evaluate the loop integrals, but subtracted the singular terms of the exact matrix element. The constant remnant observed here is thus given by the difference in the subtraction term (D.52) evaluated in Leading Pole Approximation to the same term evaluated by additionally using the High-Energy Approximation. Finally, the contributions listed in the sixth and seventh column of Table 5.3 contain the non-leading logarithms and the constant terms

Subcontributions to $\sigma^{(1)}_{\mathrm{NLLog}}$						
$p_{\mathrm{T}}^{\gamma,\mathrm{c}}$(GeV)	$\sigma^{(1)}_{\mathrm{NLLog,NoLog}}$(fb)		$\sigma^{(1)}_{\mathrm{NLLog,Log}}$(fb)		$\sigma^{(1)}_{\mathrm{NLLog,Log^2}}$(fb)	
250	$-1.55(8)\times10^{-2}$	-0.26%	$-0.107(1)$	-1.78%	$-0.238(2)$	-3.95%
450	$-4.13(8)\times10^{-3}$	-0.58%	$1.139(2)\times10^{-2}$	-1.97%	$-2.48(2)\times10^{-2}$	-3.50%
700	$-6.94(9)\times10^{-4}$	-0.74%	$-1.78(2)\times10^{-3}$	-1.91%	$-2.83(2)\times10^{-3}$	-3.05%
1000	$-1.09(1)\times10^{-4}$	-0.87%	$-2.25(3)\times10^{-4}$	-1.79%	$-3.29(3)\times10^{-4}$	-2.62%

Table 5.4: The non-leading contributions to the virtual corrections split up into terms $\sigma^{(1)}_{\mathrm{NLLog,NoLog}}$ containing no angular-dependent logarithms, into terms $\sigma^{(1)}_{\mathrm{NLLog,Log}}$ depending on single angular-dependent logarithms as well as into terms $\sigma^{(1)}_{\mathrm{NLLog,Log^2}}$ depending on angular-dependent logarithms squared.

in the high-energy expressions for the basic loop integrals, as well as the constant terms arising from the tensor reduction. Previous experience with the High-Energy Approximation makes us expect a contribution of the order of one or two per cent here. However, we observe a constant contribution of about 5-6%. The reason for the deviation in the above comparison of the finite virtual corrections is thus that the authors of Ref.[36] have neglected the non-leading terms.

To understand why these terms cause a that large effect, we further split the non-leading contributions of the basic loop integrals in a part containing purely angular-dependent logarithms squared, in terms linear in these logarithms, and in the contribution of the remaining parts. The corresponding numerical values are shown in Table 5.4. The terms in the second and third column are here calculated with the basic loop integrals evaluated by switching off the leading logarithms, the QED logarithms and all purely angular-dependent logarithms. The so-obtained cross-section then contributes on the per-mille level only, where the increase with rising values for the cut on the transverse momentum of the photon is due to terms linear in $\hat{s}/M_W^2$. The numerical values in the fourth and fifth column comprise the contributions linear in the purely angular-dependent logarithms, whereas the numerical values in the sixth and seventh column correspond to the terms containing these logarithms squared. The latter arise generally from squared logarithms in the Mandelstam variables $\hat{t}$ or $\hat{u}$ divided by the W mass, which in the High-Energy Approximation are rewritten as

$$\log^2\frac{x}{M_W^2} = \log^2\frac{\hat{s}}{M_W^2} + 2\log\frac{\hat{s}}{M_W^2}\log\frac{x}{\hat{s}} + \log^2\frac{x}{\hat{s}} \approx \log^2\frac{\hat{s}}{M_W^2} + 2\log\frac{\hat{s}}{M_W^2}\log\frac{x}{\hat{s}}, \quad (5.23)$$

where $x = \hat{t}, \hat{u}$. The last logarithm in the second term of (5.23) is purely angular-dependent, and is generally neglected in the evaluation of the virtual corrections in Leading Logarithmic Approximation. Concerning our splitting of the virtual corrections in Table 5.3, these logarithms are thus contained in the non-leading terms. As can be seen from Table 5.4, the contributions linear and quadratic in the purely angular-dependent logarithms vary

only little with increasing energy, but contribute with about 2% and 3-4%, respectively. The large size of the purely angular-dependent contributions can be explained by the appearance of the real photon in the final state of the processes (5.1), which leads to an enhancement of the cross-section in the forward and backward scattering limits. However, this is also the phase-space region where $\hat{t}$ and $\hat{u}$ are small, and thus where the purely angular-dependent logarithms of type $\log \hat{s}/\hat{t}$ and $\log \hat{s}/\hat{u}$ are large. It is the size of this last contribution which we underestimated in our original comparison of the values shown in Table 5.2.

As a first result of this thesis, we were thus able to show that if one is to calculate the virtual corrections to a given cross-section by keeping the leading logarithms only, the purely angular-dependent logarithms must generally be included in order to yield an accuracy at the per-cent level, whereas the approximation (5.23) used in Ref.[36] might lead to an error of the order of several per cent.

5.3 Results and Discussion

In this section, we present our results for the effect of the electroweak corrections on the analysis of hadronic $W\gamma$ and $Z\gamma$ production at the LHC.

Total Cross-Sections

To start with, we show in Table 5.5 the total hadronic cross-section for the three processes (5.1). The second column contains our results for the hadronic Born cross-sections. The difference in the reaction rates for the $Z\gamma$ production processes in the first and second row can be explained by the smaller branching ratio for the Z boson decaying into to charged leptons as compared to the branching ration for the Z boson decaying into neutrinos. The cross-sections in the first row of Table 5.5 are furthermore enhanced with respect to the results in the second and third row since they are summed over the final states containing electron, muon and tau neutrinos, whereas the two processes in the second and third row are only summed over the first two lepton families.

The third and fourth columns in Table 5.5 contain the absolute size of first-order corrections, as well as their relative contribution in per cent of the Born cross-section. To analyze the corrections qualitatively, we furthermore split in Table 5.6 the first-order corrections (second and third column) in the subcontributions of the finite virtual corrections (fourth and fifth column), the sum of the singular virtual and singular real corrections (sixth and seventh column) and the finite real corrections (eighth and nineth column). As a general feature, the relative size of the finite virtual corrections for the two $Z\gamma$ production processes in the first and the second row is about the same, whereas for the $W\gamma$ production process in the third row it is a factor of three smaller. The size of the singular parts in virtual and real corrections as well as the size of the finite real corrections shown in Table

The Results for the Total Hadronic Cross-Sections				
	$\sigma_{\rm PP}^{(0)}$(fb)	$\sigma_{\rm PP}^{(1),\rm tot}$(fb)		$1/\sqrt{2L\sigma_{\rm PP}^{(0)}}$ (%)
$\nu_l\bar{\nu}_l\gamma$	212.26(7)	−9.65(3)	−4.5%	0.49%
$ll\gamma$	38.99(9)	−2.61(7)	−6.7%	1.1%
$l\bar{\nu}_l\gamma$	85.96(6)	−1.58(8)	−1.8%	0.76%

Table 5.5: Our results for the total Born cross-section (second column) as well as the electroweak first-order corrections (third and fourth column) for the three considered final states. The relative corrections are given in per cent of the Born cross-section. The fourth column shows the statistical error expected from two LHC experiments collecting data at an integrated luminosity of $L = 2 \times 100/\text{fb}$.

5.6 grow with increasing number of charged final-state particles, and thus with the number of potential Bremsstrahlung emitters.

Quantitatively, the impact of the overall contribution of the virtual and real corrections for the three processes (5.1) is found to be a negative contribution of the order of -2% to -7% of the Born cross-section. This is to be compared to the last column of Table 5.5, where we display an estimate for the statistical error for two LHC experiments collecting $L = 2 \times 100$ fb^{-1} of data per annum. As can be seen, the size of the electroweak corrections well exceeds these statistical error estimates, and thus provides in principle an observable effect. On the other hand, the phenomenological predictions for hadron collider experiments generally exhibit a quite large systematical error. The latter is dominated by the error of the experimental determination of the Parton Distribution Functions, which is of the order of 5% for the valence quarks and of the order of 10% for the gluon. Even though the processes considered here do not involve gluonic initial states, it is therefore doubtful that the electroweak corrections have a sizable impact on the experimental analysis of the total cross-section. On the other hand, the electroweak corrections become larger with growing energy. As a result, the absolute values of the corrections is strongly cut dependent, and larger values can be obtained by choosing e.g. a larger cut on the transverse momentum of the photon. However, larger values for the cut parameters lead to a decreasing cross-section, and thus to a larger statistical error. For our choice for the cuts and assuming the above value for the LHC luminosity, our results predict an absolute event rate of 212.26 fb $\times$ 200/fb $\approx$ 42400 events for the $\nu_l\nu_l\gamma$ final states, whereas the corresponding event rates for $ll\gamma$ and $l\bar{\nu}_l\gamma$ are about 8000 and 17200 events.

Distributions

Considering next the dependence of the total cross-section for the three processes (5.1) on kinematical quantities, it was said in the introduction to this work that such distributions can be used to test if the theory underlying the fundamental interactions of nature is

The Subcontributions to the Electroweak Corrections								
	$\sigma_{\mathrm{PP}}^{(1),\mathrm{tot}}$(fb)		$\sigma_{\mathrm{PP,finite}}^{\mathrm{virt}}$(fb)		$\sigma_{\mathrm{PP,finite}}^{\mathrm{v+r}}$(fb)		$\sigma_{\mathrm{PP,finite}}^{\mathrm{real}}$(fb)	
$\nu_l\bar{\nu}_l\gamma$	−9.67(4)	−4.5%	−9.484(3)	−4.4%	−21.436(9)	−10.1%	21.27(4)	10.0%
$ll\gamma$	−2.61(7)	−6.7%	−1.756(4)	−4.5%	−13.01(3)	−33.4%	12.16(7)	31.2%
$l\bar{\nu}_l\gamma$	−1.58(8)	−1.8%	−0.8007(7)	−0.8%	−15.344(1)	−17.9%	14.56(8)	16.9%

Table 5.6: The subcontributions to the first-order electroweak corrections (second and third column) for the three considered processes. These comprise the finite virtual corrections (fourth and fifth column), the sum of singular virtual and singular real corrections (sixth and seventh column) and the finite real corrections (eighth and nineth column). The relative size of the subcontributions is given in per cent of the Born cross-section.

to be formulated as the same gauge theory as the Standard Model or not. If this theory involves anomalous interactions of the vector bosons forbidden by the Standard Model gauge symmetries, these non-standard interactions will cause a deviation of the experimental results from the Standard Model predictions in the high-energy domain of phase-space. If no deviation is observed, this procedure can be used to determine bounds on the anomalous coupling constants.

To match the experimental precision of the LHC experiments, the Standard Model predictions have to be calculated including QCD corrections. The latter are generally positive, and exceed the leading-order Standard Model predictions by a factor of two without jet veto [32, 81]. If applying a jet veto, the QCD corrections might become negative, but still contribute several tens of per cent of the Born cross-section [32, 81]. In calculating electroweak effects, one has thus first to check if the electroweak corrections to the distributions used to probe for anomalous couplings are sizable enough to lead to an experimentally observable effect. If this is the case, one has secondly to compare the size of the electroweak corrections to the QCD-corrected cross-sections and distributions to estimate their impact on the analysis of the anomalous coupling constants.

Distributions for $P + P \to \nu_l + \bar{\nu}_l + \gamma$

To start with, we show in Figure 5.3 the experimentally relevant distributions of the leading-order cross-section and of the electroweak corrected next-to-leading-order (NLO) cross-section for the process $P + P \to \nu_l + \nu_l + \gamma,\ l = e, \mu, \tau$. The inserted plots contain the relative contribution of the sum of real and virtual corrections in per cent of the Born result. As a first experimentally interesting observable, we show in the upper left plot of Figure 5.3 the distribution of the hadronic cross-sections in the transverse momentum of the real final-state photon. In case of the Bremsstrahlung process involving two final-state photons visible in the detector, we addressed the hadronic weight to the bin corresponding

to the transverse momentum of the photon with the highest energy. The effects of electroweak corrections to this distribution have already been studied in Ref.[37] for an on-shell final-state Z boson, with the real corrections included in the soft and collinear limits. The authors obtained large negative corrections, which can be of the order of up to -30% relative to the Born cross-section. Furthermore, the relative size of the electroweak corrections is found to increase with rising energy, such that their impact on the total cross-section is largest in the high-energy domain of phase-space. As can be seen from the upper left plots in Figure 5.3, our calculation largely confirms these results. Compared to the results presented in Ref.[37], the inclusion of the full Bremsstrahlung contributions as well as of the virtual corrections to the decay subprocesses leads to an increase in the predicted event rates, but not to a change of the overall structure. As in Ref.[37], we also find that the electroweak corrections provide a negative contribution of up to -30% relative to the Born cross-section in the phase-space region of high transverse momentum. Since this is also the phase-space region where the effects of the anomalous coupling constants are the most pronounced, it can be expected that the electroweak corrections will considerably modify the results for the anomalous coupling constants obtained from the experimental analysis. On the other hand, one has to take into account that the cross-section and thus the experimentally obtained statistics decreases quite rapidly with increasing transverse momentum. Assuming again an LHC luminosity of $L = 2 \times 100/\text{fb}$, the bin at $p_{\text{T}}^{\gamma} = 400$ GeV collects a contribution of $\mathrm{d}\sigma/\mathrm{d}p_{\text{T}}^{\gamma} \approx 10^{-2}$ fb/GeV to the total cross-section, and will in experiment thus receive an approximate event number of

$$N_{\text{ev}} \approx L \times \frac{\mathrm{d}\sigma}{\mathrm{d}p_{\text{T}}^{\gamma}} \Delta p_{\text{T}}^{\gamma} = 200\ \text{fb}^{-1} \times \frac{10^{-2}\ \text{fb}}{\text{GeV}} \frac{20\ \text{GeV}}{\text{bin}} = \frac{40}{\text{bin}}, \tag{5.24}$$

where $\Delta p_{\text{T}}^{\gamma} = 20$ GeV/bin is the bin width. The electroweak corrections are here of the order of -20%, which corresponds to eight events. Assuming the systematical error being dominated by the error of 5% arising from the Parton Distribution Functions, the effect of the electroweak corrections exceeds the statistical and systematical error bars, and should thus be visible in experiment.

As was said above, the size of the electroweak correction has to be compared to the QCD corrected distributions to be able to estimate the impact of the electroweak corrections on the analysis of the experimental data in terms of anomalous gauge couplings. The QCD-corrections for the photon transverse-momentum distribution to the production of a photon plus missing momentum have been discussed in Ref.[81]. If applying a jet veto to reduce the background and the factorization scale dependence of the NLO cross-section, the authors find negative corrections contributing some -20% of the Born cross-section. Comparing this to our results, the electroweak corrections are found to be of the same order of magnitude or even larger than the QCD-corrections, such that they have to be included in the experimental analysis in order to avoid misinterpretations of the measured reaction rates.

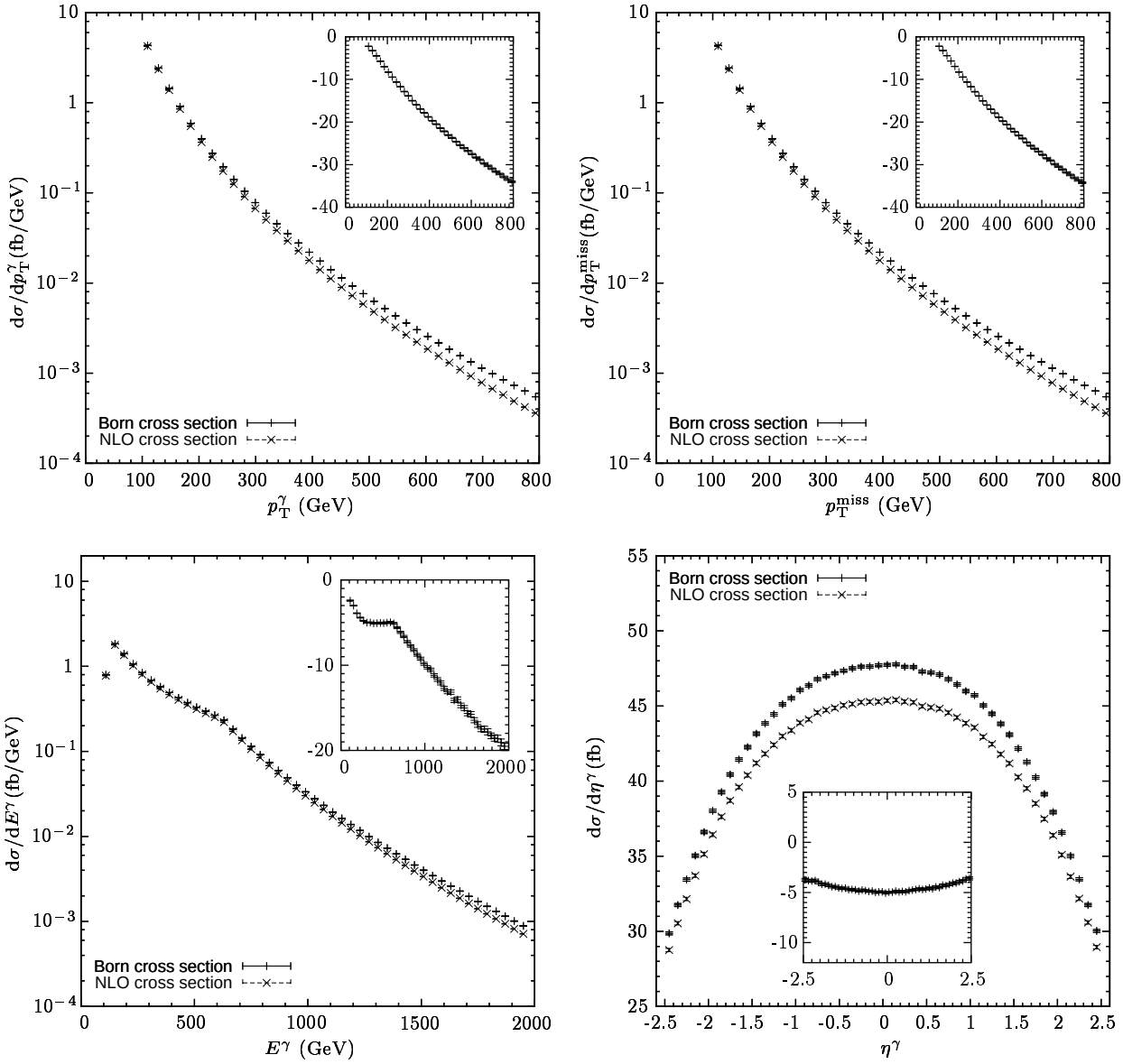

Figure 5.3: The distributions of the Born cross-section and the 1-loop corrected cross-section for $P + P \to Z\gamma \to \nu_l + \bar{\nu}_l + \gamma + (\gamma)$, $l = e, \mu, \tau$ in dependence of the photon transverse momentum (upper left plot), the missing transverse momentum (upper right plot), as well as the energy (lower left plot) and the rapidity (lower right plot) of the final-state photon. The inserted plots show the sum of virtual and real corrections in per cent of the Born cross-section. For an event with two visible photons in the final state, we addressed the hadronic weight to the bin corresponding to the rapidity or transverse momentum of photon with the largest energy.

As a second observable, we show the distribution of the hadronic cross-section in the missing transverse momentum in the upper right plot in Figure 5.3. The latter arises from the non-observability of the final-state neutrinos as well as of soft or collinear Bremsstrahlung particles. For the Born process, the missing transverse momentum is exactly equal to the transverse momentum of the photon, and a difference only arises from kinematical configurations of the Bremsstrahlung process, where the additional photon is visible in the detector. However, it can be seen from the first row in Table 5.6 that the contribution of the finite real corrections (eighth and nineth column) tends to cancel with the sum of singular parts in virtual and real corrections (sixth and seventh column). As a result, the differences in the distributions in the missing transverse momentum and the transverse momentum of the photon are negligible.

As a further observable for the process $P + P \to Z\gamma \to \nu_l + \bar{\nu}_l + \gamma + (\gamma)$, $l = e, \mu, \tau$, we show the distribution of the cross-section in the energy of the final-state photon in the lower left plot in Figure 5.3. This distribution can be used to probe for effects of the production of so far unknown particles not contained in the Standard Model. This is because any process where a photon is pair-produced with an only weakly interacting particle or with a particle dissociating into invisible decay products will lead to the same experimental signature as the here considered production of a $Z\gamma$ pair, with the Z decaying into a pair of neutrinos. Compared to the Standard Model, the production of new particles will generally lead to an excess of events in the high-energy domain of the photon spectrum.

Considering our results for the photon spectrum shown in the lower left plots in Figure 5.3, we again find that the electroweak corrections provide a large negative contribution in the experimentally interesting high-energy domain. The kink at $E^\gamma = 600$ GeV is due to the cut $\eta^{\gamma,c}$ on the rapidity of the final-state photon. This cut restricts the cosine of the photon production angle θ^γ in the laboratory frame to the interval

$$\frac{\exp^{-2\eta^{\gamma,c}} - 1}{\exp^{-2\eta^{\gamma,c}} + 1} < \cos\theta^\gamma < \frac{\exp^{2\eta^{\gamma,c}} - 1}{\exp^{2\eta^{\gamma,c}} + 1}, \tag{5.25}$$

such that for our choice $\eta^{\gamma,c} = 2.5$

$$|\sin\theta^\gamma| = \frac{p_{\mathrm{T}}^\gamma}{E^\gamma} > 0.163071 \approx \frac{1}{6}. \tag{5.26}$$

Since we also applied a cut of $p_{\mathrm{T}}^{\gamma,c} = 100$ GeV on the transverse momentum of the photon, this condition is always fulfilled for $E^\gamma < 600$ GeV and the rapidity cut is for these photon energies never applied. From $E^\gamma = 600$ GeV to higher energies, on the other hand, the rapidity cut will start to exclude more and more events, which leads to a steeper decrease of the Born and NLO distributions. A similar estimate as in (5.24) leads to the conclusion, that the event rates displayed in the lower left plot in Figure 5.3 is large enough for experimental observation up to $E^\gamma = 1$-1.5 TeV. The electroweak corrections are in this domain of the order of -10% to -15%, and will thus cause measurable effects. Note

that this is the first calculation of the electroweak corrections to the photon spectrum of $\nu_l\bar{\nu}_l\gamma$ production, such that one had up to today to rely on QCD-corrected distributions only when comparing the Standard Model predictions to the experimental data. However, due to their negative sign the electroweak corrections reduce the NLO cross-section. If taking only QCD corrections into account to probe for the production of new particles, one might according to our results encounter the situation where an excess of events in the high-energy domain is interpreted to be compatible with the Standard Model predictions and can only be resolved to be due to physics beyond the Standard Model when including the electroweak corrections.

Finally, the lower right plot of Figure 5.3 shows the distribution of the total cross-section in the photon rapidity. In case of two visible photons in the final state, we choose the rapidity of the photon with the largest energy to fill the bins. The electroweak corrections are here of the order of -3 to -5%, and are thus smaller as in the cases discussed so far. This is because a given bin receives here the largest contributions from the low-energy domain of phase-space, where the electroweak corrections are small relative to the Born cross-section. An estimate of the event rate as in (5.24) at e.g. $\eta^\gamma = 2.5$ leads to

$$N_{\mathrm{Ev}} \approx L \times \frac{\mathrm{d}\sigma}{\mathrm{d}\eta^\gamma}\Delta\eta^\gamma = 200\ \mathrm{fb}^{-1} \times 30\ \mathrm{fb}\frac{0.1}{\mathrm{bin}} = \frac{600}{\mathrm{bin}}, \tag{5.27}$$

where $\Delta\eta^\gamma = 0.1/\mathrm{bin}$ is again the bin size. The electroweak corrections contribute with -5% of the Born cross-section, which corresponds to 30 events. The event rates per bin are thus much larger as for the transverse-momentum and energy distributions discussed above. On the other hand, the electroweak corrections are maximally of the size of the systematical error of 5% arising from the determination of the Parton Distribution Functions of the valence quarks. Without any improvement on this error, it is therefore doubtful if the effect of the electroweak corrections on the rapidity distribution presented here can really be seen in the experimental analysis.

Distributions for $P + P \to l + \bar{l} + \gamma$

Turning now to the second $Z\gamma$ production process in (5.1), the distributions for $P + P \to Z\gamma \to l\bar{l}\gamma$, $l = e, \mu$ in the transverse momenta of the final-state and intermediate-state particles as well as in the final-state invariant mass are shown in Figure 5.4. Starting with the distribution in the transverse momentum of the final-state photon in the upper right plot, we attributed the hadronic weight for an event with two visible photons in the final state to the bin corresponding to the transverse momentum of the photon with the largest energy. The distribution exhibits a kink at $p_{\mathrm{T}}^\gamma = 250$ GeV, which arises from a depletion of events due to the cut ΔR^c on the rapidity-azimuthal angle separation (4.8). The phase-space region defined by photon transverse momenta above the kink receives contributions from events with high centre-of-mass energy. As a consequence, the corresponding final state momenta are generally strongly boosted and thus tend to be generated close to each other. For photon transverse momenta above the kink the cut on ΔR thus eliminates

many events, whereas below the kink it is barely effective. Estimating as in (5.24) the number of events to be expected at the LHC, we find observable event numbers in the bins up to $p_{\mathrm{T}}^{\gamma} = 300$-$350$ GeV. As can be seen from the inserted plot, the electroweak corrections contribute in this phase-space region a negative amount of the order of -20% of the Born cross-section, which confirms again the results published in Ref.[37]. The QCD corrections to the distribution in the transverse momentum of the final-state photon have for the process considered here been calculated in Ref.[81]. If applying a jet veto, they are found to lead to a positive contribution of at most 30%. In the NLO cross-section, the contributions arising from the electroweak corrections thus largely cancel the QCD corrections. An inclusion of the electroweak corrections in the experimental analysis is therefore mandatory in order to prevent that a possibly observed excess of events in the high-transverse momentum domain is misinterpreted as a QCD effect.

The transverse-momentum distribution of the Z boson is shown in the upper right plot in Figure 5.4. Since the final state does not contain any neutrinos, the transverse momentum of the Z boson can here be entirely reconstructed from its decay products. For the Born process, the momentum of the Z boson has always to balance the momentum of the final-state photon, such that no events are obtained below the cut on the photon transverse momentum at $p_{\mathrm{T}}^{\gamma,c} = 100$ GeV. The distribution for the Bremsstrahlung process, on the other hand, receives nonzero contributions from events where the transverse momenta of the two final-state bosons balance each other, such that the Z boson can emitted with transverse momentum smaller than $p_{\mathrm{T}}^{\gamma,c}$. In the upper right plot in Figure 5.4, the contributions of such events can be seen in the five bins below $p_{\mathrm{T}}^{Z} < 100$ GeV. The kink at $p_{\mathrm{T}}^{Z} = 250$ GeV can again be explained by the cut ΔR^{c} on the rapidity-azimuthal angle separation (4.8). The size of the electroweak corrections is of the order of -20% in the transverse-momentum region of experimentally observable reaction rates, and will thus provide an important impact on the determination of the gauge-boson couplings.

The distribution in the maximal transverse momentum of the two final-state leptons is displayed in the lower left plot in Figure 5.4. Note that the transverse momentum of the Z boson is divided among the final-state lepton and the final-state anti-lepton. Since in the Born case there are no events with $p_{\mathrm{T}}^{Z} < 100$ GeV, the Born distribution for the maximal lepton transverse momentum starts at $p_{\mathrm{T}}^{l,\mathrm{max}} = 50$ GeV, whereas for the Bremsstrahlung case, one can have events with $p_{\mathrm{T}}^{Z} < 100$ GeV and thus also for $p_{\mathrm{T}}^{l,\mathrm{max}} < 50$ GeV. The drop in the events rate from $p_{\mathrm{T}}^{l,\mathrm{max}} = 100$ GeV towards small values on the x-axis arises from the depletion of events due to the cut on the transverse momentum of the photon. Measurable reaction rates are here obtained up to $p_{\mathrm{T}}^{l} = 250 - 300$ GeV. The electroweak corrections contribute a large negative amount of up to -20% in this domain, and should thus provide an measurable effect on the Standard Model predictions.

Finally, we show the distribution of the cross-section in the final-state invariant mass in the lower right plot in Figure 5.4. The event rate shows here a maximum at about $M_{\mathrm{inv}} = 250$ GeV, which arises from a superposition of the increase of the parton lumi-

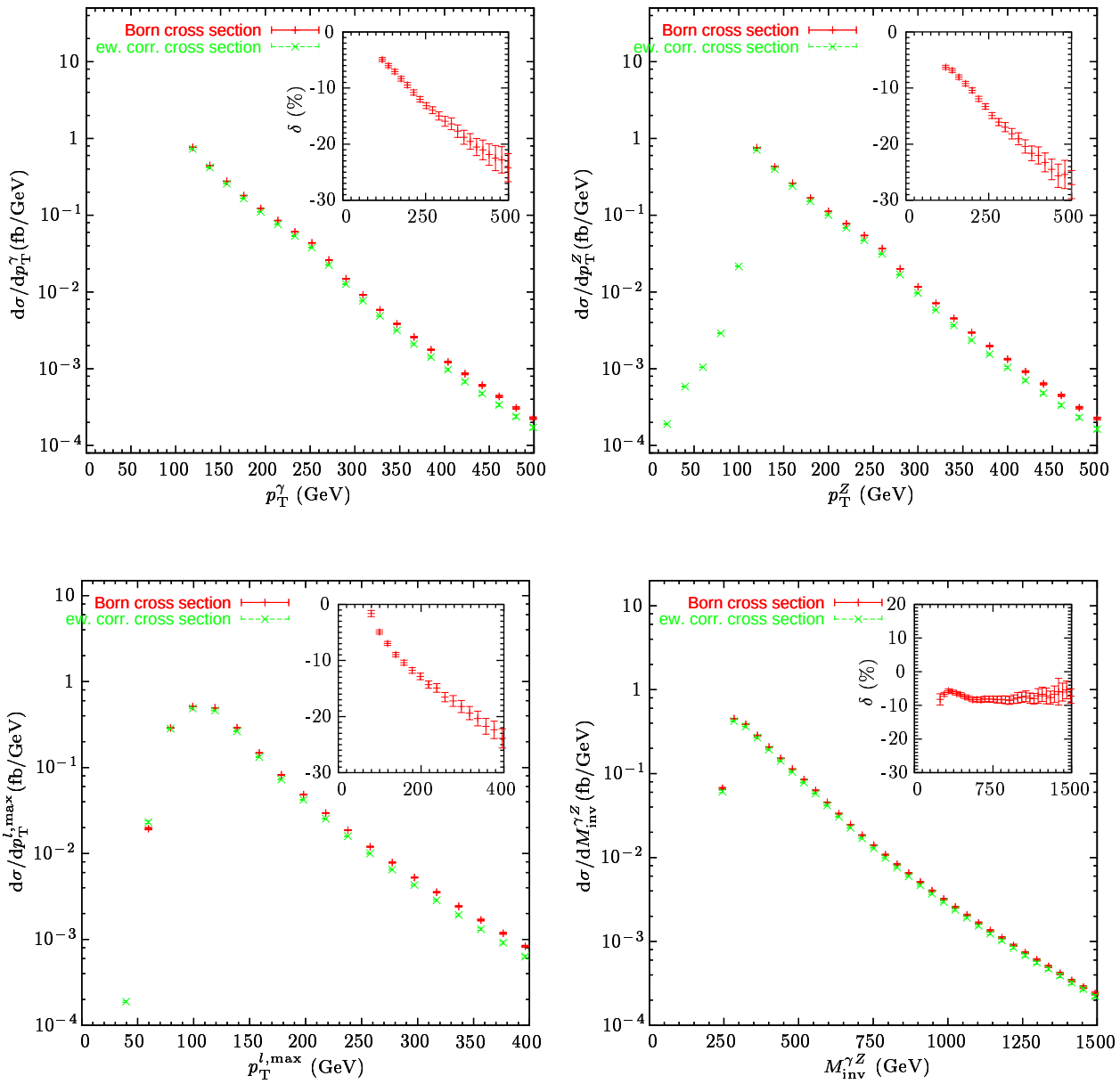

Figure 5.4: The distributions of the Born cross-section and of the 1-loop corrected cross-section for $P + P \to Z\gamma \to l + \bar{l} + \gamma + (\gamma)$, $l = e, \mu$ in dependence of the transverse momentum of the real final-state photon (upper left plot), of the transverse momentum of the intermediate-state Z boson (upper right plot), of the maximal transverse momentum of the two final-state leptons (lower left plot), and of the final-state invariant mass (lower right plot). The inserted plots show the sum of virtual and real corrections in per cent of the Born cross-section. In case of two visible photons in the final state, the hadronic weight was addressed to the bin corresponding to the transverse momentum of the photon with the highest energy.

nosities towards lower energies on one hand and the decrease of the phase-space volume due to the cuts on the final-state momenta on the other hand. An estimate like in (5.24) shows that the experimentally observed event rate should be nonzero up to $M_{\text{inv}} = 750$-1000 GeV. As can be seen from the inserted plot, the electroweak corrections contribute here an negative amount of around -7% of the Born cross-section. Earlier results for the electroweak corrections to the invariant-mass distribution have already been published in Ref.[37], where the authors calculated the corrections to the pair-production process of a photon and an on-shell final-state Z boson, with the real corrections included in the soft and collinear limits only. The authors find here large negative corrections of up to -20% relative to the Born cross-section, which increase in size towards larger invariant masses. Comparing this to our results shown in the lower right plot in Figure 5.4, we rather find the relative size of the virtual and real corrections approaching a plateau with rising energy. The difference to the results of Ref.[37] is caused by large angular-dependend logarithms which arise from events with photons collinear to the beam and which partly compensate the Sudakov logarithms. Such events can be eliminated by a cut on p_T^γ and thus contribute to the high-energy domain of the invariant mass-distribution, but not to the corresponding domain of the photon transverse momentum distribution. Compared to the results published in Ref.[37], the inclusion of real corrections thus reduces the size of the electroweak corrections in the high-energy limits to the same order of magnitude as the systematical error arising from the Parton Distribution Functions. When probing for the effects of anomalous gauge couplings using the invariant-mass distribution, it is therefore doubtful that the electroweak corrections will have a substancial impact on the outcome of the experimental analysis.

The angular distributions for the process $P + P \to Z\gamma \to l\bar{l}\gamma$, $l = e, \mu$ are shown in Figure 5.5. To be specific, the upper left plot contains the Born and electroweak NLO distributions in the photon rapidity, whereas the upper right and the lower left plots display our results for the rapidity distributions of the intermediate-state Z boson as well as of the final-state lepton. The error bars are here larger as compared to the contributions considered so far, which is due to the fact that the phase-space cuts applied to the final-state momenta exclude a larger number of events as e.g. for the $\nu\nu\gamma$ final-state. The relative size of the electroweak corrections to these three distributions can be seen from the inserted plots to be of the order about -5% to -7%, and thus of the same size as the systematical error arising from the Parton Distribution Functions. We therefore do not expect that the electroweak corrections will have a sizable impact on the experimental analysis of the above rapidity distributions.

A more interesting structure is encountered when considering the distribution in the photon-Z rapidity difference shown in the lower right plots in Figure 5.5. The relative first-order corrections are seen to yield a large positive contribution of about 10% to 15% in the bins above $|\Delta\eta^{\gamma Z}| > 4$. However, the large size of the relative corrections is here caused by the smallness of the lowest-order cross-section. The latter is caused by the rapdity cuts on the final state leptons and photons, which eliminate all events with $|\Delta\eta^{\gamma Z}| > 5$. The

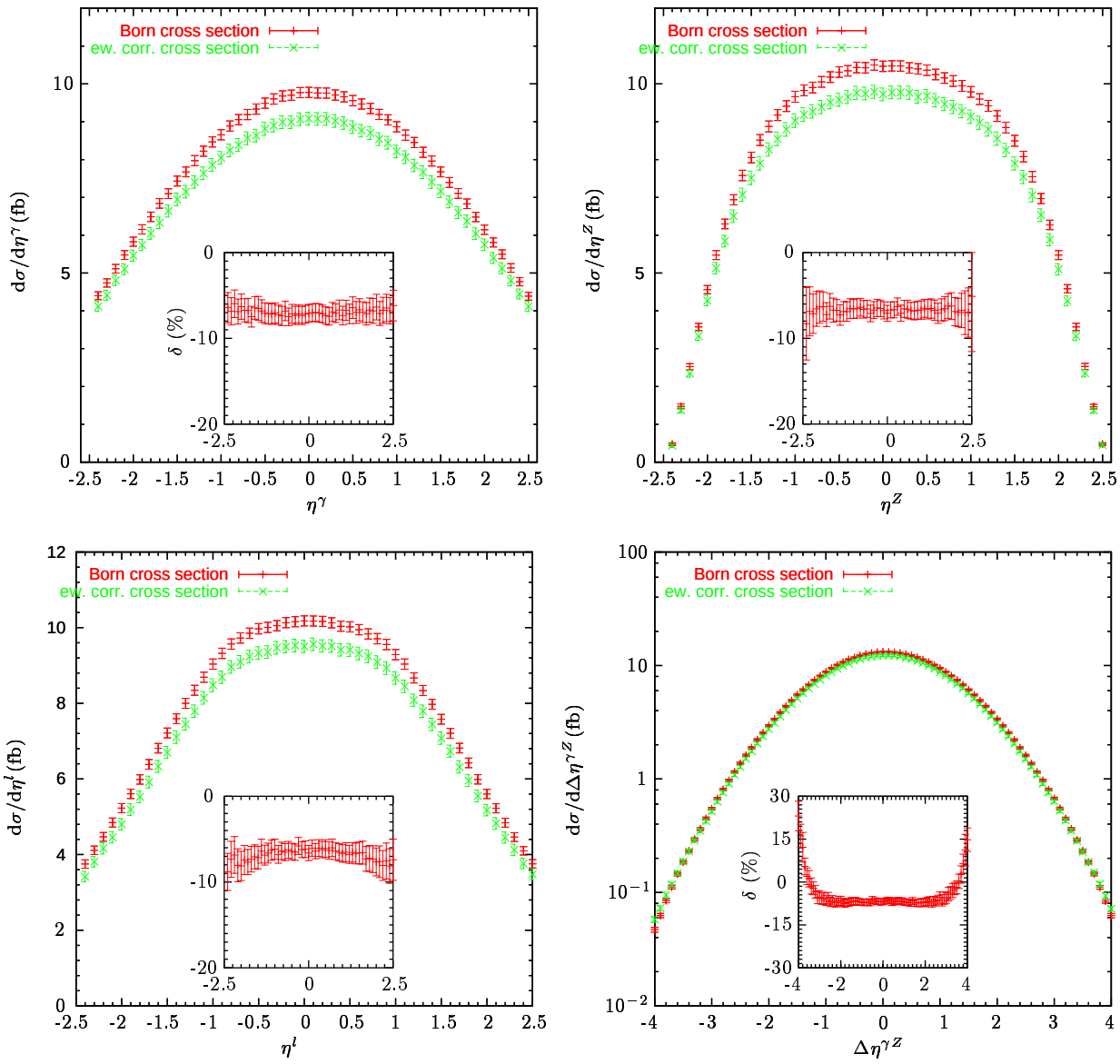

Figure 5.5: The distributions of the Born cross-section and of the 1-loop corrected cross-section for $P + P \to Z\gamma \to l + \bar{l} + \gamma + (\gamma)$, $l = e, \mu$ in dependence of photon rapidity (upper left plot), in the rapidity of the intermediate-state Z boson (upper right plot), in the rapidity of the final-state lepton (lower left plot), and the rapidity difference of the final-state photon and the decaying Z boson (lower right plot). The inserted plots show the sum of virtual and real corrections in per cent of the Born cross-section. In case of two visible photons in the final state, the hadronic weight is addressed to the bin corresponding to the rapidity of the photon with the highest energy.

bins at $|\Delta\eta^{\gamma Z}| = 4$ collect only $\mathrm{d}\sigma/\mathrm{d}\Delta\eta^{\gamma Z} \approx 10^{-1}$ fb of data, such that the event rate expected at the LHC can be estimated as in (5.27) to be

$$N_{\mathrm{ev}} \approx L \times \frac{\mathrm{d}\sigma}{\mathrm{d}\Delta\eta^{\gamma Z}} \Delta(\Delta\eta^{\gamma Z}) = 200\ \mathrm{fb}^{-1} \times 10^{-1}\ \mathrm{fb} \frac{0.1}{\mathrm{bin}} = \frac{2}{\mathrm{bin}}, \tag{5.28}$$

which is too small for experimental observation.

Distributions for $P + P \to l + \bar{\nu}_l + \gamma$

Turning next to the processes related to $W\gamma$ production, we show in Figure 5.6 the distributions for the process $P + P \to W\gamma \to l + \bar{\nu}_l + \gamma + (\gamma)$, $l = e, \mu$ in the transverse momentum of the final-state photon, in the transverse momentum of the final-state lepton, in the missing transverse momentum, as well as in the transverse mass of the final-state neutrino-lepton pair. Starting with the transverse-momentum distribution of the photon in the upper left plot in Figure 5.6, an estimate as in (5.24) shows that the event rate should be observable up to $P_{\mathrm{T}}^{\gamma} = 300$-$400$ GeV. An analysis of the effects of the electroweak corrections on this distribution has already been published in Ref.[36]. Here the authors calculate the hadronic cross-section under consideration of the W-boson decay, but include only the leading logarithmic virtual electroweak corrections for the production subprocess in the high-energy regime. For the transverse-momentum distribution of the photon, the authors find a large negative corrections which can reach up to -15% at $p_{\mathrm{T}}^{\gamma} = 400$ GeV.

As can be seen from the inset diagram in the upper left plot in Figure 5.6, we are able to confirm this result. The inclusion of the full Bremsstrahlung process, of the non-leading logarithms contributing to the virtual corrections as well as of the corrections to the decay subprocess is seen to slightly reduce the size of the virtual corrections. At $p_{\mathrm{T}}^{\gamma} = 400$ GeV, the electroweak corrections are found to contribute a negative amount of about -12% of the Born cross-section, which is well above the systematical and statistical errors. The QCD-corrections to the transverse-momentum distribution of the photon have for the process considered here been analysed in Ref.[32]. If applying a jet veto, the authors obtain large positive corrections of up to 60% of the Born cross-section for low transverse momenta, which decrease to a negative amount of -5% to -10% of the Born cross-section at $p_{\mathrm{T}}^{\gamma} = 400$ GeV. For high transverse momenta, the electroweak corrections are thus of the same order of magnitude or even larger than the QCD-corrections, and reduce the NLO distribution in addition to the decrease arising from the QCD-corrections. Again, the phase-space region where the transverse momentum of the photon is large is also the phase-space region where the effects of the anomalous coupling constants contribute most, such that an analysis of the experimental data including only QCD-corrections will lead to an overestimate of the Standard Model background.

The upper right and the lower left plots in Figure 5.6 show our results for the distributions of the hadronic cross-section in the missing transverse momentum and the transverse mo-

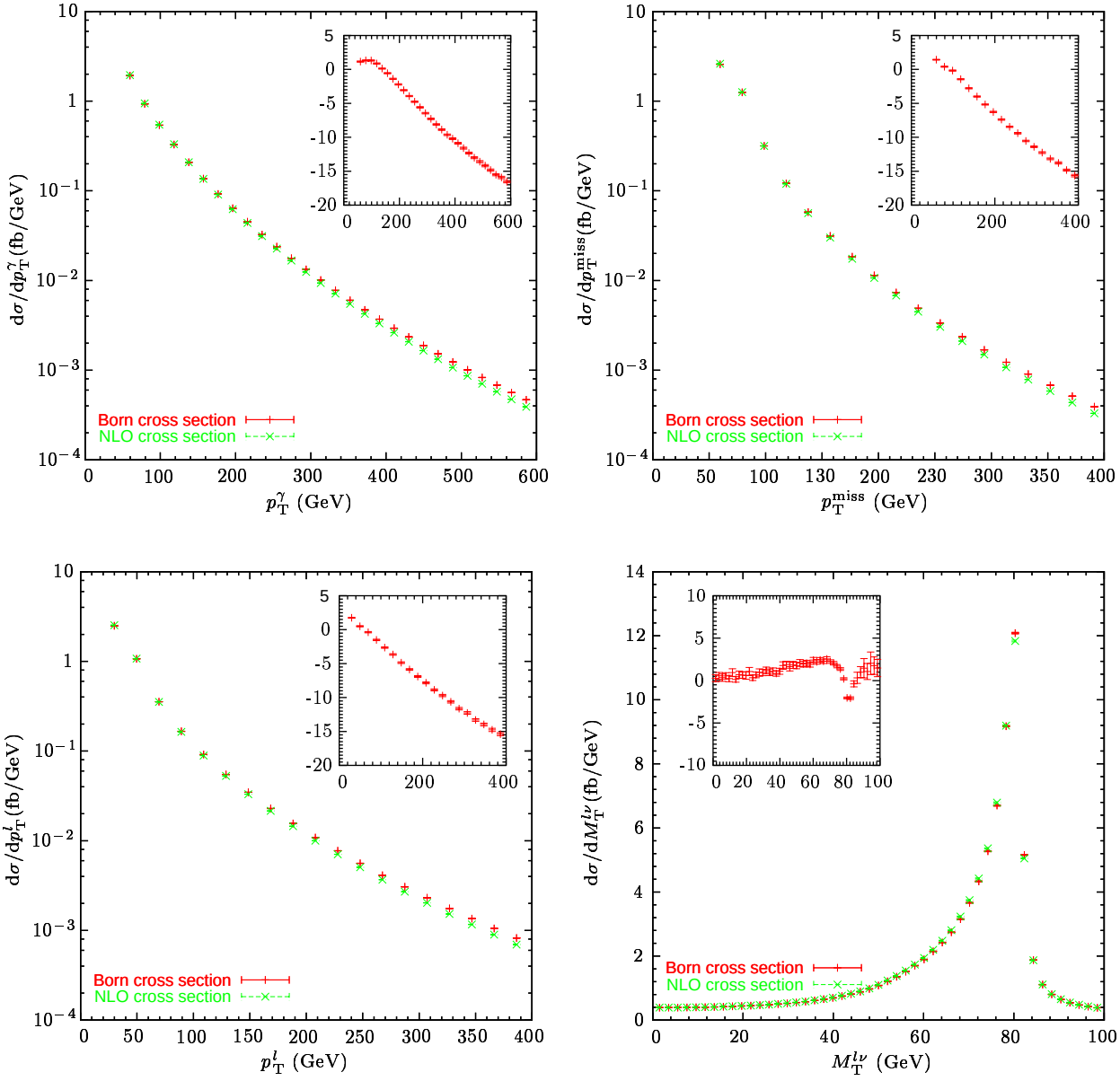

Figure 5.6: The distributions of the Born cross-section and for the 1-loop corrected cross-section for $P + P \to W\gamma \to l + \bar{\nu}_l + \gamma + (\gamma)$, $l = e, \mu$ in dependence of the transverse momentum of the final-state photon (upper left plot), the missing transverse momentum (upper right plot), the transverse momentum of the final-state lepton (lower left plot), and the transverse mass (lower right plot). The inserted plots show the size of the electroweak corrections in per cent of the Born cross-section. In case of two visible photons in the final state, the hadronic weight is addressed to the bin corresponding to the transverse momentum of the photon with the highest energy.

mentum of the final-state lepton. Compared to the corresponding photon distribution, the curves are shifted to lower transverse momenta. This is due to the fact that the photon transverse momentum for the process considered here is shared between the final-state lepton and the final-state neutrino. The event rates can be estimated as in (5.24) to be observable up to $p_{\mathrm{T}}^{\mathrm{miss}}, p_{\mathrm{T}}^{l} = 200\text{-}300$ GeV. The electroweak corrections contribute about -10% in this domain, and should thus lead to a measurable modification of the Standard Model predictions.

In the lower right plot in Figure 5.6, we display our results for the distribution of the hadronic cross-section in the transverse mass of the final-state lepton-neutrino pair as defined in (5.20). The curves terminate at the cut value $M_{\mathrm{T,c}}^{l\nu} = M_W + 20$ GeV ≈ 100.4 GeV. The W resonance can here be observed as a pronounced peak, an effect which could in principle be used for an experimental determination of the W mass. However, to do so one will in practice rather rely on the transverse-mass distribution of single W-production processes owing to the much higher reaction rates. The electroweak corrections can be seen from the inserted plot to contribute most at the peak, where they provide an amount of -3% of the Born cross-section and are thus probably too small to influence the experimental analysis.

Finally, the distributions for $P + P \to W\gamma \to l + \bar{\nu}_l + \gamma + (\gamma)$, $l = e, \mu$ in the rapidities of the final-state particles are shown in Figure 5.7. As was said in the introduction, the angular distributions for $W\gamma$ pair production have the experimentally interesting property of exhibiting a so-called radiation zero, i.e. there is a kinematical configuration where all tree-level helicity amplitudes of the parton process are exactly zero. To be explicit, the radiation zero appears at

$$\cos\hat{\theta}^{\gamma} = \frac{Q_u + Q_d}{Q_u - Q_d} = \frac{1}{3}, \tag{5.29}$$

where $\hat{\theta}$ is the production angle of the photon in the partonic centre-of-mass frame, and Q_u and Q_d denote the charge of the up-quark and the down-quark, respectively. In experiment, the radiation zero should be observable as a dip in the rapidity distributions for $W\gamma$ pair production. From a phenomenological point of view, it arises from gauge cancellations between the contributions of u-channel, t-channel, and s-channel Born diagrams, and only occurs in the Standard Model. As a consequence, any deviation of a theory describing the fundamental interactions of nature from the gauge structure of the Standard Model tends to fill the resulting dip in the angular distributions, such that an analysis of the radiation zero provides an excellent opportunity to probe for new physics.

In the upper left plot in Figure 5.7, we display our results for the rapidity distribution of the final-state photon. For a Bremsstrahlung event involving two detectable final-state photons, we choose again the rapidity of the photon with the largest energy to address the corresponding hadronic weight to a bin. However, the distribution shows no dip or decrease in the leading-order cross-section which could hint towards the existence of a ra-

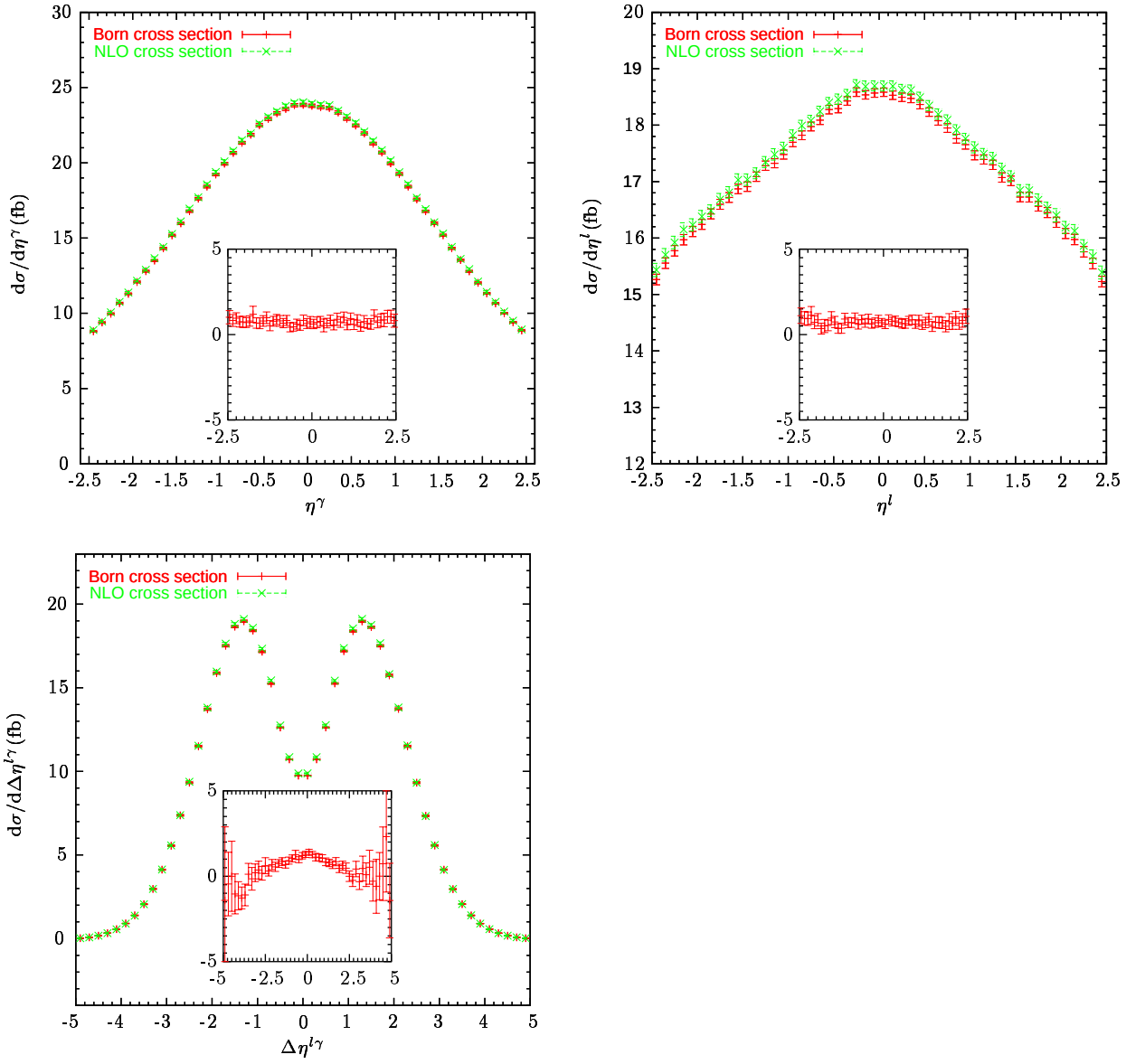

Figure 5.7: Distribution of the Born cross-section and for the 1-loop corrected cross-section for $P + P \to W\gamma \to l + \bar{\nu}_l + \gamma + (\gamma)$, $l = e, \nu$ in dependence of the rapidity of the real final-state photon (upper left plot), the rapidity of the final-state lepton (upper right plot), and the rapidity difference of the final-state lepton and the final-state photon (lower left plot). The inserted plots show the sum of virtual and real corrections in per cent of the Born cross-section. In case of two visible photons in the final state, the rapidity of the photon with the largest energy was used to fill the bins.

diation zero. The reason for this is that besides from non-standard gauge-couplings, there are unfortunately many other effects which tend to fill the dip arising from the radiation zero. One of these effects arises from the fact that in a hadronic reactions, the experiments do not measure the rapidity $\hat{\eta}^\gamma$ of the photon in the partonic centre-of-mass system, but rather the corresponding rapidity η^γ in the hadronic system. The latter is connected to the production angle (5.29) via a boost

$$\eta^\gamma = \frac{1}{2}\log\frac{1+\cos\hat{\theta}^\gamma}{1-\cos\hat{\theta}^\gamma} - \frac{1}{2}\log\frac{x_2}{x_1}, \tag{5.30}$$

where x_1, x_2 denote the partonic energy fractions. The evaluation of the hadronic cross-section involves the partonic amplitudes evaluated at many different centre-of-mass energies, which according to (5.30) exhibit each the radiation zero at a different phase-space point. As a consequence, it can be seen from the upper left plot in Figure 5.7 that the radiation zero is completely washed out in the distribution of the laboratory-frame photon rapidity. The same effect prevents the observation of the radiation zero in the rapidity distribution of the final-state lepton shown in the upper right plot in Figure 5.7. In both distributions, the electroweak corrections provide a positive contribution of about 1-2% of the Born cross-section, which is to small compared to the systematical errors to have a observable impact on the analysis of the experimental data. The smallness of the corrections has again its origin in the fact that a given bin in the above rapidity distributions receives the main contributions from the low-energy domain of phase-space, where the electroweak corrections are small.

On the other hand, the measured rapidity of a given final-state particle depends on the boost to the laboratory frame only via the logarithm in the last term of (5.30). Since this term appears independently of the considered particle, an option to eliminate the above boost effects and thus to restore the radiation zero is to consider rapidity differences. For the process considered here, the best observable is in this respect given by the distribution in the rapidity difference of the intermediate-state W boson and the final-state photon, which is expected to exhibit the exact radiation zero. However, this exact zero of the Born distribution is generally smeared out to a dip due to finite-width effects. Furthermore, the W decays into a lepton and an unobservable neutrino, such that the W rapidity in the laboratory frame cannot be measured directly. If trying to reconstruct the W rapidity from the measured kinematical properties of the final-state photon and the final-state lepton, one ends up with two solutions, and it is impossible to decide which of the two is the correct one.

As a consequence, the best one can do is to consider the distribution of the rapidity difference $\Delta\eta^{l\gamma} = \eta^l - \eta^\gamma$ of the final-state photon and the final-state lepton. Earlier studies of this rapidity difference distribution for $W\gamma$-production at the LHC [11, 32] have shown that the Born distribution exhibits a pronounced dip at $\Delta\eta^{l\gamma} = 0$. This structure has its origin in the above-mentioned two possibilities for the direction of the initial-state quarks. If plotted separately, the contributions corresponding to the two quark directions will show

two dips symmetrically situated around zero. Since the total hadronic cross-section is obtained by summing over the two parton directions, the corresponding contribution leads to a superposition of the two curves, which then has its minimum at $\Delta\eta^{l\gamma} = 0$.

However, it is shown in Ref.[11, 32] that the QCD corrections generally enhance the cross-section at the radiation zero. Depending on the process definition, the effect can be quite dramatic. If no jet veto is applied, the dip arising from the radiation zero is completely washed out. If selecting only events without final-state jets, the situation is somewhat better, but the statistics is considerably reduced and the QCD corrections at the radiation zero still enhances the cross-section by a factor of two. On the other hand, it has been shown in Ref. [36] that the electroweak corrections contribute a negative amount of -7% at $\Delta\eta^{l\gamma} = 0$, and thus lead to a slightly more pronounced dip. However, as was said above the authors take here only into account the leading logarithmic virtual corrections to the production process, without considering the real corrections. At this point, the question arises how the inclusion of the full Bremsstrahlung contributions as well as the full virtual corrections influence the analysis of the radiation zero. We show our results for the Born and NLO distributions of the hadronic cross-section in the lower left plot of Figure 5.7. In both distributions, the effects of the radiation zero is clearly visible as a dip at $\Delta\eta^{l\gamma} = 0$. However, it can be seen from the inset plot that the electroweak corrections at the dip provide a positive contribution of about 3% of the Born cross-section, and thus tend to fill the dip additionally to the QCD corrections. This effect arises again from the contributions of events involving the emission of a hard Bremsstrahlung photon, which generally lead to an enhancement of the real corrections wherever the Born cross-section is small. However, the size of the electroweak corrections is below the expected systematic error arising from the Parton Distribution functions, and leads to an enhancement of the leading-order cross-section which is a factor of 100 smaller as the increase due to the QCD corrections. For the experimental analysis of the radiation zero, the inclusion of QCD corrections should therefore be sufficient to obtain reliable results.

5.4 Conclusions and Outlook

To summarize our work, we have designed the Mathematica package `Pole` which can be employed to automatically generate the amplitudes for the radiative corrections to a given process in Leading Pole Approximation. As an output, our program returns a `Fortran` program, which can be used to integrate the generated amplitudes over phase-space. In our work, we applied `Pole` to the calculation of the electroweak corrections to $W\gamma$ and $Z\gamma$ pair-production processes. The decay of the W and the Z boson are included by considering the full matrix elements for the production of two leptons and a photon. Furthermore, the real corrections were taken into account by generating the exact matrix elements for the corresponding processes with an additional photon in the final state. The Bremsstrahlung processes were treated inclusive, i.e. the momentum of the corresponding photon was integrated over the full phase-space defined by the cut conditions. To cancel

the soft and collinear singularities, our program incorporates both, the subtraction method and the phase-space slicing technique, which we cross-checked to confirm our results. As discussed in Section 5.2, we tested the implementation of our approach extensively. The matrix elements for the Born cross-section, the real corrections and the non-factorizable virtual corrections were checked by a comparison to additionally performed by-hand calculations, whereas the amplitudes for the virtual corrections were tested by comparing to `FormCalc4`. A numerical check of our results for the finite virtual corrections was possible by comparing to the numerical values published in Ref.[36]. As a first result, we found that the High-Energy Approximation as used by the authors of Ref.[36] to calculate the virtual corrections may lead to an error of up to 5% relative to the Born cross-section, an effect which was shown in Section 5.2 to arise from neglecting purely angular-dependent logarithms.

In Section 5.3, we presented numerical results for the electroweak corrections to the cross-sections and experimentally interesting distributions for the processes $P + P \to Z\gamma \to \nu_l \bar{\nu}_l \gamma(+\gamma)$, $l = e, \mu, \tau$, $P + P \to Z\gamma \to l\bar{l}\gamma(+\gamma)$ $l = e, \mu$, and $P + P \to W\gamma \to l\bar{\nu}_l\gamma(+\gamma)$ $l = e, \mu$. For the total cross-sections, we found that the electroweak corrections to all three processes lead to small negative contributions of -2% to -5%. Compared to an estimate of the systematical error to be expected at the LHC, the size of the electroweak corrections on the total hadronic cross-section has been found to be too small to have an observable impact on the experimental analysis.

The same conclusion can be drawn from our results for the angular distributions of the hadronic cross-section. As a general feature, we here found that the electroweak corrections to the rapidity distributions of the final-state and intermediate-state particles provides a contributions of only a few per cent of the Born cross-section, which is again too small to be experimentally observed. As an observable of special experimental interest, we studied the distribution for the $W\gamma$ production process in the lepton-photon rapidity difference. The Born distribution is here predicted by the Standard Model to exhibit a pronounced dip due to the radiation zero of the corresponding partonic amplitudes. Since this dip is generally not present in Models incorporating a gauge sector different from the Standard Model, it provides an excellent opportunity to test the gauge structure of the fundamental interactions in nature. The QCD corrections to the rapidity difference distribution tend generally to fill the dip, whereas previous results for the virtual electroweak corrections were obtained to be negative, and thus to lead to a slightly more pronounced effect. However, we were able to show that the inclusion of Bremsstrahlung contributions overcompensates the effects of the virtual corrections, such that the full electroweak corrections also tend to fill the dip in the rapidity difference distributions. However, compared to the QCD corrections, the size of the electroweak corrections is negligible, such that the situation does not become much worse.

A further interesting observable is given by the invariant-mass distribution for the process $P + P \to Z\gamma \to \nu_l \bar{\nu}_l \gamma(+\gamma)$, $l = e, \mu, \tau$. The high-energy tail of this distribution provides an

excellent opportunity to probe for new physics due to a low Standard Model background. For example, models with anomalous gauge-boson couplings predict compared to the Standard Model an excess of events in the high-energy domain. Earlier calculations showed that the virtual electroweak corrections might in this domain reduce the Standard Model leading-order prediction by several tens of per cent. However, we found that an inclusion of real corrections reduces this effect considerably, and that the resulting correction does not exceed an amount of -7% of the Born cross-section. Accordingly, when using the invariant-mass distribution to study anomalous gauge-boson couplings, the comparison of the experimental data to the QCD-corrected Standard Model predictions should be sufficient to obtain reliable results.

On the other hand, another set of observables often used to probe for anomalous gauge-boson couplings are given by the distributions in the transverse momenta and energies of the final-state and intermediate-state particles in $W\gamma$ and $Z\gamma$ pair-production processes. Again, the existence of gauge couplings not contained in the Standard Model is predicted to cause an excess of events in the high-energy region of these distributions. According to our results, the electroweak corrections can reach up to -20% in this domain, and are thus of the same size or even larger as the QCD corrections. An inclusion of the electroweak corrections is thus mandatory in order to prevent a misinterpretation of the experimentally observed reaction rates. Similar results were obtained from our analysis of the photon spectrum for the $\nu_l\bar{\nu}_l\gamma$ final state, an experimental observable often used to probe for the production of so far unknown particles not contained in the Standard Model, as e.g. the gravitino. The production of such a particle will lead to an excess of events in the high-energy tail of the photon spectrum, where we found the electroweak corrections to be of the order of -15% of the Born cross-section. In the experimental analysis, the electroweak corrections thus considerably reduce the size of the Standard Model background, and therefore improve the prospects of finding effects of the production of so far unobserved particles.

As was said in Chapter 3 and Chapter 4, our computer package `Pole` was designed to work largely independent of the considered process. As a consequence, our work opens the possibility to study a large variety of future projects. As a first step, our package has further to be tested by applying it to other processes like WW, WZ, or ZZ production. To be able to compare the effects of the electroweak corrections and the QCD corrections directly, it would furthermore be desirable to incorporate both in a single phase-space generator. Using `Pole`, the amplitudes for the virtual QCD corrections can be generated by switching to the `FeynArts` QCD model file. However, in the numerical evaluation the infrared divergences cannot be regularized by a gluon mass, since the latter breaks generally gauge invariance. Accordingly, the evaluation of the virtual corrections has to be modified to regularize the infrared and collinear singularities by means of dimensional regularization. In addition, a proper treatment of the QCD Bremsstrahlung effects like e.g. final-state jets has to be implemented. A further improvement would be the use of QED-corrected parton distribution functions in the calculation of the electroweak corrections, which, however, requires the consideration of Bremsstrahlung processes with photonic ini-

tial states. To be able to directly analyze the effects of the radiative corrections on the analysis of vector-boson pair-production processes in terms of anomalous coupling constants, a generic implementation of the latter by e.g. defining a corresponding `FeynArts` model file would be a further improvement. Finally, since `Pole` was designed to work not only independent of the considered process but also of the considered model, it can in principle also be applied to obtain the predictions for vector-boson pair production in models different from the Standard Model, as e.g. the MSSM.

Appendix A

The Weyl-van der Waerden Formalism

To motivate the use of the Weyl-van der Waerden (WvdW) formalism, consider the amplitude for some given process. In the case of a one-loop amplitude, we assume that internal fermion traces and tensor integrals have already been reduced to scalar expressions, such that we can decompose the amplitude into products of fermion chains F_i and scalar prefactors C_i

$$\mathcal{A} = \sum_{i=1}^{N} C_i F_i, \tag{A.1}$$

where the general form of a product of fermion chains F_i is given by

$$F_i = \langle \overline{\Psi}_{p_1} | \Gamma^{i,1}_{\mu_{r_1},\ldots,\mu_{s_1}} | \Psi_{p_2} \rangle \times \ldots \times \langle \overline{\Psi}_{p_{n-1}} | \Gamma^{i,n}_{\mu_{rn},\ldots,\mu_{sn}} | \Psi_{p_n} \rangle. \tag{A.2}$$

Here, Ψ_p denotes the Dirac spinor of an external Fermion with momentum p, and the matrices Γ are generally products of Dirac matrices $\gamma_{\mu_{r_j}}$ and γ_5 as well as Dirac matrices $\not{q}$ contracted with 4-vectors or with the totally antisymmetric epsilon tensor in four dimensions. Of course, all open Lorentz indices $\mu_{r_1}, \ldots, \mu_{s_n}$ are contracted within one product of fermion chains. Using the usual trace techniques to evaluate the cross section of the considered process, the amplitude is squared and summed the helicities $\{\sigma_l\}$ of the external particles

$$\sum_{\{\sigma_l\}} |\mathcal{A}^{\sigma_1,\ldots,\sigma_n}|^2 = \sum_{i,j=1}^{N} C_i C_j^\star \sum_{\{\sigma_l\}} F_i \overline{F}_j. \tag{A.3}$$

and the helicity-summed product $F_i \overline{F}_j$ is re-written as a product of traces

$$\begin{aligned}
\sum_{\{\sigma_l\}} F_i \overline{F}_j &= \langle \overline{\Psi}_{p_1} | \Gamma^{i,1}_{\mu_{r_1},\ldots,\mu_{s_1}} | \Psi_{p_2} \rangle \langle \overline{\Psi}_{p_2} | \overline{\Gamma}^{j,1}_{\mu_{r'_1},\ldots,\mu_{s'_1}} | \Psi_{p_1} \rangle \times \ldots \\
&\qquad \ldots \times \langle \overline{\Psi}_{p_{n-1}} | \Gamma^{i,n}_{\mu_{rn},\ldots,\mu_{sn}} | \Psi_{p_n} \rangle \langle \overline{\Psi}_{p_n} | \overline{\Gamma}^{j,n}_{\mu_{r'_n},\ldots,\mu_{s'_n}} | \Psi_{p_{n-1}} \rangle \\
&= \mathrm{tr}\left[\Gamma^{i,1}_{\mu_{r_1},\ldots,\mu_{s_1}} (\not{p}_2 - m_2) \overline{\Gamma}^{j,1}_{\mu_{\mu_{r'_1}},\ldots,\mu_{\mu_{s'_1}}} \right] \times \ldots \times \mathrm{tr}\left[\Gamma^{i,n}_{\mu_{rn},\ldots,\mu_{sn}} (\not{p}_n - m_n) \overline{\Gamma}^{j,n}_{\mu_{r'_n},\ldots,\mu_{s'_n}} \right],
\end{aligned} \tag{A.4}$$

where m_i denotes the mass of the external particle with momentum p_i. Given N products of fermion chains F_i, one has therefore to evaluate $\mathcal{O}(N^2)$ traces to evaluate the squared amplitude numerically. Since the number N of products of fermion chains rises with the number of external particles of the considered process, this can be quite costly in CPU time for processes involving many-particle final states. It would therefore be preferable to evaluate the amplitude (A.1) numerically *before* taking the square, such that one has just to square a complex number to evaluate the cross section of the given process.

The basic idea of the WvdW formalism is now to reduce all objects belonging to higher-dimensional representations of the Lorentz group into so-called *covariant spinors* ψ_A and *contravariant spinors* $\psi^{\dot{A}}$, which belong to the irreducible representations $D(\frac{1}{2},0)$ and $D(0,\frac{1}{2})$, respectively. In this way it is possible to express the fermion chains (A.2) in terms of products of spinors belonging to these representations, and one is left with the numerical evaluation of N fermion chains rather than $\mathcal{O}(N^2)$ traces.

To see how this works in detail, note that the transition between these non-equivalent two-dimensional representations is achieved by complex conjugation and a similarity transformation mediated by the matrix

$$\epsilon_{AB} = \epsilon^{AB} = \epsilon_{\dot{A}\dot{B}} = \epsilon^{\dot{A}\dot{B}} = \begin{pmatrix} 0 & 1 \\ -1 & 0 \end{pmatrix}, \tag{A.5}$$

such that

$$\psi^A = (\epsilon^{\dot{A}\dot{B}}\psi_{\dot{B}})^\star, \qquad \psi_{\dot{A}} = (\psi^B \epsilon_{BA})^\star. \tag{A.6}$$

A basis of the irreducible representations $D(\frac{1}{2},0)$ and $D(0,\frac{1}{2})$ is given by

$$\sigma^\mu = (\mathbb{1}, -\boldsymbol{\sigma}), \qquad \overline{\sigma}^\mu = (\mathbb{1}, \boldsymbol{\sigma}), \tag{A.7}$$

respectively, where here and in the following $\sigma^a,\ a = 1\ldots 3$ are the standard Pauli matrices. The so-called spinor metric ϵ defines how to raise and lower spinor indices

$$\psi^A = \epsilon^{AB}\psi_B, \qquad \psi_A = \psi^B\epsilon_{BA}, \qquad \psi^{\dot{A}} = \epsilon^{\dot{A}\dot{B}}\psi_{\dot{B}}, \qquad \psi_{\dot{A}} = \psi^{\dot{B}}\epsilon_{\dot{B}\dot{A}}, \tag{A.8}$$

and provides the Lorentz-invariant as well as antisymmetric spinor products

$$\langle\phi\psi\rangle = \epsilon^{AB}\phi_A\psi_B = \phi_1\psi_2 - \phi_2\psi_1, \qquad \langle\phi\psi\rangle^\star = \epsilon_{\dot{A}\dot{B}}\phi^{\dot{A}}\psi^{\dot{B}} = (\phi_1\psi_2 - \phi_2\psi_1)^\star. \tag{A.9}$$

Considering an arbitrary Minkowski 4-vector p_μ, such an object belongs to the representation $D(\frac{1}{2},\frac{1}{2}) = D(\frac{1}{2},0)\otimes D(0,\frac{1}{2})$ of the Lorentz group. It is therefore associated with a two-by-two matrix K with one dotted and one undotted index

$$P_{A\dot{B}} = p_\mu\sigma_{\mu A\dot{B}} = \begin{pmatrix} p^0+p^3 & p^1+\mathrm{i}p^2 \\ p^1-\mathrm{i}p^2 & p^0-p^3 \end{pmatrix}, \tag{A.10}$$

where the indices can again be raised and lowered according to (A.8). In order to express this matrix in terms of Weyl spinors, one uses the fact that P is hermitian and can therefore be decomposed in terms of its eigenvectors and eigenvalues

$$P_{\dot{A}B} = \sum_{i=1,2} p_{i\dot{A}} p_{i,B}, \tag{A.11}$$

where

$$\lambda_{1,2} = p^0 \pm |\mathbf{p}|, \qquad p_{1,A} = \sqrt{\lambda_1} \begin{pmatrix} \mathrm{e}^{-\mathrm{i}\Phi} \cos\frac{\theta}{2} \\ \sin\frac{\theta}{2} \end{pmatrix}, \qquad p_{2,A} = \sqrt{\lambda_2} \begin{pmatrix} \sin\frac{\theta}{2} \\ -\mathrm{e}^{\mathrm{i}\Phi} \cos\frac{\theta}{2} \end{pmatrix}, \tag{A.12}$$

and θ as well as Φ denote the polar and azimuthal angles of the euclidean vector $\mathbf{p}$. Note that for $p^2 = 0$ the eigenvalue λ_2 and thus the momentum spinor p_2 vanish and the composition (A.11) contains just the momentum spinor p_1.

Turning next to fermionic wave functions, one can use the fact that a Dirac spinor belongs to the representation $D(\frac{1}{2},0) \oplus D(0,\frac{1}{2})$ of the Lorentz group, such that it can be written as a vector with two spinor-valued entries

$$\Psi = \begin{pmatrix} \phi_A \\ \psi^{\dot{A}} \end{pmatrix}. \tag{A.13}$$

For Ψ to be a solution of the Dirac equation

$$(\mathrm{i}\partial\!\!\!/ - m)\Psi = 0, \tag{A.14}$$

it has to be of plane-wave type $\Psi^{\pm} = \exp(\mp \mathrm{i}px)\Psi^{\pm}_{p,\sigma}$, where $p^2 = m^2$ is the squared mass of the considered fermion, and the spinor components of Ψ_p are given as the solution of a system of two coupled two-dimensional matrix equations

$$P_{A\dot{B}}\psi^{\pm,\dot{B}}_{p,\sigma} = \pm m\phi^{\pm}_{p,\sigma A}, \qquad P^{\dot{A}B}\phi^{\pm}_{p,\sigma B} = \pm m\psi^{\pm,\dot{A}}_{p,\sigma}. \tag{A.15}$$

We here used for the Dirac matrices γ^μ the chiral representation

$$\gamma^\mu = \begin{pmatrix} 0 & \sigma_{\mu A\dot{B}} \\ \overline{\sigma}_\mu{}^{\dot{A}B} & 0 \end{pmatrix} \qquad \gamma^5 = \mathrm{i}\gamma^0\gamma^1\gamma^2\gamma^3 = \begin{pmatrix} \sigma^0 & 0 \\ 0 & -\sigma^0 \end{pmatrix}. \tag{A.16}$$

The solutions of the system (A.15) can easily be constructed to read

$$\Psi^{\pm}_{p,\sigma} = \begin{pmatrix} \phi^{\pm}_{p,\sigma A} \\ \psi^{\pm\dot{A}}_{p,\sigma} \end{pmatrix} = \begin{pmatrix} p_{1A}\delta_{\sigma\pm} \pm p_{2A}\delta_{\sigma\mp} \\ p_1^{\dot{A}}\delta_{\sigma\mp} \mp p_2^{\dot{A}}\delta_{\sigma\pm} \end{pmatrix}, \tag{A.17}$$

where $\Psi^{+}_{p,\sigma}$ denotes an incoming fermion field of momentum p and helicity σ, whereas $\Psi^{-}_{p,\sigma}$ is the Dirac spinor of the corresponding outgoing anti-fermion. The expression for the adjoint spinor $\overline{\Psi} = \Psi^\dagger\gamma_0$ takes the form

$$\overline{\Psi}^{\pm}_{p,\sigma} = \left(\psi^{\pm A}_{p,\sigma}, \phi^{\pm}_{p,\sigma\dot{A}}\right) = \left(p_1^A\delta_{\sigma\mp} \mp p_2^A\delta_{\sigma\pm}, p_{1\dot{A}}\delta_{\sigma\pm} \pm p_{2\dot{A}}\delta_{\sigma\mp}\right), \tag{A.18}$$

where $\overline{\Psi}^{+}_{p,\sigma}$ and $\overline{\Psi}^{-}_{p,\sigma}$ are the Dirac spinors of an outgoing fermion and an incoming anti-fermion, respectively.

Finally, the decomposition of polarization vectors in terms Weyl spinors remains to be done. Since a spin-1 field transforms like an ordinary 4-vector under Lorentz transformations, one expects that the corresponding polarization vector ε^{μ} is related to a two-by-two matrix $\varepsilon_{A\dot{B}}$ as described above for a general 4-vector p^{μ}. However, in contrast to a 4-momentum, a polarization vector generally has complex entries, such that the corresponding two-by-two matrix does not need to be hermitian. The dynamics of a spin-1 field is given by Proca's equation,

$$\left[\left(\partial^2 + m^2\right) g^{\mu\nu} - \partial^{\mu}\partial^{\nu}\right] V_{\nu} = 0, \tag{A.19}$$

and the plane-wave ansatz $V_{\mu} = \varepsilon_{\mu} \exp(\mp \mathrm{i} p x)$ leads to the condition

$$P^{A\dot{B}} \varepsilon_{A\dot{B}} = 0. \tag{A.20}$$

For massive spin-1 fields, this equation has three independent solutions, which correspond to the three helicity eigenstates

$$\varepsilon_{\dot{A}B}(p) = \frac{\sqrt{2}}{M} p_{2\dot{A}} p_{1B} \delta_{\lambda+} + \frac{\sqrt{2}}{M} p_{1\dot{A}} p_{2B} \delta_{\lambda-} + \frac{1}{M} \left(p_{1\dot{A}} p_{1B} - p_{2\dot{A}} p_{2B}\right) \delta_{\lambda 0}, \tag{A.21}$$

where $M = \sqrt{p^2}$ denotes the mass of the considered boson. For massless bosons, however, there are only two polarization states, and the form of the corresponding polarization vectors depends on the chosen gauge. In the WvdW formalism, this manifests itself in the dependence of the polarization matrix $\varepsilon_{A\dot{B}}$ on an arbitrary gauge spinor g, and the solutions of the equation (A.20) are given by

$$\varepsilon_{\dot{A}B}(p) = \frac{\sqrt{2}}{\langle gp]^{\star}} g_{\dot{A}} p_B \delta_{\lambda+} + \frac{\sqrt{2}}{\langle gp\rangle} p_{\dot{A}} g_B \delta_{\lambda-}. \tag{A.22}$$

The gauge spinor g is an completely arbitrary Weyl spinor representing the freedom to choose a gauge for the external boson, such that a variation of this spinor can be used to check the gauge independence of the amplitude. Furthermore, the QED Ward identity tells us that in a physical amplitude multiplied by the denominators in (A.22) should vanish when setting $g = p_1$ everywhere. This provides a second possibility to test the results for an amplitude calculated in the WvdW formalism, if the considered process involves external photons.

Using the results presented above, one is able to re-express all Feynman rules formulated for Dirac structures in terms of Weyl structures [44]. This makes it possible to write down directly an amplitude depending on Weyl structures only. However, for processes with many-particle final states this can be quite cumbersome to do by hand and keeping track of the minus signs arising from the spinor structure of the formalism is a common source of errors. It would therefore be desirable to automatize the formalism, which is

why we choose a slightly different method here, which is somewhat easier to implement in combination with existing computer algebra programs [45].

To see how this method works in practice, consider a fermion chain

$$\langle\overline{\Psi}^{\sigma}_{p_1,\sigma_1}|\omega_{\pm}\gamma_{\mu_1}\ldots\gamma_{\mu_n}|\Psi^{\sigma'}_{p_2,\sigma_2}\rangle, \tag{A.23}$$

where $\sigma,\sigma' = +$ or $-$ and $\omega_{\pm}$ are the helicity projectors $\omega_{\pm} = (1\pm\gamma_5)/2$. We assume that in all fermion chains without helicity projectors a unity of the form $\mathbb{1} = (\omega_+ + \omega_-)$ has been inserted, such that all fermion chains are of the general form (A.23). Upon inserting the expressions (A.16), (A.17) and (A.18) one notices, that each chiral four-dimensional Dirac spinor chain translates in exactly one two-dimensional Weyl spinor chain

$$\langle\overline{\Psi}^{\pm}_{p_1,\sigma_1}|\omega_+\gamma_{\mu_1}\ldots\gamma_{\mu_n}|\Psi^{\pm}_{p_2,\sigma_2}\rangle = \begin{cases} \langle\psi^{\pm A}_{p_1,\sigma_1}|\sigma_{\mu_1 A\dot{B}}\overline{\sigma}_{\mu_2}^{\dot{B}C}\ldots\overline{\sigma}_{\mu_n}^{\dot{U}V}|\phi^{\pm}_{p_2,\sigma_2 V}\rangle, & n \text{ even}, \\ \langle\psi^{\pm A}_{p_1,\sigma_1}|\sigma_{\mu_1 A\dot{B}}\overline{\sigma}_{\mu_2}^{\dot{B}C}\ldots\sigma_{\mu_n U\dot{V}}|\psi^{\pm\dot{V}}_{p_2,\sigma_2}\rangle, & n \text{ odd}, \end{cases} \tag{A.24}$$

$$\langle\overline{\Psi}^{\pm}_{p_1,\sigma_1}|\omega_-\gamma_{\mu_1}\ldots\gamma_{\mu_n}|\Psi^{\pm}_{p_2,\sigma_2}\rangle = \begin{cases} \langle\phi^{\pm}_{p_1,\sigma_1\dot{A}}|\overline{\sigma}_{\mu_1}^{\dot{A}B}\sigma_{\mu_2 B\dot{C}}\ldots\sigma_{\mu_n U\dot{V}}|\psi^{\pm\dot{V}}_{p_2,\sigma_2}\rangle, & n \text{ even}, \\ \langle\phi^{\pm}_{p_1,\sigma_1\dot{A}}|\overline{\sigma}_{\mu_1}^{\dot{A}B}\sigma_{\mu_2 B\dot{C}}\ldots\overline{\sigma}_{\mu_n}^{\dot{U}V}|\phi^{\pm}_{p_2,\sigma_2 V}\rangle, & n \text{ odd}. \end{cases} \tag{A.25}$$

The open Lorentz indices $\mu_1,\ldots,\mu_n$ can be contracted with 4-momenta, polarization vectors, an ϵ-tensor, a metric tensor or another fermion chain. Starting with the case of two contracted spinor chains, the Fierz identities

$$\sigma_{\mu A\dot{B}}\sigma^{\mu}_{C\dot{D}} = 2\epsilon_{\dot{A}\dot{C}}\epsilon_{BD}, \qquad \overline{\sigma}_{\mu}^{\dot{A}B}\overline{\sigma}^{\mu\dot{C}D} = 2\epsilon^{\dot{A}\dot{C}}\epsilon^{BD}, \qquad \sigma_{\mu A\dot{B}}\overline{\sigma}^{\mu\,\dot{C}D} = 2\delta^{A}_{D}\delta^{\dot{C}}_{\dot{B}} \tag{A.26}$$

can be used to explicitly resolve the contraction between the two spinor chains. As an example, consider two fermion chains with an helicity projector ω_+ and even numbers n_1 and n_2 of Dirac matrices. If two such chains are contracted via two matrices of type σ, the first of the relations (A.26) leads to

$$\begin{aligned}&\langle\psi^{\pm}_{p_1,\sigma_1}|\sigma_{\mu_1}\ldots\overline{\sigma}_{\mu_{r-1}}\sigma^{\mu_r}\overline{\sigma}_{\mu_{r+1}}\ldots\overline{\sigma}_{\mu_{n_1}}|\phi^{\pm}_{p_2,\sigma_2}\rangle\langle\psi^{\pm}_{p_3,\sigma_3}|\sigma_{\nu_1}\ldots\overline{\sigma}_{\nu_{r-1}}\sigma_{\mu_r}\overline{\sigma}_{\nu_{r+1}}\ldots\overline{\sigma}_{\nu_{n_2}}|\phi^{\pm}_{p_4,\sigma_4}\rangle \\ &\quad = 2\langle\psi^{\pm}_{p_1,\sigma_1}|\sigma_{\mu_1}\ldots\overline{\sigma}_{\mu_{r-1}}\sigma_{\nu_{r-1}}\ldots\overline{\sigma}_{\nu_1}\epsilon|\psi^{\pm}_{p_3,\sigma_3}\rangle\langle\phi^{\pm}_{p_2,\sigma_2}|\epsilon\sigma_{\mu_{n_1}}\ldots\sigma_{\mu_{r+1}}\overline{\sigma}_{\nu_{r+1}}\ldots\overline{\sigma}_{\nu_{n_2}}|\phi^{\pm}_{p_4,\sigma_4}\rangle,\end{aligned} \tag{A.27}$$

and the second of the equations (A.26) can be applied analogously to the case of contraction between two matrices of the type $\overline{\sigma}$. A contraction between a matrix of the type σ and a matrix of type $\overline{\sigma}$ can finally be performed using the last of the relations (A.26)

$$\begin{aligned}&\langle\psi^{\pm}_{p_1,\sigma_1}|\sigma_{\mu_1}\ldots\overline{\sigma}_{\mu_{r-1}}\sigma^{\mu_r}\overline{\sigma}_{\mu_{r+1}}\ldots\overline{\sigma}_{\mu_{n_1}}|\phi^{\pm}_{p_2,\sigma_2}\rangle\langle\psi^{\pm}_{p_3,\sigma_3}|\sigma_{\nu_1}\ldots\sigma_{\nu_{r-1}}\overline{\sigma}_{\mu_r}\sigma_{\nu_{r+1}}\ldots\overline{\sigma}_{\nu_{n_2}}|\phi^{\pm}_{p_4,\sigma_4}\rangle \\ &= 2\langle\psi^{\pm}_{p_1,\sigma_1}|\sigma_{\mu_1}\ldots\overline{\sigma}_{\mu_{r-1}}\sigma_{\nu_{r+1}}\ldots\overline{\sigma}_{\nu_{n_2}}|\phi^{\pm}_{p_4,\sigma_4}\rangle\langle\psi^{\pm}_{p_3,\sigma_3}|\sigma_{\nu_1}\ldots\sigma_{\nu_{r-1}}\overline{\sigma}_{\mu_{r+1}}\ldots\overline{\sigma}_{\mu_{n_1}}|\phi^{\pm}_{p_2,\sigma_2}\rangle.\end{aligned} \tag{A.28}$$

Contractions involving one of the other chain types shown in (A.25) can be handled in exactly the same way as in the above example.

The second possibility, the contraction between a fermion chain and an epsilon tensor, can be resolved using the identity

$$\mathrm{i}\epsilon_{\mu\nu\rho\sigma} = \frac{1}{2}\mathrm{tr}[\sigma_\mu\overline{\sigma}_\nu\sigma_\rho\overline{\sigma}_\sigma] - g_{\mu\nu}g_{\rho\sigma} + g_{\mu\rho}g_{\nu\sigma} - g_{\mu\sigma}g_{\nu\rho}, \tag{A.29}$$

which yields for contraction of an ϵ-tensor with a matrix of type σ

$$\begin{aligned}\mathrm{i}\epsilon_{\mu\nu\rho\sigma}\langle\psi^{\pm}_{p_1,\sigma_1}|\sigma_{\mu_1}\ldots\overline{\sigma}_{\mu_{r-1}}\sigma^{\mu}\overline{\sigma}_{\mu_{r+1}}\ldots\overline{\sigma}_{\mu_{n_1}}|\phi^{\pm}_{p_2,\sigma_2}\rangle \\ = \langle\psi^{\pm}_{p_1,\sigma_1}|\sigma_{\mu_1}\ldots\overline{\sigma}_{\mu_{r-1}}\sigma_\sigma\overline{\sigma}_\rho\sigma_\nu\overline{\sigma}_{\mu_{r+1}}\ldots\overline{\sigma}_{\mu_{n_1}}|\phi^{\pm}_{p_2,\sigma_2}\rangle \\ - g_{\rho\sigma}\langle\psi^{\pm}_{p_1,\sigma_1}|\sigma_{\mu_1}\ldots\overline{\sigma}_{\mu_{r-1}}\sigma_\nu\overline{\sigma}_{\mu_{r+1}}\ldots\overline{\sigma}_{\mu_{n_1}}|\phi^{\pm}_{p_2,\sigma_2}\rangle \\ + g_{\nu\sigma}\langle\psi^{\pm}_{p_1,\sigma_1}|\sigma_{\mu_1}\ldots\overline{\sigma}_{\mu_{r-1}}\sigma_\rho\overline{\sigma}_{\mu_{r+1}}\ldots\overline{\sigma}_{\mu_{n_1}}|\phi^{\pm}_{p_2,\sigma_2}\rangle \\ - g_{\nu\rho}\langle\psi^{\pm}_{p_1,\sigma_1}|\sigma_{\mu_1}\ldots\overline{\sigma}_{\mu_{r-1}}\sigma_\sigma\overline{\sigma}_{\mu_{r+1}}\ldots\overline{\sigma}_{\mu_{n_1}}|\phi^{\pm}_{p_2,\sigma_2}\rangle,\end{aligned} \tag{A.30}$$

as well as

$$\begin{aligned}\mathrm{i}\epsilon_{\mu\nu\rho\sigma}\langle\psi^{\pm}_{p_1,\sigma_1}|\sigma_{\mu_1}\ldots\sigma_{\mu_{r-1}}\overline{\sigma}^{\mu}\sigma_{\mu_{r+1}}\ldots\overline{\sigma}_{\mu_{n_1}}|\phi^{\pm}_{p_2,\sigma_2}\rangle \\ = \langle\psi^{\pm}_{p_1,\sigma_1}|\sigma_{\mu_1}\ldots\sigma_{\mu_{r-1}}\overline{\sigma}_\nu\sigma_\rho\overline{\sigma}_\sigma\sigma_{\mu_{r+1}}\ldots\overline{\sigma}_{\mu_{n_1}}|\phi^{\pm}_{p_2,\sigma_2}\rangle \\ - g_{\rho\sigma}\langle\psi^{\pm}_{p_1,\sigma_1}|\sigma_{\mu_1}\ldots\sigma_{\mu_{r-1}}\overline{\sigma}_\nu\sigma_{\mu_{r+1}}\ldots\overline{\sigma}_{\mu_{n_1}}|\phi^{\pm}_{p_2,\sigma_2}\rangle \\ + g_{\nu\sigma}\langle\psi^{\pm}_{p_1,\sigma_1}|\sigma_{\mu_1}\ldots\sigma_{\mu_{r-1}}\overline{\sigma}_\rho\sigma_{\mu_{r+1}}\ldots\overline{\sigma}_{\mu_{n_1}}|\phi^{\pm}_{p_2,\sigma_2}\rangle \\ - g_{\nu\rho}\langle\psi^{\pm}_{p_1,\sigma_1}|\sigma_{\mu_1}\ldots\sigma_{\mu_{r-1}}\overline{\sigma}_\sigma\sigma_{\mu_{r+1}}\ldots\overline{\sigma}_{\mu_{n_1}}|\phi^{\pm}_{p_2,\sigma_2}\rangle\end{aligned} \tag{A.31}$$

in the case of an ϵ-tensor contracted with a matrix of type $\overline{\sigma}$.

Finally, the relations (A.26) can be applied to the case where two Lorentz indices are contracted within one single spinor chain. For a contraction between two matrices of type σ one has

$$\begin{aligned}\langle\psi^{\pm}_{p_1,\sigma_1}|\sigma_{\mu_1}\ldots\overline{\sigma}_{\mu_{r-1}}\sigma^{\mu}\overline{\sigma}_{\mu_{r+1}}\ldots\overline{\sigma}_{\mu_{s-1}}\sigma_\mu\overline{\sigma}_{\mu_{s+1}}\ldots\overline{\sigma}_{\mu_{n_1}}|\phi^{\pm}_{p_2,\sigma_2}\rangle \\ = -2\langle\psi^{\pm}_{p_1,\sigma_1}|\sigma_{\mu_1}\ldots\overline{\sigma}_{\mu_{r-1}}\sigma_{\mu_{s-1}}\ldots\sigma_{\mu_{r+1}}\overline{\sigma}_{\mu_{s+1}}\ldots\overline{\sigma}_{\mu_{n_1}}|\phi^{\pm}_{p_2,\sigma_2}\rangle,\end{aligned} \tag{A.32}$$

and an analogous relation also holds for a contraction between two matrices of type $\overline{\sigma}$. The contractions between one matrix of type σ and one matrix of type $\overline{\sigma}$ can be done according to

$$\begin{aligned}\langle\psi^{\pm}_{p_1,\sigma_1}|\sigma_{\mu_1}\ldots\overline{\sigma}_{\mu_{r-1}}\sigma^{\mu}\overline{\sigma}_{\mu_{r+1}}\ldots\sigma_{\mu_{s-1}}\overline{\sigma}_\mu\sigma_{\mu_{s+1}}\ldots\overline{\sigma}_{\mu_{n_1}}|\phi^{\pm}_{p_2,\sigma_2}\rangle \\ = 2\ \mathrm{tr}[\overline{\sigma}_{\mu_{r+1}}\ldots\sigma_{\mu_{s-1}}]\langle\psi^{\pm}_{p_1,\sigma_1}|\sigma_{\mu_1}\ldots\overline{\sigma}_{\mu_{r-1}}\sigma_{\mu_{s+1}}\ldots\overline{\sigma}_{\mu_{n_1}}|\phi^{\pm}_{p_2,\sigma_2}\rangle.\end{aligned} \tag{A.33}$$

A contraction between the trace in the second line of (A.33) with other spinor chains or further ϵ-tensors can then be resolved using the same methods as described above.

Applying the above relations repeatedly, one is left with a set of fermion chains, within which all Lorentz indices are contracted with 4-momenta and polarization vectors only. By inserting the expressions (A.11), (A.17), (A.18), (A.21) and (A.22) into the resulting expressions, one is left with terms that depend exclusively on the Weyl-spinor products (A.9) and Kronecker deltas in the helicities of the external particles.

Apart from fermion chains, the amplitude depends on scalar products and ϵ-tensors in the momenta and polarization vectors of the external particles. In (A.1) they are contained in the scalar coefficients C_i. The decomposition of these structures in terms of Weyl-spinor products can again be done by using the relations (A.26) and (A.29)

$$\epsilon_{\mu\nu\rho\sigma} p_1^\mu p_2^\mu p_3^\mu p_4^\mu = \frac{1}{2}\mathrm{tr}[P_1 P_2 P_3 P_4] - (p_1 p_2)(p_3 p_4) + (p_1 p_3)(p_2 p_4) - (p_1 p_4)(p_2 p_3), \tag{A.34}$$

$$2 p_1 p_2 = 2 g^{\mu\nu} p_{1\mu} p_{2\mu} = p_{1\mu} p_{2\mu} \sigma^\mu{}_{B\dot{A}} \overline{\sigma}_\mu^{\dot{A}B} = P_{1B\dot{A}} P_2{}^{\dot{A}B}, \tag{A.35}$$

and in the same way if one of the momenta is replaced by a polarization vector.

Employing the formalism described above, one is left with an amplitude which only depends on Weyl-spinor products, coupling parameters, and Kronecker deltas in the helicities of the external particles, such that the numerical evaluation of such an amplitude is rather simple. However, for the case of a one-loop amplitude regularized in dimensional regularization one is interested in evaluating the amplitude in $D = 4 - 2\varepsilon$ dimensions. This not possible in the WvdW formalism due to its manifest 4-dimensionality, i.e. it is not clear how to reduce a D-dimensional object into Weyl spinors. One has therefore to make sure, that the reduction of the fermion chains, scalar products and ϵ-tensors is performed *after* the algebraic simplification of internal fermion chains and the reduction of tensor integrals to scalar integrals. In other words, the method presented in this section has to be applied in the very end of the calculation of the amplitude, just before the numerical evaluation, when the limit $D \to 4$ has already been taken.

Appendix B

Analytical Results for the Amplitudes

In this appendix, we present our results for those parts of the amplitudes, which are compact enough to be explicitly displayed. Whereas this is not possible for the factorizable virtual corrections, we present the analytical expressions for the Born amplitude in Section B.1, the amplitude corresponding to the non-factorizable corrections in Section B.2, and the amplitudes for the QED and QCD Bremsstrahlung processes in sections B.3 and B.4, respectively.

For the notation, we consider the partonic processes

$$q_1(p_1,\sigma_1) + \bar{q}_2(p_2,\sigma_2) \to f_3(p_3,\sigma_c) + \bar{f}_4(p_4,\sigma_4) + \gamma(p_5,\lambda_1) \;\; (+\gamma(p_6,\lambda_2), \;\; +g(p_6,\lambda_2)) \quad \text{(B.1)}$$

where we denote the particle helicities by $\sigma_i = \pm 1/2, i = 1,\ldots,4$ for the fermions and $\lambda_i = \pm 1, i = 1,2$ for the photons and the gluon, whereas the quantities $p_i, i = 1,\ldots,6$ are the corresponding particle 4-momenta. The calculation of the Born and Bremsstrahlung amplitudes are carried out in the framework of the Weyl-van der Waerden Formalism [82, 83] as presented in Ref.[44].

Following Refs.[42, 84], we perform the classification of the initial and final states according to the production mechanism. Accordingly, we distinguish between events which proceed exclusively via neutral current (NC) interactions, events which are mediated by a charged current (CC) interaction and reactions where both neutral current as well as charged current interactions appear (mixed NC/CC). In the following, we denote by q ($\bar{q}$) and Q ($\bar{Q}$), $q = u, d, \ldots$, (anti-) quarks of different flavor, whereas we choose the notation l ($\bar{l}$), $l = e, \nu_e, \ldots$ for the (anti-) leptons of the Standard Model. The corresponding isospin partners are denoted by q' ($\bar{q}'$), Q' ($\bar{Q}'$) and l' ($\bar{l}'$). Using this notation, we find the seven reaction types shown in Table B.1.

(i)	NC reactions:							
	(a)	$q\bar{q}$	$\to$	l	$+$	$\bar{l}$	$+$	γ
	(b)	$q\bar{q}$	$\to$	q	$+$	$\bar{q}$	$+$	γ
	(c)	$q\bar{q}$	$\to$	Q	$+$	$\bar{Q}$	$+$	γ
(ii)	CC reactions:							
	(a)	$q\bar{q}'$	$\to$	l	$+$	$\bar{l}'$	$+$	γ,
	(b)	$q\bar{q}'$	$\to$	Q	$+$	$\bar{Q}'$	$+$	γ,
(iii)	Mixed NC/CC reactions:							
	(a)	$q\bar{q}$	$\to$	q'	$+$	$\bar{q}'$	$+$	γ,
	(b)	$q\bar{q}'$	$\to$	q	$+$	$\bar{q}'$	$+$	γ.

Table B.1: Classification of the various final states.

B.1 The Born Amplitudes

In this section we present our results for the Born amplitudes for the partonic processes (B.1). To simplify the calculation of a helicity amplitude, it is convenient to reduce the set of Feynman diagrams for a given process to the subset of so-called *generic diagrams*, from which the contributions of the remaining graphs can be obtained by employing discrete symmetries like crossing or CP. Considering processes with a vector boson in the final state, the generic diagrams are given by the minimal gauge-invariant subset of diagrams. This subset generally contains all diagrams, which reduce to the same graph after removing the final-state boson. For the process considered here, the generic diagrams are shown in Figure B.1.

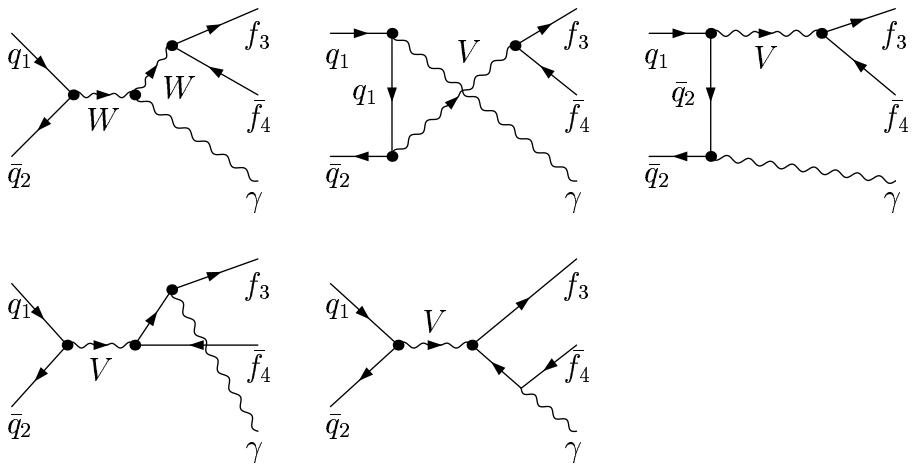

Figure B.1: The tree-level diagrams for $q_1 + \bar{q}_2 \to f_3 + \bar{f}_4 + \gamma$

We calculated the amplitudes corresponding to these diagrams in the framework of the Weyl-van der Waerden formalism [82, 83] as presented in Ref.[44]. The particle momenta and helicities are denoted by p_1, p_2, p_3, p_4, p_5 and $\sigma_1, \sigma_2, \sigma_3, \sigma_4, \lambda_1$, respectively, and all fermion masses are neglected. The squared amplitude is then generally given by a sum over the colours and helicities of the external particles

$$\left|\mathcal{A}^{(0)}(\Phi)\right|^2 = \frac{1}{9}\sum_{c_1c_2c_3c_4}\frac{1}{4}\sum_{\sigma_1\sigma_2\sigma_3\sigma_4\lambda_1}\left|\mathrm{i}\mathcal{A}^{(0)\ \sigma_1\sigma_2\sigma_3\sigma_4\lambda_1}_{c_1c_2c_3c_4}(p_1,p_2,p_3,p_4,p_5)\right|^2. \tag{B.2}$$

Splitting first the colour structure off the rest of the generic amplitude, one has

$$\mathrm{i}\mathcal{A}^{(0)\ \sigma_1\sigma_2\sigma_3\sigma_4\lambda_1}_{c_1c_2c_3c_4}(p_1,p_2,p_3,p_4,p_5) = \sum_V C^{f_3,\bar{f}_4,V}_{c_1c_2c_3c_4}\mathrm{iA}^{\sigma_1\sigma_2\sigma_3\sigma_4\lambda_1}_{q_1,\bar{q}_2,f_3,\bar{f}_4,V}(p_1,p_2,p_3,p_4,p_5), \tag{B.3}$$

where the sum over V is taken over all vector bosons of the Standard Model and the colour structures are given by

$$C^{f_3,\bar{f}_4,V}_{c_1c_2c_3c_4} = \begin{cases} \delta_{c_1c_2} & f_3,f_4\in\{l,l'\}, \quad V=A,Z,W \\ \delta_{c_1c_2}\delta_{c_3c_4} & f_3,f_4\in\{q,q'\}, \quad V=A,Z,W \\ \frac{1}{4}\lambda^a_{c_2c_1}\lambda^a_{c_3c_4} & f_3,f_4\in\{q,q'\}, \quad V=g \end{cases}. \tag{B.4}$$

Here the matrices λ^a denote the Gell-Mann matrices, i.e. the three-dimensional representation of the QCD gauge group. The colour-neutral part of the amplitude then reads

$$\begin{aligned}\mathrm{iA}^{\sigma_1\sigma_2\sigma_3\sigma_4\lambda_1}_{q_1,\bar{q}_2,f_3,\bar{f}_4,V}(p_1,p_2,p_3,p_4,p_5) = -2e^3 C^{\sigma_1}_{V\bar{q}_2q_1}C^{\sigma_3}_{Vf_3\bar{f}_4}\delta_{\sigma_1-\sigma_2}\delta_{\sigma_3-\sigma_4} \\ \times \mathrm{B}^{\sigma_1\sigma_3\lambda_1}_V(p_1,p_2,p_3,p_4,p_5,Q_{q_1},Q_{\bar{q}_2},Q_{f_3},Q_{\bar{f}_4}),\end{aligned} \tag{B.5}$$

where the quantities $Q_i, i = 1,\ldots 4$ denote the charges of the external fermions. The gauge couplings $C^{\pm}_{V\bar{f}_af_b}$ of a fermion f_1 and an anti-fermion $\bar{f}_2$ to the vector boson V are listed in Table B.2, and the conventions used here can be summarized by the following. The charges and the third component of the isospin of the fermion f are denoted by Q_f and I^3_f, respectively, whereas s_W and c_W are the sine and the cosine of the weak mixing angle. Furthermore, the strong coupling constant and the fine-structure constant are written as α_S and α. Finally, the tensors δ_{ij} and V_{ij} denote the Kronecker delta and the CKM matrix. Note, that the elementary charge e and the colour structure have already been extracted from the couplings, such that the gluonic coupling reduces to the square root of the ratio of the strong coupling constant to the electromagnetic coupling constant.

As discussed in section (2.2), the amplitude can be split into a resonant part as well as an non-resonant part. This splitting can be done of the level of the generic functions

$$\mathrm{B}^{\sigma_1\sigma_3\lambda_1}_V = \mathrm{B}^{\sigma_1\sigma_3\lambda_1}_{\mathrm{res},V} + \mathrm{B}^{\sigma_1\sigma_3\lambda_1}_{\mathrm{nres},V} \tag{B.6}$$

The resonant part comprises all contributions from diagrams containing the resonant propagator of the decaying particle V, and thus corresponds to the amplitude originating from

$$
\begin{array}{lcll}
C^{\pm}_{\gamma \bar{f}_2 f_1} & = & -Q_{f_1}\delta_{f_1 f_2}, & f_{1,2} = q, l \\
C^{\sigma}_{Z \bar{f}_2 f_1} & = & \begin{cases} -\frac{s_{\mathrm{W}}}{c_{\mathrm{W}}} Q_{f_1}\delta_{f_1 f_2}, & \text{for } \sigma = + \\ \frac{I^3_{f_1} - s^2_{\mathrm{W}} Q_{f_1}}{s_{\mathrm{W}} c_{\mathrm{W}}}\delta_{f_1 f_2}, & \text{for } \sigma = - \end{cases}, & f_{1,2} = q, l \\
C^{\sigma}_{W^- \bar{l}\nu_l} & = & \begin{cases} 0, & \text{for } \sigma = + \\ \frac{1}{\sqrt{2}s_{\mathrm{W}}}, & \text{for } \sigma = - \end{cases}, & l = e, \mu, \tau \\
C^{\sigma}_{W^+ \bar{\nu}_l l} & = & \begin{cases} 0, & \text{for } \sigma = + \\ \frac{1}{\sqrt{2}s_{\mathrm{W}}}, & \text{for } \sigma = - \end{cases}, & l = e, \mu, \tau \\
C^{\sigma}_{W^- \bar{q}_2 q_1} & = & \begin{cases} 0, & \text{for } \sigma = + \\ \frac{1}{\sqrt{2}s_{\mathrm{W}}} V^{\dagger}_{q_2 q_1}, & \text{for } \sigma = - \end{cases}, & q_1 = u, c, t, \quad q_2 = d, s, b \\
C^{\sigma}_{W^+ \bar{q}_2 q_1} & = & \begin{cases} 0, & \text{for } \sigma = + \\ \frac{1}{\sqrt{2}s_{\mathrm{W}}} V_{q_2 q_1}, & \text{for } \sigma = - \end{cases}, & q_1 = s, d, b, \quad q_2 = u, c, t \\
C^{\sigma}_{g \bar{f}_2 f_1} & = & \sqrt{\frac{\alpha_{\mathrm{S}}}{\alpha}}\delta_{f_1 f_2}, & f_{1,2} = q
\end{array}
$$

Table B.2: Gauge coupling constants of the fermion f_1 and the anti-fermion $\bar{f}_2$ to the gauge bosons $V = \gamma, Z, W^{\pm}$ and g.

the diagrams in the first row of Figure B.1. Applying the Weyl-van der Waerden Formalism as presented in Ref.[44] to these diagrams, the generic function for all helicities positive is given by

$$
\begin{aligned}
&\mathrm{B}^{\mathrm{res}\,+++}_{V,\mathrm{fac}}(p_1, p_2, p_3, p_4, p_5, Q_1, Q_2, Q_3, Q_4) \\
&\qquad = -\frac{\sqrt{2}}{\langle p_4 p_5\rangle} \frac{(\langle p_1 p_4\rangle)^2}{(p_3+p_4)^2 - M_V^2 + \mathrm{i} M_V \Gamma_V} \\
&\qquad \times \left\{ \frac{Q_1 \langle p_3 p_2\rangle^{\star}}{\langle p_1 p_5\rangle} + \frac{Q_2 \langle p_3 p_1\rangle^{\star}}{\langle p_2 p_5\rangle} - \frac{C_{V\gamma V}}{(p_1+p_2)^2 - M_V^2 + \mathrm{i} M_V \Gamma_V} \langle p_3 p_5\rangle^{\star} \langle p_2 p_1\rangle^{\star} \right\}. \quad \text{(B.7)}
\end{aligned}
$$

The non-resonant part of the Born amplitude, on the other hand, receives contributions from the remaining diagrams in the second row of Figure B.1. Expressed in Weyl-spinor

products, the generic function for all helicities positive reads

$$\mathrm{B}_V^{\mathrm{nres}\,+++}(p_1,p_2,p_3,p_4,p_5,Q_1,Q_2,Q_3,Q_4) = \sqrt{2}\frac{(\langle p_1 p_4\rangle)^2}{(p_1+p_2)^2 - M_V^2 + \mathrm{i}M_V\Gamma_V}\frac{Q_3\langle p_2 p_1\rangle^\star}{\langle p_5 p_3\rangle\langle p_5 p_4\rangle}. \tag{B.8}$$

Here M_V is the mass and Γ_V the decay width of the vector boson V and the variable $C_{V_1\gamma V_2} = Q_1 - Q_2$ denotes the coupling constant parameterizing the trilinear gauge coupling $V_1\gamma V_2$. Note, that the amplitudes for neutral current reactions can be extracted from (B.7) and (B.8) by simply setting $(Q_2 - Q_1) = C_{V\gamma V} = 0$. By adding the expressions resulting from inserting (B.7) and (B.8) into (B.5) and (B.3) one obtains the full Born amplitude. While this is gauge invariant, the resonant and non-resonant parts as defined above are not, unless applying the LPA. To obtain the gauge-invariant Born amplitude in LPA, one has to set the finite width in the s-channel propagator appearing in (B.7) to zero, and to insert the corresponding result into (B.5) and (B.3). Note that we set the gauge spinor for the external photon to $g = k_4$ to obtain the above results, which is why the contribution of the diagram with the photon coupling to the external fermion f_4 vanishes.

Dropping the superscript for resonant and non-resonant contributions in what follows, the other helicity combinations can be calculated by

$$\begin{aligned}
\mathrm{B}_V^{-++}(p_1,p_2,p_3,p_4,p_5,Q_1,Q_2,Q_3,Q_4) &= \mathrm{B}_V^{+++}(p_2,p_1,p_3,p_4,p_5,-Q_2,-Q_1,Q_3,Q_4),\\
\mathrm{B}_V^{+-+}(p_1,p_2,p_3,p_4,p_5,Q_1,Q_2,Q_3,Q_4) &= \mathrm{B}_V^{+++}(p_1,p_2,p_4,p_3,p_5,Q_1,Q_2,-Q_4,-Q_3),\\
\mathrm{B}_V^{--+}(p_1,p_2,p_3,p_4,p_5,Q_1,Q_2,Q_3,Q_4) &= \mathrm{B}_V^{+++}(p_2,p_1,p_4,p_3,p_5,-Q_2,-Q_1,-Q_4,-Q_3),
\end{aligned}$$

as well as

$$\begin{aligned}
&\mathrm{B}_V^{\sigma_1\sigma_3-}(p_1,p_2,p_3,p_4,p_5,Q_1,Q_2,Q_3,Q_4)\\
&\qquad = \left[\mathrm{B}_V^{-\sigma_1-\sigma_3+}(p_1,p_2,p_3,p_4,p_5,Q_1,Q_2,Q_3,Q_4)\right]^\star\Big|_{P_V^\star\to P_V}.
\end{aligned} \tag{B.9}$$

As was said before, once the generic amplitudes are calculated, it is possible to determine the amplitudes corresponding to the various final states shown in Table B.1 by exploiting discrete symmetries like crossing. The amplitudes for the processes displayed in Table B.1 then read

$$\mathrm{i}\mathcal{A}^{(0)\,\sigma_1\sigma_2\sigma_3\sigma_4\lambda_1}_{\mathrm{NCa}\;\;c_1c_2}(p_1,p_2,p_3,p_4,p_5) = \delta_{c_2c_1}\sum_{V=\gamma,Z}\mathrm{iA}^{\sigma_1\sigma_2\sigma_3\sigma_4\lambda_1}_{q_1,\bar{q}_2,f_3,\bar{f}_4,V}(p_1,p_2,p_3,p_4,p_5), \tag{B.10}$$

$$
\begin{aligned}
\mathrm{i}\mathcal{A}^{(0)\,\sigma_1\sigma_2\sigma_3\sigma_4\lambda_1}_{\mathrm{NCb}\;\;c_1c_2c_3c_4}(p_1,p_2,p_3,p_4,p_5) &= \delta_{c_1c_2}\delta_{c_3c_4}\sum_{V=\gamma,Z}\mathrm{iA}^{\sigma_1\sigma_2\sigma_3\sigma_4\lambda_1}_{q_1,\bar{q}_2,f_3,\bar{f}_4,V}(p_1,p_2,p_3,p_4,p_5)\\
&\quad-\delta_{c_3c_1}\delta_{c_2c_4}\sum_{V=\gamma,Z}\mathrm{iA}^{\sigma_1-\sigma_3-\sigma_2\sigma_4\lambda_1}_{q_1,\bar{f}_3,q_2,\bar{f}_4,V}(p_1,-p_3,-p_2,p_4,p_5)\\
&\quad+\frac{1}{4}\sum_a\lambda^a_{c_2c_1}\lambda^a_{c_3c_4}\mathrm{iA}^{\sigma_1\sigma_2\sigma_3\sigma_4\lambda_1}_{q_1,\bar{q}_2,f_3,\bar{f}_4,g}(p_1,p_2,p_3,p_4,p_5)\\
&\quad-\frac{1}{4}\sum_a\lambda^a_{c_3c_1}\lambda^a_{c_2c_4}\mathrm{iA}^{\sigma_1-\sigma_3-\sigma_2\sigma_4\lambda_1}_{q_1,\bar{f}_3,q_2,\bar{f}_4,g}(p_1,-p_3,-p_2,p_4,p_5),
\end{aligned}
\tag{B.11}
$$

$$
\begin{aligned}
\mathrm{i}\mathcal{A}^{(0)\,\sigma_1\sigma_2\sigma_3\sigma_4\lambda_1}_{\mathrm{NCc}\;\;c_1c_2c_3c_4}(p_1,p_2,p_3,p_4,p_5) &= \delta_{c_1c_2}\delta_{c_3c_4}\sum_{V=\gamma,Z}\mathrm{iA}^{\sigma_1\sigma_2\sigma_3\sigma_4\lambda_1}_{q_1,\bar{q}_2,f_3,\bar{f}_4,V}(p_1,p_2,p_3,p_4,p_5)\\
&\quad+\frac{1}{4}\sum_a\lambda^a_{c_2c_1}\lambda^a_{c_3c_4}\mathrm{iA}^{\sigma_1\sigma_2\sigma_3\sigma_4\lambda_1}_{q_1,\bar{q}_2,f_3,\bar{f}_4,g}(p_1,p_2,p_3,p_4,p_5),
\end{aligned}
\tag{B.12}
$$

$$
\mathrm{i}\mathcal{A}^{(0)\,\sigma_1\sigma_2\sigma_3\sigma_4\lambda_1}_{\mathrm{CCa}\;\;c_1c_2}(p_1,p_2,p_3,p_4,p_5) = \delta_{c_2c_1}\mathrm{iA}^{\sigma_1\sigma_2\sigma_3\sigma_4\lambda_1}_{q_1,\bar{q}_2,f_3,\bar{f}_4,W}(p_1,p_2,p_3,p_4,p_5),
\tag{B.13}
$$

$$
\mathrm{i}\mathcal{A}^{(0)\,\sigma_1\sigma_2\sigma_3\sigma_4\lambda_1}_{\mathrm{CCb}\;\;c_1c_2c_3c_4}(p_1,p_2,p_3,p_4,p_5) = \delta_{c_1c_2}\delta_{c_3c_4}\mathrm{iA}^{\sigma_1\sigma_2\sigma_3\sigma_4\lambda_1}_{q_1,\bar{q}_2,f_3,\bar{f}_4,W}(p_1,p_2,p_3,p_4,p_5),
\tag{B.14}
$$

$$
\begin{aligned}
\mathrm{i}\mathcal{A}^{(0)\,\sigma_1\sigma_2\sigma_3\sigma_4\lambda_1}_{\mathrm{NC/CCa}\;\;c_1c_2c_3c_4}(p_1,p_2,p_3,p_4,p_5) &= \delta_{c_1c_2}\delta_{c_3c_4}\sum_{V=\gamma,Z}\mathrm{iA}^{\sigma_1\sigma_2\sigma_3\sigma_4\lambda_1}_{q_1,\bar{q}_2,f_3,\bar{f}_4,V}(p_1,p_2,p_3,p_4,p_5)\\
&\quad-\delta_{c_3c_1}\delta_{c_2c_4}\mathrm{iA}^{\sigma_1-\sigma_3-\sigma_2\sigma_4\lambda_1}_{q_1,\bar{f}_3,q_2,\bar{f}_4,W}(p_1,-p_3,-p_2,p_4,p_5)\\
&\quad+\frac{1}{4}\sum_a\lambda^a_{c_2c_1}\lambda^a_{c_3c_4}\mathrm{iA}^{\sigma_1\sigma_2\sigma_3\sigma_4\lambda_1}_{q_1,\bar{q}_2,f_3,\bar{f}_4,g}(p_1,p_2,p_3,p_4,p_5),
\end{aligned}
\tag{B.15}
$$

$$
\begin{aligned}
\mathrm{i}\mathcal{A}^{(0)\,\sigma_1\sigma_2\sigma_3\sigma_4\lambda_1}_{\mathrm{NC/CCb}\;\;c_1c_2c_3c_4}(p_1,p_2,p_3,p_4,p_5) &= \delta_{c_1c_2}\delta_{c_3c_4}\mathrm{iA}^{\sigma_1\sigma_2\sigma_3\sigma_4\lambda_1}_{q_1,\bar{q}_2,f_3,\bar{f}_4,W}(p_1,p_2,p_3,p_4,p_5)\\
&\quad-\delta_{c_3c_1}\delta_{c_2c_4}\sum_{V=\gamma,Z}\mathrm{iA}^{\sigma_1-\sigma_3-\sigma_2\sigma_4\lambda_1}_{q_1,\bar{f}_3,q_2,\bar{f}_4,V}(p_1,-p_3,-p_2,p_4,p_5)\\
&\quad-\frac{1}{4}\sum_a\lambda^a_{c_3c_1}\lambda^a_{c_2c_4}\mathrm{iA}^{\sigma_1-\sigma_3-\sigma_2\sigma_4\lambda_1}_{q_1,\bar{f}_3,q_2,\bar{f}_4,g}(p_1,-p_3,-p_2,p_4,p_5).
\end{aligned}
\tag{B.16}
$$

Summing the squared amplitude over all colour indices and including an average factor of $1/9$ for the initial state quarks yields for the processes NCa and CCa just a factor of

$$
N_C = \frac{1}{9}\sum_{c_1c_2}\delta^2_{c_1c_2} = \frac{1}{3},
\tag{B.17}
$$

and for the process CCb a factor of

$$N_C = \frac{1}{9}\sum_{c_1 c_2} \delta^2_{c_1 c_2}\delta^2_{c_3 c_4} = 1. \tag{B.18}$$

For the remaining processes, one has to use the Fierz identity for the Gell-Mann matrices

$$\lambda^a_{ij}\lambda^a_{kl} = -\frac{2}{3}\delta_{ij}\delta_{kl} + 2\delta_{il}\delta_{kj} \tag{B.19}$$

to obtain the colour-averaged squared matrix elements. With the definitions

$$\begin{aligned} \mathrm{iA}_V &= \mathrm{iA}^{\sigma_1\sigma_2\sigma_3\sigma_4\lambda_1}_{q_1,\bar{q}_2,f_3,\bar{f}_4,V}(p_1,p_2,p_3,p_4,p_5), \\ \mathrm{i}\widehat{\mathrm{A}}_V &= \mathrm{iA}^{\sigma_1-\sigma_3-\sigma_2\sigma_4\lambda_1}_{q_1,\bar{f}_3,q_2,\bar{f}_4,V}(p_1,-p_3,-p_2,p_4,p_5) \end{aligned} \tag{B.20}$$

one has

$$\begin{aligned} \frac{1}{9}\sum_{c_1c_2c_3c_4}\left|\mathrm{i}\mathcal{A}^{(0)\,\sigma_1\sigma_2\sigma_3\sigma_4\lambda_1}_{\mathrm{NCb}\;\;c_1c_2c_3c_4}(p_1,p_2,p_3,p_4,p_5)\right|^2 &= \frac{2}{9}\left(|\mathrm{iA}_g|^2 + |\mathrm{i}\widehat{\mathrm{A}}_g|^2 + \frac{2}{3}\mathrm{Re}\left\{[\mathrm{iA}_g][\mathrm{i}\widehat{\mathrm{A}}_g]^\star\right\}\right), \\ &\quad - \frac{8}{9}\mathrm{Re}\left\{[\sum_{\gamma,Z}\mathrm{iA}_V][\mathrm{i}\widehat{\mathrm{A}}_g]^\star + [\sum_{\gamma,Z}\mathrm{i}\widehat{\mathrm{A}}_V][\mathrm{iA}_g]^\star\right\} \\ &\quad + \frac{1}{3}\left(3|\sum_{\gamma,Z}\mathrm{iA}_V|^2 + 3|\sum_{\gamma,Z}\mathrm{i}\widehat{\mathrm{A}}_V|^2 - 2\mathrm{Re}\left\{[\sum_{\gamma,Z}\mathrm{iA}_V][\sum_{\gamma,Z}\mathrm{i}\widehat{\mathrm{A}}_V]^\star\right\}\right), \end{aligned} \tag{B.21}$$

$$\frac{1}{9}\sum_{c_1c_2c_3c_4}\left|\mathrm{i}\mathcal{A}^{(0)\,\sigma_1\sigma_2\sigma_3\sigma_4\lambda_1}_{\mathrm{NCc}\;\;c_1c_2c_3c_4}(p_1,p_2,p_3,p_4,p_5)\right|^2 = \frac{2}{9}|\mathrm{iA}_g|^2 + |\sum_{\gamma,Z}\mathrm{iA}_V|^2, \tag{B.22}$$

$$\begin{aligned} \frac{1}{9}\sum_{c_1c_2c_3c_4}\left|\mathrm{i}\mathcal{A}^{(0)\,\sigma_1\sigma_2\sigma_3\sigma_4\lambda_1}_{\mathrm{NC/CCa}\;\;c_1c_2c_3c_4}(p_1,p_2,p_3,p_4,p_5)\right|^2 &= \frac{2}{9}|\mathrm{iA}_g|^2 - \frac{8}{9}\mathrm{Re}\left\{[\mathrm{i}\widehat{\mathrm{A}}_W][\mathrm{iA}_g]^\star\right\} \\ &\quad + \frac{1}{3}\left(3|\sum_{\gamma,Z}\mathrm{iA}_V|^2 + 3|\mathrm{i}\widehat{\mathrm{A}}_W|^2 - 2\mathrm{Re}\left\{[\sum_{\gamma,Z}\mathrm{iA}_V][\mathrm{i}\widehat{\mathrm{A}}_W]^\star\right\}\right), \end{aligned} \tag{B.23}$$

$$\begin{aligned} \frac{1}{9}\sum_{c_1c_2c_3c_4}\left|\mathrm{i}\mathcal{A}^{(0)\,\sigma_1\sigma_2\sigma_3\sigma_4\lambda_1}_{\mathrm{NC/CCb}\;\;c_1c_2c_3c_4}(p_1,p_2,p_3,p_4,p_5)\right|^2 &= \frac{2}{9}|\mathrm{i}\widehat{\mathrm{A}}_g|^2 - \frac{8}{9}\mathrm{Re}\left\{[\mathrm{iA}_W][\mathrm{i}\widehat{\mathrm{A}}_g]^\star\right\} \\ &\quad + \frac{1}{3}\left(3|\mathrm{iA}_W|^2 + 3|\sum_{\gamma,Z}\mathrm{i}\widehat{\mathrm{A}}_V|^2 - 2\mathrm{Re}\left\{[\mathrm{iA}_W][\sum_{\gamma,Z}\mathrm{i}\widehat{\mathrm{A}}_V]^\star\right\}\right). \end{aligned} \tag{B.24}$$

B.2 The Non-Factorizable Corrections

Goal of this section is the calculation of an analytical expression for the non-factorizable corrections to the process (B.1). To this end, we illustrate the treatment of the non-factorizable corrections discussed in Section 2.2 by applying it to the processes relevant to our work. As was said there, in calculating a 1-loop amplitude in Leading Pole Approximation, the non-factorizable corrections receive contributions from all 1-loop diagrams, where a virtual massless particle connects the production subprocess, the decay subprocesses and the resonances with each other. However, the so-defined non-factorizable part of the amplitude contains also factorizable contributions, and we will show in this section how a gauge-invariant separation of both parts can be achieved. In what follows, the resonant boson is denoted by $V = Z, W$. The 4-vectors p_{in} and the quantities m_{in} (p_{out} and m_{out}) are the momenta and masses of the incoming (outgoing) particles coupling to the virtual massless particle. Finally, q is the loop momentum and $k = p_3 + p_4$ denotes the momentum of the resonance.

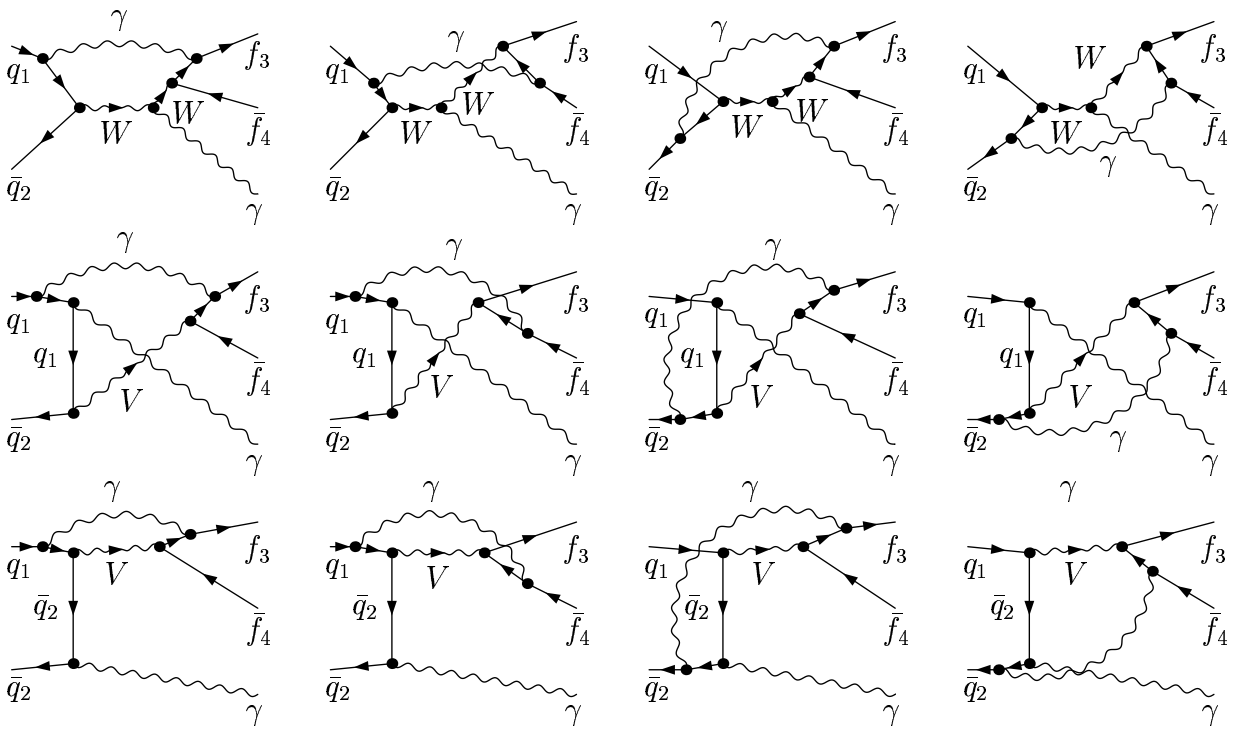

Figure B.2: The non-factorizable diagrams with the virtual massless particle connecting the initial and the final state. Depending on the considered process, the vector boson V can be either a W boson or a Z boson.

To start with, the first type of diagrams for the processes (B.1) which lead to non-factorizable corrections are shown in Figure B.2. They consist of all diagrams, where a virtual massless particle connects the production and decay subprocesses. The amplitude corresponding to these diagrams is not proportional to the resonant propagator, but shows a singular behavior for small loop momentum. To isolate this resonance, the amplitude is evaluated in ESPA, i.e. the loop momentum is set to zero wherever this does not lead to a resonance. To see how this works in detail, note that the loop integrals arising from the diagrams in Figure B.2 are given by 5-point functions and 4-point functions. All loop momenta appearing in the numerator do not contribute to the resonance structure and can be set to zero in ESPA. As a consequence, only scalar integrals remain, and the 5-point functions are of the generic form

$$\begin{aligned} &E_0(p_{\rm in}, p, k, p_{\rm out}, 0, m_{\rm in}, m_p, M_V, m_{\rm out}) \\ &\quad = \frac{(2\pi\mu)^D}{\mathrm{i}\pi^2} \int \mathrm{d}^D q \left\{ \frac{F[p_{\rm in}, k, p, p_{\rm out}, q=0]}{(q^2)((q+p_{\rm in})^2 - m_{\rm in}^2)((q+p)^2 - m_p^2)} \right. \\ &\qquad\qquad \left. \times \frac{1}{((q-k)^2 - M_V^2)((q-p_{\rm out})^2 - m_{\rm out}^2)} \right\} \end{aligned} \tag{B.25}$$

The momentum p as well as the mass m_p are here given by

$$p = \begin{cases} p_1 + p_2, & \text{in } s-\text{channel diagrams,} \\ p_{\rm in} - p_5, & \text{in } t-\text{channel diagrams,} \end{cases} \tag{B.26}$$

$$m_p = \begin{cases} m_W, & \text{in } s-\text{channel diagrams,} \\ m_{\rm in}, & \text{in } t-\text{channel diagrams.} \end{cases} \tag{B.27}$$

Besides the numerator, the ESPA implies that the loop momentum q can be also set to zero in the third propagator of the loop integral (B.25), since this propagator does not contribute to the resonance structure in the limit $k^2 \to M_V^2$. As discussed in Ref.[39], we are furthermore free to introduce a finite width before integrating out the loop momentum without worrying about gauge invariance. The resonant part of the loop integral (B.25) thus reads

$$\begin{aligned} &E_{0c,\rm nfac}^{\rm ESPA}(p_{\rm in}, p, k, p_{\rm out}, 0, m_{\rm in}, m_p, \mu_V, m_{\rm out}) \\ &\qquad = \frac{F[p_{\rm in}, k, p, p_{\rm out}, q=0]}{p^2 - m_p^2} D_{0c,\rm nfac}^{\rm ESPA}(p_{\rm in}, k, p_{\rm out}, 0, m_{\rm in}, \mu_V, m_{\rm out}), \end{aligned} \tag{B.28}$$

where

$$\begin{aligned} &D_{0c,\rm nfac}^{\rm ESPA}(p_{\rm in}, k, p_{\rm out}, 0, m_{\rm in}, \mu_V, m_{\rm out}) \\ &\quad = \frac{(2\pi\mu)^D}{\mathrm{i}\pi^2} \int \mathrm{d}^D q \left\{ \frac{1}{(q^2)(q+p_{\rm in})^2 - m_{\rm in}^2)} \frac{1}{((q-k)^2 - \mu_V^2)((q-p_{\rm out}^2) - m_{\rm out}^2)} \right\}. \end{aligned} \tag{B.29}$$

Setting the masses of external fermions to zero and taking the on-shell limit wherever this does not lead to a resonance, one has [35]

$$D^{\mathrm{ESPA}}_{0c,\mathrm{nfac}}(p_{\mathrm{in}}, k, p_{\mathrm{out}}, 0, m_{\mathrm{in}}, \mu_V, m_{\mathrm{out}}) = \frac{1}{t(k^2-\mu_V^2)}\left\{2\log\left(\frac{m_{\mathrm{in}}m_{\mathrm{out}}}{-t}+\mathrm{i}\varepsilon\right)\log\left(\frac{\lambda M_V}{-(k^2-\mu_V^2)}\right) - \log^2\left(\frac{m_{\mathrm{in}}M_V}{-\hat{t}}+\mathrm{i}\varepsilon\right) - \log^2\left(\frac{m_{\mathrm{out}}}{M_V}\right) - \frac{\pi^2}{3} - \mathrm{Li}_2\left(1-\frac{\hat{t}}{t}\right)\right\}, \quad V = W, Z. \tag{B.30}$$

Here and in the following, we adopt the notation

$$t = (p_{\mathrm{in}} - p_{\mathrm{out}})^2, \qquad \hat{t} = (p_{\mathrm{in}} - k)^2 - M_V^2, \qquad V = W, Z. \tag{B.31}$$

As can be seen, the loop integral evaluated in ESPA, and thus the amplitude corresponding to the diagrams in Figure B.2, is proportional to the resonant propagator, and the numerator contains the logarithmic infrared singularity regularized by the off-shellness $k^2 - \mu_V^2$. Applying the Leading Pole Approximation to this expression means that the momentum of the resonant particle is set on-shell everywhere except for the argument of this logarithm. The remaining diagrams in Figure B.2 contain 4-point functions, which cannot be further reduced by applying the ESPA, and are of exactly the same type as (B.30).

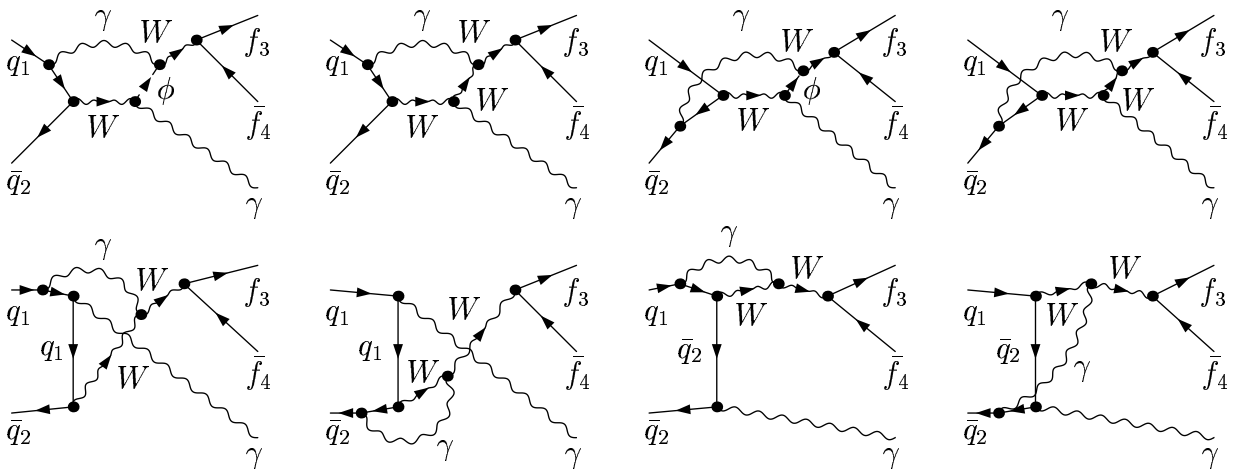

Figure B.3: The non-factorizable diagrams with the virtual massless particle connecting the initial state and the resonance.

Next, we turn to the diagrams, which contain both, factorizable as well as non-factorizable contributions. These are all the diagrams, where a virtual massless particle couples to the resonance. We here divide the diagrams in three classes, one class containing all diagrams where the massless virtual particle connects the initial state with the resonance, a second class where where the massless virtual particle connects the final state with the resonance, and a third class containing the self-energy contributions of the resonance.

The diagrams where the massless virtual particle connects the initial state with the resonance are shown in Figure B.3. Using the same notation as in the preceding case, we here encounter 4-point functions of the type

$$\begin{aligned} &D_0(p_{\rm in}, p, k, 0, m_{\rm in}, m_p, \mu_W) \\ &\quad = \frac{(2\pi\mu)^D}{\mathrm{i}\pi^2} \int \mathrm{d}^D q \, \left\{ \frac{F[p_{in}, p, k, q]}{(q^2)((q+p_{\rm in})^2 - m_{\rm in}^2)((q+p)^2 - m_p^2)((q-k)^2 - \mu_W^2)} \right\}, \end{aligned} \tag{B.32}$$

where we again used the fact that one is free to introduce a finite width before performing the loop integration without violating gauge invariance [39]. The loop integral (B.32) is already contained in the resonant factorizable corrections, where it is evaluated with the momentum of the resonant particle set on its mass shell and the infrared singularity regularized by a infinitesimal photon mass

$$\begin{aligned} &D_{0,\rm fac}(p_{\rm in}, p, k, \lambda, m_{\rm in}, m_p, M_W) \\ &= \frac{(2\pi\mu)^D}{\mathrm{i}\pi^2} \int \mathrm{d}^D q \, \left\{ \frac{F[p_{in}, k, p, q]}{(q^2 - \lambda^2)((q+p_{\rm in})^2 - m_{\rm in}^2)((q+p)^2 - m_p^2)((q-k)^2 - M_W^2)} \right\}_{k^2 = M_W^2}. \end{aligned} \tag{B.33}$$

To avoid double counting of the factorizable contribution, the contribution of the diagram to the non-factorizable corrections must then be defined as the difference

$$\begin{aligned} &D_{0,\rm nfac}(p_{\rm in}, p, k, \lambda, m_{\rm in}, m_p, \mu_W) \\ &\qquad = D_0(p_{\rm in}, p, k, 0, m_{\rm in}, m_p, \mu_W) - D_{0,\rm fac}(p_{\rm in}, p, k, \lambda, m_{\rm in}, m_p, M_W). \end{aligned} \tag{B.34}$$

The advantage of this procedure is that the so-defined factorizable and non-factorizable corrections form two separately gauge-invariant contributions to the full 1-loop amplitude. As shown in Ref.[61], the resonant part of this difference is furthermore equal to the difference evaluated in ESPA such that the loop momentum can be set to zero in the numerator and the third propagator of (B.33)

$$\begin{aligned} &D_{0,\rm nfac}(p_{\rm in}, p, k, \lambda, m_{\rm in}, m_p, M_W) \\ &\qquad = \frac{F[p_{in}, p, k, q=0]}{p^2 - m_p^2} C^{\rm ESPA}_{0c,\rm nfac}(p_{\rm in}, k, \lambda, m_{\rm in}, \mu_W) + \mathcal{O}(k^2 - \mu_W^2), \end{aligned} \tag{B.35}$$

which simplifies the calculation in the sense that we are only left with a scalar loop integral given by a 3-point function instead of the potentially tensorial 4-point function (B.32). Taking the on-shell limit wherever this does not lead to a resonance, one has for massless external fermions [35]

$$\begin{aligned} C_{0c,\mathrm{nfac}}^{\mathrm{ESPA}}(p_{\mathrm{in}},k,\lambda,m_{\mathrm{in}},\mu_W) &= \Big(C_0(p_{\mathrm{in}},k,0,m_{\mathrm{in}},\mu_W) - \big[C_0(p_{\mathrm{in}},k,\lambda,m_{\mathrm{in}},M_W)\big]_{k^2=M_W^2}\Big) \\ &= \frac{1}{\hat{t}}\left\{\log\left(\frac{m_{\mathrm{in}}M_W}{-\hat{t}}+\mathrm{i}\varepsilon\right)\right. \\ &\qquad \left.\left[\log\left(\frac{k^2-\mu_W^2}{\hat{t}}\right)+\log\left(\frac{-(k^2-\mu_W^2)}{\lambda^2}\right)+\log\left(\frac{m_{\mathrm{in}}}{M_W}\right)\right]+\frac{\pi^2}{6}\right\}. \end{aligned} \tag{B.36}$$

Again, the infrared divergence appears in the numerator of (B.36) in the form of a logarithm $\log(k^2-\mu_V^2)$, which must be evaluated off-shell. The remaining diagrams in Figure B.3 cannot be reduced to loop integrals with less propagators, and lead to the appearance 3-point functions which are exactly of the type (B.36) after subtracting the factorizable parts.

The same considerations can be applied to the diagrams shown in Figure B.4, where a resonant massless particle connects the resonance with the decay subprocess. The non-

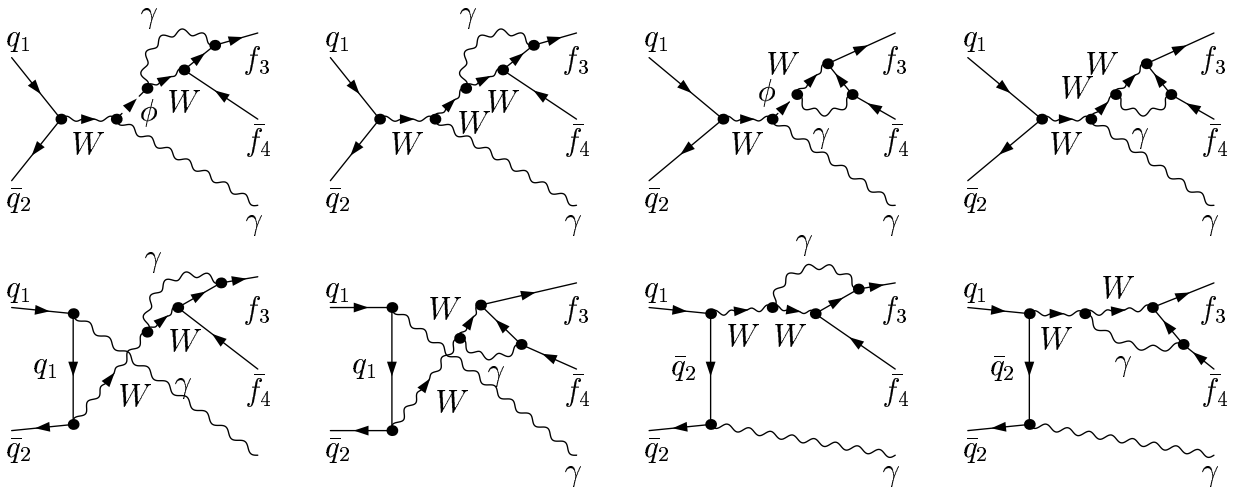

Figure B.4: The non-factorizable diagrams with the virtual massless particle connecting the resonance and the final state.

factorizable part of the corresponding 3-point functions is given by

$$\begin{aligned} C_{0c,\mathrm{nfac}}(k,p_{\mathrm{out}},0,\mu_W,m_{\mathrm{out}}) &= C_{0c}(k,p_{\mathrm{out}},0,\mu_W,m_{\mathrm{out}}) - C_{0c,\mathrm{fac}}(k,p_{\mathrm{out}},\lambda,m_W,m_{\mathrm{out}}) \\ &= \frac{(2\pi\mu)^D}{\mathrm{i}\pi^2}\int \mathrm{d}^D q\, \left\{ \frac{F[k,p_{\mathrm{out}},q]}{(q^2)((q-k)^2-\mu_W^2)((q-p_{\mathrm{out}}^2)-m_{\mathrm{out}}^2)} \right\} \\ &- \left[\frac{(2\pi\mu)^D}{\mathrm{i}\pi^2}\int \mathrm{d}^D q\, \left\{ \frac{F[k,p_{\mathrm{out}},q]}{(q^2-\lambda^2)((q-k)^2-M_W^2)((q-p_{\mathrm{out}}^2)-m_{\mathrm{out}}^2)} \right\} \right]_{k^2=M_W^2} . \end{aligned} \tag{B.37}$$

Again, the resonant part of this difference is given by the difference in ESPA, and one has

$$C_{0c,\mathrm{nfac}}(k,p_{\mathrm{out}},0,\mu_W,m_{\mathrm{out}}) = F[k,p_{\mathrm{out}},q=0]\, C^{\mathrm{ESPA}}_{0c,\mathrm{nfac}}(k,p_{\mathrm{out}},0,\mu_W,m_{\mathrm{out}}) + \mathcal{O}(k^2-\mu_W^2) \tag{B.38}$$

where for massless external fermions [35]

$$\begin{aligned} &C^{\mathrm{ESPA}}_{0c,\mathrm{nfac}}(k,p_{\mathrm{out}},0,\mu_W,m_{\mathrm{out}}) = \\ &\qquad -\frac{1}{M_W^2}\left\{ \log\left(\frac{m_{\mathrm{out}}^2}{M_W^2}\right)\log\left(\frac{-(k^2-\mu_W^2)}{\lambda M_W}\right) + \log^2\left(\frac{m_{\mathrm{out}}}{M_W}\right) + \frac{\pi^2}{6} \right\}. \end{aligned} \tag{B.39}$$

Considering finally the self-energy contributions, the corresponding diagrams are shown in Figure B.5. Note that the loop does not need to contain the vector bosons W and γ only, but can also involve charged scalars or ghosts leading to the same mass pattern. The diagrams in Figure B.5 are actually not factorizable diagrams as defined above, since they do not involve any correction to the production or decay subprocesses. However, in on-shell renormalization the factorizable corrections contain the wave-function renormalization of the decaying particle, which appears in the corrections to the vertices connecting the resonance with the production and decay subprocesses. Since the same terms also appear in the self-energy insertions of the resonant W, one has to subtract the contribution of the wave-function renormalization to avoid double counting. Furthermore, to render the self-energy contribution finite it is necessary to include the corresponding counter terms.

Altogether, one thus encounters a sum of three terms [35]

$$\begin{aligned} &B_{0c,\mathrm{nfac}}(k,0,\mu_W) = \\ &\quad B_{0c}(k,0,\mu_W) - \left[B_{0c}(k,0,\mu_W)\right]_{k^2=\mu_W^2} - (k^2-\mu_W^2)\frac{\mathrm{d}}{\mathrm{d}k^2}\left[B_0(k,0,M_W)\right]_{k^2=M_W^2} \\ &= \frac{(2\pi\mu)^D}{\mathrm{i}\pi^2}\Bigg\{ \int \mathrm{d}^D q\, \frac{F[k,q]}{(q^2)((q-k)^2-\mu_W)} - \left[\int \mathrm{d}^D q\, \frac{F[k,q]}{(q^2)((q-k)^2-\mu_W^2)}\right]_{k^2=\mu_W^2} \\ &\qquad - (k^2-\mu_W^2)\frac{\mathrm{d}}{\mathrm{d}k^2}\left[\int \mathrm{d}^D q\, \frac{F[k,q]}{(q^2-\lambda^2)((q-k)^2-M_W^2)}\right]_{k^2=M_W^2} \Bigg\}, \end{aligned} \tag{B.40}$$

where the second integral stems from the self-energy counter term, and the term involving the derivative is the subtraction term arising from the wave-function renormalization.

Again, this difference is in Leading Pole Approximation equal to the difference in ESPA, such that one can replace (B.40) by

$$B_{0c,\mathrm{nfac}}(k,0,\mu_W) = F[k,q=0]B^{\mathrm{ESPA}}_{0c,\mathrm{nfac}}(k,0,\mu_W) + \mathcal{O}(k^2-\mu_W^2). \tag{B.41}$$

Evaluating this expression for massless external fermions, and taking the on-shell limit wherever this does not lead to a resonance, one has [35]

$$B^{\mathrm{ESPA}}_{0c,\mathrm{nfac}}(k,0,\mu_W) = \frac{1}{M_W^2}\left\{\log\left(\frac{\lambda M_W}{-k^2+\mu_W^2}\right)+1\right\}. \tag{B.42}$$

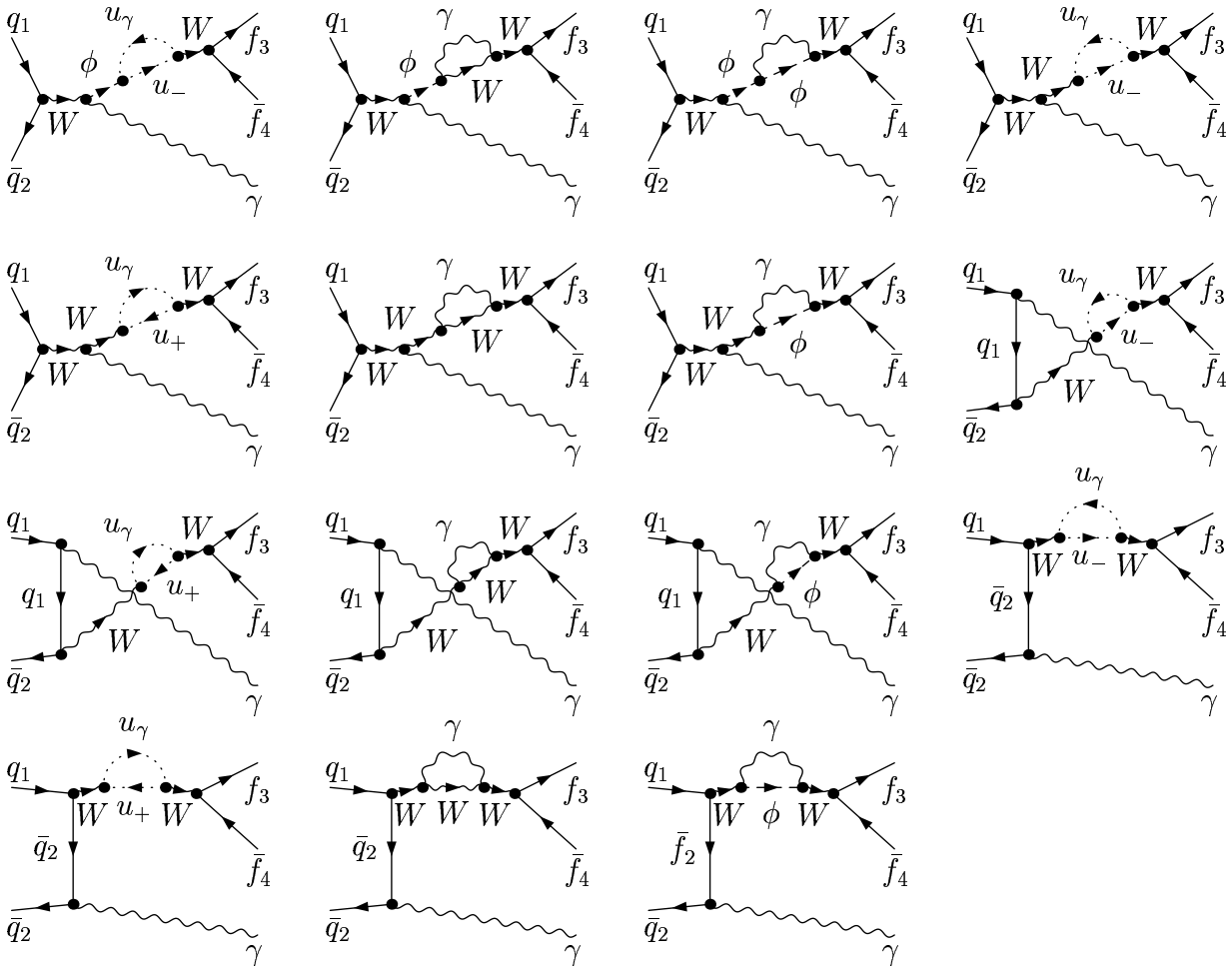

Figure B.5: The diagrams involving the self-energy of the resonance.

At this point, we are finally in the position to provide an analytical expression for the non-factorizable corrections. In fact, the amplitude calculated by the methods described above is proportional to the factorizable Born cross section in LPA

$$\mathcal{A}^{(1),\mathrm{LPA}}_{q_1 q_2,V,\mathrm{nfac}}(k^2) = \frac{1}{2}\mathcal{A}^{(0),\mathrm{LPA}}_{q_1 q_2,V}(k^2)\delta^{(1),\mathrm{virt}}_{\mathrm{nfac}}, \tag{B.43}$$

with the factorizable Born cross section $\mathcal{A}^{(0),\mathrm{LPA}}_{q_1 q_2,V}$ given by setting the finite width in the s-channel propagator of (B.7) to zero, and by inserting the resulting expression into (B.3) and (B.5). The correction factor, on the other hand, is given by

$$\delta^{(1),\mathrm{virt}}_{\mathrm{nfac}} = -\sum_{i=1,2}\sum_{j=3,4} Q_i\tau_i Q_j\tau_j \frac{\alpha}{\pi}\mathrm{Re}\left\{\Delta^V(p_i,k,p_j)\right\}, \quad V = W,Z. \tag{B.44}$$

with [35]

$$\begin{aligned}\Delta^V(p_{\mathrm{in}},k,p_{\mathrm{out}}) = &-2(p_{\mathrm{in}}p_{\mathrm{out}})(k^2-\mu_V^2)D^{\mathrm{ESPA}}_{0c,\mathrm{nfac}}(p_{\mathrm{in}},k,p_{\mathrm{out}},0,m_{\mathrm{in}},\mu_V,m_{\mathrm{out}})\\ &-2(p_{\mathrm{in}}k)C^{\mathrm{ESPA}}_{0c,\mathrm{nfac}}(p_{\mathrm{in}},k,0,m_{\mathrm{in}},\mu_W)-2(kp_{\mathrm{out}})C^{\mathrm{ESPA}}_{0c,\mathrm{nfac}}(k,p_{\mathrm{out}},0,\mu_W,m_{\mathrm{out}})\\ &-2\frac{M_V^2}{(k^2-\mu_V^2)}B^{\mathrm{ESPA}}_{0c,\mathrm{nfac}}(k,0,\mu_W)\end{aligned} \tag{B.45}$$

where again p_{in} and m_{in} (p_{out} and m_{out}) are the momenta and masses of the incoming (outgoing) particles coupling to the virtual massless particle, and $k = p_3 + p_4$ is the momentum of the resonance. Upon inserting the expressions (B.30), (B.36), (B.39) and (B.42), the correction factor can in case of a single resonance be brought to the compact generic form [35]

$$\Delta^V(p_{\mathrm{in}},k,p_{\mathrm{out}}) = 2\log\left(\frac{\lambda M_V}{-(k^2-\mu_V^2)}\right)\left[\log\left(\frac{\hat{t}}{t}\right)-1\right]-2-\mathrm{Li}_2\left(1-\frac{\hat{t}}{t}\right). \tag{B.46}$$

The kinematical variables $\hat{t}$ and t are here again given by (B.31). Note, that the form of this expression is completely independent of the considered process, such that it can be used for an arbitrary calculation involving the Pole Expansion Method with one single resonance. For several resonances, three more types of non-factorizable diagrams appear. To be specific, these are all diagrams where the virtual massless particle connects the decay products of one resonance with the decay products of another resonance, the decay products of one resonance with another resonance or two different resonances. The treatment of these cases is exactly the same as described above, resulting in two more types of loop integrals evaluated in ESPA, as well as in additional contributions to the correction factor (B.44), as we show in Appendix C.

B.3 The Real QED-Corrections

The determination of the helicity amplitudes for the real QED corrections can in principle be performed in the same way as described in Section B.1 for the case of the Born amplitudes. The calculation is much more involved, though, since the set of generic diagram comprises here 31 instead of five diagrams. These diagrams can be obtained from the ones shown in Figure B.1 in the following way. A total number of thirty diagrams is obtained by attaching the additional real photon to each fermion line and to each charged vector boson in the Born graphs shown in Figure B.1. Note that there are always two diagrams with both photons coupling to the same line, which are related to each other by an interchange of the two photons. The one remaining diagram results from both photons coupling to the intermediate vector boson via a $VV\gamma\gamma$ coupling. Apart from the increased number of diagrams, one has to calculate the generic amplitude for two different polarization combinations, since a final state with both photons having the same helicity is not related by any discrete symmetry to a final state with two photons of opposite helicity.

The classification of the final states can be done in exactly the same way as in the Born case, i.e. one simply adds an additional photon to the final states of the various reactions displayed in Table B.1. Adopting the conventions of Section B.1, the generic amplitude of the QED-Bremsstrahlung process reads

$$\mathrm{i}\mathcal{A}^{\sigma_1\sigma_2\sigma_3\sigma_4\lambda_1\lambda_2}_{\mathrm{real,QED}\ c_1c_2c_3c_4}(p_1,p_2,p_3,p_4,p_5,p_6) = \sum_V C^{f_3,\bar{f}_4,V}_{c_1c_2c_3c_4}\,\mathrm{iA}^{\sigma_1\sigma_2\sigma_3\sigma_4\lambda_1\lambda_2}_{q_1,\bar{q}_2,f_3,\bar{f}_4,V,\gamma}(p_1,p_2,p_3,p_4,p_5,p_6), \tag{B.47}$$

where the sum over V is again taken over all Standard Model bosons and

$$\begin{aligned}\mathrm{iA}^{\sigma_1\sigma_2\sigma_3\sigma_4\lambda_1\lambda_2}_{q_1,\bar{q}_2,f_3,\bar{f}_4,V,\gamma}(p_1,p_2,p_3,p_4,p_5,p_6) &= -4e^4 C^{\sigma_1}_{V\bar{q}_2q_1} C^{\sigma_3}_{V\bar{f}_3f_4} delta_{\sigma_1-\sigma_2}\delta_{\sigma_3-\sigma_4} \\ &\quad\times \mathrm{B}^{\sigma_1\sigma_3\lambda_1\lambda_2}_{V\gamma}(p_1,p_2,p_3,p_4,p_5,p_6,Q_{q_1},Q_{\bar{q}_2},Q_{f_3},Q_{\bar{f}_4}).\end{aligned} \tag{B.48}$$

The colour structure of the amplitude has here been absorbed in the factor $C^{f_3,\bar{f}_4,V}_{c_1c_2c_3c_4}$ displayed in (B.4). The couplings of the gauge boson V to the fermion f_a and the anti-fermion $\bar{f}_b$ is again denoted by $C^{\sigma_a}_{V\bar{f}_bf_a}$ and can be read off Table B.5.

As a matter of fact, the generic functions for the QED-Bremsstrahlung process can be divided into six parts,

$$\begin{aligned}&\mathrm{B}^{\sigma_1\sigma_3\lambda_1\lambda_2}_{V\gamma}(p_1,p_2,p_3,p_4,p_5,p_6,Q_1,Q_2,Q_3,Q_4) \\ &\qquad= \sum_{i=1}^{4} Q_{f_i}\mathrm{B}^{\sigma_1\sigma_3\lambda_1\lambda_2}_{i,V\gamma}(p_1,p_2,p_3,p_4,p_5,p_6,Q_1,Q_2,Q_3,Q_4) \\ &\qquad\quad + C_{V\gamma V}\mathrm{B}^{\sigma_1\sigma_3\lambda_1\lambda_2}_{5,V\gamma}(p_1,p_2,p_3,p_4,p_5,p_6,Q_1,Q_2,Q_3,Q_4) \\ &\qquad\qquad + \mathrm{B}^{\sigma_1\sigma_3\lambda_1\lambda_2}_{6,V\gamma}(p_1,p_2,p_3,p_4,p_5,p_6,Q_1,Q_2,Q_3,Q_4).\end{aligned} \tag{B.49}$$

The first four terms correspond here to the contributions of the diagrams where the additional photon γ_2 couples to one of the external fermion lines. The fifth term, on the other hand, contains the contribution of all diagrams, where the additional photon γ_2 couples to the resonance, whereas the final state photon γ_1 couples to one of the external fermion lines. Finally, there is a sixth contribution, arising from diagrams where both final-state photons couple to the resonance. The six generic functions for these cases can again be calculated in the Weyl-van der Waerden formalism, which yields for both photon helicities positive

$$\begin{aligned}
\mathrm{B}^{++++}_{1,V\gamma}(p_1,p_2,p_3,p_4,p_5,p_6,Q_1,Q_2,Q_3,Q_4) &= \frac{\langle p_4 p_1\rangle^2}{\langle p_4 p_5\rangle\langle p_4 p_6\rangle\langle p_1 p_6\rangle} \\
&\Bigg\{ P_V(p_3+p_4)\Bigg[\frac{Q_1\langle p_3 p_2\rangle^\star\langle p_4 p_1\rangle}{\langle p_1 p_5\rangle} - \frac{Q_2\langle p_4|p_2+p_5|p_3\rangle}{\langle p_2 p_5\rangle} \\
&\quad + C_{V\gamma V} P_V(p_3+p_4+p_5)\langle p_5 p_3\rangle^\star\langle p_4|p_1+p_6|p_2\rangle\Bigg] \\
&\quad - \frac{Q_3}{\langle p_3 p_5\rangle} P_V(p_3+p_4+p_5)\langle p_4|p_1+p_6|p_2\rangle\Bigg\}, \qquad \text{(B.50)}
\end{aligned}$$

$$\begin{aligned}
\mathrm{B}^{++++}_{2,V\gamma}(p_1,p_2,p_3,p_4,p_5,p_6,Q_1,Q_2,Q_3,Q_4) &= \frac{\langle p_4 p_1\rangle^2}{\langle p_4 p_5\rangle\langle p_4 p_6\rangle\langle p_2 p_6\rangle} \\
&\Bigg\{ P_V(p_3+p_4)\Bigg[\frac{-Q_2\langle p_1 p_3\rangle^\star\langle p_2 p_4\rangle}{\langle p_2 p_5\rangle} - \frac{Q_1\langle p_4|p_2+p_6|p_3\rangle}{\langle p_1 p_5\rangle} \\
&\quad + C_{V\gamma V} P_V(p_3+p_4+p_5)\langle p_5 p_3\rangle^\star\langle p_4|p_2+p_6|p_1\rangle\Bigg] \\
&\quad - \frac{Q_3}{\langle p_3 p_5\rangle} P_V(p_3+p_4+p_5)\langle p_4|p_2+p_6|p_1\rangle\Bigg\}, \qquad \text{(B.51)}
\end{aligned}$$

$$\begin{aligned}
\mathrm{B}^{++++}_{3,V\gamma}(p_1,p_2,p_3,p_4,p_5,p_6,Q_1,Q_2,Q_3,Q_4) &= \frac{\langle p_4 p_1\rangle^2}{\langle p_4 p_5\rangle\langle p_4 p_6\rangle\langle p_3 p_6\rangle} \\
&\Bigg\{ P_V(p_3+p_4+p_6)\Bigg[- \frac{Q_2\langle p_4|p_2+p_5|p_1\rangle}{\langle p_2 p_5\rangle} - \frac{Q_1\langle p_4|p_1+p_5|p_2\rangle}{\langle p_1 p_5\rangle} \\
&\quad - C_{V\gamma V} P_V(p_1+p_2)\langle p_1 p_2\rangle^\star\langle p_4|p_2+p_1|p_5\rangle\Bigg] \\
&\quad + \frac{Q_3\langle p_1 p_2\rangle^\star\langle p_3 p_4\rangle}{\langle p_3 p_5\rangle} P_V(p_1+p_2)\Bigg\}, \qquad \text{(B.52)}
\end{aligned}$$

$$\mathrm{B}^{++++}_{4,V\gamma}(p_1,p_2,p_3,p_4,p_5,p_6,Q_1,Q_2,Q_3,Q_4) = 0, \qquad \text{(B.53)}$$

$$\mathrm{B}^{++++}_{5,V\gamma}(p_1,p_2,p_3,p_4,p_5,p_6,Q_1,Q_2,Q_3,Q_4) = \frac{\langle p_4p_1\rangle^2}{\langle p_4p_5\rangle\langle p_4p_6\rangle}$$
$$\Bigg\{P_V(p_3+p_4)P_V(p_3+p_4+p_6)\langle p_6p_3\rangle^\star\Bigg[-\frac{Q_2\langle p_4|p_2+p_5|p_1\rangle}{\langle p_2p_5\rangle}+\frac{Q_1\langle p_4|p_1+p_5|p_2\rangle}{\langle p_1p_5\rangle}\Bigg]$$
$$+\frac{Q_3}{\langle p_3p_5\rangle}P_V(p_1+p_2)P_V(p_3+p_4+p_5)\langle p_1p_2\rangle^\star\langle p_4|p_2+p_1|p_6\rangle\Bigg\}, \quad \text{(B.54)}$$

$$\mathrm{B}^{++++}_{6,V\gamma}(p_1,p_2,p_3,p_4,p_5,p_6,Q_1,Q_2,Q_3,Q_4) = C^2_{V\gamma V}\frac{\langle p_4p_1\rangle^2\langle p_1p_2\rangle^\star}{\langle p_4p_5\rangle\langle p_4p_6\rangle}$$
$$P_V(p_1+p_2)P_V(p_3+p_4)\Bigg[P_V(p_3+p_4+p_5)\langle p_5p_3\rangle^\star\langle p_4|p_2+p_1|p_6\rangle$$
$$+P_V(p_3+p_4+p_6)\langle p_6p_3\rangle^\star\langle p_4|p_2+p_1|p_5\rangle\Bigg]. \quad \text{(B.55)}$$

The corresponding results for both photon helicities negative can be obtained in the same way, and they read

$$\mathrm{B}^{++-+}_{1,V\gamma}(p_1,p_2,p_3,p_4,p_5,p_6,Q_1,Q_2,Q_3,Q_4) = \frac{1}{\langle p_4p_6\rangle\langle p_3p_5\rangle^\star\langle p_1p_6\rangle}$$
$$\Bigg\{P_V(p_3+p_4)\Bigg[-\frac{Q_1\langle p_3p_2\rangle^\star}{(p_1+p_5+p_6)^2\langle p_1p_5\rangle^\star}$$
$$\Big(\langle p_4|p_1+p_5|p_3\rangle\langle p_4|p_1+p_5|p_6\rangle\langle p_1p_6\rangle+\langle p_1p_4\rangle\langle p_1p_5\rangle^\star\langle p_1p_5\rangle\langle p_2p_4\rangle\langle p_3p_2\rangle^\star\Big)$$
$$-\frac{Q_2}{\langle p_2p_5\rangle^\star}\langle p_4p_1\rangle^2(\langle p_2p_3\rangle^\star)^2-C_{V\gamma V}P_V(p_3+p_4+p_5)\langle p_1|p_4+p_5|p_3\rangle\langle p_3p_2\rangle^\star\langle p_4p_1\rangle\langle p_5p_4\rangle\Bigg]$$
$$-\frac{Q_4}{\langle p_4p_5\rangle^\star}P_V(p_3+p_4+p_5)\langle p_4p_1\rangle\langle p_3p_2\rangle^\star\langle p_1|p_4+p_5|p_3\rangle\Bigg\}, \quad \text{(B.56)}$$

$$\mathrm{B}^{++-+}_{2,V\gamma}(p_1,p_2,p_3,p_4,p_5,p_6,Q_1,Q_2,Q_3,Q_4) = \frac{1}{\langle p_4p_6\rangle\langle p_3p_5\rangle^\star\langle p_2p_6\rangle}$$
$$\Bigg\{P_V(p_3+p_4)\Bigg[-\frac{Q_2\langle p_4p_1\rangle}{(p_2+p_5+p_6)^2\langle p_2p_5\rangle^\star}$$
$$\Big(\langle p_5|p_2+p_6|p_3\rangle\langle p_4|p_2+p_6|p_3\rangle\langle p_2p_5\rangle^\star+\langle p_1p_3\rangle^\star\langle p_2p_6\rangle^\star\langle p_2p_6\rangle\langle p_2p_3\rangle^\star\langle p_4p_1\rangle\Big)$$
$$+\frac{Q_1}{\langle p_1p_5\rangle^\star}\langle p_4|p_1+p_5|p_3\rangle^2+C_{V\gamma V}P_V(p_3+p_4+p_5)\langle p_4|p_2+p_6|p_3\rangle\langle p_1|p_4+p_5|p_3\rangle\langle p_5p_4\rangle\Bigg]$$
$$+\frac{Q_4}{\langle p_4p_5\rangle^\star}P_V(p_3+p_4+p_5)\langle p_1|p_4+p_5|p_3\rangle\langle p_4|p_2+p_6|p_3\rangle\Bigg\}, \quad \text{(B.57)}$$

$$\mathrm{B}^{++-+}_{3,V\gamma}(p_1,p_2,p_3,p_4,p_5,p_6,Q_1,Q_2,Q_3,Q_4) = \frac{1}{\langle p_4p_6\rangle\langle p_3p_5\rangle^\star\langle p_3p_6\rangle}$$
$$\Bigg\{P_V(p_3+p_4+p_6)\langle p_4|p_3+p_6|p_2\rangle\Bigg[-\frac{Q_2\langle p_4p_1\rangle\langle p_3p_2\rangle^\star}{\langle p_2p_5\rangle^\star}-\frac{Q_1}{\langle p_1p_5\rangle^\star}\langle p_4|p_2+p_6|p_3\rangle$$
$$-C_{V\gamma V}P_V(p_1+p_2)\Big(\langle p_5p_1\rangle\langle p_5p_4\rangle\langle p_5p_3\rangle^\star+\langle p_5|p_2+p_1|p_3\rangle\langle p_4p_1\rangle\Big)\Bigg]$$
$$+P_V(p_1+p_2)\Bigg[-\frac{Q_3}{(p_3+p_5+p_6)^2}\langle p_6p_4\rangle\langle p_3p_6\rangle^\star\langle p_4p_1\rangle\langle p_5|p_3+p_6|p_2\rangle$$
$$-\frac{Q_4}{\langle p_4p_5\rangle^\star}\langle p_1|p_4+p_5|p_3\rangle\langle p_4|p_3+p_6|p_2\rangle\Bigg]\Bigg\}, \quad \text{(B.58)}$$

$$\mathrm{B}^{++-+}_{4,V\gamma}(p_1,p_2,p_3,p_4,p_5,p_6,Q_1,Q_2,Q_3,Q_4) = \frac{1}{\langle p_4p_6\rangle\langle p_3p_5\rangle^\star}$$
$$\left\{\frac{Q_4}{(p_4+p_5+p_6)^2\langle p_4p_5\rangle^\star}P_V(p_1+p_2)\langle p_5p_3\rangle^\star\langle p_3p_2\rangle^\star\langle p_5p_4\rangle\langle p_1|p_4+p_5|p_6\rangle\right\} \quad \text{(B.59)}$$

$$\mathrm{B}^{++-+}_{5,V\gamma}(p_1,p_2,p_3,p_4,p_5,p_6,Q_1,Q_2,Q_3,Q_4) = \frac{1}{\langle p_4p_6\rangle\langle p_3p_5\rangle^\star}$$
$$\Bigg\{P_V(p_3+p_4)P_V(p_3+p_4+p_6)\langle p_6p_3\rangle^\star\langle p_4|p_3+p_6|p_2\rangle\left[-\frac{Q_2\langle p_3p_2\rangle^\star\langle p_4p_1\rangle}{\langle p_2p_5\rangle^\star}-\frac{Q_1\langle p_4|p_2+p_6|p_3\rangle}{\langle p_1p_5\rangle^\star}\right]$$
$$+\frac{Q_4}{\langle p_4p_5\rangle}P_V(p_1+p_2)P_V(p_3+p_4+p_5)\Big(-\langle p_6p_2\rangle^\star\langle p_6p_3\rangle^\star\langle p_6p_4\rangle+\langle p_2p_3\rangle^\star\langle p_4|p_2+p_1|p_6\rangle\Big)\Bigg\}, \quad \text{(B.60)}$$

$$\mathrm{B}^{++-+}_{6,V\gamma}(p_1,p_2,p_3,p_4,p_5,p_6,Q_1,Q_2,Q_3,Q_4) = \frac{1}{\langle p_4p_6\rangle\langle p_3p_5\rangle^\star}$$
$$P_V(p_1+p_2)P_V(p_3+p_4)\Bigg\{C^2_{V\gamma V}\Bigg[P_V(p_3+p_4+p_6)\langle p_4|p_3+p_6|p_2\rangle\langle p_6p_3\rangle^\star$$
$$\Big(\langle p_5p_1\rangle\langle p_5p_4\rangle\langle p_5p_3\rangle^\star+\langle p_5|p_2+p_1|p_3\rangle\langle p_4p_1\rangle\Big)$$
$$+P_V(p_3+p_4+p_5)\langle p_1|p_4+p_5|p_3\rangle\langle p_5p_4\rangle\Big(\langle p_6p_2\rangle^\star\langle p_6p_3\rangle^\star\langle p_6p_4\rangle+\langle p_4|p_2+p_1|p_6\rangle\langle p_3p_2\rangle^\star\Big)\Bigg]$$
$$+C_{VV\gamma\gamma}\langle p_1p_4\rangle\langle p_2p_3\rangle^\star\langle p_4p_5\rangle\langle p_6p_3\rangle^\star\Bigg]\Bigg\}. \quad \text{(B.61)}$$

In the above expressions, a product like $\langle p_1|p_4+p_6|p_5\rangle$ is defined by

$$\langle a|b+c|d\rangle = \langle ab\rangle\langle db\rangle^\star + \langle ac\rangle\langle dc\rangle^\star, \tag{B.62}$$

and the parameter

$$C_{VV\gamma\gamma} = \delta_{VW} = \begin{cases} 1, & \text{for } V = W \\ 0, & \text{for } V = \gamma, Z, g \end{cases} \tag{B.63}$$

denotes the quadrilinear coupling of the two photons to the intermediate gauge boson V.

The other helicity combinations can be calculated by

$$\begin{aligned}
&\mathrm{B}^{-+\lambda_1+}_{1,V\gamma}(p_1,p_2,p_3,p_4,p_5,p_6,Q_1,Q_2,Q_3,Q_4) \\
&\qquad = -\mathrm{B}^{++\lambda_1+}_{2,V\gamma}(p_2,p_1,p_3,p_4,p_5,p_6,-Q_2,-Q_1,Q_3,Q_4), \\
&\mathrm{B}^{-+\lambda_1+}_{2,V\gamma}(p_1,p_2,p_3,p_4,p_5,p_6,Q_1,Q_2,Q_3,Q_4) \\
&\qquad = -\mathrm{B}^{++\lambda_1+}_{1,V\gamma}(p_2,p_1,p_3,p_4,p_5,p_6,-Q_2,-Q_1,Q_3,Q_4), \\
&\mathrm{B}^{-+\lambda_1+}_{i,V\gamma}(p_1,p_2,p_3,p_4,p_5,p_6,Q_1,Q_2,Q_3,Q_4) \\
&\qquad = \mathrm{B}^{++\lambda_1+}_{i,V\gamma}(p_2,p_1,p_3,p_4,p_5,p_6,-Q_2,-Q_1,Q_3,Q_4), \\
&\qquad\quad i = 3,4,5,6,
\end{aligned} \tag{B.64}$$

$$\begin{aligned}
&\mathrm{B}^{+-\lambda_1+}_{3,V\gamma}(p_1,p_2,p_3,p_4,p_5,p_6,Q_1,Q_2,Q_3,Q_4) \\
&\qquad = -\mathrm{B}^{++\lambda_1+}_{4,V\gamma}(p_1,p_2,p_4,p_3,p_5,p_6,Q_1,Q_2,-Q_4,-Q_3), \\
&\mathrm{B}^{+-\lambda_1+}_{4,V\gamma}(p_1,p_2,p_3,p_4,p_5,p_6,Q_1,Q_2,Q_3,Q_4) \\
&\qquad = -\mathrm{B}^{++\lambda_1+}_{3,V\gamma}(p_1,p_2,p_4,p_3,p_5,p_6,Q_1,Q_2,-Q_4,-Q_3), \\
&\mathrm{B}^{+-\lambda_1+}_{i,V\gamma}(p_1,p_2,p_3,p_4,p_5,p_6,Q_1,Q_2,Q_3,Q_4) \\
&\qquad = \mathrm{B}^{++\lambda_1+}_{i,V\gamma}(p_1,p_2,p_4,p_3,p_5,p_6,Q_1,Q_2,-Q_4,-Q_3), \\
&\qquad\quad i = 1,2,5,6,
\end{aligned} \tag{B.65}$$

$$\begin{aligned}
&\mathrm{B}^{--\lambda_1+}_{1,V\gamma}(p_1,p_2,p_3,p_4,p_5,p_6,Q_1,Q_2,Q_3,Q_4) \\
&\qquad = -\mathrm{B}^{++\lambda_1+}_{2,V\gamma}(p_2,p_1,p_4,p_3,p_5,p_6,-Q_2,-Q_1,-Q_4,-Q_3), \\
&\mathrm{B}^{--\lambda_1+}_{2,V\gamma}(p_1,p_2,p_3,p_4,p_5,p_6,Q_1,Q_2,Q_3,Q_4) \\
&\qquad = -\mathrm{B}^{++\lambda_1+}_{1,V\gamma}(p_2,p_1,p_4,p_3,p_5,p_6,-Q_2,-Q_1,-Q_4,-Q_3), \\
&\mathrm{B}^{--\lambda_1+}_{3,V\gamma}(p_1,p_2,p_3,p_4,p_5,p_6,Q_1,Q_2,Q_3,Q_4) \\
&\qquad = -\mathrm{B}^{++\lambda_1+}_{4,V\gamma}(p_2,p_1,p_4,p_3,p_5,p_6,-Q_2,-Q_1,-Q_4,-Q_3), \\
&\mathrm{B}^{--\lambda_1+}_{4,V\gamma}(p_1,p_2,p_3,p_4,p_5,p_6,Q_1,Q_2,Q_3,Q_4) \\
&\qquad = -\mathrm{B}^{++\lambda_1+}_{3,V\gamma}(p_2,p_1,p_4,p_3,p_5,p_6,-Q_2,-Q_1,-Q_4,-Q_3),
\end{aligned}$$

$$\begin{aligned}&\mathrm{B}_{i,V\gamma}^{--\lambda_1+}(p_1,p_2,p_3,p_4,p_5,p_6,Q_1,Q_2,Q_3,Q_4)\\&\quad=\mathrm{B}_{i,V\gamma}^{++\lambda_1+}(p_2,p_1,p_4,p_3,p_5,p_6,-Q_2,-Q_1,-Q_4,-Q_3),\qquad i=5,6\end{aligned}\tag{B.66}$$

$$\begin{aligned}&\mathrm{B}_{i,V\gamma}^{\sigma_1\sigma_4\lambda_1-}(p_1,p_2,p_3,p_4,p_5,p_6,Q_1,Q_2,Q_3,Q_4)\\&\quad=\left[\mathrm{B}_{i,V\gamma}^{-\sigma_1-\sigma_4-\lambda_1+}(p_1,p_2,p_3,p_4,p_5,p_6,Q_1,Q_2,Q_3,Q_4)\right]^\star\Big|_{P_V^\star\to P_V},\ i=1,\ldots,6.\end{aligned}\tag{B.67}$$

Finally, the generic amplitudes for the Bremsstrahlung processes corresponding to the reactions displayed in Table B.1 and the expressions for the squared amplitudes averaged over spin and colours can be obtained by the replacements

$$\mathrm{i}\mathcal{A}_{c_1c_2c_3c_4}^{(0)\,\sigma_1\sigma_2\sigma_3\sigma_4\lambda}(p_1,p_2,p_3,p_4,p_5)\longrightarrow\mathrm{i}\mathcal{A}_{\mathrm{real,QED}\ c_1c_2c_3c_4}^{\sigma_1\sigma_2\sigma_3\sigma_4\lambda_1\lambda_2}(p_1,p_2,p_3,p_4,p_5,p_6)\tag{B.68}$$

and

$$\mathrm{iA}_{q_1,q_2,f_3,\bar{f}_4}^{\sigma_1\sigma_2\sigma_3\sigma_4\lambda}(p_1,p_2,p_3,p_4,p_5)\longrightarrow\mathrm{iA}_{q_1,q_2,f_3,\bar{f}_4,\gamma}^{\sigma_1\sigma_2\sigma_3\sigma_4\lambda_1\lambda_2}(p_1,p_2,p_3,p_4,p_5,p_6)\tag{B.69}$$

from the results (B.10) to (B.24) derived in the last section.

B.4 The Real QCD-Corrections

Turning now to the QCD-Bremsstrahlung process, the classification of the final states can again be done by just adding the additional gluon to each of the final states of the reactions shown in Table B.1. Furthermore, the generic diagrams can again be obtained from the Born diagrams shown in Figure B.1 by attaching the additional gluon to the various quark lines as well as to the intermediate gluon line in the diagrams with the final state containing quarks. As opposed to the QED case, there are no diagrams where both final-state vector bosons couple to the line of the intermediate vector-boson, such that we end up with a total number of 28 generic diagrams. The generic amplitudes can then directly be obtained from corresponding expressions for the QED-Bremsstrahlung process (B.50) to (B.61). However, the resulting generic amplitude has a much more complicated colour structure as in the cases considered so far. In fact, all diagrams with the external gluon coupling to the same line have the same colour structure, such that there are five different colour structures and the amplitude can be split in five parts. Adopting again the

notation $C^{f_3,\bar{f}_4,V}_{c_1c_2c_3c_4}$ for the tensor defined in (B.4), we get

$$\begin{aligned}
&\mathrm{i}\mathcal{A}^{\sigma_1\sigma_2\sigma_3\sigma_4\lambda_1\lambda_2}_{\text{real,QCD}\ c_1c_2c_3c_4a}(p_1,p_2,p_3,p_4,p_5,p_6)\\
&\qquad=\sum_V\Bigg(\frac{\lambda^a_{cc_1}}{2}C^{f_3,\bar{f}_4,V}_{c\,c_2c_3c_4}\mathrm{iA}^{\sigma_1\sigma_2\sigma_3\sigma_4\lambda_1\lambda_2}_{1\ q_1,\bar{q}_2,f_3,\bar{f}_4,V,g}(p_1,p_2,p_3,p_4,p_5,p_6)\\
&\qquad\quad+\frac{\lambda^a_{c_2c}}{2}C^{f_3,\bar{f}_4,V}_{c_1c\,c_3c_4}\mathrm{iA}^{\sigma_1\sigma_2\sigma_3\sigma_4\lambda_1\lambda_2}_{2\ q_1,\bar{q}_2,f_3,\bar{f}_4,V,g}(p_1,p_2,p_3,p_4,p_5,p_6)\\
&\qquad\quad+\delta_{f_3q}\frac{\lambda^a_{c_3c}}{2}C^{f_3,\bar{f}_4,V}_{c_1c_2c\,c_4}\mathrm{iA}^{\sigma_1\sigma_2\sigma_3\sigma_4\lambda_1\lambda_2}_{3\ q_1,\bar{q}_2,f_3,\bar{f}_4,V,g}(p_1,p_2,p_3,p_4,p_5,p_6)\\
&\qquad\quad+\delta_{f_3q}\frac{\lambda^a_{cc_4}}{2}C^{f_3,\bar{f}_4,V}_{c_1c_2c_3c}\mathrm{iA}^{\sigma_1\sigma_2\sigma_3\sigma_4\lambda_1\lambda_2}_{4\ q_1,\bar{q}_2,f_3,\bar{f}_4,V,g}(p_1,p_2,p_3,p_4,p_5,p_6)\\
&\qquad\quad+\delta_{Vg}(\mathrm{i}C^{abc})\frac{\lambda^b_{c_2c_1}}{2}\frac{\lambda^c_{c_3c_4}}{2}\mathrm{iA}^{\sigma_1\sigma_2\sigma_3\sigma_4\lambda_1\lambda_2}_{5\ q_1,\bar{q}_2,f_3,\bar{f}_4,V,g}(p_1,p_2,p_3,p_4,p_5,p_6)\Bigg),
\end{aligned}\tag{B.70}$$

where the $\mathrm{A}_i, i=1,\ldots 4$ denote the contributions of the diagrams where the additional gluon couples to the external quark line q_i, and A_5 contains the contributions of the diagrams where the additional gluon couples to an intermediate gluon. Furthermore, we used the notations

$$\delta_{Vg}=\begin{cases}1, & \text{for } V=g\\ 0, & \text{for } V=\gamma,Z,W\end{cases},\qquad \delta_{f_3q}=\begin{cases}1, & \text{for hadronic final states}\\ 0, & \text{for leptonic final states,}\end{cases}\tag{B.71}$$

and the parameters C^{abc} denote the QCD structure constants defined by the commutator relations

$$\left[\frac{\lambda^a}{2},\frac{\lambda^b}{2}\right]=\mathrm{i}C^{abc}\frac{\lambda^c}{2}.\tag{B.72}$$

Finally, in (B.70) we used the Einstein summation convention for the sum over the colour indices b and c.

The five colour-neutral parts of the generic function in (B.70) are as in (B.48) given by

$$\begin{aligned}
\mathrm{iA}^{\sigma_1\sigma_2\sigma_3\sigma_4\lambda_1\lambda_2}_{i\ q_1,\bar{q}_2,f_3,\bar{f}_4,V,g}(p_1,p_2,p_3,p_4,p_5,p_6)&=-4e^4C^{\sigma_1}_{V\bar{q}_2q_1}C^{\sigma_3}_{V\bar{f}_3f_4}\delta_{\sigma_1-\sigma_2}\delta_{\sigma_3-\sigma_4}\\
&\quad\times\mathrm{B}^{\sigma_1\sigma_3\lambda_1\lambda_2}_{i,Vg}(p_1,p_2,p_3,p_4,p_5,p_6,Q_{q_1},Q_{\bar{q}_2},Q_{f_3},Q_{\bar{f}_4}),\qquad i=1,\ldots5,
\end{aligned}\tag{B.73}$$

where the generic functions $\mathrm{B}_{i,Vg}, i=1,\ldots,5$ can directly be obtained from the corresponding QED expressions (B.50) to (B.61) by

$$\begin{aligned}
&\mathrm{B}^{\sigma_1\sigma_3\lambda_1\lambda_2}_{i,Vg}(p_1,p_2,p_3,p_4,p_5,p_6,Q_1,Q_2,Q_3,Q_4)\\
&\qquad=\sqrt{\frac{\alpha_\mathrm{S}}{\alpha}}\,\mathrm{B}^{\sigma_1\sigma_3\lambda_1\lambda_2}_{i,V\gamma}(p_1,p_2,p_3,p_4,p_5,p_6,Q_1,Q_2,Q_3,Q_4)\qquad i=1,\ldots,5
\end{aligned}\tag{B.74}$$

To sum the squared amplitude over colours, it is convenient to write first the generic amplitude (B.70) in a more compact way. This can be done by applying the Fierz identity

(B.19) to the Gell-Man Matrices contained in the factors $C^{c_1 c c_3 c_4}_{f_3,\bar{f}_4,V}$ displayed in (B.4). Furthermore, the term proportional to $\mathrm{i}A_5^g$ can be simplified by first using the commutator relation (B.72) and by applying then the Fiertz identity to each of the resulting terms. The generic amplitude for leptonic final states f_3, $f_4 \in \{l, l'\}$ then reads

$$\mathrm{i}\mathcal{A}^{\sigma_1\sigma_2\sigma_3\sigma_4\lambda_1\lambda_2}_{\mathrm{real,QCD}\ c_1c_2c_3c_4a}(p_1,p_2,p_3,p_4,p_5,p_6) = \frac{\lambda^a_{c_2c_1}}{2}\mathrm{i}\mathrm{A}_{12,V}, \qquad V=\gamma,Z,W \tag{B.75}$$

whereas in case of a final state containing quarks, one obtains

$$\begin{aligned}
&\mathrm{i}\mathcal{A}^{\sigma_1\sigma_2\sigma_3\sigma_4\lambda_1\lambda_2}_{\mathrm{real,QCD}\ c_1c_2c_3c_4a}(p_1,p_2,p_3,p_4,p_5,p_6)\\
&\qquad = \frac{1}{1-7\delta_{Vg}}\frac{\lambda^a_{c_2c_1}}{2}\delta_{c_3c_4}\mathrm{i}\mathrm{A}_{12,V} + \frac{1}{1-7\delta_{Vg}}\frac{\lambda^a_{c_3c_4}}{2}\delta_{c_1c_2}\mathrm{i}\mathrm{A}_{34,V}\\
&\quad + \frac{1}{2}\delta_{Vg}\frac{\lambda^a_{c_3c_1}}{2}\delta_{c_2c_4}(\mathrm{i}\mathrm{A}_{13,V}+\mathrm{i}\mathrm{A}_{5,V}) + \frac{1}{2}\delta_{Vg}\frac{\lambda^a_{c_2c_4}}{2}\delta_{c_1c_3}(\mathrm{i}\mathrm{A}_{24,V}+\mathrm{i}\mathrm{A}_{5,V}),\\
&\qquad\qquad V=\gamma,Z,W,g.
\end{aligned} \tag{B.76}$$

For convenience, we here introduced the short-hand notations

$$\begin{aligned}
\mathrm{i}\mathrm{A}_{ij,V} &= \mathrm{i}\mathrm{A}^{\sigma_1\sigma_2\sigma_3\sigma_4\lambda_1\lambda_2}_{i\ ,q_1,\bar{q}_2,f_3,\bar{f}_4,V,g}(p_1,p_2,p_3,p_4,p_5,p_6) + \mathrm{i}\mathrm{A}^{\sigma_1\sigma_2\sigma_3\sigma_4\lambda_1\lambda_2}_{j\ ,q_1,\bar{q}_2,f_3,\bar{f}_4,V,g}(p_1,p_2,p_3,p_4,p_5,p_6),\\
\mathrm{i}\mathrm{A}_{5,V} &= \mathrm{i}\mathrm{A}^{\sigma_1\sigma_2\sigma_3\sigma_4\lambda_1\lambda_2}_{5\ ,q_1,\bar{q}_2,f_3,\bar{f}_4,V,g}(p_1,p_2,p_3,p_4,p_5,p_6)
\end{aligned} \tag{B.77}$$

for $i,j = 1,\ldots 4$. Writing similarly

$$\begin{aligned}
i\widehat{\mathrm{A}}_{ij,V} &= \mathrm{i}\mathrm{A}^{\sigma_1-\sigma_3-\sigma_2\sigma_4\lambda_1\lambda_2}_{i\ ,q_1,f_3,\bar{q}_2,\bar{f}_4,V,g}(p_1,p_3,p_2,p_4,p_5,p_6) + \mathrm{i}\mathrm{A}^{\sigma_1-\sigma_3-\sigma_2\sigma_4\lambda_1\lambda_2}_{j\ ,q_1,f_3,\bar{q}_2,\bar{f}_4,V,g}(p_1,p_3,p_2,p_4,p_5,p_6),\\
i\widehat{\mathrm{A}}_{5,V} &= \mathrm{i}\mathrm{A}^{\sigma_1-\sigma_3-\sigma_2\sigma_4\lambda_1\lambda_2}_{5\ ,q_1,f_3,\bar{q}_2,\bar{f}_4,V,g}(p_1,p_3,p_2,p_4,p_5,p_6)
\end{aligned} \tag{B.78}$$

for the diagrams obtained by the crossing of the external particles $\bar{q}_2$ and f_3, the amplitudes for the reactions classified in Table B.1 read

$$\mathrm{i}\mathcal{A}^{\sigma_1\sigma_2\sigma_3\sigma_4\lambda_1\lambda_2}_{\mathrm{NCa,real,QCD}\ c_1c_2a}(p_1,p_2,p_3,p_4,p_5,p_6) = \frac{\lambda^a_{c_2c_1}}{2}\sum_{V=\gamma,Z}\mathrm{i}\mathrm{A}_{12,V}, \tag{B.79}$$

$$\begin{aligned}
&\mathrm{i}\mathcal{A}^{\sigma_1\sigma_2\sigma_3\sigma_4\lambda_1\lambda_2}_{\mathrm{NCb,real,QCD}\ c_1c_2c_3c_4a}(p_1,p_2,p_3,p_4,p_5,p_6)\\
&\quad = \frac{\lambda^a_{c_2c_1}}{2}\delta_{c_3c_4}\left(\sum_{V=\gamma,Z}\mathrm{i}\mathrm{A}_{12,V} - \frac{1}{6}\mathrm{i}\mathrm{A}_{12,g} - \frac{1}{2}\left(\mathrm{i}\widehat{\mathrm{A}}_{13,g}+\mathrm{i}\widehat{\mathrm{A}}_{5,g}\right)\right)\\
&\quad + \frac{\lambda^a_{c_3c_4}}{2}\delta_{c_1c_2}\left(\sum_{V=\gamma,Z}\mathrm{i}\mathrm{A}_{34,V} - \frac{1}{6}\mathrm{i}\mathrm{A}_{34,g} - \frac{1}{2}\left(\mathrm{i}\widehat{\mathrm{A}}_{24,g}-\mathrm{i}\widehat{\mathrm{A}}_{5,g}\right)\right)\\
&\quad - \frac{\lambda^a_{c_3c_1}}{2}\delta_{c_2c_4}\left(\sum_{V=\gamma,Z}\mathrm{i}\widehat{\mathrm{A}}_{12,V} - \frac{1}{6}\mathrm{i}\widehat{\mathrm{A}}_{12,g} - \frac{1}{2}\left(\mathrm{i}\mathrm{A}_{13,g}+\mathrm{i}\mathrm{A}_{5,g}\right)\right)\\
&\quad - \frac{\lambda^a_{c_2c_4}}{2}\delta_{c_1c_3}\left(\sum_{V=\gamma,Z}\mathrm{i}\widehat{\mathrm{A}}_{34,V} - \frac{1}{6}\mathrm{i}\widehat{\mathrm{A}}_{34,g} - \frac{1}{2}\left(\mathrm{i}\mathrm{A}_{24,g}-\mathrm{i}\mathrm{A}_{5,g}\right)\right),
\end{aligned} \tag{B.80}$$

$$
\begin{aligned}
&\mathrm{i}\mathcal{A}^{\sigma_1\sigma_2\sigma_3\sigma_4\lambda_1\lambda_2}_{\mathrm{NCc,real,QCD}\ c_1c_2c_3c_4a}(p_1,p_2,p_3,p_4,p_5,p_6) = \\
&\quad = \frac{\lambda^a_{c_2c_1}}{2}\delta_{c_3c_4}\left(\sum_{V=\gamma,Z}\mathrm{iA}_{12,V} - \frac{1}{6}\mathrm{iA}_{12,g}\right) + \frac{\lambda^a_{c_3c_4}}{2}\delta_{c_1c_2}\left(\sum_{V=\gamma,Z}\mathrm{iA}_{34,V} - \frac{1}{6}\mathrm{iA}_{34,g}\right) \\
&\quad + \frac{\lambda^a_{c_3c_1}}{2}\delta_{c_2c_4}\left(\frac{1}{2}\left(\mathrm{iA}_{13,g} + \mathrm{iA}_{5,g}\right)\right) + \frac{\lambda^a_{c_2c_4}}{2}\delta_{c_1c_3}\left(\frac{1}{2}\left(\mathrm{iA}_{24,g} - \mathrm{iA}_{5,g}\right)\right),
\end{aligned}
\tag{B.81}
$$

$$
\mathrm{i}\mathcal{A}^{\sigma_1\sigma_2\sigma_3\sigma_4\lambda_1\lambda_2}_{\mathrm{CCa,real,QCD}\ c_1c_2a}(p_1,p_2,p_3,p_4,p_5,p_6) = \frac{\lambda^a_{c_2c_1}}{2}\mathrm{iA}_{12,W},
\tag{B.82}
$$

$$
\mathrm{i}\mathcal{A}^{\sigma_1\sigma_2\sigma_3\sigma_4\lambda_1\lambda_2}_{\mathrm{CCb,real,QCD}\ c_1c_2c_3c_4a}(p_1,p_2,p_3,p_4,p_5,p_6) = \frac{\lambda^a_{c_2c_1}}{2}\delta_{c_3c_4}\mathrm{iA}_{12,W} + \frac{\lambda^a_{c_3c_4}}{2}\delta_{c_1c_2}\mathrm{iA}_{34,W},
\tag{B.83}
$$

$$
\begin{aligned}
&\mathrm{i}\mathcal{A}^{\sigma_1\sigma_2\sigma_3\sigma_4\lambda_1\lambda_2}_{\mathrm{NC/CCa,real,QCD}\ c_1c_2c_3c_4a}(p_1,p_2,p_3,p_4,p_5,p_6) \\
&\quad = \frac{\lambda^a_{c_2c_1}}{2}\delta_{c_3c_4}\left(\sum_{V=\gamma,Z}\mathrm{iA}_{12,V} - \frac{1}{6}\mathrm{iA}_{12,g}\right) + \frac{\lambda^a_{c_3c_4}}{2}\delta_{c_1c_2}\left(\sum_{V=\gamma,Z}\mathrm{iA}_{34,V} - \frac{1}{6}\mathrm{iA}_{34,g}\right) \\
&\quad - \frac{\lambda^a_{c_3c_1}}{2}\delta_{c_2c_4}\left(\mathrm{i}\widehat{\mathrm{A}}_{12,W} - \frac{1}{2}\left(\mathrm{iA}_{13,g} + \mathrm{iA}_{5,g}\right)\right) - \frac{\lambda^a_{c_2c_4}}{2}\delta_{c_1c_3}\left(\mathrm{i}\widehat{\mathrm{A}}_{34,W} - \frac{1}{2}\left(\mathrm{iA}_{24,g} - \mathrm{iA}_{5,g}\right)\right),
\end{aligned}
\tag{B.84}
$$

$$
\begin{aligned}
&\mathrm{i}\mathcal{A}^{\sigma_1\sigma_2\sigma_3\sigma_4\lambda_1\lambda_2}_{\mathrm{NC/CCb,real,QCD}\ c_1c_2c_3c_4a}(p_1,p_2,p_3,p_4,p_5,p_6) \\
&\quad = \frac{\lambda^a_{c_2c_1}}{2}\delta_{c_3c_4}\left(\mathrm{iA}_{12,W} - \frac{1}{2}\left(\mathrm{i}\widehat{\mathrm{A}}_{13,g} + \mathrm{i}\widehat{\mathrm{A}}_{5,g}\right)\right) + \frac{\lambda^a_{c_3c_4}}{2}\delta_{c_1c_2}\left(\mathrm{iA}_{34,W} - \frac{1}{2}\left(\mathrm{i}\widehat{\mathrm{A}}_{24,g} - \mathrm{i}\widehat{\mathrm{A}}_{5,g}\right)\right) \\
&\quad - \frac{\lambda^a_{c_3c_1}}{2}\delta_{c_2c_4}\left(\sum_{V=\gamma,Z}\mathrm{i}\widehat{\mathrm{A}}_{12,V} - \frac{1}{6}\mathrm{i}\widehat{\mathrm{A}}_{12,g}\right) - \frac{\lambda^a_{c_2c_4}}{2}\delta_{c_1c_3}\left(\sum_{V=\gamma,Z}\mathrm{i}\widehat{\mathrm{A}}_{34,V} - \frac{1}{6}\mathrm{i}\widehat{\mathrm{A}}_{34,g}\right).
\end{aligned}
\tag{B.85}
$$

To calculate the corresponding cross-section, one has to square these amplitudes and to average over the initial- and final-state colours. Using repeatedly the Fierz-Identity (B.19), one has for the neutral current processes

$$
\frac{1}{9}\sum_{c_1c_2a}\left|\mathrm{i}\mathcal{A}^{\sigma_1\sigma_2\sigma_3\sigma_4\lambda_1\lambda_2}_{\mathrm{NCa,real,QCD}\ c_1c_2a}(p_1,p_2,p_3,p_4,p_5,p_6)\right|^2 = \frac{4}{9}\left|\sum_{V=\gamma,Z}\mathrm{iA}_{12,V}\right|^2,
\tag{B.86}
$$

$$
\begin{aligned}
&\frac{1}{9}\sum_{c_1c_2c_3c_4a}\left|\mathrm{i}\mathcal{A}^{\sigma_1\sigma_2\sigma_3\sigma_4\lambda_1\lambda_2}_{\mathrm{NCb,real,QCD}\ c_1c_2c_3c_4a}(p_1,p_2,p_3,p_4,p_5,p_6)\right|^2 \\
&\quad=\frac{4}{9}\Bigg[3\left|\sum_{V=\gamma,Z}\mathrm{iA}_{12,V}-\frac{1}{6}\mathrm{iA}_{12,g}-\frac{1}{2}(\mathrm{i}\widehat{\mathrm{A}}_{13,g}+\mathrm{i}\widehat{\mathrm{A}}_{5,g})\right|^2 \\
&\qquad+3\left|\sum_{V=\gamma,Z}\mathrm{iA}_{34,V}-\frac{1}{6}\mathrm{iA}_{34,g}-\frac{1}{2}(\mathrm{i}\widehat{\mathrm{A}}_{24,g}-\mathrm{i}\widehat{\mathrm{A}}_{5,g})\right|^2 \\
&\qquad+3\left|\sum_{V=\gamma,Z}\mathrm{i}\widehat{\mathrm{A}}_{12,V}-\frac{1}{6}\mathrm{i}\widehat{\mathrm{A}}_{12,g}-\frac{1}{2}(\mathrm{iA}_{13,g}+\mathrm{iA}_{5,g})\right|^2 \\
&\qquad+3\left|\sum_{V=\gamma,Z}\mathrm{i}\widehat{\mathrm{A}}_{34,V}-\frac{1}{6}\mathrm{i}\widehat{\mathrm{A}}_{34,g}-\frac{1}{2}(\mathrm{iA}_{24,g}-\mathrm{iA}_{5,g})\right|^2 \\
&\qquad-2\mathrm{Re}\Bigg\{\left[\sum_{V=\gamma,Z}(\mathrm{iA}_{12,V}+\mathrm{iA}_{34,V})-\frac{1}{6}(\mathrm{iA}_{12,g}+\mathrm{iA}_{34,g})-\frac{1}{2}(\mathrm{i}\widehat{\mathrm{A}}_{13,g}+\mathrm{i}\widehat{\mathrm{A}}_{24,g})\right] \\
&\qquad\quad\times\left[\sum_{V=\gamma,Z}(\mathrm{i}\widehat{\mathrm{A}}_{12,V}+\mathrm{i}\widehat{\mathrm{A}}_{34,V})-\frac{1}{6}(\mathrm{i}\widehat{\mathrm{A}}_{12,g}+\mathrm{i}\widehat{\mathrm{A}}_{34,V})-\frac{1}{2}(\mathrm{iA}_{13,g}+\mathrm{iA}_{24,g})\right]^\star\Bigg\}\Bigg],
\end{aligned}
\tag{B.87}
$$

$$
\begin{aligned}
&\frac{1}{9}\sum_{c_1c_2c_3c_4a}\left|\mathrm{i}\mathcal{A}^{\sigma_1\sigma_2\sigma_3\sigma_4\lambda_1\lambda_2}_{\mathrm{NCc,real,QCD}\ c_1c_2c_3c_4a}(p_1,p_2,p_3,p_4,p_5,p_6)\right|^2= \\
&\qquad\frac{4}{9}\Bigg[3\left|\sum_{V=\gamma,Z}\mathrm{iA}_{12,V}-\frac{1}{6}\mathrm{iA}_{12,g}\right|^2+3\left|\sum_{V=\gamma,Z}\mathrm{iA}_{34,V}-\frac{1}{6}\mathrm{iA}_{34,g}\right|^2 \\
&\qquad+3\left|\frac{1}{2}(\mathrm{iA}_{13,g}+\mathrm{iA}_{5,g})\right|^2+3\left|\frac{1}{2}(\mathrm{iA}_{24,g}-\mathrm{iA}_{5,g})\right|^2 \\
&\qquad+\mathrm{Re}\Bigg\{\left[\sum_{V=\gamma,Z}(\mathrm{iA}_{12,V}+\mathrm{iA}_{34,V})-\frac{1}{6}(\mathrm{iA}_{12,g}+\mathrm{iA}_{34,g})\right][(\mathrm{iA}_{13,g}+\mathrm{iA}_{24,g})]^\star\Bigg\}\Bigg],
\end{aligned}
\tag{B.88}
$$

whereas the corresponding expressions for the charged current processes read

$$
\frac{1}{9}\sum_{c_1c_2a}\left|\mathrm{i}\mathcal{A}^{\sigma_1\sigma_2\sigma_3\sigma_4\lambda_1\lambda_2}_{\mathrm{CCa,real,QCD}\ c_1c_2a}(p_1,p_2,p_3,p_4,p_5,p_6)\right|^2=\frac{4}{9}\left|\mathrm{iA}_{12,W}\right|^2, \tag{B.89}
$$

$$
\frac{1}{9}\sum_{c_1c_2c_3c_4a}\left|\mathrm{i}\mathcal{A}^{\sigma_1\sigma_2\sigma_3\sigma_4\lambda_1\lambda_2}_{\mathrm{CCb,real,QCD}\ c_1c_2c_3c_4a}(p_1,p_2,p_3,p_4,p_5,p_6)\right|^2=\frac{4}{9}\left(\left|\mathrm{iA}_{12,W}\right|^2+\left|\mathrm{iA}_{34,W}\right|^2\right). \tag{B.90}
$$

Finally, the squared amplitudes for the final states involving a mixed charged current and neutral current production processes are given by

$$\begin{aligned}
&\frac{1}{9}\sum_{c_1c_2c_3c_4a}\left|\mathrm{i}\mathcal{A}^{\mathrm{real}\,\sigma_1\sigma_2\sigma_3\sigma_4\lambda_1\lambda_2}_{\mathrm{NC/CCa,real,QCD}\;\;c_1c_2c_3c_4a}\right|^2 \\
&\quad=\frac{4}{9}\Bigg[3\left|\sum_{V=\gamma,Z}\mathrm{iA}_{12,V}-\frac{1}{6}\mathrm{iA}_{12,g}\right|^2+3\left|\sum_{V=\gamma,Z}\mathrm{iA}_{34,V}-\frac{1}{6}\mathrm{iA}_{34,g}\right|^2 \\
&\qquad+3\left|\mathrm{i}\widehat{\mathrm{A}}_{12,W}-\frac{1}{2}(\mathrm{iA}_{13,g}+\mathrm{iA}_{5,g})\right|^2+3\left|\mathrm{i}\widehat{\mathrm{A}}_{34,W}-\frac{1}{2}(\mathrm{iA}_{24,g}-\mathrm{iA}_{5,g})\right|^2 \\
&\qquad-2\mathrm{Re}\Bigg\{\left[\sum_{V=\gamma,Z}(\mathrm{iA}_{12,V}+\mathrm{iA}_{34,V})-\frac{1}{6}(\mathrm{iA}_{12,g}+\mathrm{iA}_{34,g})\right] \\
&\qquad\qquad\times\left[\mathrm{i}\widehat{\mathrm{A}}_{12,W}+\mathrm{i}\widehat{\mathrm{A}}_{34,W}-\frac{1}{2}(\mathrm{iA}_{13,g}+\mathrm{iA}_{24,g})\right]^\star\Bigg\}\Bigg],
\end{aligned}\tag{B.91}$$

$$\begin{aligned}
&\frac{1}{9}\sum_{c_1c_2c_3c_4a}\left|\mathrm{iA}^{\mathrm{real}\,\sigma_1\sigma_2\sigma_3\sigma_4\lambda_1\lambda_2}_{\mathrm{NC/CCb,real,QCD}\;\;c_1c_2c_3c_4a}\right|^2 \\
&\quad=\frac{4}{9}\Bigg[3\left|\sum_{V=\gamma,Z}\mathrm{i}\widehat{\mathrm{A}}_{12,V}-\frac{1}{6}\mathrm{i}\widehat{\mathrm{A}}_{12,g}\right|^2+3\left|\sum_{V=\gamma,Z}\mathrm{i}\widehat{\mathrm{A}}_{34,V}-\frac{1}{6}\mathrm{i}\widehat{\mathrm{A}}_{34,g}\right|^2 \\
&\qquad+3\left|\mathrm{iA}_{12,W}-\frac{1}{2}(\mathrm{i}\widehat{\mathrm{A}}_{13,g}+\mathrm{i}\widehat{\mathrm{A}}_{5,g})\right|^2+3\left|\mathrm{iA}_{34,W}-\frac{1}{2}(\mathrm{i}\widehat{\mathrm{A}}_{24,g}-\mathrm{i}\widehat{\mathrm{A}}_{5,g})\right|^2 \\
&\qquad-2\mathrm{Re}\Bigg\{\left[\sum_{V=\gamma,Z}(\mathrm{i}\widehat{\mathrm{A}}_{12,V}+\mathrm{i}\widehat{\mathrm{A}}_{34,V})-\frac{1}{6}(\mathrm{i}\widehat{\mathrm{A}}_{12,g}+\mathrm{i}\widehat{\mathrm{A}}_{34,g})\right] \\
&\qquad\qquad\times\left[\mathrm{iA}_{12,W}+\mathrm{iA}_{34,W}-\frac{1}{2}(\mathrm{i}\widehat{\mathrm{A}}_{13,g}+\mathrm{i}\widehat{\mathrm{A}}_{24,g})\right]^\star\Bigg\}\Bigg].
\end{aligned}\tag{B.92}$$

Appendix C

The Non-Factorizable Corrections for a General Process

In this section, we discuss in some more detail how the non-factorizable virtual corrections to an amplitude can be determined in the framework of amplitude generation using `Pole`. To summarize the procedure, the topologies for the non-factorizable diagrams are generated by means of the `Mathematica` function `CreateNFacTopologies` described in Section 3.1, which creates the topologies for the factorizable Born diagrams, and adds an extra loop propagator connecting the production and decay process, one of the latter with the resonances, the products of two decay subprocesses, two resonances with each other or a given resonance with itself. As described in Section 3.2, a field content can be addressed to the so-generated topologies by the function `InsertFieldContent`. Since only diagrams with a massless particle on the added loop propagator lead to resonant contributions, the latter function furthermore discards all diagrams not compatible with this mass pattern. However, as discussed in Section 3.3, the diagrams remaining after this procedure are partly already contained in the factorizable corrections, such that the corresponding factorizable contribution has to be subtracted from the non-factorizable corrections to avoid double counting. In Leading Pole Approximation, the resulting amplitude can then be evaluated in ESPA, i.e. with the loop momentum set to zero in the numerator of all loop integrals as well as in all propagators not leading to a resonance in the limit of zero loop momentum. In `Pole` both features are implemented in the function `CreateESPAAmps`, which simply replaces all loop integrals appearing in the non-factorizable part of a given amplitude by the difference of the non factorizable parts minus the factorizable parts of the loop integrals evaluated in ESPA.

To be specific, we here list the replacement rules applied by `CreateESPAAmps` to the non-factorizable virtual corrections. For the notation, we consider a general process involving an initial state with particles of momentum $p_{k,\mathrm{in}}$ and charges $Q_k, k = 1, 2$, an intermediate state containing n_0 stable particles with charges Q_{0j} and momenta $p_{0,\mathrm{outj}}$ as well as N resonances with momenta k_i, masses M_i, widths Γ_i and charges Q_i. Each of these resonances is assumed to decay into n_i stable massless particles with momenta $\mathrm{p_{i,outj}}$ and charges Q_{ij}.

Furthermore a general loop integral is denoted by

$$\mathcal{I}_n(p_1,\ldots,p_n,M_0^2,\ldots,M_n^2) = (2\pi\mu)^D \int d^Dq \frac{F_{\mathcal{I}_n}[q]}{[q^2-M_0^2]\,[(q+p_1)^2-M_1^2]\ldots[(q+p_1+\cdots+p_n)^2-M_n^2]}. \quad \text{(C.1)}$$

For the sake of notation, we here suppressed the dependence of the numerator on the momenta of the external particles and the masses of the loop propagators.

To start with, one has the case where the massless propagator connects a resonance with itself, which results in a self-energy contribution for the resonant particle. This type of diagram is not contained in the factorizable corrections. However, in using the on-shell renormalization scheme it contains the wave-function renormalization of the decaying particle, which is already evaluated along with the vertex corrections in the factorizable part of the amplitude and has therefore to be subtracted to avoid double counting. Furthermore, the self-energy contribution has to be rendered UV-finite by adding an appropriate counter term. The self-energies in the non-factorizable part of the amplitude are in `CreateESPAAmps` therefore subject to the replacement

$$\mathcal{B}(k_i,0,M_i^2) \to F_{\mathcal{B}}[q=0]\ \texttt{BOC}[\texttt{OffShell}[\texttt{k}_\texttt{i}^2]-\texttt{M}_\texttt{i}^2+\texttt{i}\texttt{M}_\texttt{i}\Gamma_\texttt{i},\texttt{0},\texttt{M}_\texttt{i}^2-\texttt{i}\texttt{M}_\texttt{i}\Gamma_\texttt{i}], \quad \text{(C.2)}$$

where we used the notation $\mathcal{I}_2{=}\mathcal{B}$ and

$$\begin{aligned}\texttt{BOC}[\texttt{OffShell}[\texttt{k}_\texttt{i}^2]-\texttt{M}_\texttt{i}^2+\texttt{i}\texttt{M}_\texttt{i}\Gamma_\texttt{i},\texttt{0},\texttt{M}_\texttt{i}^2-\texttt{i}\texttt{M}_\texttt{i}\Gamma_\texttt{i}] :=& \\ B_0(k_i,0,M_i^2-\mathrm{i}M_i\Gamma_i) - B_0(M_i^2-\mathrm{i}M_i\Gamma_i,0,M_i^2-\mathrm{i}M_i\Gamma_i)& \\ -(k_i^2-M_i^2+\mathrm{i}M_i\Gamma_i)B_0'(M_i^2,0,M_i^2).& \quad \text{(C.3)}\end{aligned}$$

In `Pole`, the head `OffShell` is introduced to provide the numerical evaluation with the information that the resonant momentum has to be evaluated off-shell.

The second type of diagrams can be characterized by the virtual massless particle connecting the resonance number i with one of its decay products. This type of diagrams can be disconnected in production and decay subprocesses by cutting a resonant propagator, and are thus already contained in the factorizable corrections. Denoting the momentum and the mass of the outgoing particle by $p_{i,\mathrm{out}}$ and $m_{i,\mathrm{out}}, i=1,\ldots,n_i$, respectively, the corresponding loop integral is in `CreateESPAAmps` replaced by the difference of its non-factorizable contribution minus its factorizable contribution

$$\begin{aligned}&\mathcal{C}(k_i,p_{i,\mathrm{out}}-k_i,0,M_i^2,m_{i,\mathrm{out}}^2)\to \\ &F_{\mathcal{C}}[q=0]\ \texttt{COC}[\texttt{1},\texttt{OffShell}[\texttt{k}_\texttt{i}^2]-\texttt{M}_\texttt{i}^2+\texttt{i}\texttt{M}_\texttt{i}\Gamma_\texttt{i},(\texttt{p}_{\texttt{i,out}}-\texttt{k}_\texttt{i})^2,\texttt{p}_{\texttt{i,out}}^2,\texttt{0},\texttt{M}_\texttt{i}^2-\texttt{i}\texttt{M}_\texttt{i}\Gamma_\texttt{i},\texttt{m}_{\texttt{i,out}}^2] \quad \text{(C.4)}\end{aligned}$$

where [35]

$$\begin{aligned}&\texttt{COC}[\texttt{1},\texttt{OffShell}[\texttt{k}_\texttt{i}^2]-\texttt{M}_\texttt{i}^2+\texttt{i}\texttt{M}_\texttt{i}\Gamma_\texttt{i},(\texttt{p}_{\texttt{i,out}}-\texttt{k}_\texttt{i})^2,\texttt{p}_{\texttt{i,out}}^2,\texttt{0},\texttt{M}_\texttt{i}^2-\texttt{i}\texttt{M}_\texttt{i}\Gamma_\texttt{i},\texttt{m}_{\texttt{i,out}}^2] := \\ &\quad\big(C_0(k_i,p_{i,\mathrm{out}}-k_i,0,M_i^2-\mathrm{i}M_i\Gamma_i,m_{i,\mathrm{out}}^2) \\ &\qquad -\big[C_0(k_i,p_{i,\mathrm{out}}-k_i,\lambda,M_i^2+\mathrm{i}M_i\Gamma_i,m_{i,\mathrm{out}}^2)\big]_{k_i^2=M_i^2}\big). \quad \text{(C.5)}\end{aligned}$$

Here and in the following λ denotes the infinitesimal mass parameter used to regularize the infrared divergences in the factorizable part of the amplitude.

A similar replacement is applied to diagrams where the virtual massless particle connects the production subprocess with one of the resonances. In ESPA, the loop momentum can be set to zero in the numerator of the loop integrals. Furthermore, the loop integrals may contain propagators not contributing to the resonance structure, which in ESPA can be evaluated with zero loop momentum as well. Note that such propagators do not appear in the above-discussed case of the virtual massless particle connecting resonance and decay. The reason for this is that we limit our considerations in this chapter to resonances decaying into stable particles only, such that no decay chains involving particles decaying into unstable particles can occur. Subtracting again the factorizable parts and choosing the notation $p_{k,\mathrm{in}}$ and $m_{k,\mathrm{in}}$, $k = 1, 2$ for the momentum and the mass of the incoming particle connected to the resonance, the resulting replacement rule reads

$$\begin{aligned}\mathcal{X}_n(p_{k,\mathrm{in}}, q_1, \ldots, q_n, 0, m_{k,\mathrm{in}}^2, m_1^2, \ldots, m_{n-1}^2, M_i^2) \to \prod_{r=1}^{n-1} \frac{F_{\mathcal{X}_n}(q=0)}{(k_i + \sum_{s=1}^{r} q_s)^2 - m_r^2} \\ \times \mathtt{COC}[2, \mathtt{p}_{\mathtt{k,in}}^2, (\mathtt{k_i} - \mathtt{p_{k,in}})^2, \mathtt{OffShell}[\mathtt{k}_\mathtt{i}^2] - \mathtt{M}_\mathtt{i}^2 + \mathrm{i}\mathtt{M_i}\Gamma_\mathtt{i}, 0, \mathtt{m}_{\mathtt{k,in}}^2, \mathtt{M}_\mathtt{i}^2 - \mathrm{i}\mathtt{M_i}\Gamma_\mathtt{i}], \quad \text{(C.6)}\end{aligned}$$

where here and in the following $\mathcal{X}_1 = \mathcal{C}, \mathcal{X}_2 = \mathcal{D}, \ldots$ and

$$\begin{aligned}&\mathtt{COC}[2, \mathtt{p}_{\mathtt{k,in}}^2, (\mathtt{k_i} - \mathtt{p_{k,in}})^2, \mathtt{OffShell}[\mathtt{k}_\mathtt{i}^2] - \mathtt{M}_\mathtt{i}^2 + \mathrm{i}\mathtt{M_i}\Gamma_\mathtt{i}, 0, \mathtt{m}_{\mathtt{k,in}}^2, \mathtt{M}_\mathtt{i}^2 - \mathrm{i}\mathtt{M_i}\Gamma_\mathtt{i}] := \\ &\quad \big(C_0(p_{k,\mathrm{in}}, k_i - p_{k,\mathrm{in}}, 0, m_{k,\mathrm{in}}^2, M_i^2 + \mathrm{i}M_i\Gamma_i) \\ &\qquad - \big[C_0(p_{k,\mathrm{in}}, k_i - p_{k,\mathrm{in}}, \lambda, m_{k,\mathrm{in}}^2, M_i^2 + \mathrm{i}M_i\Gamma_i)\big]_{k_i^2 = M_i^2}\big). \quad \text{(C.7)}\end{aligned}$$

A third type of 3-point function is obtained from diagrams where the resonant massless particle connects two resonant propagators. Following the same lines as above, this type of integral is replaced by

$$\begin{aligned}\mathcal{X}_n(-k_i, q_1, \ldots, q_n, 0, M_i^2, m_1^2, \ldots, m_{n-1}^2, M_j^2) \to \prod_{r=1}^{n-1} \frac{F_{\mathcal{X}_n}(q=0)}{(k_i + \sum_{s=1}^{r} q_s)^2 - m_r^2} \\ \times \mathtt{COC}[3, \mathtt{OffShell}[\mathtt{k}_\mathtt{i}^2] - \mathtt{M}_\mathtt{i}^2 + \mathrm{i}\mathtt{M_i}\Gamma_\mathtt{i}, (\mathtt{k_i} + \mathtt{k_j})^2, \mathtt{OffShell}[\mathtt{k}_\mathtt{j}^2] - \mathtt{M}_\mathtt{j}^2 + \mathrm{i}\mathtt{M_j}\Gamma_\mathtt{j}, \\ 0, \mathtt{M}_\mathtt{i}^2 - \mathrm{i}\mathtt{M_i}\Gamma_\mathtt{i}, \mathtt{M}_\mathtt{j}^2 - \mathrm{i}\mathtt{M_j}\Gamma_\mathtt{j}] \quad \text{(C.8)}\end{aligned}$$

with

$$\begin{aligned}&\mathtt{COC}[3, \mathtt{OffShell}[\mathtt{k}_\mathtt{i}^2] - \mathtt{M}_\mathtt{i}^2 + \mathrm{i}\mathtt{M_i}\Gamma_\mathtt{i}, (\mathtt{k_i} + \mathtt{k_j})^2, \mathtt{OffShell}[\mathtt{k}_\mathtt{j}^2] - \mathtt{M}_\mathtt{j}^2 + \mathrm{i}\mathtt{M_j}\Gamma_\mathtt{j}, \\ &\qquad 0, \mathtt{M}_\mathtt{i}^2 - \mathrm{i}\mathtt{M_i}\Gamma_\mathtt{i}, \mathtt{M}_\mathtt{j}^2 - \mathrm{i}\mathtt{M_j}\Gamma_\mathtt{j}] := \\ &\quad \big(C_0(-k_i, k_i + k_j, 0, M_i^2 + \mathrm{i}M_i\Gamma_i, M_j^2 + \mathrm{i}M_j\Gamma_j) \\ &\qquad - \big[C_0(-k_i, k_i + k_j, \lambda, M_i^2 + \mathrm{i}M_i\Gamma_i, M_j^2 + \mathrm{i}M_j\Gamma_j)\big]_{k_{i,j}^2 = M_{i,j}^2}\big). \quad \text{(C.9)}\end{aligned}$$

The loop integrals for the three remaining cases do not contain any factorizable contributions to the full amplitude, and can thus be evaluated by simply applying the ESPA. Besides the notation used above, we here consider two resonances i and j decaying into two particles with momenta $p_{i,\mathrm{out}1}$ and $p_{i,\mathrm{out}2}$ as well as $p_{j,\mathrm{out}1}$ and $p_{j,\mathrm{out}2}$ in what follows. The replacement for a loop integral with the virtual massless particle connecting the production subprocess with the decay subprocess is then given by

$$\begin{aligned}
&\mathcal{Y}_n(p_{k,\mathrm{in}}, q_1, \ldots, q_n, -p_{i,\mathrm{out}2}, 0, m^2_{k,\mathrm{in}}, m^2_1, \ldots, m^2_{n-1}, M_i, m^2_{i,\mathrm{out}1}) \to \\
&\quad \prod_{r=1}^{n-1} \frac{F_{\mathcal{Y}_n}(q=0)}{(k_i + \sum_{s=1}^{r} q_s)^2 - m_r^2} \\
&\quad \times \mathtt{DOC}[1, \mathtt{p}^2_{\mathtt{k},\mathrm{in}}, (\mathtt{k_i} - \mathtt{p}_{\mathtt{k},\mathrm{in}})^2, \mathtt{p}^2_{\mathtt{i},\mathrm{out}2}, \mathtt{p}^2_{\mathtt{i},\mathrm{out}1}, \\
&\qquad \mathtt{OffShell}[\mathtt{k}^2_\mathtt{i}] - \mathtt{M_i} + \mathrm{i}\mathtt{M_i}\Gamma_\mathtt{i}, (\mathtt{p}_{\mathtt{i},\mathrm{out}1} - \mathtt{p}_{\mathtt{k},\mathrm{in}})^2, \lambda, \mathtt{m}^1_{\mathtt{k},\mathrm{in}}, \mathtt{M}^2_\mathtt{i} - \mathrm{i}\mathtt{M_i}\Gamma_\mathtt{i}, \mathtt{m}^2_{\mathtt{i},\mathrm{out}1}], \quad \text{(C.10)}
\end{aligned}$$

where $\mathcal{Y}_1 = \mathcal{D}, \mathcal{Y}_2 = \mathcal{E}, \ldots$. For the loop integrals where the massless virtual particle connects a resonance with a decay product of a different resonance, on the other hand, one has

$$\begin{aligned}
&\mathcal{Y}_n(-p_{i,\mathrm{out}1}, -p_{i,\mathrm{out}2}, q_1, \ldots, q_n, -k_j, 0, m^2_{i,\mathrm{out}1}, M_i^2, m^2_1, \ldots, m^2_{n-1}, M_j^2) \to \\
&\quad \prod_{r=1}^{n-1} \frac{F_{\mathcal{Y}_n}(q=0)}{(k_i + \sum_{s=1}^{r} q_s)^2 - m_r^2} \\
&\quad \mathtt{DOC}[2, \mathtt{p}^2_{\mathtt{i},\mathrm{out}1}, \mathtt{p}^2_{\mathtt{i},\mathrm{out}2}, (\mathtt{k_i} + \mathtt{k_j})^2, \mathtt{OffShell}[\mathtt{k}^2_\mathtt{j}] - \mathtt{M}^2_\mathtt{j} + \mathrm{i}\mathtt{M_j}\Gamma_\mathtt{j}, \\
&\qquad \mathtt{OffShell}[\mathtt{k}^2_\mathtt{i}] - \mathtt{M}^2_\mathtt{i} + \mathrm{i}\mathtt{M_i}\Gamma_\mathtt{i}, (\mathtt{k_j} + \mathtt{p}_{\mathtt{i},\mathrm{out}1})^2, 0, \mathtt{m}^2_{\mathtt{i},\mathrm{out}1}, \mathtt{M}^2_\mathtt{i} - \mathrm{i}\mathtt{M_i}\Gamma_\mathtt{i}, \mathtt{M}^2_\mathtt{j} - \mathrm{i}\mathtt{M_j}\Gamma_\mathtt{j}]. \quad \text{(C.11)}
\end{aligned}$$

Finally, the remaining loop integrals originate from diagrams, where the virtual massless particle connects the decay products of two different resonances i and j, $i \neq j$ with each other. The replacement of this last type of loop integral by its counterpart in ESPA can here be achieved by

$$\begin{aligned}
&\mathcal{Z}_n(-p_{j,\mathrm{out}1}, -p_{j,\mathrm{out}2}, q_1, \ldots, q_n, -p_{i,\mathrm{out}2}, 0, m^2_{j,\mathrm{out}1}, M_j^2, m^2_1, \ldots, m^2_{n-1}, M_i^2, m^2_{i,\mathrm{out}1}) \to \\
&\quad \prod_{r=1}^{n-1} \frac{F_{\mathcal{Z}_n}(q=0)}{(p_{j,\mathrm{out}1} + p_{j,\mathrm{out}2} + \sum_{s=1}^{r} q_s)^2 - m_r^2} \\
&\qquad \mathtt{EOC}[\mathtt{p}^2_{\mathtt{j},\mathrm{out}1}, \mathtt{p}^2_{\mathtt{j},\mathrm{out}2}, (\mathtt{k_i} + \mathtt{k_j})^2, \mathtt{p}^2_{\mathtt{i},\mathrm{out}2}, \mathtt{p}^2_{\mathtt{i},\mathrm{out}1}, \mathtt{OffShell}[\mathtt{k}^2_\mathtt{j}] - \mathtt{M}^2_\mathtt{j} + \mathrm{i}\mathtt{M_j}\Gamma_\mathtt{j}, \\
&\qquad (\mathtt{p}_{\mathtt{j},\mathrm{out}1} + \mathtt{k_i})^2, (\mathtt{p}_{\mathtt{i},\mathrm{out}1} + \mathtt{k_j})^2, \mathtt{OffShell}[\mathtt{k}^2_\mathtt{i}] - \mathtt{M}^2_\mathtt{i} + \mathrm{i}\mathtt{M_i}\Gamma_\mathtt{i}, (\mathtt{p}_{\mathtt{j},\mathrm{out}1} + \mathtt{p}_{\mathtt{i},\mathrm{out}1})^2, \\
&\qquad\qquad 0, \mathtt{m}^2_{\mathtt{j},\mathrm{out}1}, \mathtt{M}^2_\mathtt{j} - \mathrm{i}\mathtt{M_j}\Gamma_\mathtt{j}, \mathtt{M}^2_\mathtt{i} - \mathrm{i}\mathtt{M_i}\Gamma_\mathtt{i}, \mathtt{m}^2_{\mathtt{i},\mathrm{out}1}], \quad \text{(C.12)}
\end{aligned}$$

where $\mathcal{Z}_1 = \mathcal{E}, \mathcal{Z}_2 = \mathcal{F}, \ldots$.

To render the amplitude resulting from the above replacements suitable for numerical evaluation, it is passed in a next step to the `Mathematica` function `CalcAmplitudes`,

which reduces the spinor structures to Weyl-spinor products and introduces abbreviations as discussed in Section 4.1. The new symbols `B0c`, `C0c`, `D0c`, and `E0c` are by this procedure left as introduced above, and `CalcAmplitudes` introduces abbreviations of type `LInt1, LInt2,...` for these quantities as well as for the loop integrals appearing in the factorizable corrections. However, whereas the latter do not contain a finite width and can therefore be evaluated numerically by the `FF`-based package LoopTools [72, 73], a separate library has to be introduced for the numerical evaluation of the loop integrals appearing in the non-factorizable corrections. To this end, the files in the `Fortran` output of `Pole` which contain the abbreviations and amplitudes for the non-factorizable virtual corrections are linked to the file `amps/looptools_nfac.F` containing the necessary expressions for the numerical evaluation of the loop integrals introduced by the procedure presented above.

Using the abbreviation $K_i = \mathtt{OffShell}[\mathtt{k_i^2}] - \mathtt{M_i^2} + \mathrm{i}\mathtt{M_i}\Gamma_\mathtt{i}$ for the off-shellness of the resonance number i, the expressions for the loop integrals as implemented in `looptools_nfac.F` read

$$\mathtt{B0C}[\mathtt{K_i}, \mathtt{0}, \mathtt{M_i^2} - \mathrm{i}\mathtt{M_i}\Gamma_\mathtt{i}] = \frac{\mathrm{i}\pi^2 K_i}{M_i^2}\left\{\log\left(\frac{\lambda M_i}{-K_i}\right) + 1\right\}, \tag{C.13}$$

$$\begin{aligned}\mathtt{C0C}[\mathtt{1}, \mathtt{K_i}, (\mathtt{p_{out}} - \mathtt{k_i})^2, \mathtt{p_{out}^2}, \mathtt{0}, \mathtt{M_i^2} - \mathrm{i}\mathtt{M_i}\Gamma_\mathtt{i}, \mathtt{m_{i,out}^2}] \\ = -\frac{\mathrm{i}\pi^2}{M_i^2}\left\{\log\left(\frac{m_{i,\mathrm{out}}^2}{M_i^2}\right)\log\left(\frac{-K_i}{\lambda M_i}\right) + \log^2\left(\frac{m_{i,\mathrm{out}}}{M_i}\right) + \frac{\pi^2}{6}\right\},\end{aligned} \tag{C.14}$$

$$\begin{aligned}&\mathtt{C0C}[\mathtt{2}, \mathtt{p_{k,in}^2}, (\mathtt{p_{k,in}} - \mathtt{k_i})^2, \mathtt{K_i}, \mathtt{0}, \mathtt{m_{k,in}^2}, \mathtt{M_i^2} - \mathrm{i}\mathtt{M_i}\Gamma_\mathtt{i}] \\ &= \frac{\mathrm{i}\pi^2}{\hat{t}}\left\{\log\left(\frac{m_{k,\mathrm{in}}M_i}{-\hat{t}} + \mathrm{i}\varepsilon\right)\left[\log\left(\frac{K_i}{\hat{t}}\right) + \log\left(\frac{-K_i}{\lambda^2}\right) + \log\left(\frac{m_{k,\mathrm{in}}}{M_i}\right)\right] + \frac{\pi^2}{6}\right\},\end{aligned} \tag{C.15}$$

where $\hat{t} = (p_{k,\mathrm{in}} - k_i)^2 - M_i^2$, as well as

$$\begin{aligned}&\mathtt{C0C}[\mathtt{3}, \mathtt{K_i}, (\mathtt{k_i} + \mathtt{k_j})^2, \mathtt{K_j}, \mathtt{0}, \mathtt{M_i^2} - \mathrm{i}\mathtt{M_i}\Gamma_\mathtt{i}, \mathtt{M_j^2} - \mathrm{i}\mathtt{M_j}\Gamma_\mathtt{j}] \\ &= \frac{\mathrm{i}\pi^2}{w_{ij}}\left\{\mathcal{L}i_2\left(\frac{M_jK_i}{M_iK_j}, \frac{1}{r_{ij}}\right) - \mathcal{L}i_2\left(\frac{M_jK_i}{M_iK_j}, r_{ij}\right) + \mathcal{L}i_2(r_{ij}, r_{ij}) + \log^2(r_{ij})\right. \\ &\qquad \left. + 2\log(r_{ij})\log\left(\frac{-K_j}{M_j\lambda}\right)\right\},\end{aligned} \tag{C.16}$$

with

$$\begin{aligned} w_{ij} &= \sqrt{\lambda((k_i+k_j)^2, M_i^2, M_j^2)} \qquad \lambda(x,y,z) = x^2+y^2+z^2-2xy-2xz-2yz, \\ r_{ij} &= \frac{1}{2M_iM_j}(-(k_i+k_j)^2 + M_i^2 + M_j^2 + w_{ij})\left(1 - \frac{\mathrm{i}\varepsilon}{w_{ij}}\right), \\ \mathcal{L}i_2(x,y) &= \mathrm{Li}_2(1-xy) + (\log(xy) - \log(x) - \log(y))\log(1-xy), \\ &\quad |\arg(x)| < \pi, |\arg(y)| < \pi, \end{aligned} \tag{C.17}$$

and the quantity Li_2 denoting the Spence function.

The corresponding expressions for the 4-point functions read [35]

$$\begin{aligned}
&\mathtt{D0C}[1, \mathtt{p}^2_{\mathtt{k,in}}, (\mathtt{p}_{\mathtt{k,in}} - \mathtt{k}_\mathtt{i})^2, \mathtt{p}^2_{\mathtt{i,out2}}, \mathtt{p}^2_{\mathtt{i,out1}}, \mathtt{K}_\mathtt{i}, (\mathtt{p}_{\mathtt{i,out1}} - \mathtt{p}_{\mathtt{k,in}})^2, \lambda, \mathtt{m}^2_{\mathtt{k,in}}, \mathtt{M}^2_\mathtt{i} - \mathrm{i}\mathtt{M}_\mathtt{i}\Gamma_\mathtt{i}, \mathtt{m}^2_{\mathtt{i,out1}}] \\
&\quad = \frac{\mathrm{i}\pi^2}{tK_i}\left\{2\log\left(\frac{m_{k,\mathrm{in}}m_{i,\mathrm{out1}}}{-t} + \mathrm{i}\varepsilon\right)\log\left(\frac{\lambda M_i}{-K_i}\right) - \log^2\left(\frac{m_{k,\mathrm{in}}M_i}{-\hat{t}} + \mathrm{i}\varepsilon\right)\right. \\
&\qquad\qquad \left. - \log^2\left(\frac{m_{i,\mathrm{out1}}}{M_i}\right) - \frac{\pi^2}{3} - \mathrm{Li}_2\left(1 - \frac{\hat{t}}{t}\right)\right\} \qquad \text{(C.18)}
\end{aligned}$$

with $\hat{t} = (p_{k,\mathrm{in}} - k_i)^2 - M_i^2$ and $t = (p_{k,\mathrm{in}} - p_{i,\mathrm{out1}})^2$,

$$\begin{aligned}
&\mathtt{D0C}[2, \mathtt{K}_\mathtt{i}, (\mathtt{k}_\mathtt{i} + \mathtt{k}_\mathtt{j})^2, \mathtt{p}^2_{\mathtt{j,out2}}, \mathtt{p}^2_{\mathtt{j,out1}}, \mathtt{K}_\mathtt{j}, (\mathtt{k}_\mathtt{i} + \mathtt{p}_{\mathtt{j,out1}})^2, 0, \mathtt{M}^2_\mathtt{i} - \mathrm{i}\mathtt{M}_\mathtt{i}\Gamma_\mathtt{i}, \mathtt{M}^2_\mathtt{j} - \mathrm{i}\mathtt{M}_\mathtt{j}\Gamma_\mathtt{j}, \mathtt{m}^2_{\mathtt{j,out1}}] \\
&\quad = \frac{\mathrm{i}\pi^2}{K_i\hat{s}_{ij} + K_jM_i^2}\left\{\sum_{\tau=\pm1}\left[\mathcal{L}i_2\left(\frac{M_jK_i}{M_iK_j}, r_{ij}^\tau\right) - \mathcal{L}i_2\left(-\frac{M_jM_i}{\hat{s}_{ij}} + \mathrm{i}\varepsilon, r_{ij}^\tau\right)\right]\right. \\
&\left. -2\mathcal{L}i_2\left(\frac{M_jK_i}{M_iK_j}, -\frac{\hat{s}_{ij}}{M_iM_j} - \mathrm{i}\varepsilon\right) - \log\left(\frac{m^2_{j,\mathrm{out1}}}{M_i^2}\right)\left[\log\left(\frac{M_jK_i}{M_iK_j}\right) + \log\left(\frac{\hat{s}_{ij}}{M_iM_j} - \mathrm{i}\varepsilon\right)\right]\right\} \qquad \text{(C.19)}
\end{aligned}$$

with $\hat{s}_{ij} = (k_i - p_{\mathrm{j,out1}})^2 - M_i^2$ and r_{ij} defined as above,

$$\begin{aligned}
&\mathtt{E0C}[\mathtt{p}^2_{\mathtt{j,out1}}, \mathtt{p}^2_{\mathtt{j,out2}}, (\mathtt{k}_\mathtt{i} + \mathtt{k}_\mathtt{j})^2, \mathtt{p}^2_{\mathtt{i,out2}}, \mathtt{p}^2_{\mathtt{i,out1}}, \mathtt{K}_\mathtt{j}, (\mathtt{p}_{\mathtt{j,out1}} + \mathtt{k}_\mathtt{i})^2, (\mathtt{p}_{\mathtt{i,out1}} + \mathtt{k}_\mathtt{j})^2, \mathtt{K}_\mathtt{i}, \\
&\quad (\mathtt{p}_{\mathtt{j,out1}} + \mathtt{p}_{\mathtt{i,out1}})^2, 0, \mathtt{m}^2_{\mathtt{j,out1}}, \mathtt{M}^2_\mathtt{j} - \mathrm{i}\mathtt{M}_\mathtt{j}\Gamma_\mathtt{j}, \mathtt{M}^2_\mathtt{i} - \mathrm{i}\mathtt{M}_\mathtt{i}\Gamma_\mathtt{i}, \mathtt{m}^2_{\mathtt{i,out1}}] \\
&\quad = -\mathrm{i}\pi^2\left(\frac{\det(Y_0)}{\det(Y)}D_0(0) + \frac{\det(Y_3)}{\det(Y)K_js_{ij}}\left\{\left[K_i\hat{s}_{ij} + K_jM_i^2\right]D_0(1) + K_js_{ij}D_0(3)\right\}\right. \\
&\left. + \frac{\det(Y_2)}{\det(Y)K_is_{ij}}\left\{\left[K_j\hat{s}_{ij} + K_iM_j^2\right]D_0(4) + K_is_{ij}D_0(2)\right\} + \frac{\hat{s}_{ij}}{K_is_{ij}}D_0(4) + \frac{\hat{s}_{ji}}{K_js_{ij}}D_0(1)\right), \qquad \text{(C.20)}
\end{aligned}$$

with $s_{ij} = (p_{i,\mathrm{out1}} + p_{j,\mathrm{out1}})^2$ and $\bar{s}_{ij} = (k_i + k_j)^2 - M_i^2 - M_j^2$ and $\hat{s}_{ij}$ defined as above. The determinants in the expression for `E0c` are given by

$$\begin{aligned}
\det(Y_0) &= \lambda(s_{ij}\bar{s}_{ij}, \hat{s}_{ij}\hat{s}_{ji}, M_i^2M_j^2) + 4s_{ij}M_i^2M_j^2(\hat{s}_{ij} + \hat{s}_{ji} - s_{ij}) \\
\det(Y_2) &= s_{ij}(K_i[\hat{s}_{ij}\hat{s}_{ji} - s_{ij}\bar{s}_{ij} + M_i^2M_j^2] + 2K_jM_i^2(\hat{s}_{ij} - s_{ij})) \\
\det(Y_3) &= s_{ij}(K_j[\hat{s}_{ij}\hat{s}_{ji} - s_{ij}\bar{s}_{ij} + M_i^2M_j^2] + 2K_iM_j^2(\hat{s}_{ji} - s_{ij})) \\
\det(Y) &= 2s_{ij}(K_iK_j(s_{ij}\bar{s}_{ij} - \hat{s}_{ij}\hat{s}_{ji} - M_i^2M_j^2) \\
&\qquad + K_i^2M_j^2(s_{ij} - \hat{s}_{ji}) + K_j^2M_i^2(s_{ij} - \hat{s}_{ij})). \qquad \text{(C.21)}
\end{aligned}$$

Among the 4-point functions $D_0(i), i = 0, \ldots 4$, the function $D_0(0)$ does not contain any complex masses and can thus be evaluated using `LoopTools`

$$D_0(0) = \mathtt{D0i}(\mathtt{dd0}, \mathtt{p}^2_{\mathtt{j,out2}}, \bar{\mathtt{s}}_{\mathtt{ij}} + \mathtt{M}^2_\mathtt{i} + \mathtt{M}^2_\mathtt{j}, \mathtt{p}^2_{\mathtt{i,out2}}, \mathtt{s}_{\mathtt{ij}}, \hat{\mathtt{s}}_{\mathtt{ij}} + \mathtt{M}^2_\mathtt{i}, \hat{\mathtt{s}}_{\mathtt{ji}} + \mathtt{M}^2_\mathtt{j}, \mathtt{m}^2_{\mathtt{j,out1}}, \mathtt{M}^2_\mathtt{j}, \mathtt{M}^2_\mathtt{i}, \mathtt{m}^2_{\mathtt{i,out1}}), \qquad \text{(C.22)}$$

whereas the function $D_0(1)$ and $D_0(4)$ are given by

$$D_0(1) = \texttt{DOC}[2, \texttt{K}_\texttt{i}, (\texttt{k}_\texttt{i}+\texttt{k}_\texttt{j})^2, \texttt{p}^2_{\texttt{j},\text{out2}}, \texttt{p}^2_{\texttt{j},\text{out1}}, \texttt{K}_\texttt{j}, (\texttt{k}_\texttt{i}+\texttt{p}_{\texttt{j},\text{out1}})^2, \texttt{0}, \texttt{M}^2_\texttt{i} - \texttt{iM}_\texttt{i}\Gamma_\texttt{i}, \texttt{M}^2_\texttt{j} - \texttt{iM}_\texttt{j}\Gamma_\texttt{j}, \texttt{m}^2_{\texttt{j},\text{out1}}], \quad \text{(C.23)}$$

$$D_0(4) = \texttt{DOC}[2, \texttt{K}_\texttt{j}, (\texttt{k}_\texttt{i}+\texttt{k}_\texttt{j})^2, \texttt{p}^2_{\texttt{i},\text{out2}}, \texttt{p}^2_{\texttt{i},\text{out1}}, \texttt{K}_\texttt{i}, (\texttt{k}_\texttt{j}+\texttt{p}_{\texttt{i},\text{out1}})^2, \texttt{0}, \texttt{M}^2_\texttt{j} - \texttt{iM}_\texttt{j}\Gamma_\texttt{i}, \texttt{M}^2_\texttt{i} - \texttt{iM}_\texttt{i}\Gamma_\texttt{i}, \texttt{m}^2_{\texttt{i},\text{out1}}]. \quad \text{(C.24)}$$

Finally, the functions $D_0(2)$ and $D_0(3)$ read

$$D_0(2) = \texttt{DOC}[1, \texttt{p}^2_{\texttt{j},\text{out1}}, (\texttt{p}_{\texttt{j},\text{out1}}+\texttt{k}_\texttt{i})^2, \texttt{p}^2_{\texttt{i},\text{out2}}, \texttt{p}^2_{\texttt{i},\text{out1}}, \texttt{K}_\texttt{i}, (\texttt{p}_{\texttt{i},\text{out1}}+\texttt{p}_{\texttt{j},\text{out1}})^2, \lambda, \texttt{m}^2_{\texttt{j},\text{out1}}, \texttt{M}^2_\texttt{i} - \texttt{iM}_\texttt{i}\Gamma_\texttt{i}, \texttt{m}^2_{\texttt{i},\text{out1}}], \quad \text{(C.25)}$$

$$D_0(3) = \texttt{DOC}[1, \texttt{p}^2_{\texttt{i},\text{out1}}, (\texttt{p}_{\texttt{i},\text{out1}}+\texttt{k}_\texttt{j})^2, \texttt{p}^2_{\texttt{j},\text{out2}}, \texttt{p}^2_{\texttt{j},\text{out1}}, \texttt{K}_\texttt{j}, (\texttt{p}_{\texttt{j},\text{out1}}+\texttt{p}_{\texttt{i},\text{out1}})^2, \lambda, \texttt{m}^2_{\texttt{i},\text{out1}}, \texttt{M}^2_\texttt{j} - \texttt{iM}_\texttt{j}\Gamma_\texttt{j}, \texttt{m}^2_{\texttt{j},\text{out1}}]. \quad \text{(C.26)}$$

Analytic expressions for the numerical evaluation for $D_0(2)$ can be obtained by replacing in (C.18) everywhere $t \to s_{ij}$, $\hat{t} \to \hat{s}_{ij}$ and $m^2_{k,\text{in}} \to m^2_{j,\text{out1}}$, whereas the corresponding replacements for $D_0(3)$ are given by $t \to s_{ij}$, $\hat{t} \to \hat{s}_{ji}$ and $m^2_{k,\text{in}} \to m^2_{i,\text{out1}}$. The above expressions for the loop integrals appearing in the non-factorizable corrections have partly been already displayed in Appendix B.2, and were here included for the sake of completeness.

Upon inserting the various expressions for the loop integrals listed above in the non-factorizable part of the virtual corrections, the latter factorizes in the factorizable part of the Born cross-section times a process-independent correction factor

$$\mathcal{A}^{(1),\text{LPA}}_{q_1q_2,V,\text{nfac}}(k^2) = \frac{1}{2}\mathcal{A}^{(0),\text{LPA}}_{q_1q_2,V}(k^2)\delta^{(1),\text{virt}}_{\text{nfac}}, \tag{C.27}$$

which can be used to check the generation of the non-factorizable virtual corrections as implemented in `Pole`. With the above notation, the correction factor reads [35]

$$\begin{aligned}\delta^{(1),\text{virt}}_{\text{nfac}} = &- \sum_{i=1}^{N-1}\sum_{i'=i+1}^{N}\sum_{j=1}^{n_i}\sum_{j'=1}^{n'_i} Q_{ij}Q_{i'j'}\frac{\alpha}{\pi}\text{Re}[\Delta_1(k_i, p_{i,\text{outj}}; k_{i'}, p_{i',\text{outj}'})] \\ &- \sum_{k=1}^{2}\sum_{i=1}^{N}\sum_{j=1}^{n_i} Q_kQ_{ij}\frac{\alpha}{\pi}\text{Re}[\Delta_2(p_{k,\text{in}}; k_i, p_{i,\text{outj}})] \\ &+ \sum_{j'=1}^{n_0}\sum_{i=1}^{N}\sum_{j=1}^{n_i} Q_{0j'}Q_{ij}\frac{\alpha}{\pi}\text{Re}[\Delta_2(-p_{0,\text{outj}'}; k_i, p_{i,\text{outj}})], \end{aligned} \tag{C.28}$$

where $p_{i,\text{outj}}$, $j = 1, 2$ denotes again the momentum of decay product number j of the resonance number i.

The quantities $\Delta_i, i = 1, 2$ are given by

$$\begin{aligned}\Delta_1(k_j, p_{j,\text{out}}; k_i, p_{i,\text{out}}) &= \frac{K_i K_j s_{ij} \det(Y_0)}{\det(Y)} D_0(0) \\ &+ \frac{K_i \det(Y_3)}{\det(Y)} F(k_j, p_{j,\text{out}}; k_i, p_{i,\text{out}}) + \frac{K_j \det(Y_2)}{\det(Y)} F(k_i, p_{i,\text{out}}; k_j, p_{j,\text{out}}) \\ &- \frac{\bar{s}_{ij}}{w_{ij}} \left\{ \mathcal{L}i_2\left(\frac{M_j K_i}{M_i K_j}, \frac{1}{r_{ij}}\right) - \mathcal{L}i_2\left(\frac{M_j K_i}{M_i K_j}, r_{ij}\right) \right. \\ &\qquad \left. + \mathcal{L}i_2(r_{ij}, r_{ij}) + \log^2(r_{ij}) + 2\log(r_{ij}) \log\left(\frac{-K_j}{M_j \lambda}\right) \right\} \\ &+ \log\left(\frac{\lambda^2}{M_i M_j}\right) \log\left(-\frac{s_{ij}}{M_i M_j} - \mathrm{i}\varepsilon\right) + 2\log\left(\frac{\lambda M_i}{-K_i}\right) + 2\log\left(\frac{\lambda M_j}{-K_j}\right) + 4, \end{aligned} \tag{C.29}$$

and

$$\Delta_2(p_{k,\text{in}}; k_i, p_{i,\text{outj}}) = 2\log\left(\frac{\lambda M_i}{-K_i}\right) \left[\log\left(\frac{\hat{t}}{t}\right) - 1\right] - 2 - \mathrm{Li}_2\left(1 - \frac{\hat{t}}{t}\right), \tag{C.30}$$

with

$$\begin{aligned} F(k_j, p_{j,\text{out}}; k_i, p_{i,\text{out}}) &= \sum_{\tau=\pm 1} \left[\mathcal{L}i_2\left(\frac{K_i M_j}{K_j M_i}, r_{ij}^{\tau}\right) - \mathcal{L}i_2\left(-\frac{M_i M_j}{\hat{s}_{ji}} + \mathrm{i}\varepsilon, r_{ij}^{\tau}\right) \right] \\ &- 2\mathcal{L}i_2\left(\frac{K_i M_j}{K_j M_i}, -\frac{\hat{s}_{ji}}{M_i M_j} - \mathrm{i}\varepsilon\right) - \mathrm{Li}_2\left(1 - \frac{\hat{s}_{ji}}{s_{ij}}\right) - \log^2\left(\frac{\hat{s}_{ji}}{M_i M_j} - \mathrm{i}\varepsilon\right) \\ &+ \log\left(\frac{s_{ij}}{M_i M_j} - \mathrm{i}\varepsilon\right) \left[\log\left(-\frac{K_j}{M_i M_j}\right) + \log\left(-\frac{K_j}{M_j^2}\right)\right]. \end{aligned} \tag{C.31}$$

Appendix D

The Treatment of Soft and Collinear Singularities

As was said in Chapter 2, the real corrections to a given process generally contain collinear and infrared divergences, which partially cancel corresponding divergences in the virtual corrections. This sum of virtual and real corrections then depends on initial-state collinear singularities only. As discussed in Section D.1, the latter have to be split off the partonic cross-section before convoluting the latter with the parton distribution functions to yield the hadronic cross-section of the considered process. This procedure defines the infrared-safe partonic cross-section, which receives contributions from the Born cross-section, the virtual corrections, and the real corrections. In Section D.2 and D.3, we show how the real corrections can be split in singular and finite parts by the phase-space slicing technique and the subtraction method, respectively, whereas in Section D.4 we perform the same kind of splitting for the virtual corrections. Finally, in Section D.5 we explicitly demonstrate the matching of the soft and collinear singularities contained in the resulting singular parts of the real and virtual corrections. All expressions derived in this section are valid for the QED case of photon emission only, but can for processes not involving three-gluon self-interactions also be applied to the QCD case if one replaces everywhere the charges of the external particles by the corresponding couplings of the gluon [85].

D.1 The $\overline{\text{MS}}$-Subtraction of the Initial-State Collinear Singularities

As we discussed in Section 2.1, the cross-section for a hadronic process can generally be written as a convolution

$$\sigma_{\mathrm{P_1P_2}}(S) = \sum_{q_1,q_2=u,\bar{u},..} \int_0^1 \mathrm{d}x_1 \int_0^1 \mathrm{d}x_2 \Phi_{q_1|P_1}(x_1)\Phi_{q_2|P_2}(x_2)\sigma_{q_1q_2}(x_1x_2S), \qquad \text{(D.1)}$$

of the partonic cross-section $\sigma_{q_1q_2}$ with the parton distribution functions (PDFs) $\Phi_{q_1|P_1}(x_1)$. Whereas the partonic cross-section can generally be calculated perturbatively, the PDFs

parameterize the low-energetic parton binding within the hadron, and are usually determined experimentally in Deep Inelastic Scattering (DIS) experiments. As discussed in Section 2.1, in doing so one usually splits universal terms containing the initial-state singularities off the DIS cross-section, and fits the latter to the experimental data. This results in a set of modified PDFs

$$\overline{\Phi}_{q_i|P_i}(x_i,\mu_{\mathrm{F}}) = \Phi_{q_i|P_i}(x_i) + \frac{\alpha}{2\pi}\delta\Phi_{q_i|P_i}(x_i,\mu_{\mathrm{F}}), \qquad i=1,2, \tag{D.2}$$

where $\delta\Phi_{q_i|P_i}$ contains the subtracted universal terms in the sense that these terms are now determined experimentally as part of the PDFs. The form of these terms is restricted by the requirements that they must be universal and that they have to contain the initial-state collinear singularities. However, the partonic cross-section contains non-singular universal terms as well, and one can choose if one wants to absorb these terms in the PDFs or not. This ambiguity is usually fixed by a so-called *factorization scheme*, which uniquely defines the terms to be reabsorbed in the PDFs. The two most common factorization schemes are the DIS-scheme and the $\overline{\mathrm{MS}}$-scheme. Whereas PDFs determined using the DIS-scheme also contain universal non-singular terms, we will use the $\overline{\mathrm{MS}}$-scheme in this work, where only singular terms are reabsorbed in the PDFs. To be specific, the redefinition (D.2) in the $\overline{\mathrm{MS}}$-scheme reads

$$\begin{aligned}\overline{\Phi}^{\overline{\mathrm{MS}}}_{q_i|P_i}(x_i,\mu_F) &= \Phi_{q_i|P_i}(x_i) \\ &+ \frac{\alpha}{2\pi}Q_i^2\int_{x_i}^1\frac{\mathrm{d}z}{z}\,\Phi^{\overline{\mathrm{MS}}}_{q_i|P_i}\left(\frac{x_i}{z},\mu_F\right)\left[\frac{1+z^2}{1-z}\left(\log\left(\frac{\mu_F^2}{m_i^2}\right)-2\log(1-z)-1\right)\right]_+,\end{aligned} \tag{D.3}$$

where m_i is a regulator for the mass of the initial-state quark $q_i = 1,2$ and we used the (+)-prescription

$$\int_a^b \mathrm{d}x\,[f(x)]_+\,g(x) = \int_a^b \mathrm{d}x f(x)g(x) - \int_0^b \mathrm{d}x f(x)g(1). \tag{D.4}$$

Due to the universality of both, the PDFs and the terms split off the DIS cross-section, the distributions (D.3) can now be used to calculate the cross-section of an arbitrary hadronic process involving the above hadrons P_i in the initial state. However, such a process usually involves a typical energy scale different from the DIS momentum transfer, such that one has first to perform an evolutions of the PDFs from the DIS energy scale μ_F to the energy scale Q of the considered process by means of the GLAP equations. Inserting the resulting expressions into the hadronic cross-section (D.1), one has up to order α

$$\begin{aligned}\sigma_{\mathrm{P_1P_2}}(S) = &\sum_{q_1,q_2=u,\bar{u},..}\int_0^1\mathrm{d}x_1\int_0^1\mathrm{d}x_2\overline{\Phi}^{\overline{\mathrm{MS}}}_{q_1|P_1}(x_1,Q^2)\overline{\Phi}^{\overline{\mathrm{MS}}}_{q_2|P_2}(x_2,Q^2)\sigma_{q_1\bar{q}_2}(x_1x_2S) \\ &-\frac{\alpha}{2\pi}\sum_{i=1,2}\sum_{\substack{j=1,2\\ j\neq i}}Q_i^2\int_{x_i}^1\frac{\mathrm{d}z}{z}\sigma^{(0)}_{q_1\bar{q}_2}(x_1x_2s)\Phi^{\overline{\mathrm{MS}}}_{q_i|P_i}\left(\frac{x_i}{z}\right)\Phi^{\overline{\mathrm{MS}}}_{q_j|P_j}(x_j) \\ &\times\left[\frac{1+z^2}{1-z}\left(\log\left(\frac{Q^2}{m_i^2}\right)-2\log(1-z)-1\right)\right]_+.\end{aligned} \tag{D.5}$$

Substituting

$$x_i \to x_i z, \qquad x_j \to x_j, \qquad z \to z, \qquad i = 1,2, \qquad j \neq i \tag{D.6}$$

in the second and third line, this yields a convolution of the redefined PDFs with a modified partonic cross-section

$$\sigma_{\mathrm{P_1P_2}}(S) \quad = \quad \sum_{q_1,q_2=u,\bar{u},..} \int_0^1 \mathrm{d}x_1 \int_0^1 \mathrm{d}x_2 \overline{\Phi}^{\overline{\mathrm{MS}}}_{q_1|P_1}(x_1,Q^2) \overline{\Phi}^{\overline{\mathrm{MS}}}_{q_2|P_2}(x_2,Q^2) \sigma^{\mathrm{IR-safe}}_{q_1\bar{q}_2}(\hat{s},Q^2), \tag{D.7}$$

where the latter is given by

$$\sigma^{\mathrm{IR-safe}}_{q_1\bar{q}_2}(\hat{s},Q^2) = \sigma_{q_1\bar{q}_2}(x_1x_2S) - \sigma^{\mathrm{PDF}}_{q_1\bar{q}_2,\mathrm{sing.}}(x_1x_2S,Q^2). \tag{D.8}$$

The quantity $\hat{s} = x_1x_2S$ denotes the centre-of-mass energy of the partonic process in what follows. The correction term is then given by a convolution of the Born cross-section evaluated at $s = zx_1x_2S$, such that the corresponding phase-space integration can be re-parameterized to read

$$\sigma^{\mathrm{PDF}}_{q_1\bar{q}_2,\mathrm{sing.}}(\hat{s},Q^2) = \frac{1}{2\hat{s}} \sum_{i=1,2} \int_0^1 \mathrm{d}z \int \mathrm{d}\Phi_i(z) \left| \mathcal{A}^{\mathrm{PDF}}_{q_1\bar{q}_2,\mathrm{sing.}}(\Phi_i(z)) \right|^2, \tag{D.9}$$

with the squared amplitude given by

$$\begin{aligned} \left| \mathcal{A}^{\mathrm{PDF}}_{q_1\bar{q}_2,\mathrm{sing.}}(\Phi_i(z)) \right|^2 = \frac{\alpha}{2\pi} Q_i^2 \left| \mathcal{A}^{(0)}_{q_1\bar{q}_2}(\Phi_i(z)) \right|^2 \\ \times \frac{1}{z} \left[\frac{1+z^2}{1-z} \left(\log\left(\frac{Q^2}{m_i^2}\right) - 2\log(1-z) - 1 \right) \right]_+ . \end{aligned} \tag{D.10}$$

As was said before, this term contains the contribution of collinear Bremsstrahlung emission to the DIS cross-section evaluated at the typical energy scale Q^2 of the considered process. This is the reason for the appearance of the phase-space $\Phi_i(z)$, which is defined by a boost to the centre-of-mass frame where the energy of the initial-state quark q_i has been reduced by a factor of z due to Bremsstrahlung emission. Note that the correction term (D.9) does not result from the perturbative calculation of the partonic cross-section but rather from the definition of the PDFs. It compensates for the fact that the low-energy contributions are contained both, in the experimentally determined PDFs and in the perturbatively calculated partonic cross-section. Due their universality, the form of the low-energy terms in the partonic cross-section is exactly given by (D.9) such that they cancel in the difference (D.8).

D.2 Phase-Space Slicing

In this section we present a first method to split a given Bremsstrahlung cross-section into singular and finite parts. As was said in Section 2.3, the basic idea of this so-called *phase-space slicing* technique is to restrict the phase-space integration over the Bremsstrahlung momentum k by imposing a cut δ_s on the energy E as well as a cut δ_c on the angles between the Bremsstrahlung momentum and the momenta of the emitters, which we collectively denote by θ in what follows. In doing so, one splits the phase-space and thus the corresponding partonic cross section for the Bremsstrahlung process into a finite part and a singular part, where the finite part does not contain any soft or collinear divergences anymore and can thus be integrated over phase-space numerically. The singular parts can be divided into a piece arising from the soft part of the phase-space integration, where the energy of the Bremsstrahlung particle is restricted by $E < \delta_s\sqrt{\hat{s}}/2$, and a part arising from the hard collinear region, defined by $E > \delta_s\sqrt{\hat{s}}/2$ for the energy and $1 - \delta_c < \cos(\theta) < 1$ for the emission angles.

To start with, the singular part of the amplitude arising from the soft phase-space region factorizes in the amplitude $\mathcal{A}^{(0)}_{q_1 q_2}$ of the Born process times a correction factor

$$\sigma^{\text{real}}_{q_1 q_2,\text{soft}}(\hat{s}) = \frac{\alpha}{4\pi\hat{s}} \sum_{i=1}^{n} \sum_{\substack{j=1 \\ j\neq i}}^{n} \tau_i \tau_j Q_i Q_j \int \mathrm{d}\Phi_0 \left|\mathcal{A}^{(0)}_{q_1 q_2}(\Phi_0)\right|^2 \delta^{\text{soft}}_{ij}(\Phi_0), \tag{D.11}$$

where the process-independent correction factor can be written as [42]

$$\delta^{\text{soft}}_{ij}(\Phi_0) = \log\left(\frac{\delta_s^2 \hat{s}}{\lambda^2}\right)\left[1 - \log\left(\frac{s_{ij}}{m_i^2}\right)\right] - \log\left(\frac{4E_i^2}{m_i^2}\right) + \frac{1}{2}\log^2\left(\frac{4E_i^2}{m_i^2}\right) + \frac{\pi^2}{3} + \mathrm{Li}_2\left(1 - \frac{4E_iE_j}{s_{ij}}\right). \tag{D.12}$$

Here E_i and $Q_i, i = 1, \ldots n$ denote the energies and charges of the n external particles, respectively. The relative sign $\tau_i, i = 1, \ldots n$ is defined to be positive (negative), if the particle i is incoming (outgoing). In deriving (D.12), the masses m_i of the external particles were only kept as regulators for the collinear divergences, i.e. where they appear in logarithms diverging for $m_i \to 0$. Furthermore, we introduced the shorthand $s_{ij} = 2p_ip_j$, and λ denotes the regulator for the mass of the Bremsstrahlung particle.

The singular part of the Bremsstrahlung cross-section arising from the hard collinear phase-space region, on the other hand, can be split in a contribution containing the collinear divergences arising from the initial state and a contribution containing the final-state collinear divergences

$$\sigma^{\text{real}}_{q_1 q_2,\text{coll}}(\hat{s}) = \sigma^{\text{real,init.}}_{q_1 q_2,\text{coll.}}(\hat{s}) + \sigma^{\text{real,final}}_{q_1 q_2,\text{coll.}}(\hat{s}). \tag{D.13}$$

Restricting ourselves to the case of helicity-summed cross sections only, the contribution stemming from final-state radiation is proportional to the squared Born amplitude [42]

$$\sigma^{\text{real,final}}_{q_1q_2,\text{coll}}(\hat{s}) = \sum_{i=3}^{n} \frac{\alpha}{4\pi\hat{s}} Q_i^2 \int \mathrm{d}\Phi_0 \left|\mathcal{A}^{(0)}_{q_1q_2}(\Phi_0)\right|^2 \times \left\{\left[\frac{3}{2} + \log\left(\frac{\delta_s^2\hat{s}}{4E_i^2}\right)\right]\left[1 - \log\left(\frac{4E_i^2}{m_i^2}\frac{\delta_c}{2}\right)\right] + 3 - \frac{2\pi^2}{3}\right\}, \quad \text{(D.14)}$$

where we adopt the same notation as above, and the fermion masses are again kept in the collinear logarithms only. In case of Bremsstrahlung radiation off an initial-state particle, the energy of the emitting particle is reduced by the amount carried away by the emitted particle. The collision energy is then no longer fixed, such that the initial-state contribution to (D.13) is given by a convolution of the Born cross-section [42]

$$\sigma^{\text{real,init.}}_{q_1q_2,\text{coll.}}(\hat{s}) = \sum_{i=1,2} \frac{\alpha}{4\pi\hat{s}}\, Q_i^2 \int_0^{1-\delta_s} \mathrm{d}z \int \mathrm{d}\Phi_i(z) \times \frac{1}{z}\left|\mathcal{A}^{(0)}_{q_1q_2}(\Phi_i(z))\right|^2 \left[\frac{1+z^2}{1-z}\log\left(\frac{\hat{s}}{m_i^2}\frac{\delta_c}{2}\right) - \frac{2z}{1-z}\right]. \quad \text{(D.15)}$$

Here the z-dependence of the phase-space element $\Phi_i(z)$ indicates, that the amplitude is not evaluated in the centre-of-mass frame, but rather in the boosted frame where the momentum of the initial-state particle i is multiplied with a factor z.

When evaluating the integrand in (D.15) numerically, one has to cope with the instabilities arising from the limits $z \to 0$ as well as for $z \to 1$ in case of a small value for δ_s. The singularity at $z = 0$ can be suppressed by a cut on the squared centre-of-mass energy after the radiation of the Bremsstrahlung photon. In that way, one obtains a lower integration bound $z > z_{\min} = s_{\min}/\hat{s}$ for the integration over the energy fraction of the emitted photon, where $\hat{s} = x_1x_2S$ is again the partonic centre of mass energy squared. To stabilize the integrand at $z = 1$, on the other hand, we subtract the Born cross-section at $z = 1$ from the Born cross-section on the right-hand side of (D.15) and compensate for this subtraction with a separate term

$$\begin{aligned}\sigma^{\text{real,init.}}_{q_1q_2,\text{coll.}}(\hat{s}) = {} & \sum_{i=1,2} \frac{\alpha}{4\pi\hat{s}} Q_i^2 \int_0^{1-\delta_s} \mathrm{d}z \left\{\int \mathrm{d}\Phi_i(z)\frac{1}{z}\left|\mathcal{A}^{(0)}_{q_1q_2}(\Phi_i(z))\right|^2 \left[\frac{1+z^2}{1-z}\log\left(\frac{\hat{s}}{m_i^2}\frac{\delta_c}{2}\right) - \frac{2z}{1-z}\right]\right. \\ & \left. - \int \mathrm{d}\Phi_0 \left|\mathcal{A}^{(0)}_{q_1q_2}(\Phi_0)\right|^2 \left[\frac{1+z^2}{1-z}\log\left(\frac{\hat{s}}{m_i^2}\frac{\delta_c}{2}\right) - \frac{2z}{1-z}\right]\right\} \\ & + \sum_{i=1,2} \frac{\alpha}{4\pi\hat{s}} Q_i^2 \int \mathrm{d}\Phi_0 \left|\mathcal{A}^{(0)}_{q_1q_2}(\Phi_0)\right|^2 \int_0^{1-\delta_s} \mathrm{d}z \left[\frac{1+z^2}{1-z}\log\left(\frac{\hat{s}}{m_i^2}\frac{\delta_c}{2}\right) - \frac{2z}{1-z}\right], \quad \text{(D.16)}\end{aligned}$$

where we used that $\Phi_i(1)$ is equal to the phase-space Φ_0 of the Born process. The integral in the first two lines is then regular at $z = 1$, such that δ_s can be set to zero in the upper integration bound. The integral in the last line of (D.16) can be calculated analytically, yielding

$$\begin{aligned}\sigma^{\text{real,init.}}_{q_1q_2,\text{coll.}}(\hat{s}) = &\sum_{i=1,2}\frac{\alpha}{4\pi\hat{s}}Q_i^2\int_0^1\frac{\mathrm{d}z}{z}\int\mathrm{d}\Phi_i(z)\left|\mathcal{A}^{(0)}_{q_1q_2}(\Phi_i(z))\right|^2\left[\frac{1+z^2}{1-z}\log\left(\frac{\hat{s}}{m_i^2}\frac{\delta_c}{2}\right)-\frac{2z}{1-z}\right]_+\\ &+\sum_{i=1,2}\frac{\alpha}{4\pi\hat{s}}Q_i^2\int\mathrm{d}\Phi_0\left|\mathcal{A}^{(0)}_{q_1q_2}(\Phi_0)\right|^2\\ &\times\left[2+\log\delta_s^2\left(1-\log\left(\frac{\hat{s}}{m_i^2}\frac{\delta_c}{2}\right)\right)-\frac{3}{2}\log\left(\frac{\hat{s}}{m_i^2}\frac{\delta_c}{2}\right)\right],\end{aligned}\tag{D.17}$$

where we again employed the (+)-prescription (D.4). Putting finally all pieces together, and using charge conservation to rewrite

$$Q_i^2 = (\tau_iQ_i)^2 = -\sum_{\substack{j=1\\j\neq i}}^{n}Q_i\tau_iQ_j\tau_j,\tag{D.18}$$

the singular part of the Bremsstrahlung cross-section can be written as a sum of two terms, one arising from the initial-state contributions, and a second one arising from the final-state contributions

$$\sigma^{\text{real,slic.}}_{q_1q_2,\text{sing}}(\hat{s}) = \frac{\alpha}{4\pi\hat{s}}\sum_{i=1}^{2}\sum_{\substack{j=1\\j\neq i}}^{n}Q_i\tau_iQ_j\tau_j\Delta^{\text{init,slic.}}_{ij,\text{sing.}}+\frac{\alpha}{4\pi\hat{s}}\sum_{i=3}^{n}\sum_{\substack{j=1\\j\neq i}}^{n}Q_i\tau_iQ_j\tau_j\Delta^{\text{final,slic.}}_{ij,\text{sing.}}.\tag{D.19}$$

Using $E_1 = E_2 = \sqrt{\hat{s}}/2$, the initial-state contribution is given by

$$\begin{aligned}\Delta^{\text{init,slic.}}_{ij,\text{sing.}} = &-\int_0^1\frac{\mathrm{d}z}{z}\int\mathrm{d}\Phi_i(z)\left|\mathcal{A}^{(0)}_{q_1q_2}(\Phi_i(z))\right|^2\left[\frac{1+z^2}{1-z}\log\left(\frac{\hat{s}}{m_i^2}\frac{\delta_c}{2}\right)-\frac{2z}{1-z}\right]_+\\ &+\int\mathrm{d}\Phi_0\left|\mathcal{A}^{(0)}_{q_1q_2}(\Phi_0)\right|^2\left\{\frac{\pi^2}{3}+\mathrm{Li}_2\left(1-\frac{2\sqrt{\hat{s}}E_j}{s_{ij}}\right)-2+\log\left(\frac{m_i^2}{\lambda^2}\right)-\frac{3}{2}\log\left(\frac{\hat{s}}{m_i^2}\frac{\delta_c}{2}\right)\right.\\ &\left.-\log\left(\frac{\delta_s^2\hat{s}}{\lambda^2}\right)\log\left(\frac{s_{ij}}{m_i^2}\right)+\frac{1}{2}\log^2\left(\frac{\hat{s}}{m_i^2}\right)+\log\delta_s^2\log\left(\frac{\hat{s}}{m_i^2}\frac{\delta_c}{2}\right)\right\}\end{aligned}\tag{D.20}$$

whereas one has for the final-state term

$$\begin{aligned}&\Delta^{\text{final,slic.}}_{ij,\text{sing.}} =\\ &\int\mathrm{d}\Phi_0\left|\mathcal{A}^{(0)}_{q_1q_2}(\Phi_0)\right|^2\left\{\pi^2+\mathrm{Li}_2\left(1-\frac{4E_iE_j}{s_{ij}}\right)-\frac{9}{2}+\log\left(\frac{m_i^2}{\lambda^2}\right)+\frac{3}{2}\log\left(\frac{4E_i^2}{m_i^2}\frac{\delta_c}{2}\right)\right.\\ &\left.+\log\left(\frac{\delta_s^2\hat{s}}{4E_i^2}\right)\log\left(\frac{4E_i^2}{m_i^2}\frac{\delta_c}{2}\right)-\log\left(\frac{\delta_s^2\hat{s}}{\lambda^2}\right)\log\left(\frac{s_{ij}}{m_i^2}\right)+\frac{1}{2}\log^2\left(\frac{4E_i^2}{m_i^2}\right)\right\}.\end{aligned}\tag{D.21}$$

D.3 Subtraction Method

As a second method providing a splitting of the Bremsstrahlung cross-section in singular and finite parts we present the so-called *subtraction method* [85] in this section. The basic idea is here to construct an auxiliary function, which contains all infrared and collinear singularities and to subtract this function from the squared Bremsstrahlung matrix element. The resulting expression for the finite real corrections is then zero in the soft and collinear limits, and can thus be integrated over phase-space without encountering any numerical instabilities. To compensate for this subtraction, the auxiliary function is analytically integrated over the Bremsstrahlung momentum. The result of this integration then depends on the phase-space of the Born process only and can thus be added to the virtual corrections on the level of squared amplitudes to cancel the soft and collinear divergences.

As was said before, the infrared and collinear divergences arise from the phase-space regions, where the Bremsstrahlung particle is emitted with vanishing energy and emission angle, respectively. To isolate these contributions from the Bremsstrahlung cross-section, the corresponding phase-space integral is written as a convolution of the phase-space part connected to the Bremsstrahlung process, times the phase-space element of the non-radiative process

$$\int \mathrm{d}\Phi_{\mathrm{real}} = \int \mathrm{d}k \otimes \int \mathrm{d}\tilde{\Phi}(k), \tag{D.22}$$

The phase-space $\tilde{\Phi}(k)$ is here given by a prescription, which embeds the phase-space of the original process Φ_0 into the phase-space Φ_{real} of the Bremsstrahlung process. Considering unpolarized observables only, the singular part of the squared Bremsstrahlung amplitude factorizes into the square of the Born amplitude $\mathcal{A}^{(0)}$ times a factor containing the singularities, such that the subtraction function can be chosen to have the generic form

$$\left|\mathcal{A}^{\mathrm{subtr}}_{q_1 q_2}(\Phi_{\mathrm{real}})\right|^2 = \sum_{n_b=1}^{N_b} \sum_{\substack{i,j=1 \\ i\neq j}}^{n} g^{\mathrm{sub}}_{ij}(p_i, p_j, k_{b_b}) \left|\mathcal{A}^{(\mathrm{sub},ij)}_{q_1 q_2}(\tilde{\Phi}^{n_b}_{ij})\right|^2, \tag{D.23}$$

with

$$\left|\mathcal{A}^{(\mathrm{sub},ij)}_{q_1 q_2}(\tilde{\Phi}^{n_b}_{ij})\right|^2 = -4\pi\alpha\tau_i\tau_j Q_i Q_j \left|\mathcal{A}^{(0)}_{q_1 q_2}(\tilde{\Phi}^{n_b}_{ij})\right|^2, \tag{D.24}$$

Here n is again given by the number of external particles of the Born process. Furthermore, the quantities p_i and Q_i denotes the momentum and the charge of the external particle i and the relative sign $\tau_i, i = 1, \ldots n$ is defined to be positive (negative), if the particle i is incoming (outgoing). The sum over the index n_b accounts here for the fact that if the Bremsstrahlung particle appears N_b times in the final state, a separate subtraction term has to be introduced for each of the potential Bremsstrahlung particles. In what follows, we skip the dependence of the phase-space on n_b and denote the Bremsstrahlung momentum by $k = k_{n_b}$.

The embedding prescription $\tilde{\Phi}_{ij}$ of the n-particle phase-space Φ_0 into the $n+1$-particle phase-space Φ_{real} has to respect all mass-shell relations as well as momentum conservation in the soft and collinear limits. Moreover, it has to take into account that an initial-state particle of momentum p contributes only a fraction zp to the hard process after emission of the Bremsstrahlung particle with momentum $k = (1-z)p$. Similarly, a final-state particle with momentum p is produced with momentum $p+k$ in the hard scattering process. To summarize these requirements, the mapping $\tilde{\Phi}_{ij}$ is subject to the conditions

$$\tilde{p}_i \overset{k\to 0}{\to} p_i, \qquad i = 1, \ldots, n, \tag{D.25}$$

in the infrared limit as well as

$$\tilde{p}_i \overset{p_i k\to 0}{\to} \begin{cases} p_i + k & i > 2, \\ zp_i & i = 1, 2, \end{cases}, \tag{D.26}$$

$$\tilde{p}_i \overset{p_j k\to 0}{\to} p_i, \qquad i, j = 1, \ldots, n, i \neq j \tag{D.27}$$

in the collinear limits. The embedding prescription $\tilde{\Phi}_{ij}$ and the subtraction functions g_{ij}^{sub} thus depend on the particles i and j being incoming or outgoing. Referring to the particle i as the *emitter* and to the particle j as *spectator* in what follows, one therefore encounters four kinematically different cases.

For the case of both, the emitter and the spectator being part of the final state, the above conditions on the phase-space projection are met by the choice [85]

$$\tilde{p}_i^\mu = p_i^\mu + k^\mu - \frac{y_{ij}}{1-y_{ij}} p_j^\mu, \qquad \tilde{p}_j^\mu = \frac{1}{1-y_{ij}} p_j^\mu, \qquad \tilde{k}^\mu = k^\mu, \qquad \tilde{p}_l^\mu = p_l^\mu,$$
$$i, j > 2, l = 1, \ldots, n, l \neq i, j, \tag{D.28}$$

where here and in the following we use the shorthands

$$x_{ij} = \frac{p_i p_j + p_j k - p_i k}{p_i p_j + p_j k}, \qquad y_{ij} = \frac{p_i k}{p_i p_j + p_i k + p_j k},$$
$$z_{ij} = \frac{p_i p_j}{p_i p_j + p_j k}, \qquad v_{ij} = \frac{p_i p_j - p_i k - p_j k}{p_i p_j}. \tag{D.29}$$

In case of an initial-state emitter and a final-state spectator the momentum projection is given by

$$\tilde{p}_i^\mu = x_{ij} p_i^\mu, \qquad \tilde{p}_j^\mu = p_j^\mu + k^\mu - (1-x_{ji}) p_i^\mu, \qquad \tilde{k}^\mu = k^\mu, \qquad \tilde{p}_l^\mu = p_l^\mu,$$
$$i = 1, 2, \quad j > 2, \quad l = 1, \ldots, n, l \neq i, j, \tag{D.30}$$

whereas the corresponding expression for initial-state emitter and final-state spectator can be obtained from (D.30) by exchanging $i \leftrightarrow j$ everywhere.

Finally, in case of an initial-state emitter and an initial-state spectator the embedding $\tilde{\Phi}_{ij}$ involves the transformations

$$\tilde{p}_i^\mu = v_{ij} p_i, \qquad \tilde{p}_j = p_j, \qquad \tilde{p}_l^\mu = \Lambda^\mu{}_\nu p_l^\nu, \qquad \tilde{k}^\mu = \Lambda^\mu{}_\nu k^\nu \qquad i,j = 1,2, \quad l = 3,\ldots,n, \tag{D.31}$$

with the boost matrix

$$\Lambda^\mu{}_\nu = g^\mu{}_\nu - \frac{(P_{ij}+\tilde{P}_{ij})^\mu (P_{ij}+\tilde{P}_{ij})_\nu}{P_{ij}^2 + P_{ij}\tilde{P}_{ij}} + \frac{2\tilde{P}_{ij}^\mu P_{ij,\nu}}{P_{ij}^2}. \tag{D.32}$$

Here, $\tilde{P}_{ij}$ is given by the total initial-state momentum after the projection $\tilde{P}_{ij}^\mu = \tilde{p}_i^\mu + \tilde{p}_j^\mu$, whereas

$$P_{ij} = p_1 + p_2 - k = \sum_{k=3}^{n} p_k. \tag{D.33}$$

The subtraction functions corresponding to the four cases read

$$g_{ij}^{\text{sub}}(p_i,p_j,k) = \begin{cases} \frac{1}{(p_i k)(1-y_{ij})}\left[\frac{2}{1-z_{ij}(1-y_{ij})} - 1 - z_{ij}\right], & i,j > 2, \\ \frac{1}{(p_i k)x_{ij}}\left[\frac{2}{2-x_{ij}-z_{ij}} - 1 - z_{ij}\right], & i > 2, \quad j = 1,2, \\ \frac{1}{(p_i k)x_{ji}}\left[\frac{2}{2-x_{ji}-z_{ji}} - 1 - x_{ji}\right], & i = 1,2, \quad j > 2, \\ \frac{1}{(p_i k)v_{ij}}\left[\frac{2}{1-v_{ij}} - 1 - v_{ij}\right], & i = 1,2, \quad j = 1,2. \end{cases} \tag{D.34}$$

The above results contain all information we need to construct the subtraction function (D.23). The latter can then be subtracted from the squared Bremsstrahlung amplitude to cancel all infrared and collinear singularities. Integrating the so-obtained squared amplitude over the full phase-space of the Bremsstrahlung process yields the finite part of the Bremsstrahlung cross-section

$$\sigma_{q_1q_2,\text{finite}}^{\text{real,subtr}}(\hat{s}) = \frac{1}{2\hat{s}} \int \mathrm{d}\Phi_{\text{real}} \left(\left|\mathcal{A}_{q_1q_2}^{\text{real}}(\Phi_{\text{real}})\right|^2 - \left|\mathcal{A}_{q_1q_2}^{\text{subtr}}(\Phi_{\text{real}})\right|^2 \right). \tag{D.35}$$

To compensate for this subtraction, one has to add the phase-space integral of the squared subtraction amplitude to the total cross-section again. However, in order to make the collinear and infrared divergences contained in the virtual corrections cancel in this sum, one has first to integrate the subtraction function (D.23) over the momentum of the Bremsstrahlung particle. The resulting expression has the generic form [85]

$$\begin{aligned} \sigma_{q_1q_2,\text{sing.}}^{\text{real,subtr.}}(\hat{s}) &= \frac{1}{2\hat{s}} \int \mathrm{d}\Phi_{\text{real}} \left|\mathcal{A}_{q_1q_2}^{\text{subtr}}(\Phi_{\text{real}})\right|^2 \\ &= -\frac{\alpha}{4\pi\hat{s}} \sum_{\substack{i,j=1 \\ i\neq j}}^{n} \tau_i\tau_j Q_i Q_j \int_0^1 \mathrm{d}z \int \mathrm{d}\tilde{\Phi}_{ij}(z) \frac{1}{z} \mathcal{G}_{ij}^{\text{sub}}(r_{ij},z) \left|\mathcal{A}_{q_1q_2}^{(0)}(\tilde{\Phi}_{ij}(z))\right|^2, \end{aligned} \tag{D.36}$$

where $\tilde{s}_{ij} = 2\tilde{p}_i\tilde{p}_j$ and the convolution over z stems from the contributions where the Bremsstrahlung particle couples to the initial state, thus reducing the collision energy by a fraction $0 < z < 1$. As in the case of the phase-space slicing, the singularity of the integrand at $z = 0$ can be suppressed by a lower cut on the partonic centre-of-mass energy, leading to a lower integration bound of $z_{\min} = s_{\min}/\hat{s}$.

For the integrated subtraction functions $\mathcal{G}_{ij}^{\text{sub}}$, one has again the four kinematical cases described above

$$\mathcal{G}_{ij}^{\text{sub}}(r_{ij}, z) = \begin{cases} \delta(z-1)\left[\mathcal{L}(|r_{ij}|, m_i^2) + C_{ij}\right] & i,j > 2 \\ \frac{1}{1-z}\left[2\log\left(\frac{2-z}{1-z}\right) - \frac{3}{2}\right] & i > 2, j = 1,2, \\ \frac{1+z^2}{1-z}\log\left(\frac{|r_{ij}|}{m_i^2}\right) - \frac{2}{1-z}(z + \log(2-z)) & \\ \qquad + (1+z)\log(1-z) & i = 1,2, j > 2 \\ \frac{1+z^2}{1-z}\log\left(\frac{|r_{ij}|}{m_i^2}\right) - \frac{2z}{1-z} & i = 1,2, j = 1,2, \end{cases} \tag{D.37}$$

with $\mathcal{L}$, r_{ij} and C_{ij} given by

$$\mathcal{L}(s_{ij}, m_i^2) = \log\left(\frac{\lambda^2}{s_{ij}}\right)\left(1 + \log\left(\frac{m_i^2}{s_{ij}}\right)\right) - \frac{1}{2}\log^2\left(\frac{m_i^2}{s_{ij}}\right) + \frac{1}{2}\log\left(\frac{m_i^2}{s_{ij}}\right), \tag{D.38}$$

and

$$r_{ij} = \begin{cases} \tilde{s}_{ij} = (\tilde{p}_i + \tilde{p}_j)^2 & i,j > 2, \\ \frac{\tilde{s}_{ij}}{z} = \frac{(\tilde{p}_i+\tilde{p}_j)^2}{z} & i = 1,2, j > 2, \\ \hat{s} = (p_1 + p_2)^2 & i,j = 1,2. \end{cases} \qquad C_{ij} = \begin{cases} -\frac{\pi^2}{3} + \frac{3}{2} & i,j > 2, \\ \frac{\pi^2}{6} - 1 & i = 1,2, j > 2, \\ -\frac{\pi^2}{2} + \frac{3}{2} & i > 2, j = 1,2, \\ -\frac{\pi^2}{3} + 2 & i,j = 1,2. \end{cases} \tag{D.39}$$

However, the expression (D.36) is not yet suited for numerical evaluation, since the integrated subtraction functions $\mathcal{G}_{ij}^{\text{sub}}$ are singular at the upper integration bound $z = 1$. It is the limit $z \to 1$ that corresponds to the infrared and collinear phase-space limits, such that to obtain an numerically stable integrand, one has to isolate the corresponding contribution. To this end, one subtracts this endpoint contribution from the full integrand

and adds it again with the z-dependence integrated out analytically

$$\sigma^{\text{real,subtr.}}_{q_1q_2,\text{sing.}}(\hat{s}) = -\frac{\alpha}{4\pi\hat{s}}\sum_{\substack{i,j=1\\i\neq j}}^{n}\tau_i\tau_jQ_iQ_j\left\{\int_0^1 \mathrm{d}z\int \mathrm{d}\tilde{\Phi}_{ij}(z)\mathcal{G}^{\text{sub}}_{ij}(r_{ij},z)\frac{1}{z}\left|\mathcal{A}^{(0)}_{q_1q_2}(\tilde{\Phi}_{ij}(z))\right|^2\right.$$
$$\left. - \int_0^1 \mathrm{d}z\int \mathrm{d}\tilde{\Phi}_{ij}(1)\mathcal{G}^{\text{sub}}_{ij}(r_{ij},z)\left|\mathcal{A}^{(0)}_{q_1q_2}(\tilde{\Phi}_{ij}(1))\right|^2\right\}$$
$$- \frac{\alpha}{4\pi\hat{s}}\sum_{\substack{i,j=1\\i\neq j}}^{n}\tau_i\tau_jQ_iQ_j\int \mathrm{d}\tilde{\Phi}_{ij}(1)\left[\mathcal{L}(|\tilde{s}_{ij}|,m_i^2)+C_{ij}\right]\left|\mathcal{A}^{(0)}_{q_1q_2}(\tilde{\Phi}_{ij}(1))\right|^2. \quad \text{(D.40)}$$

Furthermore, one has

$$\lim_{z\to 1}\mathrm{d}\tilde{\Phi}_{ij}(z) = \mathrm{d}\Phi_0 \qquad \forall i,j=1,\ldots,n, \quad \text{(D.41)}$$

as can be seen from the embedding prescriptions (D.28), (D.30) and (D.31), where $\mathrm{d}\Phi_0$ is the phase-space element of the original process. To be able to treat (D.40) in the same way as the singular Bremsstrahlung contributions (D.20) and (D.21) for the phase-space slicing, the phase-space elements $\tilde{\Phi}_{ij}$ in (D.40) can for the initial-state contributions $i=1,2$ be identified with the phase-space elements $\Phi_i(z)$, which are again defined by a boost to the system, where the initial-state particle i carries a momentum zp_i. Altogether, the singular part of the Bremsstrahlung cross-section then reads

$$\sigma^{\text{real,subtr.}}_{q_1q_2,\text{sing.}}(\hat{s}) = -\frac{\alpha}{4\pi\hat{s}}\sum_{\substack{i,j=1\\i\neq j}}^{n}\tau_i\tau_jQ_iQ_j\int_0^1\frac{\mathrm{d}z}{z}\int \mathrm{d}\Phi_i(z)\left[\mathcal{G}^{\text{sub}}_{ij}(r_{ij},z)\right]_+\left|\mathcal{A}^{(0)}_{q_1q_2}(\Phi_i(z))\right|^2$$
$$- \frac{\alpha}{4\pi\hat{s}}\sum_{\substack{i,j=1\\i\neq j}}^{n}\tau_i\tau_jQ_iQ_j\int \mathrm{d}\Phi_0\left[\mathcal{L}(|s_{ij}|,m_i^2)+C_{ij}\right]\left|\mathcal{A}^{(0)}_{q_1q_2}(\Phi_0)\right|^2, \quad \text{(D.42)}$$

where we again introduced the (+)-prescription (D.4), s_{ij} is calculated from the momenta in Φ_0, whereas the momenta $\tilde{p}_i$ and $\tilde{p}_i$ in the definition (D.39) of r_{ij} are taken from the phase-space $\Phi_i(z)$ in the first part of the (+)-prescription, and from the phase-space $\Phi_i(1)=\Phi_0$ in the second part of the (+)-prescription. Note that the case of both the emitter and the spectator being part of the final state does not contribute to the first integral due to the δ-function in the first line of (D.37). The remaining terms can then be split again in initial-state and final-state contributions

$$\sigma^{\text{real,subtr.}}_{q_1q_2,\text{sing.}}(\hat{s}) = \frac{\alpha}{4\pi\hat{s}}\sum_{i=1}^{2}\sum_{\substack{j=1\\j\neq i}}^{n}Q_i\tau_iQ_j\tau_j\Delta^{\text{init,subtr.}}_{ij,\text{sing.}} + \frac{\alpha}{4\pi\hat{s}}\sum_{i=3}^{n}\sum_{\substack{j=1\\j\neq i}}^{n}Q_iQ_j\Delta^{\text{final,subtr.}}_{ij,\text{sing.}}. \quad \text{(D.43)}$$

Upon inserting (D.37), the initial-state contribution can then be written as

$$\Delta^{\text{init,subtr.}}_{ij,\text{sing.}} = -\int \mathrm{d}\Phi_0 \left[\mathcal{L}(|s_{ij}|, m_i^2) + C_{ij}\right] \left|\mathcal{A}^{(0)}_{q_1 q_2}(\Phi_0)\right|^2 - \int_0^1 \frac{\mathrm{d}z}{z} \int \mathrm{d}\Phi_i(z) \left[\frac{1+z^2}{1-z} \log\left(\frac{|r_{ij}|}{m_i^2}\right) + D_j(z)\right]_+ \left|\mathcal{A}^{(0)}_{q_1 q_2}(\Phi_i(z))\right|^2, \quad \text{(D.44)}$$

with

$$D_j(z) = \begin{cases} -\frac{2z}{1-z}, & j = 1,2 \\ -\frac{2}{1-z}(z + \log(2-z)) + (1+z)\log(1-z), & j > 2. \end{cases}, \quad \text{(D.45)}$$

and the final-state contribution is given by

$$\Delta^{\text{final,subtr.}}_{ij,\text{sing.}} = -\int \mathrm{d}\Phi_0 \left[\mathcal{L}(|s_{ij}|, m_i^2) + C_{ij}\right] \left|\mathcal{A}^{(0)}_{q_1 q_2}(\Phi_0)\right|^2 - \delta_{j<3} \int_0^1 \frac{\mathrm{d}z}{2z\hat{s}} \int \mathrm{d}\Phi_j(z) \left[\frac{1}{1-z}\left(2\log\left(\frac{2-z}{1-z}\right) - \frac{3}{2}\right)\right]_+ \left|\mathcal{A}^{(0)}_{q_1 q_2}(\Phi_j(z))\right|^2. \quad \text{(D.46)}$$

D.4 The Finite Virtual Corrections

As pointed out before, in calculating the virtual corrections to a given process, one generally encounters soft and collinear divergences, which cancel when adding the corresponding Bremsstrahlung contribution. However, in order to implement this cancellation in a numerically stable way, it would be preferable to extract the singular parts from the virtual corrections before integrating out the phase-space. To do so, one makes use of the fact that the singular part of the virtual corrections takes an universal form, and that the corresponding cross section factorizes into the Born cross section times a correction factor. In that way one is able to write the singular part of the virtual corrections as

$$\sigma^{\text{virt}}_{q_1 q_2,\text{sing}}(\hat{s}) = \frac{1}{2\hat{s}} \int \mathrm{d}\Phi_0 \; 2\mathrm{Re}\left[\left(\mathcal{A}^{(0)}_{q_1 q_2}(\Phi_0)\right)^\star \mathcal{A}^{(1)}_{q_1 q_2,\text{sing.}}(\Phi_0)\right], \quad \text{(D.47)}$$

where [42]

$$2\mathrm{Re}\left[\left(\mathcal{A}^{(0)}_{q_1 q_2}(\Phi_0)\right)^\star \mathcal{A}^{(1)}_{q_1 q_2,\text{sing}}(\Phi_0)\right] = \frac{\alpha}{2\pi} \sum_{\substack{i,j=1 \\ i\neq j}}^{n} \tau_i \tau_j Q_i Q_j \left|\mathcal{A}^{(0)}_{q_1 q_2}(\Phi_0)\right|^2 (\mathcal{L}(s_{ij}, m_i) + C_{ij}). \quad \text{(D.48)}$$

Here $\mathcal{A}^{(0)}_{q_1 q_2}$ denotes again the Born amplitude, whereas the function $\mathcal{L}$ as well as the constants C_{ij} are again given by (D.38) and (D.39). Furthermore, the relative sign $\tau_i, i = 1, \ldots n$ is defined to be positive (negative), if the particle i is incoming (outgoing) and the masses $m_i, i = 1, \ldots, n$ are only kept as regulators for the collinear divergences. Finally, we

used $s_{ij} = 2p_i p_j$, and λ denotes the regulator for the mass of the Bremsstrahlung particle. The finite parts in (D.47) are of course arbitrary, and one is free to include additional finite terms in the definition of the singular virtual corrections.

Following our discussion in Chapter 2, we intend to treat the virtual corrections in Leading Pole Approximation (LPA), whereas we evaluate the real corrections exactly. However, this produces a mismatch between the form of the soft and collinear singularities appearing in the virtual corrections on one hand and the soft an collinear singularities contained in the Bremsstrahlung cross-section on the other hand. To solve this problem, we here adopt the approach to apply the Leading Pole Approximation to the finite part of the virtual corrections only, i.e. we apply the LPA *after* having subtracted the squared amplitude (D.48) from the full virtual corrections. The finite virtual corrections are then given by

$$\sigma^{\text{virt,LPA}}_{q_1 q_2,\text{finite}}(\hat{s}) = \frac{1}{2\hat{s}} \int \mathrm{d}\Phi_0 \; 2\text{Re}\left[\left(\mathcal{A}^{(0),\text{LPA}}_{q_1 q_2}(\Phi_0)\right)^\star \mathcal{A}^{(1),\text{LPA}}_{q_1 q_2,\text{finite}}(\Phi_0) \right] \tag{D.49}$$

where

$$\begin{aligned} 2\text{Re}\left[\left(\mathcal{A}^{(0),\text{LPA}}_{q_1 q_2}(\Phi_0)\right)^\star \mathcal{A}^{\text{virt,LPA}}_{q_1 q_2,\text{finite}}(\Phi_0) \right] = \\ 2\text{Re}\left[\left(\mathcal{A}^{(0),\text{LPA}}_{q_1 q_2}(\Phi_0)\right)^\star \mathcal{A}^{\text{virt,LPA}}_{q_1 q_2}(\Phi_0) \right] - 2\text{Re}\left[\left(\mathcal{A}^{(0),\text{LPA}}_{q_1 q_2}(\Phi_0)\right)^\star \mathcal{A}^{\text{virt,LPA}}_{q_1 q_2,\text{sing.}}(\Phi_0) \right]. \end{aligned} \tag{D.50}$$

Applying the LPA to the singular part (D.48) corresponds to replace the Born amplitude by the Born Amplitude in LPA

$$A^{(0)}_{q_1 q_2}(\Phi_0) \overset{LPA}{\approx} A^{(0),\text{LPA}}_{q_1 q_2,V}(\Phi_0) = \frac{W^{(0)}_{-1}(m_V^2)}{k^2 - \mu_V^2} \tag{D.51}$$

and to replace the quantity $\tilde{s}_{ij}$ in the function $\mathcal{L}$ by the corresponding quantity $\tilde{s}^{\text{osh}}_{ij}$ evaluated from the on-shell projected momenta. Here $W^{(0)}_{-1}$ denotes the residuum of the Born amplitude at the Pole, k stands for the resonant momenta and m_V as well as μ_V denote the real and complex mass of the resonant particles, respectively. Altogether, one thus has for the subtraction term in (D.50)

$$2\text{Re}\left[\left(\mathcal{A}^{(W0)}_{q_1 q_2}(\Phi_0)\right)^\star \mathcal{A}^{(1)}_{q_1 q_2,\text{sing}}(\Phi_0) \right] = \left| A^{(0),\text{LPA}}_{q_1 q_2,V}(\Phi_0) \right|^2 (\mathcal{L}(\tilde{s}^{\text{osh}}_{ij}, m_i) + C_{ij}). \tag{D.52}$$

As discussed in the next section, we add the singular virtual corrections to the Bremsstrahlung contributions to compensate for the subtraction (D.50). According to our approach to extract the singular term from the virtual corrections *before* applying the LPA, the exact singular terms (D.48) are added to the real corrections rather than the singular terms (D.52) evaluated in LPA. In this way, we make sure that the evaluation of the virtual correction in Leading Pole Approximation does not spoil the cancellation of soft and collinear singularities in the total cross-section.

D.5 Analytical Cancellation of the Infrared and Collinear Singularities

Using the results of the preceding sections, we are now in the position to explicitly demonstrate the cancellation of the infrared and collinear singularities. To start with, we add the singular terms of the Bremsstrahlung cross-sections to the singular virtual corrections. For the phase-space slicing approach, the resulting expression can again be divided in terms arising from initial-state radiation, and terms arising from final-state radiation, such that by adding (D.19) to (D.47) one obtains

$$\sigma^{\text{virt}}_{q_1q_2,\text{sing}}(\hat{s}) + \sigma^{\text{real,slic.}}_{q_1q_2,\text{sing.}}(\hat{s}) = \frac{1}{2\hat{s}} \int \mathrm{d}\Phi_0 \left| \mathcal{A}^{(\text{v+r}),\text{init.}}_{q_1q_2,\text{finite}}(\Phi_0) \right|^2 + \frac{1}{2\hat{s}} \sum_{i=1}^{2} \int \mathrm{d}z \int \mathrm{d}\Phi_i(z) \left| \mathcal{A}^{(\text{v+r}),\text{init},+}_{q_1q_2,\text{sing.}}(\Phi_i(z)) \right|^2 + \frac{1}{2\hat{s}} \int \mathrm{d}\Phi_0 \left| \mathcal{A}^{(\text{v+r}),\text{final}}_{q_1q_2,\text{finite}}(\Phi_0) \right|^2 . \quad \text{(D.53)}$$

The squared amplitude for the initial-state contribution in the first integral

$$\left| \mathcal{A}^{(\text{v+r}),\text{init.}}_{q_1q_2,\text{finite}}(\Phi_0) \right|^2 = \frac{\alpha}{2\pi} \sum_{i=1}^{2} \sum_{\substack{j=1 \\ j\neq i}}^{n} Q_i\tau_i Q_j\tau_j \left| \mathcal{A}^{(0)}_{q_1q_2}(\Phi_0) \right|^2 \times \left[\frac{\pi^2}{3} - 2 + C_{ij} + \mathrm{Li}_2\left(1 - \frac{4E_iE_j}{s_{ij}}\right) + \log\left(\frac{\hat{s}}{s_{ij}}\frac{\delta_c}{2}\right)\left(\frac{3}{2} + \log\delta_s^2\right) + \frac{1}{2}\log^2\left(\frac{\hat{s}}{s_{ij}}\right) \right] \quad \text{(D.54)}$$

as well as the squared amplitude for the final-state contribution in the third integral

$$\left| \mathcal{A}^{(\text{v+r}),\text{final}}_{q_1q_2,\text{finite}}(\Phi_0) \right|^2 = \frac{\alpha}{2\pi} \sum_{i=3}^{n} \sum_{\substack{j=1 \\ j\neq i}}^{n} Q_i\tau_i Q_j\tau_j \left| \mathcal{A}^{(0)}_{q_1q_2}(\Phi_0) \right|^2 \left[\pi^2 - \frac{9}{2} + C_{ij} + \mathrm{Li}_2\left(1 - \frac{4E_iE_j}{s_{ij}}\right) + \log\left(\frac{4E_i^2}{s_{ij}}\frac{\delta_c}{2}\right)\left(\frac{3}{2} + \log\left(\frac{\delta_s^2\hat{s}}{4E_i^2}\right)\right) + \frac{1}{2}\log^2\left(\frac{4E_i}{s_{ij}}\right) \right] \quad \text{(D.55)}$$

then neither depend on the mass regulator λ of the Bremsstrahlung particle nor on the masses of the external particles m_i, and are therefore already infrared safe. In the above expressions, the constants C_{ij} are again given in (D.39), Li_2 denotes the Spence function and δ_s as well as δ_c denote the slicing cuts on the energy and the production angle of the Bremsstrahlung particle, respectively.

The squared amplitude in the second integral, on the other hand, is given by the the part of the initial-state contribution (D.20) containing the (+)-prescription

$$\left|\mathcal{A}^{(\mathrm{v+r}),\mathrm{init.},+}_{q_1q_2,\mathrm{sing.}}(\Phi_i(z))\right|^2 = -\frac{\alpha}{2\pi}\sum_{\substack{j=1\\j\neq i}}^{n} Q_i\tau_i Q_j\tau_j \left|\mathcal{A}^{(0)}_{q_1q_2}(\Phi_i(z))\right|^2 \frac{1}{z}\left[\frac{1+z^2}{1-z}\log\left(\frac{\hat{s}}{m_i^2}\frac{\delta_c}{2}\right) - \frac{2z}{1-z}\right]_+ . \quad \text{(D.56)}$$

Here the collinear singularities cancel only partially and a dependence of the total partonic cross-section on the initial-state masses remains. If considering leptonic reactions, these masses are known, and the above expression can be used without being altered. In case of a hadronic reaction, on the other hand, the initial-state masses are experimentally not defined, which leads to large uncertainties in the predictions for the corresponding cross-section. However, as stated in Section D.1, the logarithms in the initial-state quark masses are generally split off the partonic DIS cross-section before determining the PDFs by a fit of the hadronic DIS cross-section to the experimental data, and are thus already contained in the PDFs. To compensate for this, the corresponding terms have to be subtracted according to (D.8), such that one obtains as a final result for the sum of the singular real and the singular virtual corrections

$$\begin{aligned}\sigma^{\mathrm{virt+real}}_{q_1q_2,\mathrm{finite}}(\hat{s},Q^2) &= \sigma^{\mathrm{virt}}_{q_1q_2,\mathrm{sing.}}(\hat{s}) + \sigma^{\mathrm{real,slic.}}_{q_1q_2,\mathrm{sing.}}(\hat{s}) - \sigma^{\mathrm{PDF}}_{q_1q_2,\mathrm{sing.}}(\hat{s},Q^2)\\ &= \frac{1}{2\hat{s}}\int \mathrm{d}\Phi_0 \left|\mathcal{A}^{(\mathrm{v+r}),\mathrm{init.}}_{q_1q_2,\mathrm{finite}}(\Phi_0)\right|^2 + \frac{1}{2\hat{s}}\sum_{i=1}^{2}\int \mathrm{d}z \int \mathrm{d}\Phi_i(z) \left|\mathcal{A}^{(\mathrm{v+r}),\mathrm{init},+}_{q_1q_2,\mathrm{finite.}}(\Phi_i(z))\right|^2\\ &\quad + \frac{1}{2\hat{s}}\int \mathrm{d}\Phi_0 \left|\mathcal{A}^{(\mathrm{v+r}),\mathrm{final}}_{q_1q_2,\mathrm{finite}}(\Phi_0)\right|^2, \quad \text{(D.57)}\end{aligned}$$

where the initial-state contribution containing the (+)-prescription

$$\left|\mathcal{A}^{(\mathrm{v+r}),\mathrm{init},+}_{q_1q_2,\mathrm{finite.}}(\Phi_i(z))\right|^2 = -\frac{\alpha}{2\pi}\sum_{\substack{j=1\\j\neq i}}^{n} Q_i\tau_i Q_j\tau_j \left|\mathcal{A}^{(0)}_{q_1q_2}(\Phi_i(z))\right|^2 \times \frac{1}{z}\left[\frac{1+z^2}{1-z}\left(\log\left(\frac{\hat{s}}{Q^2}\frac{\delta_c}{2}\right) + 2\log(1-z) + 1\right) - \frac{2z}{1-z}\right]_+ \quad \text{(D.58)}$$

is now independent of the masses of the initial-state partons.

The cancellation of the soft and collinear singularities in case of the subtraction methods can be done following the same lines. The endpoint contribution in the first lines of (D.44) and (D.46) cancels here exactly the singular contribution of the virtual corrections, which was actually the motivation for choosing the form (D.47) for the latter. In this way, it can immediately be seen that the resulting expression for the final state is independent

of both, the photon mass λ as well as the mass regulators m_i, whereas the initial-state contribution is finite in the infrared limit, but still depends on the masses of the initial-state partons. This dependence cancels again when compensating for the fact that the corresponding terms are already contained in the PDFs, which is equivalent to subtracting the term (D.9) from the partonic cross-section, as we discussed in Section D.1.

Using (D.43), (D.47) and (D.9), one therefore obtains the final result

$$\begin{aligned}\sigma^{\text{virt+real}}_{q_1q_2,\text{finite}}(\hat{s},Q^2) &= \sigma^{\text{virt}}_{q_1q_2,\text{sing}}(\hat{s}) + \sigma^{\text{real,subtr.}}_{q_1q_2,\text{sing.}}(\hat{s}) - \sigma^{\text{PDF}}_{q_1q_2,\text{sing.}}(\hat{s},Q^2) \\ &= \frac{1}{2\hat{s}}\sum_{i=1}^{2}\int \mathrm{d}z \int \mathrm{d}\Phi_i(z) \left|\mathcal{A}^{(\text{v+r}),\text{init},+}_{q_1q_2,\text{finite}}(\Phi_i(z))\right|^2 \\ &\quad + \frac{1}{2\hat{s}}\sum_{j=1}^{2}\int \mathrm{d}z \int \mathrm{d}\Phi_j(z) \left|\mathcal{A}^{(\text{v+r}),\text{final},+}_{q_1q_2,\text{finite}}(\Phi_j(z)\right|^2, \quad \text{(D.59)}\end{aligned}$$

where squared amplitude of the initial-state contribution is given by

$$\begin{aligned}\left|\mathcal{A}^{(\text{v+r}),\text{init},+}_{q_1q_2,\text{finite}}(\Phi_i(z))\right|^2 &= -\frac{\alpha}{2\pi}\sum_{\substack{j=1\\j\neq i}}^{n} Q_i\tau_i Q_j\tau_j \left|\mathcal{A}^{(0)}_{q_1q_2}(\Phi_i(z))\right|^2 \\ &\quad \times \frac{1}{z}\left[\frac{1+z^2}{1-z}\left(\log\left(\frac{|r_{ij}|}{Q^2}\right) + 2\log(1-z) + 1\right) + D_j(z)\right]_+ \quad \text{(D.60)}\end{aligned}$$

with $D_j(z)$ and r_{ij} given in (D.45) and (D.39), whereas the corresponding expression for the final-state contribution reads

$$\begin{aligned}&\left|\mathcal{A}^{(\text{v+r}),\text{final},+}_{q_1q_2,\text{finite}}(\Phi_j(z))\right|^2 \\ &\quad = \frac{\alpha}{2\pi}Q_i\tau_i(\tau_1Q_1+\tau_2Q_2)\left|\mathcal{A}^{(0)}_{q_1q_2}(\Phi_j(z))\right|^2 \frac{1}{z}\left[\frac{1}{1-z}\left(2\log\left(\frac{2-z}{1-z}\right) - \frac{3}{2}\right)\right]_+. \quad \text{(D.61)}\end{aligned}$$

As can be seen from (D.58) and (D.60), the dependence of the partonic cross-section on the ratio of the quark masses over the squared centre-of-mass energy has been replaced by a dependence on the ratio of squared centre-of-mass energy over the typical energy scale Q of the considered process. Since this ratio is generally small, the corresponding logarithms are regularized in the sense that the partonic cross-section can be evaluated in the limit of vanishing mass of the external particles, without receiving large contributions from logarithms in these parameters.

Appendix E

The Multi-Channel Importance Sampling Technique

In the course of our work presented so far, we addressed the question how singularities arising from the resonances as well as from the soft and collinear phase-space limits can be regularized. In doing so, one is left with an amplitude which is finite in the soft, collinear and on-shell limits, but exhibits peaks when scanning over phase-space. As a result, the squared amplitude is difficult to integrate in a numerically stable way, since the most important contributions arise from only few as well as very small regions of the phase-space. A method to solve this problem is provided by the technique of *importance sampling*. The basic idea of this method is to let the phase-space generator scan the phase-space not in a uniform way, but to generate the bulk of events in phase-space regions where the integrand is large.

To see how this works in detail, consider once more a hadronic cross-section

$$\sigma_{\mathrm{P_1P_2}}(S,Q^2) = \sum_{q_1,q_2=u,\bar{u},..} \int_0^1 \mathrm{d}x_1 \int_0^1 \mathrm{d}x_2 \overline{\Phi}_{q_1|P_1}(x_1,\mu_F)\overline{\Phi}_{q_2|P_2}(x_2,\mu_F)\sigma^{\mathrm{IR-safe}}_{q_1q_2}(x_1x_2S,Q^2). \tag{E.1}$$

The quantities $\overline{\Phi}$ denote again the redefined parton distribution functions, Q is the typical energy scale for the considered process ans $\sigma^{\mathrm{IR-safe}}_{q_1q_2}$ is the infrared-safe partonic cross-section

$$\sigma^{\mathrm{IR-safe}}_{q_1q_2} = \frac{1}{2x_1x_2S}\int \mathrm{d}\Phi \left|\mathcal{A}(\Phi)\right|^2, \tag{E.2}$$

where here and in the following, we collectively denote the various phase-spaces and amplitudes contributing to (E.2) by Φ and $\mathcal{A}$. As a first complication, the hadronic cross-section (E.1) exhibits a peak in the low-energy limit $x_1, x_2 \to 0$, where the parton distributions and the flux factor $1/(x_1x_2S)$ of the partonic cross section diverge. This divergence can be avoided by imposing a lower cut $\hat{s}_{\mathrm{min}}$ on the partonic centre-of-mass energy squared. To make the implications of this cut more transparent, we substitute

$$x_1 \to \tau = x_1x_2 = \frac{\hat{s}}{S}, \qquad x_2 \to x = x_2, \tag{E.3}$$

such that

$$\sigma_{\mathrm{P_1P_2}}(S,Q^2) = \frac{1}{2S}\sum_{q_1,q_2=u,\bar{u},..}\int_{\tau_{\min}}^1\frac{\mathrm{d}\tau}{\tau}\int_\tau^1\frac{\mathrm{d}x}{x}\overline{\Phi}_{q_1|P_1}(\frac{\tau}{x},\mu_F)\overline{\Phi}_{q_2|P_2}(x,Q^2)\sigma^{\mathrm{IR-safe}}_{q_1q_2}(\tau S,\mu_F). \quad \text{(E.4)}$$

For a sufficiently large cut $\tau_{\min}=\hat{s}_{\min}/S$ on the τ integration, the arguments x and τ/x of the PDFs can then be kept away from the divergence at $x_1=x_2=0$. Furthermore, if the argument of the first PDF reaches $\tau/x=\tau_{min}$, the other PDF reaches its minimal value at $x=1$, and vice versa, such that the contributions of the PDFs to the integrand is flattened without choosing a specific mapping. However, one has now to flatten the increase of the integrand due to the factor $1/(x\tau)$. Starting with the x-integration, the mapping of x on random numbers

$$\int\frac{\mathrm{d}x}{x}=\int\mathrm{d}r\frac{\mathrm{d}x(r)}{\mathrm{d}r}\frac{1}{x(r)} \quad \text{(E.5)}$$

can be chosen to flatten the $1/x$ singularity by

$$\frac{\mathrm{d}x(r)}{\mathrm{d}r}\propto x(r). \quad \text{(E.6)}$$

Solving this equations with the initial conditions $x(0)=\tau$ and $x(1)=1$, one has

$$x(r)=\tau^{1-r},\qquad g_x(x)=\left(\frac{\mathrm{d}x(r)}{\mathrm{d}r}\right)^{-1}=-\frac{1}{x\log\tau}. \quad \text{(E.7)}$$

Here the general idea of the importance sampling technique becomes apparent. A scan over the random number used to parameterize x now shows a flat integrand, such that the corresponding integration is converging very rapidly. To put it in another way, the mapping $x(r)$ is chosen such that the bulk of events for x is generated in the interval where the integrand is large, such that the integration error of this contribution decreases more rapidly as it would be the case for a flat mapping.

The τ-integration now exhibits a peak of the form $(\log\tau)/\tau$, which can be flattened by the same procedure as adopted for x to obtain

$$\tau(r)=\tau_{\min}^{\sqrt{1-r}},\qquad g_\tau(\tau)=\left(\frac{\mathrm{d}\tau(r)}{\mathrm{d}r}\right)^{-1}=\frac{-2}{\log^2(\tau_{\min})}\frac{\log\tau}{\tau}. \quad \text{(E.8)}$$

Going back to the original integral (E.1) for the hadronic cross-section, numerical calues for x_1 and x_2 can then be obtained from inserting the expressions for x and τ in (E.7) and (E.8) into (E.3)

$$x_1=\frac{\tau(r)}{x(r')},\qquad x_2=x(r'), \quad \text{(E.9)}$$

where r, r' are the random numers used to calculate x and τ. The corresponding density g_{in} is then given by the product of the Jacobians in (E.8) and (E.7) expressed in terms of x_1 and x_2

$$g_{\text{in}}(x_1, x_2) = \frac{2}{\log^2(\tau_{\min})} \frac{1}{x_1 x_2^2} \tag{E.10}$$

As a second problem, the expressions (D.57) and (D.59) in the sum of the singular terms extracted from the virtual and real corrections exhibit a singular behavior in the limits $z \to 0$ and $z \to 1$ for the energy fraction z of the Bremsstrahlung particle. The problematic terms involve a (+) prescription, which leads to a vanishing integrand in the limit $z \to 1$. However, the denominators $1/(1-z)$ are diverging in these limit, and have thus to be regularized by an upper limit $z_{\max}$. In case of using the phase-space slicing to treat the soft and collinear divergences, this limit is naturally given by the slicing cut $z_{\max} = 1 - \delta_s$. In case of using the subtraction method, the upper limit has to be set to one minus a small but finite value. In the same way, the divergence at $z = 0$ in the first part of the (+)-prescriptions can be regularized by imposing a lower cut $\hat{s}_{\min}$ on the center of partonic mass energy $\hat{s}$, which leads to a lower integration bound

$$z_{\min} = \hat{s}_{\min}/\hat{s} = \frac{\tau_{\min}}{\tau}, \qquad z_{\max} = 1 - \delta_s. \tag{E.11}$$

The integration over z is then numerically stable, but converging slowly due to the peaks of type $1/z(1-z)$ and $1/(1-z)$.

To improve the convergence, one can again choose the mapping of z on random numbers such that the inverse Jacobian reproduces the peaking structure of the integrand. To flatten the peak of type $1/(z(1-z))$ in the first part of the (+)-prescriptions, the same steps as performed for x and τ above lead to

$$z(r) = \frac{\mathrm{e}^{\frac{r-B}{A}}}{1 + \mathrm{e}^{\frac{r-B}{A}}}, \qquad g_z(z) = \frac{A}{z(1-z)} \tag{E.12}$$

where we introduced the shorthands

$$A = \log\left(\frac{z_{\max}}{1-z_{\max}} \frac{1-z_{\min}}{z_{\min}}\right)^{-1}, \qquad B = -A \log\left(\frac{z_{\min}}{1-z_{\min}}\right). \tag{E.13}$$

The second term arising from the (+)-prescription in (D.58) and (D.60), on the other hand, only exhibits a singularity at $z = 1$ where the integrand behaves as $1/(1-z)$, such that it is not necessary to impose a lower integration bound and the mapping reads

$$z'(r) = 1 - \mathrm{e}^{r \log(1-z_{\max})}, \qquad g_{z'}(z') = -\frac{1}{\log(1-z_{\max})} \frac{1}{(1-z')}. \tag{E.14}$$

Note, that in spite of calculating the values of z and z' using different mappings, the corresponding functions $z(r)$ and $z'(r)$ coincide in the limit $r \to 1$, such that the (+)-prescription still yields a vanishing integrand in this limit.

Turning next to the phase-space integration (E.2) of the partonic cross-section, the phase-space element $\mathrm{d}\Phi$ can generally be written as

$$\mathrm{d}\Phi = (2\pi)^{4-3n} \prod_{i=3}^{n_f} \mathrm{d}^4 p_i \rho(p), \tag{E.15}$$

where

$$\rho(p) = \delta^{(4)}(p_1 + p_2 - \sum_{i=3}^{n} p_i) \prod_{i=1}^{n_f} \delta(p_i^2 - m^2)\theta(p_i^0) \tag{E.16}$$

denotes the phase-space density. Here and in what follows, we let $p = \{p_i, i = 1, \ldots, n_f\}$ collectively stand for the momenta of the n_f final-state particles. For numerical evaluation, it is convenient to replace the integration over n_f 4-momenta by the integration over a suitable, $3n_f - 4$-dimensional set Φ of kinematical variables. Considering a given diagram, the phase-space measure $\mathrm{d}\Phi$ can then formally be decomposed in terms of the phase-space elements $\mathrm{d}\Phi_t$ corresponding to the t-channel subprocesses contained in the diagram as well as the phase space elements $\mathrm{d}\Phi_s$ for the appearing $1 \to 2$ decays. For an example illustrating this decomposition see Ref.[62].

To parametrize the phase space element for a t-channel subprocess involving the incoming momenta p_1 and p_2 and outgoing momenta p_3 and p_4, a convenient choice for the integration variables is given by the azimuthal angle $\varphi^\star$ in the rest frame of $p = p_1 + p_2$ as well as the Mandelstam variable

$$t = (p_1 - p_3)^2 = p_3^2 + p_1^2 - \frac{(p^2 + p_3^2 - p_4^2)(p^2 + p_1^2 - p_2^2) - \lambda^{\frac{1}{2}}(p^2, p_3^2, p_4^2)\lambda^{\frac{1}{2}}(p^2, p_1^2, p_2^2)\cos\theta^\star}{2p^2}, \tag{E.17}$$

where $\theta^\star$ is the polar angle in the rest frame of $p = p_1 + p_2$ and

$$\lambda(x, y, z) = x^2 + y^2 + z^2 - 2xy - 2xz - 2yz. \tag{E.18}$$

The integral over the phase-space element for such a subprocess can then be rewritten as

$$\int d\Phi_t = \frac{1}{4\lambda(p^2, p_1^2, p_2^2)} \int_0^{2\pi} \mathrm{d}\varphi^\star \int_{-t_{\min}}^{-t_{\max}} \mathrm{d}|t|, \tag{E.19}$$

where the boundaries $t_{\substack{\min \\ \max}}$ are determined by (E.17) and $-1 < \cos\theta^\star < 1$ or appropriate angular cuts. In terms of these new integration variables, the momenta of the subprocess can in the parametrized as

$$p_1^\star = \begin{pmatrix} \frac{p^2 + p_1^2 - p_2^2}{2\sqrt{p^2}} \\ 0 \\ 0 \\ \pm\frac{\lambda^{\frac{1}{2}}(p^2, p_1^2, p_2^2)}{2\sqrt{p^2}} \end{pmatrix}, \; p_2^\star = \begin{pmatrix} \frac{p^2 + p_2^2 - p_1^2}{2\sqrt{p^2}} \\ 0 \\ 0 \\ \pm\frac{\lambda^{\frac{1}{2}}(p^2, p_1^2, p_2^2)}{2\sqrt{p^2}} \end{pmatrix}, \; p_3^\star = \mathcal{R}(\varphi^\star, \cos\theta^\star(t)) \begin{pmatrix} \frac{p^2 + p_3^2 - p_4^2}{2\sqrt{p^2}} \\ 0 \\ 0 \\ \pm\frac{\lambda^{\frac{1}{2}}(p^2, p_3^2, p_4^2)}{2\sqrt{p^2}} \end{pmatrix}, \tag{E.20}$$

and $p_4^\star = p_1^\star + p_2^\star - p_3^\star$, where $\mathcal{R}(\varphi, \cos\theta)$ denotes a rotation in three dimensions by an azimuthal angle φ and an polar angle θ

$$\mathcal{R}(\varphi, \cos\theta) = \begin{pmatrix} 1 & 0 & 0 & 0 \\ 0 & \cos\varphi & \sin\varphi & 0 \\ 0 & -\sin\varphi & \cos\varphi & 0 \\ 0 & 0 & 0 & 1 \end{pmatrix} \begin{pmatrix} 1 & 0 & 0 & 0 \\ 0 & \cos\theta & 0 & \sin\theta \\ 0 & 0 & 1 & 0 \\ 0 & -\sin\theta & 0 & \cos\theta \end{pmatrix}. \tag{E.21}$$

To obtain the momenta of the final-state particles in the laboratory frame, one has first to rotate $p_1^\star$ in direction of p_1, and secondly to apply a boost from the rest frame of $p_1 + p_2$ to the laboratory frame

$$p_i = \mathcal{B}(p_0, -\mathbf{p})\mathcal{R}(-\hat{\phi}, \cos\hat{\theta})p_i^\star, \qquad i = 3, 4, \tag{E.22}$$

where the matrix $\mathcal{B}(p_0, \mathbf{p})$ connects a boosted momentum q' with the original momentum q by

$$q_0' = \frac{p_0}{m}q_0 + \mathbf{pq}, \qquad \mathbf{q}' = \mathbf{q} + \frac{\mathbf{p}}{m}\frac{\mathbf{pq}}{m^2 - p_0^2} + \frac{\mathbf{p}}{m}q_0, \qquad m = \sqrt{p_0^2 - \mathbf{p}^2}. \tag{E.23}$$

The angles $\hat{\phi}$ and $\hat{\theta}$ in (E.22) are given as the azimuthal and polar angles parameterizing the spatial part of the vector $p_1^\star = \mathcal{B}(p_0, \mathbf{p})p_1$.

Turning now to the case of a particle with momentum p decaying into two particles with momenta p_1 and p_2, the integration variables can be taken to be the polar angle $\theta^\star$ as well as the azimuthal angle $\phi^\star$ in the rest frame of the decaying particle. The integral over the corresponding phase-space element then reads

$$\int d\Phi_s = \frac{\lambda^{\frac{1}{2}}(p^2, p_1^2, p_2^2)}{8p^2} \int_0^{2\pi} \mathrm{d}\varphi^\star \int_{\cos\theta_{\min}}^{\cos\theta_{\max}} \mathrm{d}\cos\theta^\star, \tag{E.24}$$

where the quantities $\cos\theta_{\substack{\min \\ \max}}$ are again given by ∓ 1 or appropriate cuts. The momenta in the laboratory frame are then given by

$$p_1 = \mathcal{B}(p_0, -\mathbf{p})\mathcal{R}(\varphi^\star, \cos\theta^\star) \begin{pmatrix} \frac{p^2 + p_1^2 - p_2^2}{2\sqrt{p^2}} \\ 0 \\ 0 \\ \frac{\lambda^{\frac{1}{2}}(p^2, p_1^2, p_2^2)}{2\sqrt{p^2}} \end{pmatrix}, \qquad p_2 = p - p_1. \tag{E.25}$$

For the numerical evaluation of an integral over the phase-space element parametrized as described above, one has therefore to generate $3n_f - 4$ random distributions for the invariants, for the azimuthal and polar angles of the decay subprocesses, as well as for the Mandelstam variables t and the azimuthal angles of the t-channel subprocesses. In practice, one generates of course random variables $r_i, i = 1, \ldots 3n_f - 4$ in the interval $[0, 1]$,

and maps these random numbers on the kinematical variables. The easiest way to do so would be a linear mapping $x = (x_{\max} - x_{\min})r + x_{\min}$ for a given kinematical variable x. However, the form of this mapping is completely arbitrary.

As was said before, the idea of the method of importance sampling is to use this freedom of choice to flatten the integrand in order to obtain a numerically stable integration. To this end, we start from a general mapping $\Phi = \mathbf{h}(\mathbf{r})$ of the random numbers $0 < r_i < 1,\ i = 1, \ldots 3n_f - 4$ on the phase-space elements Φ. The phase-space integral can then be rewritten as

$$\int \mathrm{d}\Phi\ \rho\big(p(\Phi)\big)\left|\mathcal{A}\big(p(\Phi)\big)\right|^2 = \int_0^1 \prod_{i=1}^{3n_f-4} \mathrm{d}r_i \frac{\left|\mathcal{A}\big(p(\mathbf{h}(\mathbf{r}))\big)\right|^2}{g\big(p(\mathbf{h}(\mathbf{r}))\big)}, \tag{E.26}$$

where the function g is for a single diagram given by

$$\frac{1}{g(p(\Phi))} = \rho\big(p(\Phi)\big)\left|\frac{\partial \mathbf{h}(\mathbf{r})}{\partial \mathbf{r}}\right|_{\mathbf{r}=\mathbf{h}^{-1}(\Phi)}. \tag{E.27}$$

One can now choose the function $\mathbf{h}$ such that g mimics the peaking behavior of the squared amplitude. Setting g equal to a constant times the shape of the peak, the functions h can be determined as the integral over $1/g$. The proportionality factor appearing in g as well as the integration constant contained in h can the be determined by requiring $h(0) = x_{\min}$ and $h(1) = x_{\max}$, where x denotes the kinematical variable causing the peak. To be explicit, if the propagator decaying in an s-channel subprocess or appearing in a t-channel subprocess is of Breit-Wigner type, the squared amplitude behaves as

$$|\mathcal{A}|^2 \propto \frac{1}{(k^2 - M^2)^2 + M^2\Gamma^2}, \tag{E.28}$$

and the mapping reads

$$h(r) = M\Gamma \tan\left[y_1 + (y_2 - y_1)r\right] + M^2, \qquad y_{1/2} = \arctan\left(\frac{k^2_{\min/\max} - M^2}{M\Gamma}\right), \tag{E.29}$$

whereas in the case of a propagator with mass m and vanishing width the peak and the corresponding mapping have the form

$$|\mathcal{A}|^2 \propto \frac{1}{(k^2 - M^2)^\nu}, \tag{E.30}$$

and

$$h_\nu(r) = \begin{cases} \left[r(k^2_{\max} - m^2)^{1-\nu} + (1-r)(k^2_{\min} - m^2)^{1-\nu}\right]^{\frac{1}{1-\nu}} + m^2, & \text{for } \nu \neq 1, \\ \exp\left[r\log(k^2_{\max} - m^2) + (1-r)\log(k^2_{\min} - m^2)\right] + m^2, & \text{for } \nu = 1. \end{cases} \tag{E.31}$$

The parameter ν in (E.30) can be tuned to optimize the Monte Carlo integration. The naive expectation $\nu = 2$ is not necessarily the best choice, since the propagator pole can be partially canceled in the collinear limit.

The corresponding functions g can then be calculated following the procedure described above, and one has

$$\frac{1}{g(k^2)} = \frac{(y_2 - y_1)[(k^2 - M^2)^2 + M^2\Gamma^2]}{M\Gamma} \tag{E.32}$$

in the Breit Wigner case and

$$\frac{1}{g(k^2)} = \begin{cases} (1-\nu)^{-1}\left[(k^2_{\max} - m^2)^{1-\nu} - (k^2_{\min} - m^2)^{1-\nu}\right](k^2 - m^2)^{\nu}, & \text{for } \nu \neq 1, \\ \left[\log(k^2_{\max} - m^2) + \log(k^2_{\min} - m^2)\right](k^2 - m^2), & \text{for } \nu = 1 \end{cases} \tag{E.33}$$

in case of a peak with vanishing width. Moreover, all variables x for which the squared amplitude does not exhibit a peaking behavior are mapped linearly according to

$$x = (x_{\max} - x_{\min})r + x_{\min}. \tag{E.34}$$

In summary, to flatten the resonance structure arising from a given diagram, one simply multiplies the functions g stemming from the various propagators with the mappings g_z and g_{in} as well as all prefactors arising from the decomposition of the phase-space element into s-channel and t-channel subprocesses. The resulting product then exhibits peaks at exactly the same phase-space points as the squared amplitude corresponding to the diagram, such that the integrand on the right-hand side of (E.26) to be integrated over the random numbers $\mathbf{r}$ is essentially flat. The integration can then be done by simply averaging the integrand over the integration domain. Considering our original integral on the left-hand side of (E.26), the method presented here simply achieves a concentration of the generated values for the kinematical integration variables on the phase-space regions, where the integrand contributes most, hence the name *importance sampling*.

However, up to this point, we have neglected the fact that different diagrams can lead to peaks in different phase space regions, such that one single mapping g designed to flatten the squared amplitude as a whole does generally not exist. Following the method presented so far, a single mapping can only flatten one peaking structure in one single phase-space region, leaving the integral numerically unstable due to the remaining peaks. A solution to this problem is given by the *multichannel* approach. The idea is to introduce different channels, i.e. mappings $\Phi_k = \mathbf{h}_k(\mathbf{r}), k = 1, \ldots, M$ for each of the M peaking structures of the squared amplitude, and to evaluate the phase-space integral as an average over these channels. To be explicit, the phase-space integral (E.26) for M different channels can be

written as

$$\int \mathrm{d}\Phi\ \rho\big(p(\Phi)\big)\left|\mathcal{A}\big(p(\Phi)\big)\right|^2 = \sum_{j=1}^{M}\int \mathrm{d}\Phi\ \frac{g_j\big(p(\Phi)\big)}{g_{\mathrm{tot}}\big(p(\Phi)\big)}\left|\mathcal{A}\big(p(\Phi)\big)\right|^2$$
$$= \sum_{j=1}^{M}\int_0^1 \prod_{i=1}^{3n_f-4}\mathrm{d}r_i \frac{\left|\mathcal{A}\big(p(\mathbf{h}_j(\mathbf{r}))\big)\right|^2}{g_{\mathrm{tot}}\big(p(\mathbf{h}_j(\mathbf{r}))\big)}, \quad \text{(E.35)}$$

where

$$g_{\mathrm{tot}}(p(\Phi)) = \sum_{j=1}^{M} g_j(p(\Phi)), \qquad \frac{1}{g_j(p(\Phi))} = \rho\big(p(\Phi)\big)\left|\frac{\partial \mathbf{h}_j(\mathbf{r})}{\partial \mathbf{r}}\right|_{\mathbf{r}=\mathbf{h}_j^{-1}(\Phi)}. \quad \text{(E.36)}$$

The function g_{tot} now has a peak at each point where the amplitude becomes large as well, such that the integration is numerically stable in the whole phase-space region. By explicitly summing over all peaking structures, one is furthermore sure not to miss the contribution of one of the peaks.

Finally, the numerical integration can be further improved by taking into account the size of the contribution of each peak to the final value of the phase-pace integral. For example, a peaking structure could be excluded by a cut on the energies of the external particles. In that case, one would like to suppress the evaluation of the corresponding channel to speed up the numerical evaluation. This can be done by not treating the various mappings in the same way, but to address so-called *a-priori weights* $\alpha_k \in [0,1], k = 1,\ldots,M$, $\sum_{j=1}^{M}\alpha_j = 1$ to each channel [86], which basically give the probability that the considered channel is evaluated. After a certain number of integration steps, the weights can then be optimized according to the size of the contributions of the various peaking structures, thus excluding the evaluation of those channels which do not contribute at all. In practice, one creates one more random variable $r_0 \in [0,1]$ which is used to pick the channel k to be evaluated with probability α_k. The phase space integral can then be written as

$$\int \mathrm{d}\Phi\ \rho\big(p(\Phi)\big)\left|\mathcal{A}\big(p(\Phi)\big)\right|^2 = \sum_{j=1}^{M}\alpha_j\int \prod_{i=1}^{3n_f-4}\mathrm{d}r_i \frac{\left|\mathcal{A}\big(p(\mathbf{h}_j(\mathbf{r}))\big)\right|^2}{g_{\mathrm{tot}}\big(p(\mathbf{h}_j(\mathbf{r}))\big)}$$
$$= \int_0^1 \mathrm{d}r_0\,\theta(r_0-\beta_{k-1})\theta(\beta_k - r_0)\int_0^1 \prod_{i=1}^{3n_f-4}\mathrm{d}r_i \frac{\left|\mathcal{A}\big(p(\mathbf{h}_j(\mathbf{r}))\big)\right|^2}{g_{\mathrm{tot}}\big(p(\mathbf{h}_j(\mathbf{r}))\big)}, \quad \text{(E.37)}$$

where

$$\beta_0 = 0, \qquad \beta_k = \sum_{j=1}^{k}\alpha_j, \quad k = 1,\ldots.M-1, \qquad \beta_M = 1 \quad \text{(E.38)}$$

and the total density is now given by

$$g_{\mathrm{tot}}(k(\Phi)) = \sum_{j=1}^{M}\alpha_j g_j(k(\Phi)). \quad \text{(E.39)}$$

The actual values of the a-priori weights can then be adopted during the integration. For the adaptive optimization of the weights, we here present the algorithm described in Ref. [86]. The idea is to minimize the expected Monte Carlo error after each generation of N phase-space points by using its α-dependence

$$\delta\overline{I}_n = \sqrt{\frac{W(\alpha) - \overline{I}_n^2}{N}}, \qquad W(\alpha) = \frac{1}{N}\sum_{j=1}^{N}\left[\frac{\left|\mathcal{A}\big(p(\mathbf{h}_j(\mathbf{r}))\big)\right|^2}{g_{\mathrm{tot}}}\right]^2, \tag{E.40}$$

where the Monte Carlo estimate $\overline{I}_n$ is given by

$$\overline{I}_n = \sum_{n=1}^{N}\frac{\left|\mathcal{A}\big(p(\mathbf{h}_j(\mathbf{r}))\big)\right|^2}{g_{\mathrm{tot}}}. \tag{E.41}$$

The new weights can then be calculated according to

$$\alpha_k^{\mathrm{new}} \propto \alpha_k \sqrt{\frac{1}{N}\sum_{j=1}^{N}\frac{g_k\big(p(\mathbf{h}_j(\mathbf{r}))\big)}{g_{\mathrm{tot}}}\left[\frac{\left|\mathcal{A}\big(p(\mathbf{h}_j(\mathbf{r}))\big)\right|^2}{g_{\mathrm{tot}}}\right]^2}, \qquad \sum_{j=1}^{M}\alpha_j^{\mathrm{new}} = 1. \tag{E.42}$$

For the phase-space integration in the framework of `Pole`, we used the generic Monte-Carlo generator contained in the program `Lusifer` [43]. Except for the initial-state mappings (E.7) and (E.8) this generator contains all features and methods discussed in this chapter. To determine which channels are actually possible for a given process, the generator takes as an input the possible couplings of the considered model, which is in the `Fortran` output of `Pole` provided by the file `int/model_lusifer.F`. With the help of this input, all possibilities to connect the initial state to the final state of the given process are determined and the corresponding propagator structure is stored and divided into t-channel subprocesses and s-channel decays. The output returns the momenta constructed in the way described above, as well as the density g_{tot}, by which the squared amplitude has to be divided to flatten the integrand. The final results for the integral as well as for the corresponding Monte-Carlo error are then be calculated according to (E.41) and (E.40), respectively.

Bibliography

[1] S.L. Glashow. *Nucl. Phys.*, **22**:579–588, 1961.

[2] S. Weinberg. *Phys. Rev. Lett.*, **19**:1264–1266, 1967.

[3] A. Salam. Originally printed in *Svartholm: Elementary Particle Theory, Proceedings Of The Nobel Symposium Held 1968 At Lerum, Sweden*, Stockholm 1968, 367-377.

[4] D.J. Gross and F. Wilczek. *Phys. Rev.*, **D8**:3633–3652, 1973.

[5] H.D. Politzer. *Phys. Rev. Lett.*, **30**:1346–1349, 1973.

[6] H. Fritzsch, M. Gell-Mann, and H. Leutwyler. *Phys. Lett.*, **B47**:365–368, 1973.

[7] D. Abbaneo et al. *hep-ex/0112021*, 2001.

[8] The Electroweak Working Group. *hep-ex/0412015*, 2004.

[9] S. Villa. *Nucl. Phys. Proc. Suppl.*, **142**:391–396, 2005.

[10] K. Hagiwara, R.D. Peccei, D. Zeppenfeld, and K. Hikasa. *Nucl. Phys.*, **B282**:253, 1987.

[11] U. Baur, S. Errede, and G. Landsberg. *Phys. Rev.*, **D50**:1917–1930, 1994.

[12] M.A. Samuel and T. Abraha. *hep-ph/9706336*, 1997.

[13] N. Arkani-Hamed, S. Dimopoulos, and G.R. Dvali. *Phys. Lett.*, **B429**:263–272, 1998.

[14] E.A. Mirabelli, M. Perelstein, and M.E. Peskin. *Phys. Rev. Lett.*, **82**:2236–2239, 1999.

[15] G.F. Giudice, R. Rattazzi, and J.D. Wells. *Nucl. Phys.*, **B544**:3–38, 1999.

[16] S. Dimopoulos, S. Thomas, and J.D. Wells. *Nucl. Phys.*, **B488**:39–91, 1997.

[17] S. Dimopoulos, M. Dine, S. Raby, and S. Thomas. *Phys. Rev. Lett.*, **76**:3494–3497, 1996.

[18] S. Ambrosanio, G.L. Kane, G.D. Kribs, S.P. Martin, and S. Mrenna. *Phys. Rev.*, **D54**:5395–5411, 1996.

[19] S. Ambrosanio, G.D. Kribs, and S.P. Martin. *Phys. Rev.*, **D56**:1761–1777, 1997.

[20] P. Bambade. *hep-ex/0307056*, 2003.

[21] D. Fayolle. *hep-ex/0201035*, 2002.

[22] D. Acosta et al. *Phys. Rev. Lett.*, **94**:041803, 2005.

[23] D. Acosta et al. *hep-ex/0501050*, 2005.

[24] D. Acosta et al. *hep-ex/0501021*, 2005.

[25] V.M. Abazov et al. *hep-ex/0502036*, 2005.

[26] V.M. Abazov. *hep-ex/0504019*, 2005.

[27] A.W. Askew. *Measurement of the $W\gamma \to \mu\nu\gamma$ cross section, limits on anomalous trilinear vector boson couplings, and the radiation amplitude zero in p anti-p collisions at $\sqrt{s}$= 1.96 TeV.* PhD thesis. FERMILAB-THESIS-2004-31.

[28] M.H. Kirby. *Measurement of $W + \gamma$ production in proton- antiproton collisions at $\sqrt{s}$ = 1.96 TeV.* PhD thesis. FERMILAB-THESIS-2004-32.

[29] J. Abdallah et al. *Eur. Phys. J.*, **C38**:395–411, 2005.

[30] D. Acosta et al. *Phys. Rev. Lett.*, **89**:281801, 2002.

[31] S. Haywood et al. *Electroweak physics. hep-ph/0003275*, 1999.

[32] D. De Florian and A. Signer. *Eur. Phys. J.*, **C16**:105–114, 2000.

[33] L.J. Dixon, Z. Kunszt, and A. Signer. *Phys. Rev.*, **D60**:114037, 1999.

[34] J.M. Campbell and R.K. Ellis. *Phys. Rev.*, **D60**:113006, 1999.

[35] E. Accomando, A. Denner, and A. Kaiser. *Nucl. Phys.*, **B706**:325–371, 2005.

[36] E. Accomando, A. Denner, and S. Pozzorini. *Phys. Rev.*, **D65**:073003, 2002.

[37] W. Hollik and C. Meier. *Phys. Lett.*, **B590**:69–75, 2004.

[38] R.G. Stuart. *Phys. Lett.*, B262:113–119, 1991.

[39] A. Aeppli, G.J. van Oldenborgh, and D. Wyler. *Nucl. Phys.*, **B428**:126–146, 1994.

[40] A. Aeppli, F. Cuypers, and G.J. van Oldenborgh. *Phys. Lett.*, **B314**:413–420, 1993.

[41] W. Beenakker, F.A. Berends, and A.P. Chapovsky. *Nucl. Phys.*, **B548**:3–59, 1999.

[42] A. Denner, S. Dittmaier, M. Roth, and D. Wackeroth. *Nucl. Phys.*, **B587**:67–117, 2000.

[43] S. Dittmaier and M. Roth. *Nucl. Phys.*, **B642**:307–343, 2002.

[44] S. Dittmaier. *Phys. Rev.*, **D59**:016007, 1999.

[45] T. Hahn. *Nucl. Phys. Proc. Suppl.*, **116**:363–367, 2003.

[46] F. Bloch and A. Nordsieck. *Phys. Rev.*, **52**:54–59, 1937.

[47] T.D. Lee and M. Nauenberg. *Phys. Rev.*, **133**:B1549–B1562, 1964.

[48] T. Kinoshita. *J. Math. Phys.*, **3**:650–677, 1962.

[49] V.N. Gribov and L.N. Lipatov. *Yad. Fiz.*, **15**:781–807, 1972.

[50] G. Altarelli and G. Parisi. *Nucl. Phys.*, **B126**:298, 1977.

[51] A. Sirlin. *Phys. Rev. Lett.*, **67**:2127–2130, 1991.

[52] M. Beneke, A.P. Chapovsky, A. Signer, and G. Zanderighi. *Nucl. Phys.*, **B686**:205–247, 2004.

[53] M. Beneke, A.P. Chapovsky, A. Signer, and G. Zanderighi. *Phys. Rev. Lett.*, **93**:011602, 2004.

[54] A. Denner, S. Dittmaier, M. Roth, and D. Wackeroth. *Nucl. Phys.*, **B560**:33–65, 1999.

[55] W. Beenakker et al. *Nucl. Phys.*, **B500**:255–298, 1997.

[56] U. Baur and D. Zeppenfeld. *Phys. Rev. Lett.*, **75**:1002–1005, 1995.

[57] G. Passarino. *Nucl. Phys.*, **B574**:451–494, 2000.

[58] E. Accomando, A. Ballestrero, and E. Maina. *Phys. Lett.*, **B479**:209–217, 2000.

[59] W. Beenakker, F.A. Berends, and A. P. Chapovsky. *Nucl. Phys.*, **B573**:503–535, 2000.

[60] W. Beenakker, A. P. Chapovsky, A Kanaki, C. G. Papadopoulos, and R. Pittau. *Nucl. Phys.*, **B667**:359–393, 2003.

[61] A. Denner, S. Dittmaier, and M. Roth. *Nucl. Phys.*, **B519**:39–84, 1998.

[62] M. Roth. *Precise Predictions for Four-Fermion Production in Electron-Positron Annihilation.* PhD thesis, ETH Zürich, 1999.

[63] E.N. Argyres et al. *Phys. Lett.*, **B358**:339–346, 1995.

[64] F.A. Berends et al. *Nucl. Phys.*, **B206**:61, 1982.

[65] R. Kleiss. *Z. Phys.*, **C33**:433, 1987.

[66] S. Catani and M.H. Seymour. *Phys. Lett.*, **B378**:287–301, 1996.

[67] S. Catani and M.H. Seymour. *Nucl. Phys.*, **B485**:291–419, 1997.

[68] T. Hahn. *Comput. Phys. Commun.*, **140**:418–431, 2001.

[69] T. Hahn. *Nucl. Phys. Proc. Suppl.*, **89**:231–236, 2000.

[70] J.A.M. Vermaseren. *math-ph/0010025*, 2000.

[71] T. Hahn. *Nucl. Phys. Proc. Suppl.*, **135**:333–337, 2004.

[72] G.J. van Oldenborgh. *Comput. Phys. Commun.*, **66**:1–15, 1991.

[73] G.J. van Oldenborgh and J.A.M. Vermaseren. *Z. Phys.*, C46:425–438, 1990.

[74] J. Pumplin et al. *JHEP*, **07**:012, 2002.

[75] S. Eidelman et al. *Review of Particle Physics. Physics Letters*, **B592**:1+, 2004.

[76] A.D. Martin, R.G. Roberts, W.J. Stirling, and R.S. Thorne. *Eur. Phys. J.*, **C39**:155–161, 2005.

[77] H. Spiesberger. *Phys. Rev.*, **D52**:4936–4940, 1995.

[78] S. Pozzorini. *Electroweak radiative corrections at high energies*. PhD thesis, Zürich University, 2001.

[79] A. Denner and S. Pozzorini. *Eur. Phys. J.*, **C18**:461–480, 2001.

[80] A. Denner and S. Pozzorini. *Eur. Phys. J.*, **C21**:63–79, 2001.

[81] U. Baur, T. Han, and J. Ohnemus. *Phys. Rev.*, **D57**:2823–2836, 1998.

[82] H. Weyl. *The Theory of Groups and Quantum Mechanics*. Dover, New York, 1931.

[83] B.L. van der Waerden. *Group Theory and Quantum Mechanics*. Springer, Berlin, 1974.

[84] D.Y. Bardin, M.S. Bilenky, D. Lehner, A. Olchevski, and T. Riemann. *Nucl. Phys. Proc. Suppl.*, **37B**:148–157, 1994.

[85] S. Dittmaier. *Nucl. Phys.*, **B565**:69–122, 2000.

[86] R. Kleiss and R. Pittau. *Comput. Phys. Commun.*, **83**:141–146, 1994.

Acknowledgments

- First of all, I am very grateful to Ansgar Denner for providing me with the interesting topic of this thesis. He was always available to answer my questions, and his patient and pedagogical way of explaining physics contributed much to the fact that I enjoyed my work at any time during the past three years.

- I would also like to thank Daniel Wyler, who provided the support at Zürch University as well as the legendary pre-Christmas "Fondue & Bowling" events.

- I am further grateful to Markus Roth for providing and explaining the phase-space generator Lusifer, to Thomas Hahn who helped me out in Problems with FeynArts and FormCalc, to Elena Accomando for her patience in the long and dark hours of numerical comparison, as well as to Phillipp Höfliger for allowing me to run parts of my processes on his computer.

- I am furthermore grateful to all my colleagues at Zürich University and at the PSI for contributing joyful entertainment during the lunch and coffee breaks. Among them, I would like to set apart my office mates Lars and Andreas, who helped me out with discussions and advices whenever problems appeared, Kai Diener (including Doerthe & Cordt) for providing valuable contributions to both, my life on the professional and on the private side, and finally my card-game fellows Tobias "Atze" Goerdt, The Dark Lord of Coffee Enrico "Rrräh" Lunghi, Tobias "Minni Oma" Huber, Lucky Daniel, Tobi "Uma" Kaufmann and Alejandro "The Body" Daleo for defeating me every single week in "Doppelkopf".

- Outside the world of physics, I was lucky to have a bunch of friends with whom life in Zürich was a lot of fun. I would here like to set apart my flatmates Fiffi, Nicolas, Phillipp, Christian as well as my semi-flatmate Nicole for making me spend many painful Sundays on the couch, as well as the Salornay-team for unforgettable summer weeks in Burgundy and Morocco.

- I thank also my girlfriend Raphaëlle Dianoux for wonderful weekends and vacations, for showing continuous interest in my work in spite of my somewhat contradictory reports about the status and end of my thesis and for making me an expert in changing trains through French customs in less then four minutes.

- Finally, I would never have been able to finish my university and PhD studies without the continuous mental support of my parents Elisabeth and Manfred Meier and my brother Uli Meier.